A Chemo-Mechanical Approach to Model Cell Contraction and Spreading on Elastic Substrates

by

Mehdi Farsad

B.Sc., Sharif University of Technology, 2000

M.Sc., Sharif University of Technology, 2002

A thesis submitted to the

Faculty of the Graduate School of the

University of Colorado in partial fulfillment

of the requirements for the degree of

Doctor of Philosophy

Department of Civil, Environmental, and Architectural Engineering

2011

This thesis entitled:
A Chemo-Mechanical Approach to Model Cell Contraction and Spreading on Elastic Substrates
written by Mehdi Farsad
has been approved for the Department of Civil, Environmental, and Architectural Engineering

Prof. Franck Vernerey

Prof. Richard Regueiro

Date

The final copy of this thesis has been examined by the signatories, and we find that both the content and the form meet acceptable presentation standards of scholarly work in the above mentioned discipline.

Farsad, Mehdi (Ph.D., Civil Engineering)

A Chemo-Mechanical Approach to Model Cell Contraction and Spreading on Elastic Substrates

Thesis directed by Prof. Franck Vernerey

Abstract

Biological tissues are very particular types of materials that have the ability to change their structure, properties and chemistry in response to external cues. Contractile cells, i.e. fibroblasts, are key players of tissue adaptivity as they are capable of reorganizing their surrounding extra-cellular matrix (ECM) by contracting and generating mechanical forces. This contractile behavior is attributed to the development of a stress-fiber (SF) network within the cell's cytoskeleton, a process that is known to be highly dependent of the nature of the mechanical environment (such as ECM stiffness or the presence of stress and strain). To describe these processes in a consistent manner, the present thesis introduces a multiphasic formulation (fluid/solid/solute mixture) that accounts for four major elements of cell contraction: cytoskeleton, cytosol, SF and actin monomers, as well as their interactions. The model represents the cross-talks between mechanics and chemistry through various means: (a) a mechano-sensitive formation and dissociation of an anisotropic SF network described by mass exchange between actin monomer and polymers, (b) a bio-mechanical model for SF contraction that captures the well-known length-tension and velocity-tension relation for muscles cells and (c) a convection/diffusion description for the transport of fluid and monomers within the cell. Numerical investigations show that the multiphasic model is able to capture the dependency of cell contraction on the stiffness of the mechanical environment and accurately describes the development of an oriented SF network observed in contracting fibroblasts. From a numerical view-point, cell and substrate are discretized on a single, regular finite element mesh, while the potentially complex cell geometry is defined in

terms of a level-set function that is independent of discretization. Field discontinuities across the cell membrane are then naturally enforced using enriched shape functions traditionally used in the XFEM formulation. The resulting method provides a flexible platform that can handle complex cell geometries, avoid expensive meshing techniques, and can potentially be extended to study cell growth and migration on an elastic substrate. In addition, the XFEM formalism facilitates the consideration of the cell's cortical elasticity, a feature that is known to be important during cell deformation. The proposed method is illustrated with a few biologically relevant examples of cell-substrate interactions. Generally, the method is able to capture some key phenomena observed in biological systems and displays numerical versatility and accuracy at a moderate computational cost.

Recent research have shown that cell spreading is highly dependent on the contractile behavior of the cell and mechanical properties of the environment it is located in. The dynamics of such process is critical for the development of tissue engineering strategy but is also a key player in wound contraction, tissue maintenance and angiogenesis. To better understand the underlying physics of such phenomena, this presentation describes a mathematical formulation of cell spreading and contraction that couples the processes of stress fiber formation, protrusion growth through actin polymerization at the cell edge and dynamics of cross-membrane protein (integrins) enabling cell-substrate attachment. The model is based on mixture model which accurately capture the interactions and mass exchange between three constituents, namely, the cell's cytoskeleton, actin monomers and stress fibers. On the one hand, monomers are allowed to polymerize into stress fiber to generate contraction while on the other hand, they may polymerize into an actin meshwork at the cell's boundary to push the membrane forward. In addition, a mechano-sensitive model of the diffusion and attachment integrins to the substrate permit to quantify the physics of the above processes in terms of substrate mechanical properties. A numerical solution of this moving boundary problem is then derived using the extended finite element method, combined with a level-set formulation. Consistent with experimental observations, our model is able to capture

the dependency of cell spreading area and contraction on substrate stiffness and the cell's mechanical environment.

Dedication

To my father who granted his life to me.

To my mother, my wife, my lovely son and daughter, my sister, and my brothers.

Acknowledgements

I would like to thank my advisor, Professor Franck Vernerey, for his great support throughout the past three years of my life at University of Colorado, Boulder. With his endless help, I have gained so much in the field of bio-mechanics, as well as accomplished my PhD research. I am continually inspired by his commitment to his research and his teaching.

I would also like to thank Prof. Ronald Pak, Prof. Richard Regueiro, Prof. Harihar Rajaram, and Prof. Stephanie Bryant for serving in my committee. I am grateful for their valuable guidance and insights. In particular, I would like to thank my friend, Prof. Alireza Doostan who helped me with his most valuable constructive ideas.

I also would like to thank my research group members: Mohammadreza Kabiri, Noom, Louis, Valentin, Erick, Krista, Lauren, Ralph, Jonathan, and Spencer for sharing their knowledge and ideas with me. I was very fortunate to have their support and encouragement throughout my studying process.

My great appreciation goes to my parents, Mohammadvali Farsad and Nasrin Amyari. Especially to my Father, who has passed away during my PhD program, he has not only given me love, support, but also his critical thinking and enthusiasm particularly to my career.

Above all, I would like to thank my beloved wife, Azadeh Khazaei who helped me throughout the work. Her endless help, love, and encouragement will continue to inspire me in the future. I appreciate her help and her support, without her I doubt that I would be confident in my work. Together with my dedication, here, I send my love to my kids, Kiyarash and Keemia, my sister, Mandana, and my brothers, Mohsen and Alireza.

Contents

Chapter

1 Introduction 1

2 An Eulerian/XFEM Formulation for the Large Deformation of Cortical Cell Membrane 11

2.1 Abstract 11

2.2 Introduction 12

2.3 Kinematics 15

2.3.1 Generalities 15

2.3.2 Deformation measures 16

2.3.3 Evolution equation of the cortical membrane orientation 17

2.4 Governing equations and constitutive relations 18

2.4.1 Principle of virtual power and governing equations 18

2.4.2 Constitutive relation 21

2.5 Numerical solution: an XFEM strategy 23

2.5.1 Extended finite element method (XFEM) 23

2.5.2 Linearized XFEM equations 25

2.6 Numerical investigation of the role of the cortical membrane on cell deformation 30

2.6.1 Effect of cortical stiffness on cell deformation 30

2.6.2 Relationship between cortical stiffness and membrane curvature . . . 31

2.6.3 Relative influence of cytoskeleton and cortical membrane on cell contraction . . . 32
2.7 Summary and conclusions . . . 34

3 Bridging the Scales to Explore Cellular Adaptation and Remodeling 40
3.1 Abstract . . . 40
3.2 Introduction . . . 40
3.3 From molecular sensing to cell organization . . . 42
3.4 From cell contraction to tissue deformation . . . 46
3.5 Conclusion . . . 48

4 A Constrained Mixture Approach to Mechano-Sensing and Force Generation in Contractile Cells 50
4.1 Abstract . . . 50
4.2 Introduction . . . 51
4.3 Constrained mixture description of cells . . . 54
4.3.1 Continuum assumptions and kinematics . . . 54
4.3.2 Anisotropic SF distribution . . . 57
4.4 Mass transport and mass exchange . . . 59
4.4.1 Mass balance of individual constituents . . . 60
4.4.2 Mass balance of the mixture . . . 62
4.4.3 Mass transport through the cytoskeleton . . . 62
4.4.4 Mass exchange and SF formation . . . 63
4.5 Force generation and mechanical equilibrium . . . 65
4.5.1 Mechanical equilibrium of the cell . . . 65
4.5.2 Active contraction of SF . . . 66
4.5.3 Cytoskeleton elasticity . . . 71
4.6 Model prediction . . . 72

4.6.1 Non-dimensionalization and solution strategy 73
4.6.2 Homogeneous cell contraction 74
4.6.3 Contraction of a square cell attached at its corners 77
4.6.4 Effect of cell morphology on cell SF structure 81
4.7 Concluding remarks 82

5 An XFEM-based numerical strategy to model mechanical interactions between biological cells and a deformable substrate 87
5.1 Abstract 87
5.2 Introduction 88
5.3 A constrained mixture model of contractile cells 91
5.3.1 Continuum description of cell's structure 91
5.3.2 Balance of mass and SF evolution 93
5.3.3 Balance of momentum 94
5.3.4 Fluid flux and cytoskeleton elasticity 95
5.3.5 Mechano-sensitive SF formation and contraction 97
5.4 Governing equations for the cell-substrate interaction problem 100
5.4.1 Substrate elasticity 101
5.4.2 Adhesion complexes 101
5.4.3 Summary of the governing equations under plane stress conditions: Strong form 102
5.4.4 Summary of the governing equations: Weak form 104
5.5 Levelset- XFEM formulation 105
5.5.1 Numerical strategy for cell-substrate interactions 105
5.5.2 Multifield Extended Finite-Element formulation 108
5.5.3 Discretization and time integration 109
5.6 Numerical investigation of cell contraction on elastic substrates 111

5.6.1 Convergence analysis 113
5.6.2 Effect of cell morphology on SF development 114
5.6.3 Effect of substrate's stiffness on cell contraction and deformation . . . 115
5.6.4 Effect of cortical stiffness on cell contractility 116
5.7 Summary and Concluding remarks 117

6 A mathematical model to characterize the chemical mechanical interactions in cells and their effect on spreading and contraction 123
6.1 Abstract 123
6.2 Introduction 124
6.3 Mathematical model of cell contraction/growth 128
6.3.1 Mass balance 131
6.3.2 Momentum balance of mixture 133
6.3.3 Free energy and equilibrium state of constituents 137
6.3.4 The rate of growth 144
6.4 Numerical solution of governed equations 146
6.4.1 Numerical strategy for cell contraction/spreading on substrate 146
6.4.2 Discretization and time integration 149
6.4.3 Cell growth and levelset evolution 152
6.5 Simulations to verify the mathematical model 153
6.5.1 Effect of substrate stiffness on cell contractile and spreading behavior 154
6.5.2 Effect of ligand concentration on cell contractile and spreading behavior 157
6.6 Summary and concluding remarks 158

7 Summary, Concluding Remarks, and Suggestions for Future Work 164

Bibliography 170

Appendix

A Computing angular SF distribution using structure matrix 184

B Governing equations for plane stress assumptions 187

C Incremental weak form of the governed equations 189

D Discretized form of the governed equations 192

E Components of final equation (6.72) 196

F Computing the details of equations (6.74)-(6.76) 199

Tables

Table

2.1 Physical constants used in simulations 30

4.1 Parameters used in the simulations. 75

5.1 Parameters used in the simulations. 112

6.1 Parameters used in the simulations. 154

Figures

Figure

2.1 Initial and current configuration of cell in a two-dimensional plane x-y. . . . 16

2.2 The general outline of a cell along with the surrounding matrix and boundary conditions. . . . 18

2.3 a) enriched nodes and completely enriched elements for a closed interface. b) level-set function and cutting plane to define a circular cell in a square domain. c) a typical Heaviside (step) function to define strong discontinuity. d) a typical ridge function to define weak discontinuity. . . . 25

2.4 The updated Lagrangian algorithm used in the nonlinear solution of the XFEM equations to determine cell deformation. . . . 36

2.5 (a) Initial configuration and (b) Deformed configuration of a cell on adhesion islands ([14]). (c) deformed configurations of a square cell without and (d) with cortical membrane. . . . 37

2.6 The models used in the analytical and numerical solutions. a) The deformed configuration of the cell to be modeled, b) the analytical model and c) the numerical model. . . . 37

2.7 Effect of normalized cortex's stiffness on normalized membrane curvature predicted by the numerical (XFEM) and theoretical solutions. . . . 38

2.8 Effect of the cytoskeleton's Young's modulus on the normalized curvature of the cortical membrane. . . . 38

2.9 Effect of cytoskeleton's Poisson's ratio on the normalized curvature of cortical membrane. 39
2.10 Effect of cortical contraction (surface tension) on the normalized curvature of the cortical membrane. 39

3.1 Multiscale decomposition of important biological processes responsible for tissue remodeling. 41
3.2 Molecular mechanisms of SF formation and contraction. The feedback mechanism between the two phenomena constitutes the basis of the proposed model. 42
3.3 (a) Prediction of SF distribution on stiff substrate, (b) observation from [18, 117, 61, 19] and (c) resulting substrate deviatoric stress (model prediction). (d) Cell architecture and force generation in terms of substrate stiffness (model predictions). 45
3.4 a) Predicted substrate stress (deviatoric) and SF distribution when the substrate stiffness in the horizontal direction is 100 times that in the vertical direction. (b) Predicted substrate stress (deviatoric) and SF distribution for an elogated cell on an isotropic substrate. A comparison with experimental observation of SF distribution as reported in [18, 117, 61, 19] 48

4.1 *Illustration of the continuum formulation of the cell [117], decomposed into the cytoplasm and the cortical membrane. In the cytoplasm, a material point is seen as a mixture of four constituents, namely the passive cytoskeletal network, the contractile SF, the cytosol and dissolved G-actin monomers.* 55
4.2 Illustration of SF volume fraction at a continuum point and its representation with a Von-Mises distribution function. 58
4.3 Relationship between parameters b and η. 59
4.4 Decomposition of the Cauchy stress. 67

4.5 *Active and passive response of a SF . The uniaxial contractile stress is T^p and the normal strain ϵ is a function of the ratio of the final fiber length ℓ and initial fiber length ℓ_0.* 68

4.6 *(a) Strain-tension relationship $f(\epsilon)$ and (b) strain-rate tension relationship $g(\dot{\epsilon})$ are used in the study to capture the length and velocity-tension relation, respectively, observed in muscle cells.* 69

4.7 Three-dimensional representation of the cell contraction $T^\star$ as a function of SF strain ϵ/ϵ_0 and strain rate $\dot{\epsilon}/\dot{\epsilon}_0$. 70

4.8 *(a) The geometry of the cell and boundary conditions. The cell of length $\ell_0 = 40\mu m$ is free to contract in the vertical direction but is constrained in the horizontal direction by linear springs of stiffness K. b) Generated SF at steady state.* 76

4.9 *Time evolution of cell deformation, contractile stress and SF anisotropy for different values of support stiffness $K^\star$.* 77

4.10 *Time evolution of cell deformation, contractile stress and SF anisotropy for different values of mechano-sensitivity coefficient k_1^f.* 78

4.11 *Effect of support stiffness on steady state cell deformation, contractile stress and SF anisotropy for different values of mechano-sensitivity coefficient $k_1^{f\star}$.* 79

4.12 *SF volume fraction ϕ^p and distribution at steady-state for three values of support stiffness (ranging from very low to very high). The principal direction of SF are indicated by lines and the parameter η refers to the degree of anisotropy ($\eta = 0.5$ for an isotropic network and $\eta = 0$ for an unidirectional fiber direction). The polar fiber distribution ($\phi_\theta^p(\theta)$) is also shown for 5 characteristic points in the cell.* 84

4.13 *Steady-state contractile force F at focal adhesions as a function of support stiffness $K^\star$ as predicted with the proposed model. The steady-state morphology and corresponding SF distribution are are shown for characteristic values of $K^\star$. For comparison, experimental results from Ghibaudo et al. [62] on the variation contractile forces in terms of pillar stiffness (spring constant) are also reported.* 85

4.14 *Mechanical work of the cell in terms of substrate stiffness : Qualitative comparison of model prediction and experiments on cardiomyocytes [51]* 85

4.15 *Effect of cell morphology on SF distribution. (a) Definition of focal adhesion complexes, boundary conditions and finite-element discretization ($\ell_0 = 40\mu m$). (b) Computed SF orientation and density for three different shapes and (c) comparison with experimental observations of fibril distribution in cardiomyocytes by Parker and co-workers [18, 117, 61, 19]* 86

5.1 A typical cell on a substrate: the definition of domains and boundaries, and cell's main constituents. 92

5.2 Equilibrium of forces in the body and boundary of a cell. 94

5.3 Initial and current configurations of cell and substrate domains. 97

5.4 Feedback mechanism between SF formation and contraction 98

5.5 Tension of a single stress fiber as a function of strain and rate of strain. . . . 100

5.6 The general details of adhesion complexes between cell and substrate combined of integrins and ligands; together with the boundary conditions applied to cell and substrate. 102

5.7 (a) Example of levelset function used to describe cell geometry, (b) Heavy side and (c) Ridge functions used to enrich the finite element interpolation. (d) Degrees of freedom associated with nodes in and outside of the cell. The enriched nodes are shown with blue squares. 106

5.8 The nonlinear updated Lagrangian algorithm used to solve Eq. (5.52). 111

5.9 a) Discretization convergence of the numerical solution to estimate average SF volume fraction in cell by changing mesh size. b) Proof of quadratic convergence of the discretization according to Eq. 5.54. 119

5.10 Linear convergence of the nonlinear solution method 119

5.11 a-d) Initial configurations of cells with different shapes on substrate. The dimensions of the adhesion island are $1.5\mu m \times 1.5\mu m$ for all cases. e-h) Deformed configuration of the cells together with the first invariant of the stress in the substrate. i-k) Experimental results of SF formation in myocites ([18, 117, 61, 19]). l-n) Deformed configuration cells with different shapes together with their stress fiber orientation in steady state to be compared with the experiments depicted in parts i-k. 120

5.12 Changes of the normalized force applied to the substrate by the cell in an adhesion island as a function of normalized substrate's stiffness and normalized time, together with the volume fraction and orientation of SFs generated in the cell. 121

5.13 The changes of the work done by focal adhesion force on the cell with substrate's stiffness; and the substrate's first invariant of stress tensor I_1 for different substrates young's modulus: a) $E^s = 1\ Pa$, b) $E^s = 1000\ Pa$, c) $E^s = 20000\ Pa$. 121

5.14 The effect of cortex stiffness on its curvature and SFs formation. a) $E_\sigma = 0$, b)$E_\sigma = 100N/m$. 122

6.1 General configuration of an axisymmetric cell located on an elastic substrate, and cell's main constituents 129

6.2 Integrin-ligand complexes: a) Ligands, low affinity integrins, and bound/unbound high-affinity integrins, b) Integrin states, c) relative displacement between two sides of integrin-ligand complex. 130

6.3 A cycle of actin polymerization beneath the cell membrane: a) G-actin monomers try to insert between the existing filament and cell membrane, b) Cell membrane is bent such that one monomer is bound at the end of the existing filament, and c) Cell membrane returns to its unbent configuration. 142

6.4 (a) Levelset function, enriched element and enriched nodes, (b) Heavy side and (c) Ridge functions used to enrich the finite element interpolation. . . . 147

6.5 a) Changes of cell area and stress fiber volume fraction during growth for different substrate stiffness, and b) a) Experimental results of reference [180]. 161

6.6 Changes of cell area and high-affinity integrin concentration at steady state for different substrate stiffness, and comparison with experimental results of [138] 162

6.7 Changes of cell area at steady state for different ligand concentration, and comparison with experimental results of [129] 162

6.8 Changes of integrin-ligand complex force at steady state for different substrate stiffness and ligand concentration, and comparison with experimental results of [62] 163

A.1 Illustration of SF volume fraction at a continuum point and its representation with a Von-Mises distribution function. 185

A.2 Relationship between parameters b and η. 186

Chapter 1

Introduction

Biological tissues are very particular types of materials that have the ability to change their structure, properties and chemistry in response to external cues. This fast response capability can be attributed to the out-of-equilibrium nature of the tissue structure, resulting from a constant cross-talk between a population of cells and their surrounding extra-cellular matrix (ECM). These interactions allow cells to sense stimuli conveyed by the ECM [95] (such as force, deformation or flow) and the ECM to restructure due to the action of cells (characterized by traction forces [149, 34] or enzyme degradation [166]). In this context, a large number of studies have demonstrated that cell contraction and architecture were strongly dependent on substrate stiffness [169, 139, 70, 98], giving mechanics a central role in cell-substrate interactions. Experimental studies on contractile cells (such as myofibroblasts) generally show that larger substrate stiffness results in higher cell stability that manifests itself by large spreading areas and generation of significant traction forces. In addition, actin staining procedures have shown that fibroblast contraction is associated with the formation of highly aligned stress-fibers (SF) within the cell's structure (cytoskeleton) that anchor at the point of cell-substrate adhesion and often span the entire length of the cell. The distribution and orientation of these fibers correlate very well with the presence of contractile forces applied by cells to their underlying substrate. These phenomena clearly illustrate the intricate interplay between mechano-sensing, force generation and cytoskeletal structure, which is essential to tissue remodeling.

Despite our more and more accurate understanding of the molecular mechanisms responsible for contraction, there are still many questions concerning the nature and mechanisms of mechano-sensing and force generation [160]. To tackle these questions, it is necessary to develop mathematical models that are capable of describing the cross-talk between cellular mechanics and biochemistry in a quantitative fashion. From a modeling standpoint, cell contractility has often been considered in terms of prestress or prestrain, either within the context of fibrous networks [107] or continuum mechanics [110, 166]. While such simplified models capture well the mechanical aspects of cell contraction, they are unable to explain many features occurring from chemo-mechanical interaction at the molecular scale, such as dependency of contractility on substrate stiffness and ligand density. More recent studies by Desphandes et al. [37, 39] introduced a bio-mechanical model that is able to describe cytoskeleton contraction by considering molecular mechanisms associated with SF formation and focal adhesion assembly. This approach provides a promising means of capturing the chemo-mechanics of cell contraction but it neglects the multiphasic aspect of the cell's body in which monomer transport, interstitial fluid (cytosol) pressure and mass exchange can take place. The inclusions of the above physics is critical to respect fundamental physical principles such as mass conservation, but also in capturing key cellular phenomena such as osmotic loading and transport phenomena. In continuum mechanics, these types of phenomena have traditionally been described by the theory of porous media and mixtures [12, 13, 155, 17, 127, 144, 166]; these formulations were very successful in describing phenomena such as growth [86, 58], free swelling [144] and osmosis [66]. Applications to the cell have thus far been limited to the flow-dependent mechanical response and swelling behavior of chondrocytes in response to their osmotic environment [68].

Recent studies have highlighted the role of the cortical membrane on cell deformation. This important component of the cell's cytoskeleton can be described as a dense layer of actin bundles beneath the surface membrane ([84, 142]) that acts as a protective layer against cell damage. This thin actin layer is also known to play a large role during cell migration in three-

dimensional environments by initiating bleb formation on the surface of cells ([154, 33, 52]). A number of models have been proposed to better understand the behavior of the cortical membrane and its role in cell morphology. Hansen et al. ([72, 73]) developed a numerical network model to establish a connection between the elasticity of red blood cell membrane and its random molecular structure. Other relevant studies include the work of Bar-zive ([3]) on the phenomenon of pearling caused by mechanical interactions between surface tension and the elasticity of the actin cortex below the membrane ([77, 92]). In this approach, a simple model based on a line tension approximation of cortical membrane elasticity provided good prediction of cell shape in different environments. This was followed by the work of Bischofs et. al. ([14]) in which the authors derived an analytical model based on Laplace's law to investigate the influence of the cortical membrane on the shape of contractile fibroblasts attached to periodically distributed adhesion islands. By comparing their model with experimental observations, they showed that the method could predict the magnitude of the membrane curvature for cells of different sizes. While the aforementioned studies concentrated on the role of cortical membrane only, the properties of the (bulk) cytoskeleton are also known to play a significant role on cell morphology. Accurate mechanical models of cells should therefore consider the combined effects of bulk cytoskeleton and cortex elasticity. However, from a computational viewpoint, the difference of length-scales between a cell (50-500 microns) and its cortical membrane thickness (less than a micron) poses a challenge that is inherent to most multiscale problems ([162]); providing an accurate description of the cortical membrane on the length-scale of a single cell results in a very expensive numerical problem and vice-versa. This may explain why existing models of cell deformation have neither considered the cortical membrane nor have presented a coarse description of it ([158]).

During spreading, cell extends a branched network of actin filaments on the border of cell called lamellipodia [30, 64, 115, 124]. Lamellipodia is typically 0.5 μm thick and 1-10 μm long from front to back [30]. Lamellipodia protrusion depends on actin polymerization

that depends on signals received according to the cell's environment mechanical properties [31, 126]. The polymerization of actin fibers leads to the generation of physical force beneath the plasma membrane that pushes it forward [32, 40, 115, 124]. Also, some research show that in spreading/migrating cells, there are periodic contractions of lamellipodia that depend on cell's environment properties. The period of contraction depends on F-actin movement along lamellipodia. They proved that cofilin decreases the period and shortens lamellipodia width [63]. In contrast with the pushing force, the resistance of membrane as an elastic material, and the instantly backward movement of the generated fiber network (called retrograde flow), prevents cell spreading [159, 167, 177]. Retrograde flow may be the result of contractile force that comes from myosin motors [137, 89]. At the end of spreading, cell optimizes its surface by enhancing the adhesion to the substrate on the edges of the cell, and by the contraction of polymerized stress fibers in the body of the cell.

Focal adhesions provide a mechanical attachment between cell membrane and substrate (or extracellular matrix). These adhesion complexes are multi protein links generated as the result of mechanosensing (feeling substrate mechanical properties by cell and responding to them [15]). The cell part of focal adhesions (Fig. 6.2) includes on-membrane proteins called integrins, and a submembrane plaque consists of a lot of proteins such as talin, α-actinin, filamin, FA kinase, vinculin, paxillin, and tensin [36]. Some of these proteins provide the mechanical requirements for the adhesion beneath the membrane, while some others receive or send signals to form or dissociate the adhesion [36]. It has been observed in previous research that the formation of FAs is a function of the traction generated in the cell-substrate contact area, such that, the traction increases the concentration of adhesion complexes [151, 123, 11, 182, 112, 111]. Also, it has been proved that the mentioned traction changes by the shape of cell and the cytoskeleton's structure [116, 20, 23]. On the substrate side of focal adhesions, the mechanical properties of substrate and the density of ligands are important factors determining the formation of FAs and their concentration [138, 99]. Previous observations proved that greater substrate stiffness and higher ligand concentration

on its surface lead to increase in formation of FAs [129, 138].

Mechanical models of cells can generally be split in two categories: formulations based on prestress fibrous network [107, 14] and those based on continuum mechanics [110, 166]. Due to their flexibility, continuum models are thus far been successful at capturing the chemo-mechanical interactions responsible for the mechano-sensitivity of cells ([37, 39]). For instance, mixture models have proved very efficient at accurately characterizing certain key mechanisms of cell behavior, including transport, chemical reaction and mass exchange [165]. In addition, the role of the cortical membrane surrounding the cell, known to be a critical player in cell deformation, has been the object of several modeling investigations. Models based on fibrous network mechanics have been the first to provide compelling arguments onto the role of membrane stiffness on cell curvature [14]. However, more recently, we have shown that continuum models can naturally incorporate the effect of cortex stiffness with a surface elasticity formulation based on the extended-finite element method [163]. The issue of modeling mechanical interactions between cells and a substrate have mostly been achieved by via cohesive laws in finite element models ([103, 125, 178, 176]).While successful at capturing interesting behaviors such as debonding, this strategy generally suffers from the fact that cell and substrate are defined on two distinct domains that typically exhibit complex geometries and possibly evolve in time. In many cases, such methods consequently leads to potential meshing issues and require a very fine discretization to reach accurate results. In addition, these models are not able to consider chemo-mechanical interactions happen on cell membrane and substrate surface to generate adhesion complexes. To fill this gap, the authors of reference [36] presented a mechanism based on integrins chemo-mechanical free energy equilibrium on cell membrane to describe what happens during integrin-ligand complex formation. But their research does not consider the vital effect of pushing and resisting forces during cell spreading as well as the effects of considering cell as a mixture. Furthermore, some models were presented to describe the rate of cell or fillopodia growth based on the fact that polymerization of new actin filaments beneath the membrane is the fundamen-

tal phenomenon leads to cell/fillopodia spreading [122, 93]. In another recent approach, the authors of reference [83] integrated in their model the kinematics of fish epidermal keratocyte growth and kinetics of the proteins that play important role in extension/detachment steps of cell crawling/spreading. But membrane forces and chemo-mechanical interactions on cell membrane between integrins cannot be captured in this model.

In this thesis, we fill the mentioned gaps above as it follows:

Chapter 2 proposes to consider the actin cortex as a two-dimensional membrane, of negligible thickness, surrounding the cell. In this context, modeling cortical membrane mechanics can be cast within the framework of surface elasticity, originally introduced by Gurtin and Murdoch in ([71]). Existing work on surface elasticity have traditionally concentrated on surface effects in nanomaterials ([54, 181]) in the context of infinitesimal deformation. However, because cell deformation can be quite significant in many applications, a contribution of this chapter is to extend the surface elasticity formulation to the case of large deformation and to investigate its predictive power on the influence of cortical membrane on cell deformation. The equations of surface elasticity are therefore redefined in the general case of large deformation, following an Eulerian approach. As such, we develop the equation of equilibrium for the general case of a cell embedded in a matrix, for which the effect of the cortical membrane is important. A numerical strategy, based on the extended finite element method (XFEM) is then introduced in order to solve the system of coupled partial differential equations. The presented method possesses the following advantages. First, the presented framework uses Eulerian formulation that is suitable for large deformations of the cell. Second, the geometry of the cell is entirely defined by level-set functions that are defined independently from the finite element mesh. Simple, regular FEM meshes may thus be used regardless of the geometric complexity of the cell. Third and finally, the different elastic properties and constitutive response of cell cortex is described with a continuum description that naturally fits into the XFEM methodology. Thus, no special treatment is necessary to model jumps in stress, strain and displacement arising due to the cortical membrane.

Chapter 3 discusses recent efforts [163, 161, 165] that have been undertaken to understand certain aspects of tissue dynamics by integrating mechano-chemical interactions from molecular to tissue scale via a hierarchical multiscale paradigm. We particularly concentrate on explaining the mechanisms by which the mechanical environment (stiffness, attachment, stress) of a tissue influences its structural evolution. Numerous experimental studies have shown that at the tissue scale, remodeling is partially due to the generation of contractile stresses by cells (such as myofibroblasts) on their surrounding fibrous matrix [174, 5, 76]. At the cellular scale, cell contractility is explained by mechano-sensitive molecular processes which govern the formation of *stress-fibers* (SF), that are mechanically active components of the cytoskeleton. While the above phenomena involve a variety of complicated signaling pathways that are studied in details by the biology community, the objective of the present study is to develop robust and flexible framework that can incorporate such biologically relevant phenomena in the future. Thus, for the time being, we present an experimentally and physically motivated empirical model, in which we show here that while occurring at different time and length-scales, mechanisms at cellular and tissue levels can be integrated in a single modeling framework, enabling us to obtain some useful insights. In particular, the model suggests that feed-back mechanisms occur both at the molecular and cellular levels, allowing tissues to timely react to any change in their mechanical environment.

Chapter 4 proposes to extend the range of applications of mixture models to describe the coupled biochemical/mechanical processes responsible for cell contraction. The formulation is based on a description of cells that incorporate four key components of contractility: a passive solid cytoskeleton, an interstitial fluid representing the cytosol, an anisotropic network of SF and a pool of globular actin monomers that freely diffuse in the cytosol. To address the well known difficulties regarding to stress partitioning and boundary conditions associated with classical theory of mixtures [128], we take the following approach. First, it is assumed that the two solid constituents (passive cytoskeleton and SF) undergo the same motion, which is consistent with the class of constrained mixture models introduced in [86].

Second, we adopt key concepts of poromechanics[153] that consists of describing the motion of a fluid constituents relative to solid constituent through diffusion-type relation (initially originated by Fick and Darcy). In this context, the mixture problem is well-posed and provide a flexible and robust theoretical framework to study the interactions between mechanics and chemistry (incorporating mass and energy exchange between constituents). The key features of the proposed model are as follows: (a) The SF network is described in statistical terms with a Von-Mises distribution whose characteristics (mean, deviation) evolve in time. (b) The generation of contractile force by SF follows length-tension and velocity-tension curves that are known to accurately capture the behavior of sarcomeric structures. (c) The anisotropic formation and dissociation of the SF network depend on the level of contractile stress in existing SF and (d) SF formation is limited by the diffusion and quantity of globular actin monomers present in the cytoplasm. By capturing these important physics, we show that the formulation is capable to reproducing the mechano-sensitivity of cell contraction with respect to substrate stiffness as well as the general architecture of contractile cells.

Chapter 5 introduces a continuum formulation, combined with a numerical approach based on the Extended Finite Element (XFEM) and the levelset methods to study the mechanical cross-talks between contractile cells (fibroblasts) and a two-dimensional deformable substrate. The mechano-chemistry of cell contraction is described in terms of a constrained mixture formulation that was recently developed by the authors [165] to capture the phenomena of mechano-sensitive stress-fiber (SF) formation (and dissociation) and contraction. In short, the model is based on the description of the contractile apparatus of cell in terms of two solid constituents: the cytoskeleton and a population of contractile stress fibers as well as two fluid constituents: the cytosol and soluble contractile units (that can polymerize into stress fibers). The interactions between a cell and its substrate are possible through localized adhesive regions, known as the focal adhesion. From a numerical view-point, the complicated problem of the interactions between two domains (cell and substrate) of different geometry and constitution is greatly simplified by using the advantages of XFEM

[43, 105, 9]. Without loss of generality, considering cell and substrate as by two-dimensional domains satisfying plane-stress conditions, we introduce a single finite element mesh for both domains. Cell geometry is then defined in terms of an analytical levelset function defining the contour of cell boundary independently of discretization. Degrees of freedom pertaining to cell are then only associated with nodes belonging to the interior of the domain defined by the levelset, while discontinuities across the cell boundary are naturally represented by enriching finite element shape function with discontinuous functions following the standard XFEM equations. The key advantages of this contribution are then as follows:

- Complex cell geometries may naturally be handled independently of finite-element discretization.
- Because cell and substrate domains are discretized with the same mesh, the numerical treatment of cell-substrate cohesion is accurate and simple.
- The XFEM enrichment functions enable the incorporation of the stiffness of the cortical membrane surrounding the cell; this feature is known to be critical to realistically capture cell morphology.
- The formulation is flexible and has the potential to be extended for describing cell spreading and migration using level-set evolution equations.

Chapter 6 presents a single mathematical model for cell contraction and growth based on chemical and mechanical interactions in cell such that it accounts for the effect of all following phenomena:

(1) A mixture model for cell contractile behavior is developed based on the mass exchange and chemo-mechanical reactions between main constituents as well as G-actin and cytosol flux in the cell. For this purpose, the equilibrium state corresponding to free energy of G-actin and stress fiber controls polymerization and depolymerization

of fibers in according to [56]. In addition, a similar strategy is followed to consider mass exchange between G-actin and cytoskeleton as a fibrous network.

(2) Instead of modeling focal adhesions by elastic springs in predefined areas, our model includes integrins in cell membrane and ligands on substrate to capture focal adhesions (integrin-ligand complexes) formation during the process discussed above [96].

(3) A growth model is presented to investigate the rate of cell spreading at the growing border of cell as well as cell area at steady state. In the proposed model, cell grows on its boundary by formation of new cytoskeleton based on the important criteria mentioned in literature such as G-actin and cytoskeleton volume fraction at the cell's boundary, cell membrane forces, cell contractile behavior, substrate properties, and focal adhesion formation.

(4) The existing numerical approaches (such as [103, 125, 178, 176]) use two different mesh for cell and substrate, and connect them by contact meshes that are needed to be very fine to provide enough accuracy in addition to all numerical issues accompanied with interactions between two different domains. Thus, we introduce a numerical approach based on extended finite element (XFEM) and levelset method [43, 105, 9], to provide the following features:

- The same mesh is used for cell and substrate to avoid the difficulties of dealing with two different mesh interaction.
- Cell border is defined as the intersection of a 2D curve, called levelset function, and cell 1D domain (Fig. 6.4a), as a result, we do not have to change the mesh during cell evolution to define cell's border.
- Cell surface tension is naturally taken into account using XFEM/levelset features [163].

Chapter 2

An Eulerian/XFEM Formulation for the Large Deformation of Cortical Cell Membrane

2.1 Abstract

Most animal cells are surrounded by a thin layer of actin meshwork below their membrane, commonly known as the actin cortex (or cortical membrane). An increasing number of studies have highlighted the role of this structure in many cell functions including contraction and locomotion but modeling has been limited by the fact that the membrane thickness (about 1 μm) is usually much smaller than the typical size of a cell ($10 - 100\mu m$). To overcome theoretical and numerical issues resulting from this observation, the present chapter introduces a continuum formulation, based on surface elasticity, that views the cortex as an infinitely thin membrane that can resist tangential deformation. To accurately model the large deformations of cells, equilibrium equations and constitutive relations are introduced within the Eulerian viewpoint such that all quantities (stress, rate of deformation) lie in the current configuration. A solution procedure is then introduced based on a coupled extended finite element approach (XFEM) that enables a continuum solution to the boundary value problem in which discontinuities in both strain and displacement (due to cortical elasticity) are easily handled. We validate the approach by studying the effect of cortical elasticity on the deformation of a cell adhering on a stiff substrate and undergoing internal contraction. Results show very good prediction of the proposed method when compared with experimental observations and analytical solutions for simple cases. In particular, the model can be

used to study how cell properties such as stiffness and contraction of both cytoskeleton and cortical membrane lead to variations in cell's surface curvature. These numerical results show that the proposed method can be used to gain critical insights into how the cortical membrane affects cell deformation and how it may be used to as a means to determine a cell's mechanical properties by measuring curvatures of its membrane.

2.2 Introduction

Functions and health of biological tissues such as skin, cartilage and cardiac tissues rely on the interaction between population of cells (e.g. fibroblasts and chondrocytes) and their surrounding fibrous extracellular matrix (ECM). These interactions strongly depend on many internal characteristics, including ECM and cell properties, deformation and orientation, as well as external factors such as the existence of external loads and their variation in time ([134]). Any change in cell behavior and morphology (due to disease, for instance), ECM properties and structure (from aging or injuries) or external forces affect the mechanical and chemical equilibrium of tissues. This may result in significant consequences, including tissue remodeling and reorganization ([76]), change in cell phenotype, angiogenesis ([21]) or apoptosis ([169, 98]). Research advances will depend on our ability to characterize and predict the very factors that determine cell shapes in various environments. In this quest, the derivation of accurate mechanical models of cell deformation plays a key role. Traditionally, research on cell mechanics has concentrated on the deformation of the cytoplasm (that comprises the cytoskeleton and the cytosol) for which three main families of models have been developed: structural models, polymer-based models and multiphasic models. Structural models, such as the tensegrity model ([87, 88, 171, 141]) have been successful at relating the general deformation of cells to the nature of their individual components, including actin filaments and microtubules. In contrast, continuum models such as polymer-based theories ([100]) and biphasic mixtures ([67, 2]) provide a less precise but more flexible platform for the description of a wider range of phenomena. For instance, polymer-based models are able

to explain the inherent stress-stiffening of the cytoskeleton filament network measured in experiments ([100]), while biphasic model are ideal to describe the flow-dependent behavior of the cytoplasm ([2]).

In addition to the cytoplasm, recent studies have highlighted the role of the cortical membrane on cell deformation. This important component of the cell's cytoskeleton can be described as a dense layer of actin bundles beneath the surface membrane ([84, 142]) that acts as a protective layer against cell damage. This thin actin layer is also known to play a large role during cell migration in three-dimensional environments by initiating bleb formation on the surface of cells ([154, 33, 52]). A number of models have been proposed to better understand the behavior of the cortical membrane and its role in cell morphology. Hansen et al. ([72, 73]) developed a numerical network model to establish a connection between the elasticity of red blood cell membrane and its random molecular structure. Other relevant studies include the work of Bar-zive ([3]) on the phenomenon of pearling caused by mechanical interactions between surface tension and the elasticity of the actin cortex below the membrane ([77, 92]). In this approach, a simple model based on a line tension approximation of cortical membrane elasticity provided good prediction of cell shape in different environments. This was followed by the work of Bischofs et. al. ([14]) in which the authors derived an analytical model based on Laplace's law to investigate the influence of the cortical membrane on the shape of contractile fibroblasts attached to periodically distributed adhesion islands. By comparing their model with experimental observations, they showed that the method could predict the magnitude of the membrane curvature for cells of different sizes. While the aforementioned studies concentrated on the role of cortical membrane only, the properties of the (bulk) cytoskeleton are also known to play a significant role on cell morphology. Accurate mechanical models of cells should therefore consider the combined effects of bulk cytoskeleton and cortex elasticity. However, from a computational viewpoint, the difference of length-scales between a cell (50-500 microns) and its cortical membrane thickness (less than a micron) poses a challenge that is inherent to most multiscale problems

([162]); providing an accurate description of the cortical membrane on the length-scale of a single cell results in a very expensive numerical problem and vice-versa. This may explain why existing models of cell deformation have neither considered the cortical membrane nor have presented a coarse description of it ([158]).

To overcome this issue, the present study proposes to consider the actin cortex as a two-dimensional membrane, of negligible thickness, surrounding the cell. In this context, modeling cortical membrane mechanics can be cast within the framework of surface elasticity, originally introduced by Gurtin and Murdoch in ([71]). Existing work on surface elasticity have traditionally concentrated on surface effects in nanomaterials ([54, 181]) in the context of infinitesimal deformation. However, because cell deformation can be quite significant in many applications, a contribution of this chapter is to extend the surface elasticity formulation to the case of large deformation and to investigate its predictive power on the influence of cortical membrane on cell deformation. The equations of surface elasticity are therefore redefined in the general case of large deformation, following an Eulerian approach. As such, we develop the equation of equilibrium for the general case of a cell embedded in a matrix, for which the effect of the cortical membrane is important. A numerical strategy, based on the extended finite element method (XFEM) is then introduced in order to solve the system of coupled partial differential equations. The presented method possesses the following advantages. First, the presented framework uses Eulerian formulation that is suitable for large deformations of the cell. Second, the geometry of the cell is entirely defined by level-set functions that are defined independently from the finite element mesh. Simple, regular FEM meshes may thus be used regardless of the geometric complexity of the cell. Third and finally, the different elastic properties and constitutive response of cell cortex is described with a continuum description that naturally fits into the XFEM methodology. Thus, no special treatment is necessary to model jumps in stress, strain and displacement arising due to the cortical membrane.

The chapter is organized as follows. In the next section, a description of the cell's

deformation is provided, and relevant kinematic variables are introduced. Section 3 then concentrates on deriving the governing equations of surface elasticity and introduces a set of simple elastic constitutive relations for the cytoskeleton and cortical membrane. Numerical considerations are subsequently discussed in section 4 with the description of an updated Lagrangian XFEM/level-set formulation that is used to investigate the effect of cortex elasticity on the deformation of a contractile cell (section 5). A summary of the method and concluding remarks are finally provided in section 6.

2.3 Kinematics

The first step in deriving the surface elasticity formulation for large deformation is to define consistent measures of deformation. While the Lagrangian formalism can be used to define total strain measures, many of the complexities associated with mapping mathematical quantities from one material configuration to another can be avoided by using an Eulerian approach. This section therefore introduces a rate form of material motion and deformation, consistent with the Eulerian framework.

2.3.1 Generalities

Let us consider a two-dimensional domain Ω in the x-y plane representing a cell Ω_c and its surrounding matrix (Ω_m) such that $\Omega = \Omega_c \bigcup \Omega_m$ (Fig. 2.1). The interface between the two domains (representing the cell/matrix interface) is denoted as Γ. In order to introduce the kinematics in the context of large deformations, let us first consider the above domain in two different configurations as shown in the figure. At an initial time $t = t_0$, we represent the medium in the so-called reference configuration (in which the domain and its boundary are represented by Ω_0 and Γ_0, respectively) such that the coordinate of a material point P in a Cartesian coordinate system (x, y) is given by $\mathbf{X} = \{X, Y\}$. A current configuration (in which the domain and its boundary are represented by Ω and Γ, respectively) is then introduced at an arbitrary time t such that the coordinate of the material point P is now

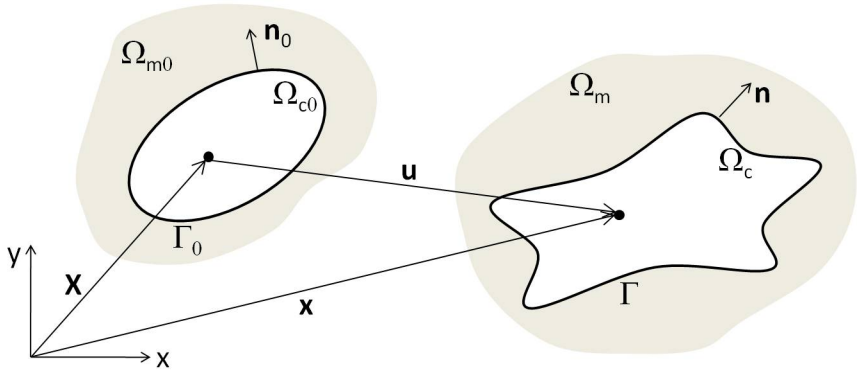

Figure 2.1: Initial and current configuration of cell in a two-dimensional plane x-y.

given by $\mathbf{x} = \chi(\mathbf{X}, t)$, where χ is assumed to be a smooth function of time and space, except on Γ. Adopting an Eulerian approach, the bulk deformation of the cell and the matrix can be related to the velocity $\mathbf{v}(\mathbf{x}, t)$ of materials point at any time such that:

$$\mathbf{v}(\mathbf{x}, t) = \frac{D\mathbf{u}}{Dt} \quad \text{where} \quad \mathbf{u} = \mathbf{x} - \mathbf{X} \tag{2.1}$$

where $\mathbf{u}$ is the displacement and D/Dt denotes the material time derivative that evaluates the variation of a field ($\mathbf{u}$ in the above equation), following a particle P in its motion.

2.3.2 Deformation measures

In order to accurately describe the deformation of a cell and its surrounding thin cortical membrane, the present work introduces three strain measures that are associated with (a) the deformation of the cell body, (b) the decohesion between the cell and the surrounding matrix and (c) the deformation of the cortical membrane. Following the Eulerian framework, a description of the bulk deformation and rotation of the cell is provided by the rate of deformation tensor $\mathbf{D}(\mathbf{x}, t)$ and the spin $\mathbf{W}(\mathbf{x}, t)$ as follows:

$$\mathbf{D} = \frac{1}{2}\left(\nabla\mathbf{v} + (\nabla\mathbf{v})^T\right) \quad \text{and} \quad \mathbf{W} = \frac{1}{2}\left(\nabla\mathbf{v} - (\nabla\mathbf{v})^T\right) \tag{2.2}$$

where ∇ represents the gradient operator with respect to $\mathbf{x}$ and the superscript T is used for the transpose operation. In addition, the present approach allows for a discontinuous

velocity field across the cell/matrix interface Γ. As such, a measure of cell/matrix decohesion can simply be introduced through the discontinuity (or jump) $[\mathbf{v}](\mathbf{x},t)$ in velocity as follows:

$$[\mathbf{v}](\mathbf{x},t) = \mathbf{v}^{+}(\mathbf{x},t) - \mathbf{v}^{-}(\mathbf{x},t) \tag{2.3}$$

where $\mathbf{x}$ belongs to Γ and $\mathbf{v}^{+}(\mathbf{x})$ and $\mathbf{v}^{-}(\mathbf{x})$ denote velocities on different sides of the interface. Finally, assuming a thin cortical membrane compared to the size of the cell, its deformation may be defined by invoking the concept of surface strain, originally introduced in ([71]). For this, we introduce a tangential projection operator (in the current configuration) on the cell boundary at point $\mathbf{x}$ as follows:

$$\mathbf{P} = \mathbf{I} - \mathbf{n} \otimes \mathbf{n} \tag{2.4}$$

where $\mathbf{I}$ is the second-order identity tensor while $\mathbf{n} = \mathbf{n}(\mathbf{x},t)$ is the normal vector to the cell surface in the current configuration. With this definition, the components of the projection of a vector $\mathbf{a}$ and a tensor $\mathbf{A}$ on a surface of normal $\mathbf{n}$ are given by:

$$\mathbf{a}_s = \mathbf{P} \cdot \mathbf{a} \quad \text{and} \quad \mathbf{A}_s = \mathbf{P} \cdot \mathbf{A} \cdot \mathbf{P} \tag{2.5}$$

This geometrical preliminary may now be applied to the definition of the rate of deformation $\mathbf{D}_s$ of the cortical membrane as the tangential projection of the bulk rate of deformation $\mathbf{D}$ onto the cell surface:

$$\mathbf{D}_s = \mathbf{P} \cdot \mathbf{D} \cdot \mathbf{P} \tag{2.6}$$

Note that the tensor $\mathbf{D}_s$ keeps the same dimension as $\mathbf{D}$ but represents a deformation in space (tangential space) whose dimension is smaller than the original space Ω.

2.3.3 Evolution equation of the cortical membrane orientation

In general, the cell and matrix geometries are defined in the initial configuration. This means that while the normal vector $\mathbf{n}_0$ and projection operator $\mathbf{P}_0 = \mathbf{I} - \mathbf{n}_0 \otimes \mathbf{n}_0$ are entirely known, their counterparts $\mathbf{n}$ and $\mathbf{P}$ in the current configuration need to be determined. Using

the fact that:

$$\mathbf{n} = \mathbf{Q} \cdot \mathbf{n}_0 \quad \text{and} \quad \mathbf{P} = \mathbf{Q} \cdot \mathbf{P}_0 \cdot \mathbf{Q}^T \tag{2.7}$$

where $\mathbf{Q}$ is the orthonormal transformation (rotation) that maps normal vector from the initial to current configuration. Using the fact that $\mathbf{W} = \dot{\mathbf{Q}}\mathbf{Q}^T$, one can show that:

$$\dot{\mathbf{n}} = \mathbf{W} \cdot \mathbf{n} \quad \text{and} \quad \dot{\mathbf{P}} = \mathbf{W}\mathbf{P} + \mathbf{P}\mathbf{W}^T \tag{2.8}$$

where a superimposed dot denotes the material time derivative. Equation (2.8) may thus be integrated in time in order to determine $\mathbf{n}$ and $\mathbf{P}$ and compute the rate of surface deformation $\mathbf{D}_s$ appearing in (2.6).

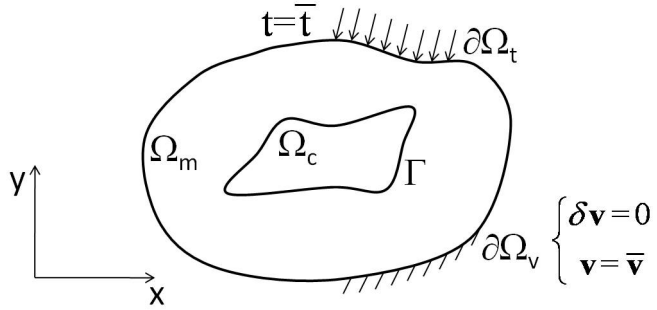

Figure 2.2: The general outline of a cell along with the surrounding matrix and boundary conditions.

2.4 Governing equations and constitutive relations

This section concentrates on deriving the equations governing the mechanical equilibrium of a cell undergoing a combination of deformations as introduced above. The equilibrium equations are derived from the energetic considerations while simple elastic relations are given to describe the cell response.

2.4.1 Principle of virtual power and governing equations

Considering a first order continuum theory in quasi-static conditions (the kinetic energy of the system is negligible in comparison with deformation and external energies), one can

introduce a virtual internal power δP_{int} associated with the medium contained in Ω as follows:

$$\delta P_{int} = \int_{\Omega} (\mathbf{T} - \mathbf{T}^0) : \delta \mathbf{D} \; d\Omega + \int_{\Gamma} (\mathbf{T}_s - \mathbf{T}_s^0) : \delta \mathbf{D}_s \; d\Gamma + \int_{\Gamma} \mathbf{T}_d \cdot [\delta \mathbf{v}] \; d\Gamma \tag{2.9}$$

where ":" is the double tensor contraction and $\delta \mathbf{D}$, $\delta \mathbf{D}_s$ and $[\delta \mathbf{v}]$ are small virtual variations of bulk deformation, surface deformation and decohesion around the equilibrium state, respectively. The quantities $\mathbf{T}$, $\mathbf{T}_s$ and $\mathbf{T}_d$ are then defined as power conjugates to the aforementioned deformations and are recognized as the conventional Cauchy stress, surface Cauchy stress and cohesive force, respectively. Furthermore, we also introduced $\mathbf{T}^0$ and $\mathbf{T}_s^0$ as the contractile stresses in the bulk and interface, respectively.

Before we write the form of the virtual external power, we make the assumption that the cell is entirely contained in the domain Ω such that its boundary Γ does not intersect with the domain boundary $\partial\Omega$. This assumption simplifies our analysis as there are no boundary conditions applied on the cell membrane Γ. Further, the domain boundary $\partial\Omega$ is decomposed in two parts according to the nature of the boundary conditions. Introducing as $\partial\Omega_u$ the section of the domain boundary on which a fixed velocity $\bar{\mathbf{v}}$ is applied and as $\partial\Omega_t$ the section of the boundary subjected to a surface traction $\bar{\mathbf{t}}$, the entire boundary can be reconstructed as $\partial\Omega = \partial\Omega_u \cup \partial\Omega_t$. The external virtual power δP_{ext} finally takes the form:

$$\delta P_{ext} = \int_{\Omega} \rho \; \mathbf{b} \cdot \delta \mathbf{v} \; d\Omega + \int_{\partial\Omega_t} \bar{\mathbf{t}} \cdot \delta \mathbf{v} \; d\partial\Omega \tag{2.10}$$

where ρ is the mass density and $\mathbf{b}$ is a body force per unit mass. We also note that the virtual field $\delta \mathbf{v}$ must vanish on the boundary $\partial\Omega_u$ as required by variational principles. Mechanical equilibrium of the cell and its surrounding matrix is then satisfied upon minimialization of the total potential energy of the system. In other words, the virtual power:

$$\delta P_{int} - \delta P_{ext} \tag{2.11}$$

vanishes for any virtual velocity field in Ω and on Γ. We next use equation (2.11) to derive the governing equations (strong form) driving the motion of the cell and its cortical membrane.

First integrating (2.9) by parts and using the divergence theorem, we can rewrite the virtual internal power as:

$$\begin{aligned}\delta P_{int} &= -\int_{\Omega}\left(\nabla\cdot\tilde{\mathbf{T}}\right)\cdot\delta\mathbf{v}\;d\Omega-\int_{\Gamma}\left[\left(\tilde{\mathbf{T}}\cdot\mathbf{n}\right)\cdot\delta\mathbf{v}\right]\;d\Gamma\\ &- \int_{\Gamma}\nabla_s\cdot\tilde{\mathbf{T}}_s\cdot\delta\mathbf{v}^s d\Gamma+\int_{\Gamma}\mathbf{T}_d\cdot[\delta\mathbf{v}]\,d\Gamma+\int_{\partial\Omega_t}\left(\tilde{\mathbf{T}}\cdot\mathbf{n}\right)\cdot\delta\mathbf{v}d\partial\Omega \qquad (2.12)\end{aligned}$$

where $\mathbf{n}$ is the normal unit vector to the surfaces Γ and $\partial\Omega$, $\tilde{\mathbf{T}}=\mathbf{T}-\mathbf{T}^0$ and $\tilde{\mathbf{T}}_s=\mathbf{T}_s-\mathbf{T}_s^0$. Furthermore, we introduced the notation $\nabla_s\cdot\tilde{\mathbf{T}}_s$ to represent the surface divergence of the surface stress $\tilde{\mathbf{T}}_s$. At this point, it is necessary to introduce the average operator $\langle\rangle$ that computes the average of an arbitrary field f on the interface Γ. We write:

$$\langle f\rangle=\frac{1}{2}\left(f^+ + f^-\right) \qquad (2.13)$$

where f^+ and f^- denote the value of f on opposite sides of the interface. Referring to the work of ([71]), we can now use the following equalities:

$$\begin{aligned}\left[(\tilde{\mathbf{T}}\cdot\mathbf{n})\cdot\delta\mathbf{v}\right] &= \left[\tilde{\mathbf{T}}\cdot\mathbf{n}\right]\cdot\langle\delta\mathbf{v}\rangle+\langle\tilde{\mathbf{T}}\cdot\mathbf{n}\rangle\cdot[\delta\mathbf{v}] \qquad (2.14)\\ \nabla_s\tilde{\mathbf{T}}_s\cdot\delta\mathbf{v}_s &= \nabla_s\tilde{\mathbf{T}}_s\cdot\langle\delta\mathbf{v}\rangle \qquad (2.15)\end{aligned}$$

together with (2.12) and (2.11), to obtain a useful form of the principle of virtual power. For any virtual fields $\delta\mathbf{v}$, $[\delta\mathbf{u}]$ and $\langle\delta\mathbf{u}\rangle$, we have:

$$\begin{aligned}&-\int_{\Omega}\left(\nabla\cdot\tilde{\mathbf{T}}+\rho\mathbf{b}\right)\cdot\delta\mathbf{v}\;d\Omega-\int_{\Gamma}\left(\left[\tilde{\mathbf{T}}\cdot\mathbf{n}\right]+\nabla_s\tilde{\mathbf{T}}_s\right)\cdot\langle\delta\mathbf{v}\rangle\;d\Gamma\\ &-\int_{\Gamma}\left(\langle\tilde{\mathbf{T}}\cdot\mathbf{n}\rangle-\mathbf{T}_d\right)\cdot[\delta\mathbf{v}]\,d\Gamma+\int_{\partial\Omega_t}\left(\tilde{\mathbf{T}}\cdot\mathbf{n}-\bar{\mathbf{t}}\right)\cdot\delta\mathbf{v}\;d\partial\Omega\;=\;0 \qquad (2.16)\end{aligned}$$

This implies that each integrand appearing in the above expression must vanish for any material point in Ω, Γ and $\partial\Omega_t$. This leads to a system of three coupled differential equations for stresses as follows:

$$\begin{aligned}\nabla\cdot\tilde{\mathbf{T}}+\rho\mathbf{b} &= 0 \quad \text{in} \quad \Omega \qquad (2.17)\\ \left[\tilde{\mathbf{T}}\cdot\mathbf{n}\right]+\nabla_s\tilde{\mathbf{T}}_s &= 0 \quad \text{on} \quad \Gamma \qquad (2.18)\\ \langle\tilde{\mathbf{T}}\cdot\mathbf{n}\rangle-\mathbf{T}_d &= 0 \quad \text{on} \quad \Gamma \qquad (2.19)\end{aligned}$$

subjected to boundary conditions

$$\begin{cases} \tilde{\mathbf{T}} \cdot \mathbf{n} = \bar{\mathbf{t}} & \text{on} \quad \partial\Omega_t \\ \mathbf{v} = \bar{\mathbf{v}} & \text{on} \quad \partial\Omega_v \end{cases} \tag{2.20}$$

Equations (2.17), (2.18) and (2.19) represent the bulk equilibrium, the balance of forces in the cortical membrane and the balance of cohesive forces between a cell and the extracellular matrix, respectively.

2.4.2 Constitutive relation

For the sake of simplicity, we now introduce a set of simple elastic constitutive relations for the cytoskeleton and the cortical membrane. While the present analysis is general enough to consider more realistic nonlinear material responses, the present work concentrates on linear elastic relations between stress and strain. The Eulerian framework described here requires that constitutive relations are given in a rate form, i.e., it is written in terms of a material time derivative of the Cauchy stress and rates of deformation. However, to ensure that elastic energy is conserved during deformation, it is important to describe the elastic response of the cytoskeleton in terms of a hyper-elastic potential Ψ that is a function of the deformation gradient $\mathbf{F} = \nabla_{\mathbf{X}}\mathbf{x}$ where $\nabla_{\mathbf{X}}$ is the gradient operator in the reference configuration. A common model used for isotropic elastic materials is provided by the Neo-Hookean model, for which the strain energy function Ψ is expressed in terms of the Lame constants λ and μ as follows:

$$\rho_0 \Psi = \frac{1}{2}\lambda \left(lnJ\right)^2 - \mu \; lnJ + \frac{1}{2}\mu \left(I_1 - 3\right) \tag{2.21}$$

where ρ_0 is the mass density of the cytoplasm in the reference configuration and the strain invariants I_1 and J are given by $I_1 = trace\left(\mathbf{F}^T\mathbf{F}\right)$ and $J = det\left(\mathbf{F}\right)$. Following [10], it can be shown that the above model implies that an objective stress rate $\mathbf{T}^{\sigma J}$ (more specifically the Jaumann rate) can be written in terms of the rate of deformation $\mathbf{D}$ introduced in (2.2)

as follows:

$$\mathbf{T}^{\sigma J} = \mathbf{C}^{\sigma^J} : \mathbf{D} \tag{2.22}$$

where the components of the fourth order elastic matrix $\mathbf{C}^{\sigma J}$ take the form

$$C^{\sigma J}_{ijkl} = 2\left(\mu - \lambda\ lnJ\right)\delta_{ik}\delta_{jl} + \lambda\ \delta_{ij}\delta_{kl} \tag{2.23}$$

In the above equation, δ is the Dirac-delta function. Let us now introduce the elastic response of the cortical membrane. Concentrating on plane stress problems, the membrane surrounding the cell may be viewed as a one-dimensional cable undergoing axial deformation ϵ. As a result, the cortical stiffness may be defined in terms of a scalar quantity, denoted as K_s such that the rate of elastic energy P^s corresponding to an axial strain rate $\dot{\epsilon}$ is written:

$$P^s = \frac{1}{2}\ K_s\ \dot{\varepsilon}^2 = \frac{1}{2}\ K_s\ \mathbf{D}_s : \mathbf{D}_s \tag{2.24}$$

where we used the fact that $\mathbf{D}_s : \mathbf{D}_s = \dot{\epsilon}^2$. An objective rate of surface stress $\mathbf{T}^{s,\sigma J}$ may thus be defined as the derivative of P^s with respect to the rate of deformation $\mathbf{D}_s$ as:

$$\mathbf{T}^{s,\sigma J} = \frac{\partial^2 \Psi^s}{\partial \mathbf{D}_s\ \partial \mathbf{D}_s} : \mathbf{D}_s = \mathbf{S}_s : \mathbf{D}_s \tag{2.25}$$

where the components $S_{s,ijkl}$ of the cortical membrane elastic tensor are written in terms of the cortex stiffness K_s as follows:

$$S_{s,ijkl} = K_s\ \delta_{ik}\ \delta_{jl}. \tag{2.26}$$

Finally, the present study concentrates on the case of "free cells" that are not interacting with an extracellular matrix. The surrounding matrix material is therefore not considered, and thus, no cohesive forces are present. This means that $\mathbf{T}^d = \mathbf{0}$ throughout this study. To complete the form of the constitutive framework, it is now of interest to relate the material time derivative of stresses (that is not an objective measure) to the Jaumann stress rate introduced above. Following [10], we write:

$$\dot{\mathbf{T}} = \frac{D\mathbf{T}}{Dt} = \mathbf{T}^{\sigma J} + \mathbf{W}\cdot\mathbf{T} + \mathbf{T}\cdot\mathbf{W}^T \tag{2.27}$$

where $\mathbf{W}$ is the spin tensor defined in (2.2). It can be shown that the above equation is true for both bulk and surface stress and thus can be used to compute rates of $\mathbf{T}_s$, $\mathbf{T}_s^0$ and $\mathbf{T}^0$ appearing in this study.

2.5 Numerical solution: an XFEM strategy

This section provides a numerical strategy to solve governing equations (2.17),(2.18) and (2.19), together with constitutive relations (2.25) and (4.52). A particularity of these equations is that they give rise to discontinuities in strain rate and velocities across the cell's interface, a feature that cannot be naturally handled with linear finite elements. The XFEM formalism ([43, 9]) is therefore utilized to overcome this issue.

2.5.1 Extended finite element method (XFEM)

The XFEM equations are developed within the so-called updated Lagrangian method (for more information on this method, the reader is referred to [10]), by using the final weak form derived in (2.16). The solution of these equations typically gives rise to discontinuities across the interface Γ. Indeed, the existence of surface tension is associated to a jump in strain across the interface (commonly called weak discontinuity) while the existence of a decohesion (through the cohesive law) leads to a jump in displacement across Γ (commonly called strong discontinuity). Many numerical techniques, such as the finite element method, are developed for continuous fields and therefore fail to describe such discontinuities. To address this issue, the XFEM was first introduced to incorporate a jump in displacement occurring as a result of a propagating crack in a continuous medium ([43], [79]). A key feature of this method is that the description of the discontinuity is independent of spatial discretization. Thus, Belytschko et al. used XFEM in ([9]) and ([7]) to define solids by implicit surfaces and also to model dislocations and interfaces. The method was further improved to model weak discontinuities, such as described in ([105]). This method provides a natural platform on which (2.16) can be solved with great flexibility and minimal computation cost. In the

present formulation, the domain Ω is first subdivided into four-node quadrilateral elements in which an approximation $\tilde{\mathbf{v}}(\mathbf{x})$ of the velocity field is sought. To account for the existence of continuous, strong, and weak discontinuous fields within an element, $\tilde{\mathbf{v}}(\mathbf{x})$ is written as the sum of three terms that are parametrized by $\mathbf{v}$, $\bar{\mathbf{v}}$ and $\bar{\bar{\mathbf{v}}}$ as follows:

$$\tilde{\mathbf{v}}^e(\mathbf{x}) = \sum_{I=1}^{n} \mathbf{N}_I(\mathbf{x})\mathbf{v}_I + \sum_{J=1}^{m} \mathbf{N}_J(\mathbf{x})(H(\mathbf{x}) - H(\mathbf{x}_J))\bar{\mathbf{v}}_J + \sum_{J=1}^{m} \mathbf{N}_J(\mathbf{x})\chi_J(\mathbf{x})\bar{\bar{\mathbf{v}}}_J \tag{2.28}$$

where

$$\mathbf{N}_I(\mathbf{x}) = \begin{bmatrix} N_I(\mathbf{x}) & 0 \\ 0 & N_I(\mathbf{x}) \end{bmatrix} \tag{2.29}$$

The functions $N_I(\mathbf{x})$ are finite element shape functions associated with node I, $N_J(\mathbf{x})$ are the shape functions associated with the nodes of an element that has been cut by the interface (see Fig. 2.3), and n is the total number of nodes per element, while m is the number of enriched nodes ($m \leq n$). Furthermore, the quantities $H(\mathbf{x})$ and $\chi(\mathbf{x})$ are enrichment functions with the required discontinuities (Heaviside function and ridge function, respectively ([105], [106])). Referring to Fig. 2.3c and 2.3d, the Heaviside function introduces a jump in velocity (strong discontinuity), in contrast, a ridge function causes a jump in the spatial derivative of the velocity (weak discontinuity) across the interface. In one-dimension, the Heaviside and ridge function take the form:

$$H(\phi) = \begin{cases} 1 & \phi > 0 \\ 0 & \phi < 0 \end{cases} \quad \text{and} \quad \chi_j(\mathbf{x}) = |\phi(\mathbf{x})| - |\phi(\mathbf{x}_j)| \tag{2.30}$$

To define the geometry of a cell in the reference configuration (defined by Ω_0 and Γ_0), we introduce a level-set function $\phi(\mathbf{X})$ such that the interface (or cell boundary) is defined as the intersection of a level-set surface with a cutting plane, as depicted in Fig. 2.3b. With this description, the sign of ϕ is opposite in two sides of the discontinuity. An attractive feature of using level-sets is that the initial unit normal vector $\mathbf{n}_0$ to the interface (Fig. 2.1)

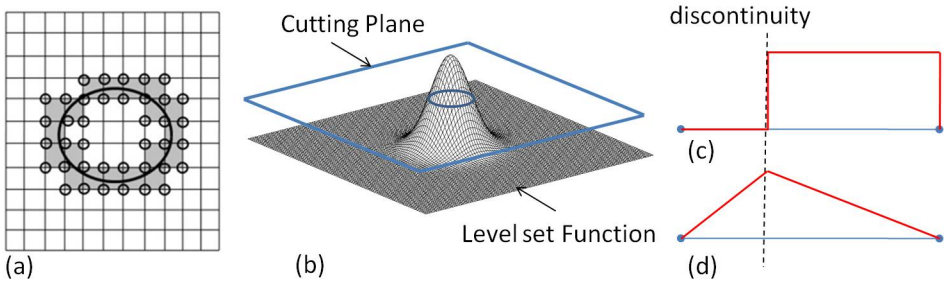

Figure 2.3: a) enriched nodes and completely enriched elements for a closed interface. b) level-set function and cutting plane to define a circular cell in a square domain. c) a typical Heaviside (step) function to define strong discontinuity. d) a typical ridge function to define weak discontinuity.

is determined by the material gradient $\nabla_{\mathbf{X}}$ of the function $\phi(\mathbf{X})$ with respect to $\mathbf{X}$ as follows:

$$\mathbf{n}_0(x) = \frac{\nabla_{\mathbf{X}}\phi(x)}{||\nabla_{\mathbf{X}}\phi(x)||} \tag{2.31}$$

Using this definition and evolution equations (2.8), the projection operator $\mathbf{P}$ in the current configuration may be obtained by time integration.

2.5.2 Linearized XFEM equations

To derive a finite element form of the governing equation, we first associate each node of an element with velocity degrees of freedom $\mathbf{v}^e$ that comprise contributions from three terms introduced in (2.28):

$$\mathbf{v}^e = \begin{bmatrix} \mathbf{v} & \bar{\mathbf{v}} & \bar{\bar{\mathbf{v}}} \end{bmatrix}^T \tag{2.32}$$

Note that the full set of degrees of freedom only appear when an element intersects with the cell boundary. Using the XFEM approximation (2.28), the rates of deformation $\{\mathbf{D}^e\}$ and $\{\mathbf{D}^e_s\}$ within an element are written in Voigt notation as:

$$\{\mathbf{D}^e\} = \begin{bmatrix} D^e_{11} \\ D^e_{22} \\ 2D^e_{12} \end{bmatrix} = \mathbf{B}\cdot\mathbf{v}^e \quad \text{and} \quad \{\mathbf{D}^e_s\} = \begin{bmatrix} D^e_{s11} \\ D^e_{s22} \\ 2D^e_{s12} \end{bmatrix} = \mathbf{M}_p\cdot\{\mathbf{D}^e\} \tag{2.33}$$

where the $\mathbf{B}$ matrix relates nodal velocities and rate of deformation and takes the form:

$$\mathbf{B} = \begin{bmatrix} \mathbf{B}_1 & \mathbf{B}_2 & ... & \mathbf{B}_{n+m} \end{bmatrix} \quad \text{and} \quad \mathbf{B}_I = \begin{bmatrix} \frac{\partial \bar{N}_I(\mathbf{x})}{\partial x_1} & 0 \\ 0 & \frac{\partial \bar{N}_I(\mathbf{x})}{\partial x_2} \\ \frac{\partial \bar{N}_I(\mathbf{x})}{\partial x_2} & \frac{\partial \bar{N}_I(\mathbf{x})}{\partial x_1} \end{bmatrix} \tag{2.34}$$

while the matrix $\mathbf{M}_p$ represents the tangential projection (in Voigt notation) of the bulk quantity $\mathbf{D}$ to obtain the rate of surface deformation $\mathbf{D}_s$ as shown in (2.6). It can be shown ([181]) that $\mathbf{M}_p$ is written:

$$\mathbf{M}_p = \begin{bmatrix} P_{11}^2 & P_{12}^2 & P_{11}P_{12} \\ P_{12}^2 & P_{22}^2 & P_{22}P_{12} \\ 2P_{11}P_{12} & 2P_{22}P_{12} & P_{12}^2 + P_{11}P_{22} \end{bmatrix} \tag{2.35}$$

where P_{ij} are the components of the projection tensor $\mathbf{P}$ introduced in (2.4). To obtain a discretized weak form of the governing equation, let us first consider the virtual powers considered in (2.9) and (2.10) and decompose the integration over the entire domain Ω into a sum of integration over element domains Ω_e. Further using the XFEM interpolation (2.33), one can show that numerical approximations $\delta\tilde{P}_{int}$ and $\delta\tilde{P}_{ext}$ of virtual powers (2.9) and (2.10) are written:

$$\begin{aligned} \delta\tilde{P}_{int} &= \sum_e \left\{ \int_{\Omega^e} \{\delta\mathbf{D}^e\}^T \cdot \{\mathbf{T}\}\ d\Omega + \int_\Gamma \{\delta\mathbf{D}_s^e\}^T \cdot \{\mathbf{T}_s\}\ d\Gamma \right. \\ &- \left. \int_{\Omega_e} \{\delta\mathbf{D}^e\}^T \cdot \{\mathbf{T}^0\}\ d\Omega - \int_{\Gamma_e} \{\delta\mathbf{D}_s^e\}^T \cdot \{\mathbf{T}_s^0\}\ d\Gamma_e \right\} \\ \delta\tilde{P}_{ext} &= \sum_e \left\{ \int_{\Omega_e} \rho\ \delta(\mathbf{v}^e)^T \cdot \mathbf{b}\ d\Omega + \int_{\partial\Omega_{te}} \delta(\mathbf{v}^e)^T \cdot \bar{\mathbf{t}}\ d\partial\Omega_{te} \right\} \end{aligned} \tag{2.36}$$

where stress measures are written in Voigt notation in the form $\{\mathbf{T}\} = \begin{bmatrix} T_{11} & T_{22} & T_{12} \end{bmatrix}^T$. Moreover, because we assumed that there is no cohesion between cell and its surrounding matrix, the above equation is true for a vanishing cohesive term $\mathbf{T}_d = 0$. To derive a numerical solution of the nonlinear governing equations, it is now necessary to linearize the above expressions. For this, we linearize stresses following $\{\mathbf{T}\} = \{\mathbf{T}\} + \{\dot{\mathbf{T}}\}\delta t$, where δt

is a small time increment. Following expressions (2.27) for the material time derivative of Cauchy stresses, the spin dependence of the objective stress rate take the form:

$$\{\mathbf{W}\cdot\mathbf{T}+\mathbf{T}\cdot\mathbf{W}^T\}=\mathbf{T}^v W=\mathbf{T}^v\left(\mathbf{G}\cdot\dot{\mathbf{d}}^e\right) \tag{2.37}$$

where $\mathbf{T}^v=\begin{bmatrix}2T_{12} & -2T_{12} & T_{22}-T_{11}\end{bmatrix}^T$ and:

$$\mathbf{G}=\begin{bmatrix}\mathbf{G}_1 & \mathbf{G}_2 & ... & \mathbf{G}_{m+n}\end{bmatrix} \text{ and } \mathbf{G}_I=0.5\begin{bmatrix}\frac{\partial\bar{\mathbf{N}}_I(\mathbf{x})}{\partial x_2} & -\frac{\partial\bar{\mathbf{N}}_I(\mathbf{x})}{\partial x_1}\end{bmatrix} \tag{2.38}$$

Equation (2.37) can also be written for surface and contractile stresses $\mathbf{T}_s$, $\mathbf{T}^0$ and $\mathbf{T}^0_s$, respectively. Finallly using constitutive relations (4.52) and (2.25), linearized versions of the virtual powers read:

$$\begin{aligned}
\delta\tilde{P}_{int} &= \sum_e\Bigg(\int_{\Omega^e}(\mathbf{B}\cdot\delta\mathbf{v}^e)^T(\{\mathbf{T}\}+\{\mathbf{C}\}\cdot(\mathbf{B}\cdot\mathbf{v}^e)\cdot\delta t+\mathbf{T}^v(\mathbf{G}\cdot\mathbf{v}^e)\cdot\delta t)\;d\Omega^e\\
&+\int_{\Gamma^e}(\mathbf{M}_p\cdot\mathbf{B}\cdot\delta\mathbf{v}^e)^T(\{\mathbf{T}^s\}+\{\mathbf{C}_s\}\cdot(\mathbf{M}_p\cdot\mathbf{B}\cdot\mathbf{v}^e)\cdot\delta t+\mathbf{T}^v_s(\mathbf{G}\cdot\mathbf{v}^e)\cdot\delta t)\;d\Gamma^e\\
&-\int_{\Omega^e}(\mathbf{B}\cdot\delta\mathbf{v}^e)^T\cdot(\{\mathbf{T}^0\}+\{\mathbf{T}^0\}^{\sigma J}\cdot\delta t+\mathbf{T}^{0,v}(\mathbf{G}\cdot\mathbf{v}^e)\cdot\delta t)\;d\Omega^e\\
&-\int_{\Gamma^e}(\mathbf{M}_p\cdot\mathbf{B}\cdot\delta\mathbf{v}^e)^T\cdot(\{\mathbf{T}^0_s\}+\{\mathbf{T}^0_s\}^{\sigma J}\cdot\delta t+\mathbf{T}^{0,v}_s(\mathbf{G}\cdot\mathbf{v}^e)\cdot\delta t)\;d\Gamma^e\Bigg) \qquad (2.39)\\
\delta\tilde{P}_{ext} &= \sum_e\left(\int_{\Omega^e}\rho\;(\mathbf{N}\cdot\delta\mathbf{v}^e)^T\cdot\mathbf{b}\;d\Omega^e+\int_{\partial\Omega^e_t}(\mathbf{N}\cdot\delta\mathbf{v}^e)^T\cdot\bar{\mathbf{t}}\;d\partial\Omega^e_t\right) \qquad (2.40)
\end{aligned}$$

In the above equation, the second order matrices $\{\mathbf{C}\}$ and $\{\mathbf{C}_s\}$ are the cytoskeleton and cortical membrane elastic matrices in Voigt notation, respectively (note that we deleted the superscript "σJ" and "e" to lighten the expression). In addition, the relationship between the stiffness matrix $\{\mathbf{C}_s\}$ of cortical membrane and its elasticity matrix $\{\mathbf{S}\}^s$ was taken as:

$$\{\mathbf{C}_s\}=\mathbf{M}_p^T\;\{\mathbf{S}\}^s\;\mathbf{M}_p \tag{2.41}$$

where $\mathbf{M}_p$ is defined in (2.35). After factorizing and simplifying the above expressions, one can derive a more convenient form of the virtual powers as:

$$\begin{aligned}
\delta\tilde{P}_{int} &= \sum_e \delta\mathbf{v}^{eT}\left(\int_{\Omega^e}\mathbf{B}^T(\{\mathbf{T}\}+\{\mathbf{C}\}\cdot(\mathbf{B}\cdot\delta\mathbf{v}^e)+\mathbf{T}^v(\mathbf{G}\cdot\delta\mathbf{v}^e))\;d\Omega^e\right.\\
&+ \int_{\Gamma^e}\mathbf{B}^T\cdot{\mathbf{M}_p}^T(\{\mathbf{T}^s\}+\{\mathbf{C}_s\}\cdot(\mathbf{M}_p\cdot\mathbf{B}\cdot\delta\mathbf{v}^e)+\mathbf{T}_s^v(\mathbf{G}\cdot\delta\mathbf{v}^e))\;d\Gamma^e\\
&- \int_{\Omega^e}\mathbf{B}^T\cdot(\{\mathbf{T}^0\}+\{\delta\mathbf{T}^0\}+\mathbf{T}^{0,v}(\mathbf{G}\cdot\delta\mathbf{v}^e))\;d\Omega^e\\
&- \left.\int_{\Gamma^e}\mathbf{B}^T\cdot{\mathbf{M}_p}^T\cdot(\{\mathbf{T}_s^0\}+\{\delta\mathbf{T}_s^0\}+\mathbf{T}_s^{0,v}(\mathbf{G}\cdot\delta\mathbf{v}^e))\;d\Gamma^e\right) \qquad (2.42)\\
\delta\tilde{P}_{ext} &= \sum_e \delta\mathbf{v}^{eT}\left(\int_{\Omega^e}\rho\;\mathbf{N}^T\cdot\mathbf{b}\;d\Omega^e+\int_{\partial\Omega_t^e}\mathbf{N}^T\cdot\bar{\mathbf{t}}\;d\partial\Omega_t^e\right) \qquad (2.43)
\end{aligned}$$

Finally using the principal of virtual power (2.11) and substituting the approximations of the virtual powers (2.42) and (2.43), we obtain the following finite element equation:

$$\sum_e(\mathbf{K}_{int}^e)\cdot\delta\mathbf{d}=\sum_e(\mathbf{F}_{ext}^e-\mathbf{F}_{int}^e) \qquad (2.44)$$

where $\mathbf{K}_{int}^e$ denotes the internal stiffness of element e and takes the form:

$$\begin{aligned}
\mathbf{K}_{int}^e &= \int_{\Omega^e}\mathbf{B}^T\cdot\{\mathbf{C}\}\cdot\mathbf{B}+\mathbf{B}^T\cdot\mathbf{T}^v\cdot\mathbf{G}\;d\Omega^e\\
&+ \int_{\Gamma^e}\mathbf{B}^T\cdot\mathbf{M}_p^T\cdot\{\mathbf{C}_s\}\cdot\mathbf{M}_p\cdot\mathbf{B}+\mathbf{B}^T\cdot\mathbf{M}_p^T\cdot\mathbf{T}_s^v\cdot\mathbf{G}\;d\Gamma^e\\
&- \int_{\Omega^e}\mathbf{B}^T\cdot\mathbf{T}^{0,v}\cdot\mathbf{G}\;d\Omega^e-\int_{\Gamma^e}\mathbf{B}^T\cdot\mathbf{M}_p^T\cdot\mathbf{T}_s^{0,v}\cdot\mathbf{G}\;d\Gamma^e \qquad (2.45)
\end{aligned}$$

while the internal and external forces associated with element e are written as:

$$\begin{aligned}
\mathbf{F}_{int}^e &= \int_{\Omega^e}\mathbf{B}^T\cdot\{\mathbf{T}\}\;d\Omega^e+\int_{\Gamma^e}\mathbf{B}^T\cdot\mathbf{M}_p^T\cdot\{\mathbf{T}^s\}\;d\Gamma^e\\
&- \int_{\Omega^e}\mathbf{B}^T\cdot\{\mathbf{T}^0\}\;d\Omega^e-\int_{\Gamma^e}\mathbf{B}^T\cdot{\mathbf{M}_p}^T\cdot\{\mathbf{T}_s^0\}\;d\Gamma^e \qquad (2.46)\\
\mathbf{F}_{ext}^e &= \int_{\Omega^e}\rho\;\mathbf{N}^T\cdot\mathbf{b}\;d\Omega^e+\int_{\partial\Omega_t^e}\mathbf{N}^T\cdot\bar{\mathbf{t}}\;d\partial\Omega_t^e \qquad (2.47)
\end{aligned}$$

The quantities are then numerically evaluated using Gaussian quadrature for which four integration points are considered in normal and partially enriched elements. However, integration in fully enriched elements is carried out by subdividing elements into sub-triangles

following [44] and integration on the cell surface follows from the assumption that the interface is straight within an element (this only requires two integration points on the interface). The reader is referred to [54] for a more complete description of the integration scheme used in this study. The finite element equation (2.44) has been implemented in a Fortran computer program following the flowchart presented in Fig. 2.4. To summarize, a solution $\mathbf{d}$ of the nodal displacements is obtained as a function of time by computing a solution of (2.44) at different time increments Δt and proceeding to time integration of various quantities such as velocities and the projection operator. At each time increment, the determination of incremental displacements $\Delta\mathbf{d}$ follows from an iterative Newton-Raphson procedure such that $\Delta\mathbf{d} = \sum_{nitr} \delta\mathbf{d}$, where the vector $\delta\mathbf{d}$ denotes the nodal displacements of each iteration and $nitr$ stands for the number of nonlinear iterations. After each iteration, stresses, coordinates and normal vectors are updated using general evolution equations (2.27) and (2.8). Finally, the total nodal displacements are calculated by $\mathbf{d} = \sum_{ninc} \Delta\mathbf{d}$, where $ninc$ stands for the number of increments.

A significant advantage in using the above formulation is that the complex shapes of cells (Fig. 2.2) are described with a level-set function independently of finite-element discretization. Issues related with meshing complex shapes (in two and three-dimensions) are therefore totally alleviated. Another important remark is that while, in general, cell motion depends on the deformation of the external matrix due to cell-matrix cohesion, the lack of a cohesive stress $\mathbf{T}_d$ precludes these interactions. As a result, cell and matrix may be considered as two independent bodies undergoing independent deformations. Since the two bodies are originally defined as connected domains on a single finite element mesh, the capability of XFEM to describe discontinuities in velocities between the two domains is critical.

2.6 Numerical investigation of the role of the cortical membrane on cell deformation

The objective of this section is to validate the model and provide a general analysis of the role of the cortical membrane on cell deformation using the proposed model. For the sake of simplicity, the study concentrates on an initially square cell whose displacements are constrained at its four corner in order to mimic adhesion to a stiff substrate (Fig. 2.5a). Furthermore, the cell is described by material properties shown in table 2.1 and following [37], the cytoskeleton is subjected to an isotropic contractile stress $\mathbf{T}^0 = T^0\mathbf{I}$ generated by randomly oriented stress fibers in the cytoskeleton. On the computational side, the domain Ω was discretrized into a $19*19$ regular finite element square mesh, of total size $50\mu m$. The cell domain Ω_c was defined by a level-set function representing a square domain spanning about 15 elements, for which the four corner elements were subjected to a constrained displacement. We have shown that this choice of discretization gave a good combination of efficiency and convergence.

Table 2.1: Physical constants used in simulations

Constant	Value	Reference
E	77 Pa	([37])
ν	0.3	([37])
K_s	0.1 N/m	
T_s^0	0 N/m	
T^0	45 Pa	([37])

2.6.1 Effect of cortical stiffness on cell deformation

The first example consists in investigating the general effect of the cortical membrane on cell deformation. The deformed configuration of the cell is then studied in two cases: (a) no cortical stiffness and (b) the cortical stiffness is given by $K_s = 0.1\ N/m$. As shown in Fig. 2.5, the presence of a cortical membrane (when $K_s = 0.1\ N/m$) results in the

homogenization of surface strains and surface curvatures. This is not surprising as cortical stiffness acts against surface deformation. A consequence of this is that the cell boundary is characterized by a circular shape between two adhesion regions, a result that is confirmed by the experimental work of Bischofs et al. ([14]) on fibroblasts (Fig. 2.5b). Furthermore, upon observing the stress distribution in the cytoskeleton in Fig. 2.5, one sees that a cell without cortical membrane is subjected to a large stress concentration near its corner while internal stresses are more uniform when cortical stiffness increases. This suggests a possible role of the cortical membrane in protecting the cell against large stresses and possible damage, especially in adhesion regions that are prone to undergo large variations of both surface and bulk deformation.

2.6.2 Relationship between cortical stiffness and membrane curvature

Let us now investigate how membrane curvature varies in terms of cortical stiffness K_s and contractile stress T^0. In particular, it is of interest to compare the numerical solution derived in this chapter to the analytical solution of a cable, attached at its two ends and subjected to a distributed external force T^0 acting perpendicular to the cable's direction (Fig. 2.6b). If we consider the external force as the cytoskeleton's contractile stress, this problem provides a benchmark with which to compare our numerical solution, when cytoskeleton elasticity becomes negligible compared to cortical stiffness. Considering that the spanning distance, d, does not change during deformation and that the cortex has constant curvature with line tension T_s and stiffness K_s, one can show that the radius of curvature, R, of the membrane is ([14]):

$$R = \frac{T_s}{T^0} = \frac{K_s}{T^0}\left(\frac{L-\alpha d}{\alpha d}\right) \tag{2.48}$$

where $L = 2R\ arcsin(d/2R)$ and αd are the current and reference length of the arc, respectively. Rearranging the equations finally leads to the following relationship between the

cortex curvature κ, the cortical stiffness K_s and the contractile stress T^0:

$$\frac{1}{\kappa d} = \frac{K_s}{T^0\, d}\left(\frac{2}{\alpha\kappa d}\; arcsin\left(\frac{\kappa d}{2}\right) - 1\right) \tag{2.49}$$

To compare analytical and numerical prediction, we then studied the relationship between the non-dimensional surface curvature κd and the ratio $K^s/T^0 d$ of cortical stiffness and contractile stress as depicted in Fig. 2.7. Results show a net decrease of membrane curvature with increasing cortical stiffness, with noticeable differences between the analytical and numerical predictions for small values of $K^s/T^0 d$. These trends may be explained as follows. For large values of $K^s/T^0 d$, the stiffness of the cortical membrane is significantly higher than the stiffness of the bulk cytoskeleton, and the assumptions of the analytical model are acceptable. As a consequence, numerical and analytical prediction coincide. However, for small values of $K^s/T^0 d$, the effect of the bulk cytoskeleton has a large influence on cell deformation, a feature that is not predicted by the analytical model. In this case, bulk stiffness provides a resistance to membrane curvature by limiting the deformation of the internal cytoskeleton. These results show significantly smaller surface curvature than that of analytical prediction. These results are important for two reasons: (a) they validate the proposed numerical method to study the effect of the membrane cortex on cell deformation in the region of large cortical stiffness and (b) they extend the range of prediction provided by the analytical solution by incorporating the role of cytoskeleton elasticity on membrane curvature.

2.6.3 Relative influence of cytoskeleton and cortical membrane on cell contraction

Next, we propose to investigate the effects of three intrinsic cell properties (cytoskeleton's Young's modulus E, cytoskeleton's Poisson's ratio ν and cortical tension T_s^0) on the curvature of the cortical membrane. Such knowledge is potentially relevant in understanding how cells can modify their shape by adjusting the properties of their cytoskeleton.

2.6.3.1 Young's modulus

In this example, the Eulerian XFEM formulation is used to assess the effect of the cytoskeleton's Young's modulus on the cell membrane curvature after deformation. For this we considered a cell whose properties are given in table 2.1 and for which the Young's modulus is varied from 77 to 150 Pa. Results are summarized in Fig. 2.8. The results show how an increase in cytoskeleton's Young's modulus tends to decrease membrane curvature. This effect is particularly noticeable for small values of cortical stiffness. These results therefore emphasize the fact that the role of the cortical membrane on cell's deformation is increasingly important, and cannot be neglected, as cytoskeleton stiffness decreases.

2.6.3.2 Poisson's ratio

Another material parameter of interest is the Poisson's ratio of the cytoskeleton. The next investigation therefore consisted in varying the value of ν from 0 to 0.5 (for which the cytoskeleton becomes an incompressible material), while keeping the other material parameters constant and equal to those presented in table 2.1. Fig. 2.9 shows the changes of the normalized cortex curvature as a function of the non-dimensional parameter $K_s/T^0\ d$ for values of Poisson's ratios. General trends show that increasing the Poisson's ratio results in increasing the resistance of the cytoskeleton and therefore, decreasing membrane curvatures. Moreover, it is observed that for high Poisson's ratio (close to 0.5), the curvature becomes independent of the surface stiffness for small values of the cortical stiffness. This may be explained by the fact that for high Poisson's ratios, the cytoskeleton becomes nearly incompressible and shear deformation is favored over volume changes. Cytoskeleton stress is thus modified near the membrane, limiting the magnitude of tangential stretch and homogenizing membrane curvature, even for relatively low membrane stiffness. Furthermore, it is interesting to note that even for an incompressible cytoskeleton ($\nu \approx 0.5$), we observe a change in cell area. In fact, our results show that due to the plane stress assumptions, an increase

in the cell's thickness is possible (with increasing out-of-plane deformation) such that the global volume of the cell is preserved.

2.6.3.3 Cortical contraction

In addition to cytoskeletal contraction T^0, contractile cells may change their shape by applying a cortical tension T_s^0. This process is thought to be at the origin of cell blebbing ([154]). The last example therefore investigates how the application of surface tension T_s^0 triggers changes in cell deformation, as shown in Fig. 2.10.

Results indicate that the application of surface tension tends to decrease surface curvature, and that this effect is increasingly pronounced as surface stiffness decreases. In the case of high surface stiffness, surface tension has a small effect on cortical deformation and thus becomes negligible on the general deformation of the cell. These trends can be explained by viewing the tensed cortical membrane as a cable that is straightened by applying an axial force on its two ends. In a similar way, surface tension works to make the cortical membrane return to its original straight line, providing an efficient way for the cell to control its shape through active cortical contraction.

2.7 Summary and conclusions

In summary, this chapter presented a new theoretical/computational framework to model the large deformation of cells, accounting for the effect of a stiff surrounding cortical membrane. Under the assumption of a very small cortical thickness, the equations of surface elasticity, originally developed for free surface stresses in solids, were developed in the case of large deformations following the Eulerian description. A numerical formulation, based on the XFEM/level-set method was then introduced and utilized to study the effect of cortical elasticity on the deformation of a contractile cell. The contributions and advantages of the proposed method can be summarized as follows:

- The geometry of the cell is entirely represented by level-set functions that are defined independently from the finite element mesh. Simple, regular FEM meshes may thus be used regardless of the geometric complexity of the cell.

- Discontinuities in velocities and deformations resulting from the governing equations are naturally taken into account within the XFEM methodology.

- The model provides an efficient and flexible way to incorporate the contribution of cortical membrane in cell mechanics. In particular, it can easily be extended to incorporate more sophisticated descriptions of the cell's cytoskeleton and its cortical membrane.

Our analysis on the effects of the cortical membrane on cell deformation generally showed that by adding stiffness to the cell's surface, the presence of the cortex induced homogeneous membrane strains and curvature. While this aspect had been shown with a simple analysis considering a cable deforming under the action of an external perpendicular force, the model neglected the effects of cytoskeletal elasticity on surface deformation. Because it is able to incorporate the effect of both cytoskeleton and cortical membrane deformation, the proposed framework could overcome these limitations and accurately capture the distinct role of surface and bulk elasticity in cell deformation. Results showed that while the analytical solution provides a good approximation of membrane curvature when the cytoskeleton is much softer than the cortical membrane, it greatly overestimated its value for low values of cortical stiffness. The numerical method was then used to investigate the variation of cell deformation for various cytoskeleton elastic parameters as well as cortical tension and elasticity. This technique may therefore prove very useful in the determination of cell properties through the analysis of its shape. Besides this, the proposed framework establishes a fast and efficient method that can accurately account for cortical elasticity in future research on cell contraction, migration and cell-matrix interactions.

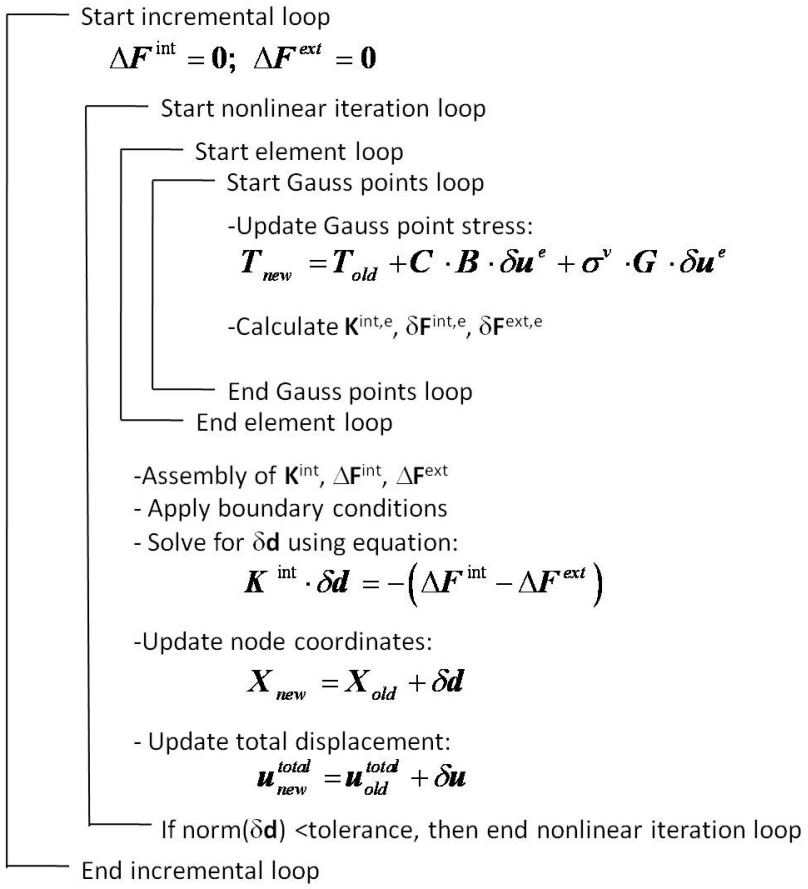

Figure 2.4: The updated Lagrangian algorithm used in the nonlinear solution of the XFEM equations to determine cell deformation.

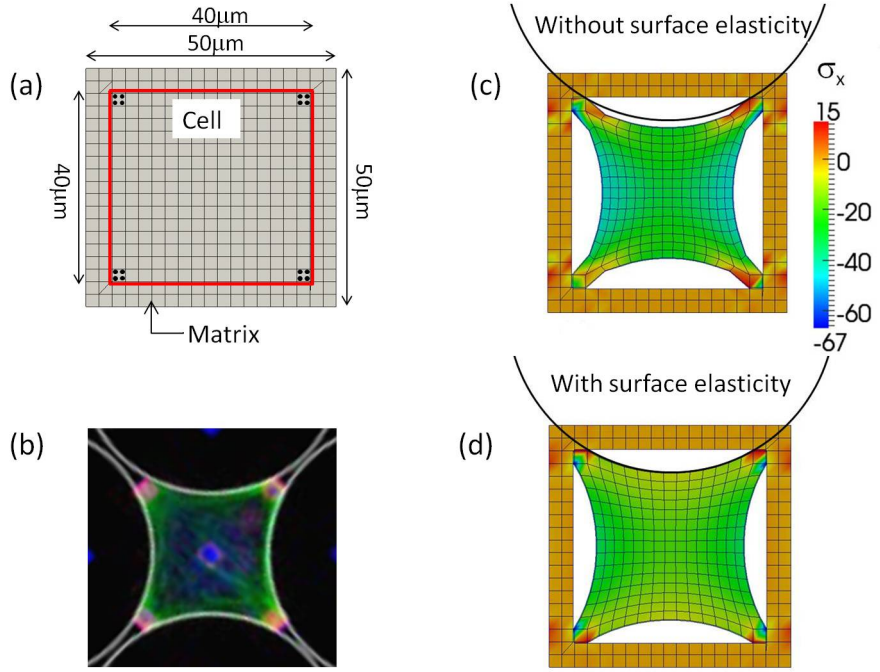

Figure 2.5: (a) Initial configuration and (b) Deformed configuration of a cell on adhesion islands ([14]). (c) deformed configurations of a square cell without and (d) with cortical membrane.

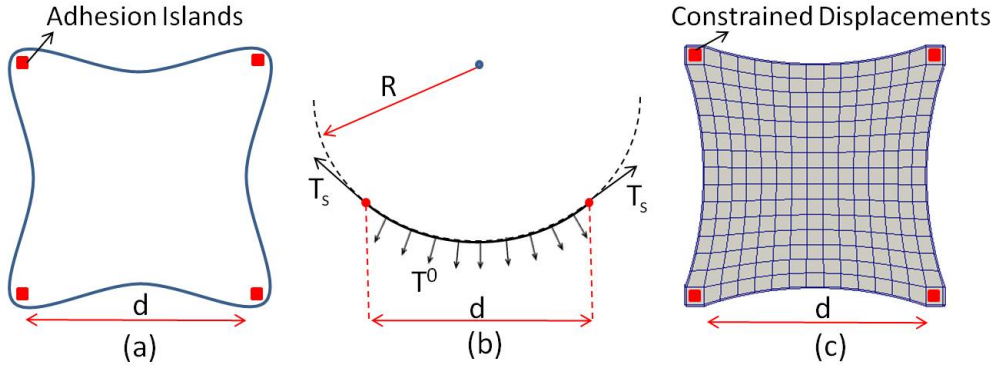

Figure 2.6: The models used in the analytical and numerical solutions. a) The deformed configuration of the cell to be modeled, b) the analytical model and c) the numerical model.

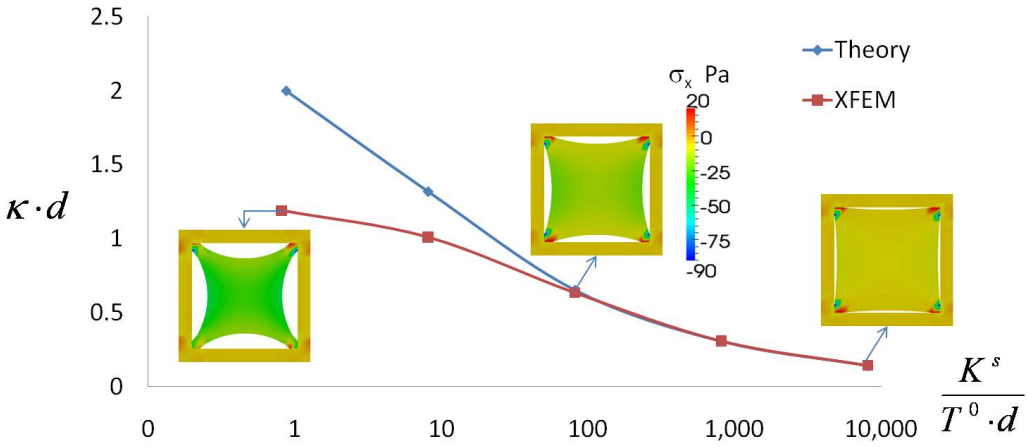

Figure 2.7: Effect of normalized cortex's stiffness on normalized membrane curvature predicted by the numerical (XFEM) and theoretical solutions.

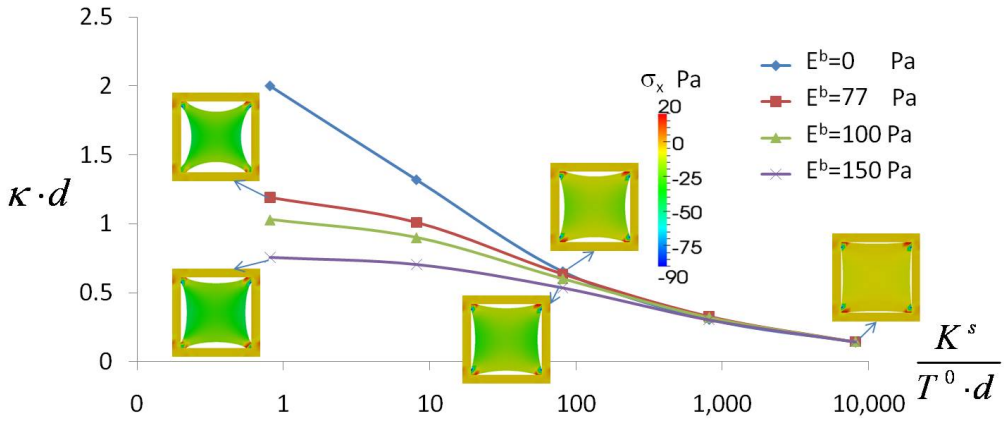

Figure 2.8: Effect of the cytoskeleton's Young's modulus on the normalized curvature of the cortical membrane.

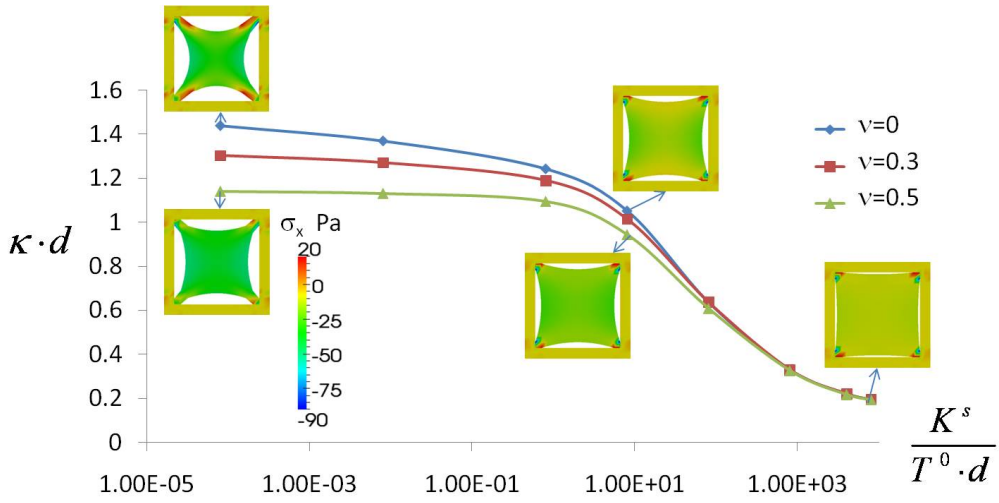

Figure 2.9: Effect of cytoskeleton's Poisson's ratio on the normalized curvature of cortical membrane.

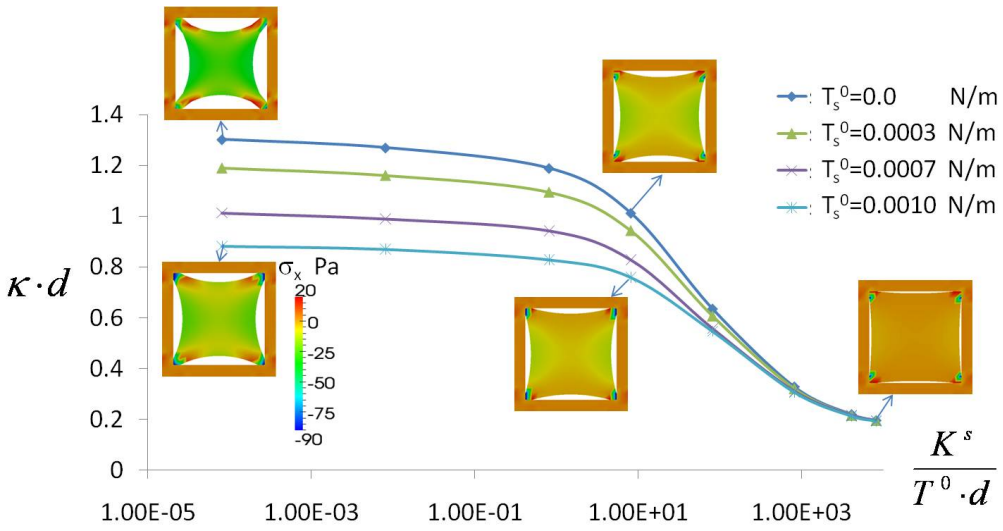

Figure 2.10: Effect of cortical contraction (surface tension) on the normalized curvature of the cortical membrane.

Chapter 3

Bridging the Scales to Explore Cellular Adaptation and Remodeling

3.1 Abstract

This short chapter presents a multiscale framework to better understand the mechanisms of biological tissue evolution from molecular to tissue scale. For this, a bottom-up strategy is proposed in which mechano-sensitive molecular processes, the evolution of cell architecture and contraction as well as the interaction between cells and the extra-cellular matrix can be integrated in a single framework. Preliminary studies based on this approach suggest that mechano-sensitive feed-back mechanisms at several length-scales may be a key element to understand tissue adaptivity to this mechanical environment.

3.2 Introduction

One of the fundamental research questions in mechano-biology is to seek the main processes and mechanisms by which biological tissues are able to adaptively change their properties and structure in response to external stimuli. Any knowledge gained along this direction has the potential to shine a light on important phenomena such as morphogenesis [76], remodeling and growth [131], wound healing [102], but also the dynamics of cancer evolution [118, 101, 21]. Past research has shown that the responsive behavior of living tissue results from constant interactions between populations of cells and their surrounding extracellular matrix (ECM). In short, these interactions enable cells to sense stimuli conveyed by the ECM [95] (such as force, deformation or flow) and respond accordingly by changing

the structure of the ECM [149, 34].

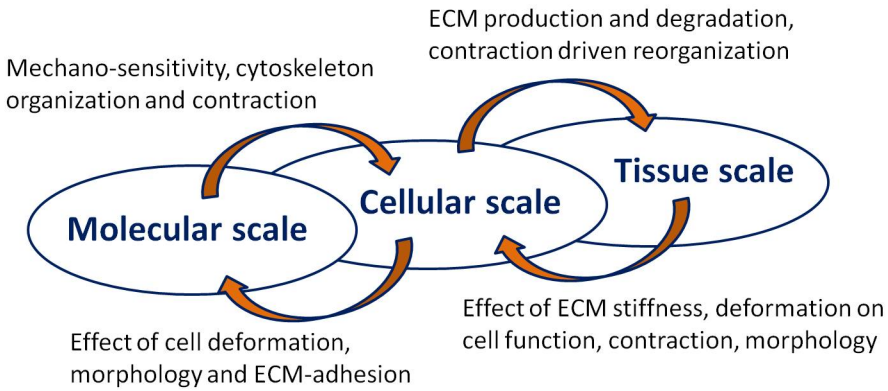

Figure 3.1: Multiscale decomposition of important biological processes responsible for tissue remodeling.

The complex dynamics of such interactions is found to rely on mechanical forces acting on a hierarchy of length and time scales: molecular, cellular and tissue (Fig. 3.1); this has traditionally hindered the development of quantitative and predictive models. However, recent advances in computational science and multiscale modeling suggest a possible new route to help better understand tissue dynamics.

The present chapter discusses recent efforts [163, 161, 165] that have been undertaken to understand certain aspects of tissue dynamics by integrating mechano-chemical interactions from molecular to tissue scale via a hierarchical multiscale paradigm. We particularly concentrate on explaining the mechanisms by which the mechanical environment (stiffness, attachment, stress) of a tissue influences its structural evolution. Numerous experimental studies have shown that at the tissue scale, remodeling is partially due to the generation of contractile stresses by cells (such as myofibroblasts) on their surrounding fibrous matrix [174, 5, 76]. At the cellular scale, cell contractility is explained by mechano-sensitive molecular processes which govern the formation of *stress-fibers* (SF), that are mechanically active components of the cytoskeleton. While the above phenomena involve a variety of complicated signaling pathways that are studied in details by the biology community, the objective of the present

study is to develop robust and flexible framework that can incorporate such biologically relevant phenomena in the future. Thus, for the time being, we present an experimentally and physically motivated empirical model, in which we show here that while occurring at different time and length-scales, mechanisms at cellular and tissue levels can be integrated in a single modeling framework, enabling us to obtain some useful insights. In particular, the model suggests that feed-back mechanisms occur both at the molecular and cellular levels, allowing tissues to timely react to any change in their mechanical environment.

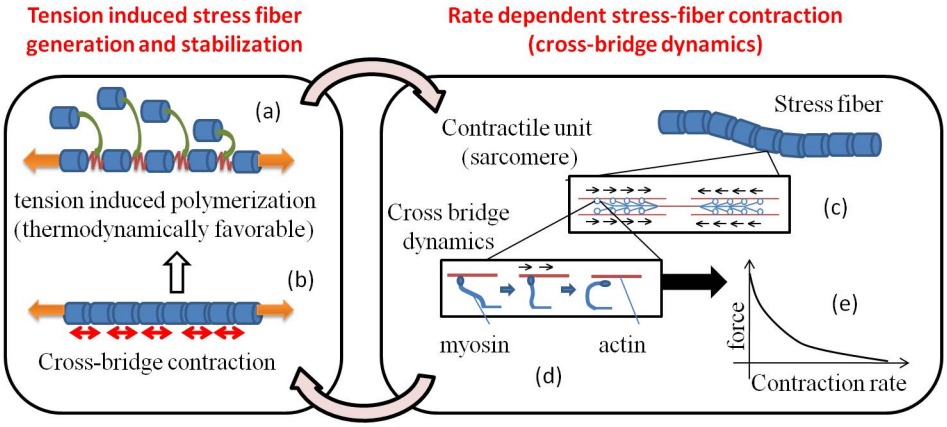

Figure 3.2: Molecular mechanisms of SF formation and contraction. The feedback mechanism between the two phenomena constitutes the basis of the proposed model.

3.3 From molecular sensing to cell organization

Let us first discuss how information from the molecular scale may be used to describe the structural organization and contraction at the cellular level. The capacity of a contractile cell to spread, deform and generate tensional forces is principally due to the existence of a network of SF. Studies have shown that SF organization and contractility were strongly influenced by the nature of the cell's mechanical environment (such as stiffness, deformation or loading frequency [41]). For instance, it was shown that SF tend to align in directions of maximum effective stiffness and stretch (for static loading). From a modeling standpoint,

it is known that the above phenomena are the result of non-equilibrium processes that involve mass/energy exchanges within the cell and across its membrane. For instance, SF formation arises from mass exchange with actin and myosin monomers while contraction would not be possible without the supply of energy in the form of ATP. Such interactions between constituents (fluid, solid, molecules) have been very well described in the context of the mixture theory [143]. This class of mathematical models is based on a continuous description of the behavior and interactions of various constituents in order to represent deformation, relative motion and mass exchange while verifying the fundamental principles of continuum mechanics (mass, momentum and energy balance). Furthermore, since this class of models allows for mass and energy exchange across the cell, it can potentially be extended for describing the non-equilibrium thermodynamics of (open) cellular systems. In this context, it has been proposed by the authors to view contractile cells as a mixture of three principal constituents: (a) a solid cytoskeleton made of a mechanically passive component (microtubules and intermediate filaments), (b) anisotropic active SF network and (c) a fluid phase that consists of water in which a pool of dissolved monomers can assemble into SF under certain conditions. The mechanisms of conversion of monomers into SF together with the contraction of existing SF are precisely what drives cellular force generation and organization.Experimental studies suggest that while different cell types exhibit differences in their dynamics and strength of contraction, they show strong similarities regarding the fundamental contraction mechanisms. In that respect, a realistic model for cell contractility can be built on two key hypotheses:

(1) *SF formation is promoted by the existence of a state of mechanical tension.* One of the main mechanisms that drive the reorientation of stress fibers is the strong dependency of the polymerisation process on the contractile stress of the SF. Experiments have shown that the process of SF polymerization starts with the activation of the RhoA enzyme [25] and its downstream effector ROCK that induces myosin

light chain phosphorylation; this in turn enables their assembly in filaments as well as their interaction with actin. Once formed into filaments, SF are stabilized when subjected to a state of tension. This phenomenon may be explained as follows; from a thermodynamical point of view the evolution of a SF occurs in a manner such that its total free energy decreases. When in tension, the incorporation of new contractile units in a filament results in relaxing the strain energy of SF and thus decreasing its free energy [135] (Fig.3.2a,b). In other words, upon nucleation, SF formation and stabilization are therefore thermodynamically favored mechanisms when tension is present; this ultimately leads to an overall higher density of SF in cells.

(2) *SF contraction decreases with rate of SF shortening.* The contractile behavior of SF is explained by their sarcomeric structure (Fig. 3.2c) in which actin-myosin cross-bridge dynamics occurs in a similar fashion as that observed in muscles. From a molecular viewpoint, force is generated from myosin heads stepping on actin filament by binding to it, pulling and detaching (Fig. 3.2d). An increased rate of SF shortening is associated with a rise in the rate of myosin detachment, and consequently in a drop of the total number of myosin heads bound to the actin filament. Since the force applied by myosin on the actin filament is proportional to the number of bound myosin heads, the resulting force decreases with rate of shortening. This behavior is often described in terms of the tension-velocity relation [80], showing a hyperbolic decline in SF contractility with rate of shortening (Fig. 3.2e).

Altogether, the above hypotheses are the basis of feed-back mechanisms cells may use to sense and react to their mechanical environment. Thus, upon initial SF formation, maximal SF contraction occurs in directions that offer the most resistance to shortening (hypothesis 2). In turn, SF contraction induces a state of tension that promotes the formation of more SF (hypothesis 1), until the stock of actin and myosin monomers is depleted. This explains the fact that SF tend to align in directions of maximum stiffness. In addition, the model

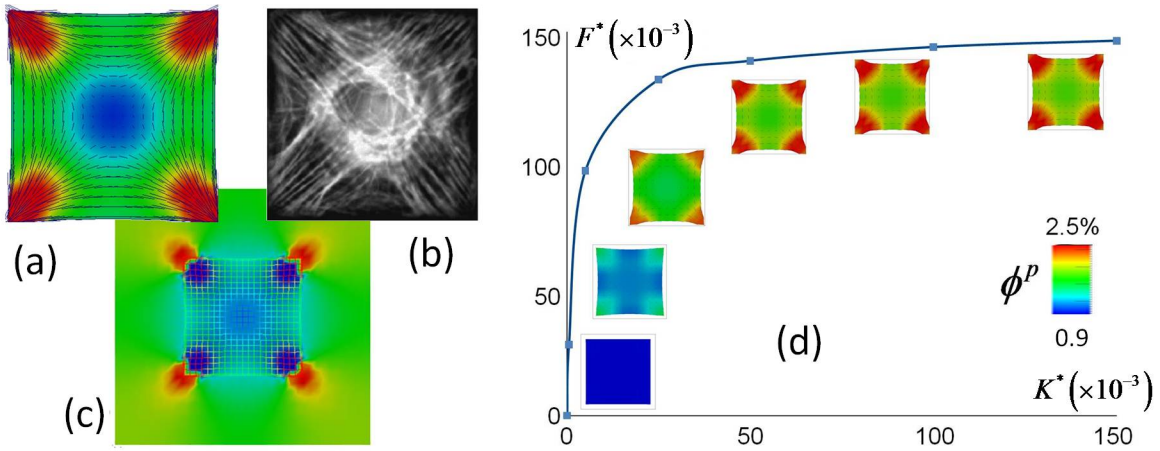

Figure 3.3: (a) Prediction of SF distribution on stiff substrate, (b) observation from [18, 117, 61, 19] and (c) resulting substrate deviatoric stress (model prediction). (d) Cell architecture and force generation in terms of substrate stiffness (model predictions).

predicts that the characteristic time of cell contraction arises from two processes: the rate of SF assembly and the dynamics of cross-bridge attachment and detachment. The cell-specific contribution of each mechanism may be determined by further experimental studies. To evaluate model prediction in various situations, finite element simulations were used to predict SF distribution in a square cell attached at its corner (Fig. 3.3). Consistent with experimental observations, SF generally tend to align in diagonal directions, where shortening is most resisted while cell contraction is found to increase in a nonlinear fashion with substrate stiffness. It is important to note that the simulations presented in this study are non-dimensional, i.e, the magnitude of the contractile forces and dynamics of contraction are measured relatively to the typical force in a single SF (during isometric deformation) and rate constants describing the Hill model and SF formation. In other words, cell-specific behavior may be obtained by using biologically relevant molecular models for SF formation and contraction. The information gained at the cellular scale may then be upscaled to the tissue level by considering a representative tissue volume whose behavior relies on cell-ECM interactions.

3.4 From cell contraction to tissue deformation

Cells and their surrounding ECM form a very intricate dynamical system, whose interactions entirely determine the fate of living tissues. As discussed above, cells can feel the mechanical properties of their environment, and respond by changing their structure, applying traction or reorienting in specific directions [74, 15, 60]. In turn, the surrounding ECM actively changes structure under cellular forces; this ultimately leads to large scale tissue remodeling [74]. Studies have shown that few important factors drive the remodeling process. First, ECM properties and anisotropy dictate the orientation and spreading of cells. In general, cells tend to align in the direction of maximum stiffness [120], in the direction of ECM fibers [173, 46] and in the direction of the tensile strain [78, 47]. Second, the effect of mechanical constraints on tissue structure is known to be important; for instance, many studies have shown that cell orientation and gel morphology was strongly affected by the nature of boundary conditions imposed to cell-populated gels [4, 15, 6]. Third and finally, cell-cell communication through ECM deformation is likely to be an important factor of remodeling. In other words, by contracting and deforming the ECM, a cell sends a mechanical signal to its neighbors, resulting in stronger tissue contraction [75, 85, 27]. The dramatic effect of this collaborative behavior can be readily observed during the large compaction of cell-populated gels once a critical density is reached [48].

From a modeling viewpoint, bridging cell-scale to tissue-scale can be accomplished by computational homogenization, a method that consists in extracting macroscopic information (such as tissue deformation) by performing spatial and temporal averages of the local interactions between cells and their surrounding matrix. Concentrating on contractile cells on elastic substrate and assuming a spatially periodic cell distribution, a representative material volume may be built (Fig. 3.3c) consisting of a single cell adhering to an elastic substrate through pre-existing focal adhesion complex. Coupling this strategy with the cellular model (previous section) enables further investigations onto the mechanism of cell-ECM interac-

tions. It is important to note that by considering a substrate whose behavior is time independent (as it is purely elastic), the time scale at the tissue level is entirely driven by the cell dynamics. However, in more realistic situations, i.e. the ECM is visco-elastic, the characteristic time scale of tissue remodeling is the result of interactions between the time dependence of both cell and ECM. Here, we illustrate the method by assessing the influence of substrate stiffness and anisotropy on the cell architecture and the development of contractile stresses at the tissue level. In particular, while the temporal aspect is certainly important, we focus here on the state of cells and matrix once they reached chemical and mechanical equilibrium (steady state). Cells in an isotropic environment have been shown to take a stellate morphology and increase their contraction and stress-fiber network with substrate stiffness. These observations can qualitatively be reproduced by considering an isotropic square cell on an elastic substrate for which the elastic is varied. As large substrate stiffness provides more resistance to cell contraction, SF density and cell contraction increase significantly with substrate stiffness, resulting in a rise in substrate deformation. This seems to indicate that a very small window of substrate stiffness exists such that cells can deform the substrate: for low stiffness, cells do not contract while for high stiffness, the substrate is too stiff to deform.

The evolution of cell morphology, including spreading area, alignement and polarization , is also known to be strongly dependent on substrate properties. Cells typically polarize and align their SF in direction of maximum effective substrate stiffness [15]. To better understand this behavior, we first considered a strongly anisotropic elastic substrate whose stiffness differs by a ratio of 100 between two perpendicular directions. Simulations show that cells interacting with this substrate exhibit a SF network that is totally aligned with the direction of maximum stiffness, which subsequently induce more substrate strain in this particular direction (Fig. 3.4a). This cell architecture suggests that cell morphology may develop in direction of maximum stiffness as observed experimentally. To further understand

the development of anisotropy, we then considered the reciprocal situation of an isotropic substrate and an anisotropic cell morphology (Fig. 3.4b), in which adhesions are located at the cell's corners. In this case, the model shows that the cell realigns its SF along its principal axis, regardless of substrate isotropy; this consequently induces substrate deformation along the long axis of the cell. This has consequences in more biologically relevant settings where the ECM is made of a fibrous network (collagen and elastin) whose fibers tend to align in the direction of stretch. In this situation, the model suggests that elongated cells apply traction forces that tend to align fibers (and thus increase ECM stiffness) along their long axis. In other words, the models clearly suggests that the evolution of the ECM (or substrate) and cells are completely dependent on one-another and may not be considered separately. ECM properties and deformation are influenced by cells and vice-versa; this creates a series of cross-talks that feedback onto themselves to drive macroscopic tissue evolution.

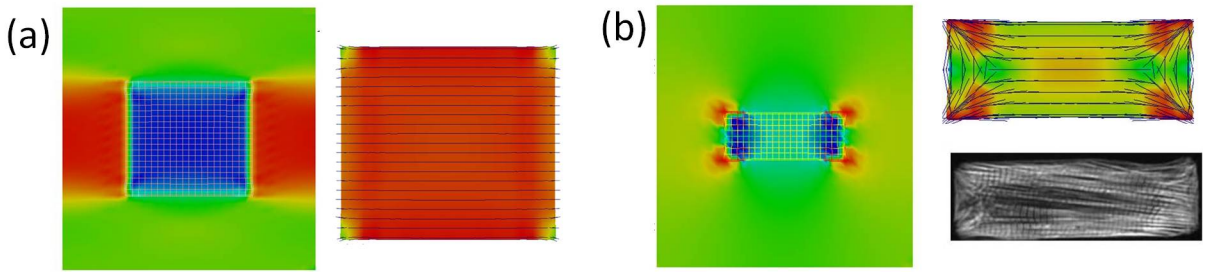

Figure 3.4: a) Predicted substrate stress (deviatoric) and SF distribution when the substrate stiffness in the horizontal direction is 100 times that in the vertical direction. (b) Predicted substrate stress (deviatoric) and SF distribution for an elogated cell on an isotropic substrate. A comparison with experimental observation of SF distribution as reported in [18, 117, 61, 19] is also shown.

3.5 Conclusion

Biological tissue remodeling and evolution depend on a variety of processes that occur at very different length and time scales and strongly interact with one-another. Consequently, accurate mathematical models must not only accurately describe phenomena at

each scale but integrate them into a single multiscale framework. This chapter proposes such a strategy by considering three distinct length-scales that are essential to tissue dynamics, namely, molecular, cellular and tissue scales. In particular, we discussed how relevant molecular mechanisms of mechano-transduction can be considered to describe the evolution of cell architecture and contraction in terms of their mechanical environment. Furthermore, using homogenization techniques, we investigated how certain aspects of the interactions between cells and an elastic substrate may lead to global tissue reorganization and deformation. In particular, the model suggests that feed-back mechanisms at several scales may be a contributing factor to the quick and adaptive response of a tissue to its mechanical environment. To conclude, while our knowledge of molecular and cellular mechanisms is currently skyrocketing due to more and more powerful experimental techniques , the need of multiscale modeling in biology has never been greater in order to interpret how molecular, cellular and tissue phenomena are linked. Upon maturation, it is anticipated that the predictive power of these types of models will lie in (a) providing refined interpretations of the macroscopic behavior of cells in different situations in terms of the key molecular phenomena and their interactions and (b) virtually predict changes in cell behavior with respect to modifications in their environment or composition. This aspect will particularly be critical in developing cures for a variety of diseases.

Chapter 4

A Constrained Mixture Approach to Mechano-Sensing and Force Generation in Contractile Cells

4.1 Abstract

Biological tissues are very particular types of materials that have the ability to change their structure, properties and chemistry in response to external cues. Contractile cells, i.e. fibroblasts, are key players of tissue adaptivity as they are capable of reorganizing their surrounding extra-cellular matrix (ECM) by contracting and generating mechanical forces. This contractile behavior is attributed to the development of a stress-fiber (SF) network within the cell's cytoskeleton, a process that is known to be highly dependent of the nature of the mechanical environment (such as ECM stiffness or the presence of stress and strain). To describe these processes in a consistent manner, the present chapter introduces a mutiphasic formulation (fluid/solid/solute mixture) that accounts for four major elements of cell contraction: cytoskeleton, cytosol, SF and actin monomers, as well as their interactions. The model represents the cross-talks between mechanics and chemistry through various means: (a) a mechano-sensitive formation and dissociation of an anisotropic SF network described by mass exchange between actin monomer and polymers, (b) a bio-mechanical model for SF contraction that captures the well-known length-tension and velocity-tension relation for muscles cells and (c) a convection/diffusion description for the transport of fluid and monomers within the cell. Numerical investigations show that the multiphasic model is able to capture the dependency of cell contraction on the stiffness of the mechanical

environment and accurately describes the development of an oriented SF network observed in contracting fibroblasts.

4.2 Introduction

Biological tissues are very particular types of materials that have the ability to change their structure, properties and chemistry in response to external cues. This fast response capability can be attributed to the out-of-equilibrium nature of the tissue structure, resulting from a constant cross-talk between a population of cells and their surrounding extra-cellular matrix (ECM). These interactions allow cells to sense stimuli conveyed by the ECM [95] (such as force, deformation or flow) and the ECM to restructure due to the action of cells (characterized by traction forces [149, 34] or enzyme degradation [166]). In this context, a large number of studies have demonstrated that cell contraction and architecture were strongly dependent on substrate stiffness [169, 139, 70, 98], giving mechanics a central role in cell-substrate interactions. Experimental studies on contractile cells (such as myofibroblasts) generally show that larger substrate stiffness results in higher cell stability that manifests itself by large spreading areas and generation of significant traction forces. In addition, actin staining procedures have shown that fibroblast contraction is associated with the formation of highly aligned stress-fibers (SF) within the cell's structure (cytoskeleton) that anchor at the point of cell-substrate adhesion and often span the entire length of the cell. The distribution and orientation of these fibers correlate very well with the presence of contractile forces applied by cells to their underlying substrate. These phenomena clearly illustrate the intricate interplay between mechano-sensing, force generation and cytoskeletal structure, which is essential to tissue remodeling.

Despite our more and more accurate understanding of the molecular mechanisms responsible for contraction, there are still many questions concerning the nature and mechanisms of mechano-sensing and force generation [160]. To tackle these questions, it is necessary

to develop mathematical models that are capable of describing the cross-talk between cellular mechanics and biochemistry in a quantitative fashion. From a modeling standpoint, cell contractility has often been considered in terms of prestress or prestrain, either within the context of fibrous networks [107] or continuum mechanics [110, 166]. While such simplified models capture well the mechanical aspects of cell contraction, they are unable to explain many features occurring from chemo-mechanical interaction at the molecular scale, such as dependency of contractility on substrate stiffness and ligand density. More recent studies by Desphandes et al. [37, 39] introduced a bio-mechanical model that is able to describe cytoskeleton contraction by considering molecular mechanisms associated with SF formation and focal adhesion assembly. This approach provides a promising means of capturing the chemo-mechanics of cell contraction but it neglects the multiphasic aspect of the cell's body in which monomer transport, interstitial fluid (cytosol) pressure and mass exchange can take place. The inclusions of the above physics is critical to respect fundamental physical principles such as mass conservation, but also in capturing key cellular phenomena such as osmotic loading and transport phenomena. In continuum mechanics, these types of phenomena have traditionally been described by the theory of porous media and mixtures [12, 13, 155, 17, 127, 144, 166]; these formulations were very successful in describing phenomena such as growth [86, 58], free swelling [144] and osmosis [66]. Applications to the cell have thus far been limited to the flow-dependent mechanical response and swelling behavior of chondrocytes in response to their osmotic environment [68].

The present chapter proposes to extend the range of applications of mixture models to describe the coupled biochemical/mechanical processes responsible for cell contraction. The formulation is based on a description of cells that incorporate four key components of contractility: a passive solid cytoskeleton, an interstitial fluid representing the cytosol, an anisotropic network of SF and a pool of globular actin monomers that freely diffuse in the cytosol. To address the well known difficulties regarding to stress partitioning and boundary

conditions associated with classical theory of mixtures [128], we take the following approach. First, it is assumed that the two solid constituents (passive cytoskeleton and SF) undergo the same motion, which is consistent with the class of constrained mixture models introduced in [86]. Second, we adopt key concepts of poromechanics[153] that consists of describing the motion of a fluid constituents relative to solid constituent through diffusion-type relation (initially originated by Fick and Darcy). In this context, the mixture problem is well-posed and provide a flexible and robust theoretical framework to study the interactions between mechanics and chemistry (incorporating mass and energy exchange between constituents). The key features of the proposed model are as follows: (a) The SF network is described in statistical terms with a Von-Mises distribution whose characteristics (mean, deviation) evolve in time. (b) The generation of contractile force by SF follows length-tension and velocity-tension curves that are known to accurately capture the behavior of sarcomeric structures. (c) The anisotropic formation and dissociation of the SF network depend on the level of contractile stress in existing SF and (d) SF formation is limited by the diffusion and quantity of globular actin monomers present in the cytoplasm. By capturing these important physics, we show that the formulation is capable to reproducing the mechano-sensitivity of cell contraction with respect to substrate stiffness as well as the general architecture of contractile cells.

The chapter is organized as follows. In the next section, we provide the basis for the continuum description of the cell's body that contains both kinematics and structural components. Section 3 then concentrates on the conservation and exchange of mass occurring within the cell during contraction while mechanical equilibrium, SF contractility and cell elasticity are discussed in section 4. Results and predictions of the proposed model are then described in section 5 in which several problems are considered together with comparisons with experimental studies. A general discussion of the model, potential improvements and concluding remarks are finally provided in section 6.

4.3 Constrained mixture description of cells

4.3.1 Continuum assumptions and kinematics

From a material's view point, a cell can be considered as a complex composite structure, composed of a large variety of interacting constituents, which may be solid (such as microtubules, actin filaments, intermediate filaments), fluid (the cytosol) or dissolved species (such as ions, monomers, diverse proteins). Under the assumptions that the characteristic length-scale associated with each constituent is small compared to its size, a cell can be viewed as a multiphasic continuum that can be very well described within the framework of mixture theory. Since the objective of the present chapter is to characterize the chemo-mechanical processes responsible for cell sensing and contraction, we propose to consider four constituents that are critical components of the contractile apparatus of a cell: (a) porous and passive cytoskeleton, made of a network of incompressible filaments and referred with the superscript s (as in solid), (b) an incompressible fluid representing the cytosol, referred with the superscript f (as in fluid), (c) dissolved globular actin monomers, referred by the superscript m (as in monomer) and (d) a network of contractile SF referred by the superscript p (as in polymer). The latter is the active constituent of the cytoskeleton. An illustration of this decomposition is given in Fig. 4.1. It should be noted that the notion of incompressibility is to be understood within the context of "homogenized equivalent constituents", this enables us to avoid complications associated with incompressible constituents in their natural state as described in [127]. The reasons for choosing these four constituents lie in the nature of chemo-mechanical processes responsible for contractility; SF (from actin monomers) are critical elements of contraction and the presence of the cytoskeleton must be included to assess cell deformation. In addition, the existence of the cytosol is essential for monomer transport and its mechanical function in resisting the cell's internal pressure.

Considering a planar cell (under plane stress conditions) as a closed domain Ω_0 delimited by a boundary Γ_0 in its initial configuration, one may locate a material point P by

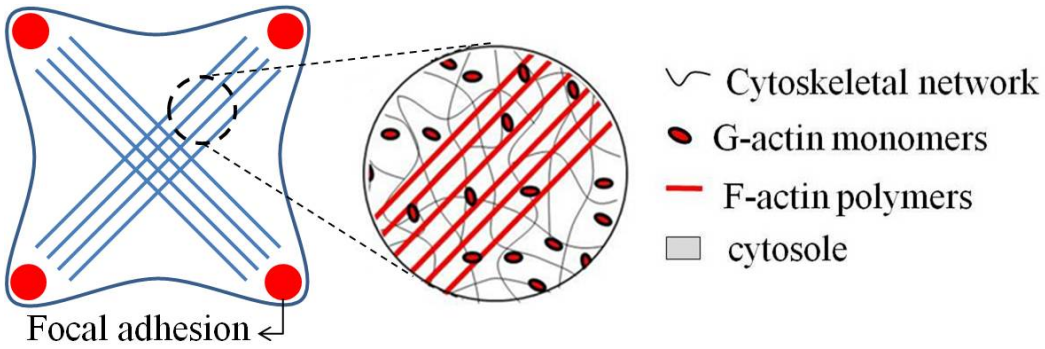

Figure 4.1: *Illustration of the continuum formulation of the cell [117], decomposed into the cytoplasm and the cortical membrane. In the cytoplasm, a material point is seen as a mixture of four constituents, namely the passive cytoskeletal network, the contractile SF, the cytosol and dissolved G-actin monomers.*

its position vector $\mathbf{X}$ in a Cartesian coordinate vector $X_i, i = 1, 2$. Upon deformation, at any time t, a material point associated with each constituent (represented by superscript $\alpha = s, f, m, p$) occupies a position $\mathbf{x}^\alpha$ defined by a continuous and differentiable function $\boldsymbol{\chi}^\alpha$ as:

$$\mathbf{x}^\alpha = \boldsymbol{\chi}^\alpha (\mathbf{X}, t) . \tag{4.1}$$

The material derivative D^α/Dt following the motion of constituent α can then be introduced such that the velocity $\mathbf{v}^\alpha$ of each constituent is given as:

$$\mathbf{v}^\alpha = \frac{D^\alpha \mathbf{x}^\alpha}{Dt}. \tag{4.2}$$

Following these definitions, the relationship between spatial and material time derivatives for a continuous and differentiable function $A(\mathbf{x}, t)$ reads:

$$\frac{D^\alpha A}{Dt} = \frac{\partial A}{\partial t} + \nabla A \cdot \mathbf{v}^\alpha \tag{4.3}$$

where ∇ is the spatial gradient operator. In this chapter, a Lagrangian viewpoint is adopted for the solid deformation while an Eulerian description is adopted for fluid flow and monomer transport. In other words, the solid skeleton is considered as a reference frame in which we compute motion and velocities. In this frame, we introduce relative velocities $\tilde{\mathbf{v}}^\alpha$ as:

$$\tilde{\mathbf{v}}^\alpha = \mathbf{v}^\alpha - \mathbf{v} \tag{4.4}$$

where $\mathbf{v} = \mathbf{v}^s$. We now make a fundamental assumption regarding material motion. As noted by Humphrey and Rajagopal in their treatise on growth [86], there are many difficulties associated with the definition of mixture motion, as well as the partial stresses arising from different solid constituents. These issues result from the fact that based on the knowledge of mixture velocity, there exist a variety of ways to find the individual velocities of constituents. To circumvent this problem, we assume here that all solid constituents located at the same material point at time t follow the same motion. In other words, we assume that SF velocity is equal to the passive cytoskeleton velocity, or equivalently:

$$\tilde{\mathbf{v}}^p = \mathbf{0} \tag{4.5}$$

This assumption enforces a constraint to the model as discussed in [86], which motivates our appellation *"constraint mixture model"*. Futhermore since cell deformation is measured by the deformation of the passive cytoskeleton, it can be measured with the Green-Lagrange strain in the passive cytoskeleton:

$$\mathbf{E} = \frac{1}{2}\left(\mathbf{F}^T \cdot \mathbf{F} - \mathbf{I}\right), \qquad \mathbf{F} = \mathbf{F}^s = \frac{\partial \mathbf{x}}{\partial \mathbf{X}} \tag{4.6}$$

where $\mathbf{F}$ is the deformation gradient, $\mathbf{I}$ is the identity tensor and $\mathbf{x} = \mathbf{x}^s$. Finally, in order to follow the changes in cell constitution in time, we define the volume fraction ϕ^α, associated with each constituent representing the relative quantity of each constituent at a continuum point.

$$\phi^\alpha(\mathbf{x}, t) = \frac{V^\alpha}{V} \tag{4.7}$$

where V^α is unit volume of constituent α contained in a unit volume V of mixture at a material point $\mathbf{x}$ in the current configuration. Assuming that the cell is saturated with the four constituents, volume fractions satisfy the following relationship:

$$\sum_{\alpha=1}^{4} \phi^\alpha = \phi^s + \phi^f + \phi^m + \phi^p = 1 \tag{4.8}$$

at all times. A consequence of the above equation is that while the volume fraction of each constituent may change during cell deformation due to volume changes or mass exchange, their sum remains constant.

4.3.2 Anisotropic SF distribution

A particularity of the cell's internal structure is the presence of an evolving, strongly-oriented network of SF. For such anisotropic fibrous network, the volume fraction $\phi^p(\mathbf{x})$ does not provide sufficient information and the description needs to be enriched to account for the angular distribution of fibers. Concentrating on the case of a two-dimensional planar fibrous assembly in the neighborhood of a continuum point, the direction of an individual SF is designated by the angle θ measured between the fiber axis and the direction given by the base vector x_1. Based on this, a volume fraction ϕ^p_θ can be introduced as the ratio of the volume of fibers oriented in the θ-direction and the total volume. This gives rise to a distribution function ϕ^p_θ representing the variation in fiber density with direction, as shown in Fig. 4.2a. In this chapter, we propose to describe this distribution by the π-periodic Von-Mises distribution function (which may be though of as a periodic version of the normal distribution) defined as [59]:

$$\phi^p_\theta(\theta) = \phi^p \left(\frac{exp\left[b\ cos\left(2\theta - 2\theta_0\right)\right]}{I_0(b)} \right) \tag{4.9}$$

where $I_0(b)$ is the Bessel's function of the first kind of order zero defined as:

$$I_0(b) = \frac{1}{\pi} \int_0^\pi exp\left(b\ cos\theta\right) d\theta. \tag{4.10}$$

The Von-Mises distribution is represented in Fig. 4.2b when the largest fiber density is along the θ_0-direction. On the figure, it can clearly be seen that the parameter b in (A.1) captures the degree of anisotropy. In particular, when increasing b from 0 to ∞, the SF orientation varies from a totally isotropic distribution to a strongly oriented distribution in the direction $\theta = \theta_0$. To further simplify the formulation, the fiber distribution can be represented at a

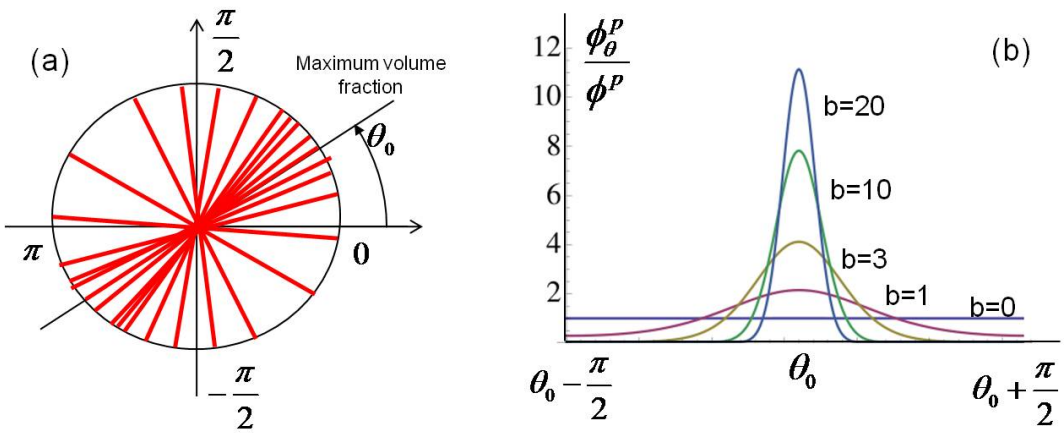

Figure 4.2: Illustration of SF volume fraction at a continuum point and its representation with a Von-Mises distribution function.

continuum point by a structure tensor $\mathbf{\Phi}^p$, a concept that was originally used to represent the evolution of the anisotropic structure of soft biological tissues during large deformations and remodeling [104, 59]. In a nutshell, this tensor is related to the fiber distribution ϕ^p_θ through a directional averaging operation $\langle\langle\bullet\rangle\rangle$ as follows:

$$\mathbf{\Phi}^p = \langle\langle \phi^p_\theta \rangle\rangle \quad \text{where} \quad \langle\langle\bullet\rangle\rangle = \frac{1}{\pi}\int_{-\pi/2}^{\pi/2} \bullet \ \mathbf{M}_\theta \ d\theta \tag{4.11}$$

where the matrix $\mathbf{M}_\theta$ is related to fiber direction vector $\mathbf{a} = [\cos\theta \ \ \sin\theta]^T$ by:

$$\mathbf{M}_\theta = \mathbf{a} \otimes \mathbf{a} = \begin{bmatrix} \cos^2\theta & \cos\theta\sin\theta \\ \cos\theta\sin\theta & \sin^2\theta \end{bmatrix}. \tag{4.12}$$

From this definition, one can show that the structure tensor $\mathbf{\Phi}^p$ is symmetric and is related to the total volume fraction ϕ^p of SF appearing in (4.8) by:

$$\phi^p = \langle \phi^p_\theta \rangle = tr(\mathbf{\Phi}^p) \quad \text{where} \quad \langle\bullet\rangle = \frac{1}{\pi}\int_{-\pi/2}^{\pi/2} \bullet \ d\theta. \tag{4.13}$$

Here, we introduced the averaging operation $\langle\bullet\rangle$ that relates the total volume fraction of SF to the volume fraction in specific directions. It is particularly useful to realize that, for a two-dimensional distribution, the symmetry of $\mathbf{\Phi}^p$ implies that it can be represented in terms of three independent variables $\{\phi^p, \eta, \theta_0\}$, where η refers to the degree of anisotropy and θ_0

shows the principal direction of SF. In this context, the structure tensor may be constructed in the form:

$$\mathbf{\Phi}^p = \phi^p \left[\eta \mathbf{I} + (1 - 2\eta)\mathbf{M}_{\theta_0}\right]. \tag{4.14}$$

where $\mathbf{I}$ is the identity tensor and the matrix $\mathbf{M}_{\theta_0}$ was defined in (4.11). It can be seen that if $\eta = 0$, all fibers are aligned in the same direction (defined by angle θ_0), whereas as $\eta \to 1/2$, the distribution becomes isotropic. Because of their similar physical interpretation, it is possible to find a relationship between parameters b (appearing in the Von-Mises distribution) and η by substituting (A.1) into (4.14). One can show that:

$$\eta = \frac{1}{\pi} \int_{-\pi/2}^{\pi/2} \frac{exp\left[b\ cos\left(2\theta\right)\right] sin^2\theta}{I_0\left(b\right)} d\theta. \tag{4.15}$$

This integral may be computed numerically to determine the b/η curve as shown in Fig. 4.3b. This ensures that there is a one-to-one mapping between the structure tensor shown in (4.14) and the Von-Mises distribution (A.1).

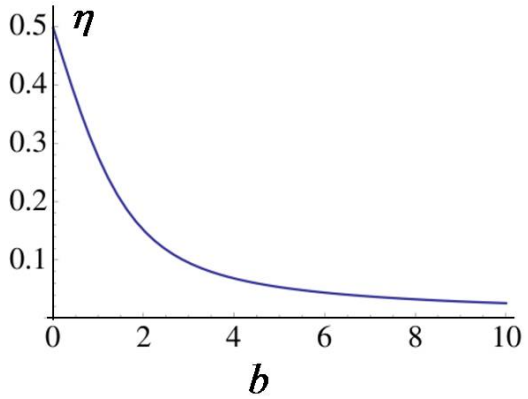

Figure 4.3: Relationship between parameters b and η.

4.4 Mass transport and mass exchange

Cell contractility relies on the mass exchange through the polymerization of G-actin monomers into actin filaments that are a key structural component of SF. These reactions are possible through the transport of G-actin monomers to the site of reaction, a process

that depends on the combination of cytosol flow and G-actin diffusion [49]. The present section discusses the mathematical description of these phenomena.

4.4.1 Mass balance of individual constituents

To accurately describe mass transport and mass transfer, it is essential to ensure that mass is conserved throughout the process of cell contraction. In this context, let us introduce an effective density that represents the mass of the αth constituent per unit volume of mixture as follows:

$$\rho^\alpha = \phi^\alpha \rho_r^\alpha \qquad \alpha = s, f, m \tag{4.16}$$

$$\rho_\theta^\alpha = \phi_\theta^\alpha \rho_r^\alpha \qquad \alpha = p \tag{4.17}$$

where ρ_r^α is the real density of constituent α. A particularity of the present approach is the description of the anisotropic SF distribution through the direction dependent mass density ρ_θ^p. As we will see below, this definition is an important feature of the model as it enables a natural description of the evolution of SF evolution through the mass balance equation. Thus, in the presence of mass exchange between constituents, the conservation of mass for each constituent is written in terms of mass source (or sink) term $\rho_r^\alpha \Gamma^\alpha$ that represents the rate of added mass to the $\alpha - th$ component per current volume. In the particular case of incompressible constituents (i.e., the real densities ρ_r^α are constant in time and space), we can write:

$$\rho_r^\alpha \frac{\partial \phi^\alpha}{\partial t} + \rho_r^\alpha \nabla \cdot (\phi^\alpha \mathbf{v}^\alpha) = \rho_r^\alpha \Gamma^\alpha \qquad \alpha = s, f, m \tag{4.18}$$

$$\rho_r^\alpha \frac{\partial \phi_\theta^\alpha}{\partial t} + \rho_r^\alpha \nabla \cdot (\phi_\theta^\alpha \mathbf{v}^\alpha) = \rho_r^\alpha \Gamma_\theta^\alpha \qquad \alpha = p \tag{4.19}$$

where the second equation represents the evolution of SF density in certain direction (denoted as θ). In particular, the quantity Γ_θ^α denotes the rate of SF polymerization (if positive) or depolymerization (if negative). Writing the above equations with respect to the cytoskeleton

motion, we obtain:

$$\frac{D\phi^\alpha}{Dt} + \phi^\alpha \nabla \cdot \mathbf{v} + \nabla \cdot (\phi^\alpha \tilde{\mathbf{v}}^\alpha) = \Gamma^\alpha \qquad \alpha = s, f, m \tag{4.20}$$

$$\frac{D\phi_\theta^\alpha}{Dt} + \phi_\theta^\alpha \nabla \cdot \mathbf{v} + \nabla \cdot (\phi_\theta^\alpha \tilde{\mathbf{v}}^\alpha) = \Gamma_\theta^\alpha \qquad \alpha = p \tag{4.21}$$

where we used the material time derivative $D/Dt = D^\alpha/Dt$ with respect to the cytoskeleton following (4.3). Following the directional averaging operation defined in the previous section and applying it to each term in (4.21), the balance of mass for SF can be written in the following tensorial form

$$\frac{D\mathbf{\Phi}^p}{Dt} + \mathbf{\Phi}^p \nabla \cdot \mathbf{v} = \mathbf{\Gamma}^p \qquad \text{where} \qquad \mathbf{\Gamma}^p = \langle\langle \Gamma_\theta^p \rangle\rangle \tag{4.22}$$

and we used the fact that $\tilde{\mathbf{v}}^p = 0$. The tensor $\mathbf{\Gamma}^p$ can be interpreted as the anisotropic rate of mass creation of SF per unit volume at time t. Similarly to the structure tensor $\mathbf{\Phi}^p$, the maximum and minimum rates of F-actin formation are the largest and smallest eigenvalues of $\mathbf{\Gamma}^p$, while their directions are given by the eigenvectors of $\mathbf{\Gamma}^p$. To describe the transport of cytosol and G-actin monomers, one can also introduce the flux:

$$\mathbf{J}^\alpha = \phi^\alpha \tilde{\mathbf{v}}^\alpha \qquad \alpha = f, m \tag{4.23}$$

such that the final system of equations describing the mass balance of solid (cytoskeleton), fluid (cytosol), G-actin monomers and SF, respectively reads:

$$\frac{D\phi^s}{Dt} + \phi^s \nabla \cdot \mathbf{v} = 0 \tag{4.24}$$

$$\frac{D\phi^f}{Dt} + \nabla \cdot \mathbf{J}^f + \phi^f \nabla \cdot \mathbf{v} = 0 \tag{4.25}$$

$$\frac{D\phi^m}{Dt} + \nabla \cdot \mathbf{J}^m + \phi^m \nabla \cdot \mathbf{v} = \Gamma^m \tag{4.26}$$

$$\frac{D\mathbf{\Phi}^p}{Dt} + \mathbf{\Phi}^p \nabla \cdot \mathbf{v} = \mathbf{\Gamma}^p. \tag{4.27}$$

It is also important to mention that the total mass balance of SF (averaged over all directions) is found by considering the trace of (4.27), i.e.

$$\frac{D\phi^p}{Dt} + \phi^p \nabla \cdot \mathbf{v} = \Gamma^p. \tag{4.28}$$

4.4.2 Mass balance of the mixture

The mass conservation of the mixture is typically determined by adding the various contributions from each constituent. Summing equations (4.24), (4.25), (4.26) and (4.28), we obtain:

$$\nabla \cdot \mathbf{J}^f + \nabla \cdot \mathbf{J}^m + \nabla \cdot \mathbf{v} = \Gamma^m + \Gamma^p. \tag{4.29}$$

Assuming that no mass is added to the cell during the contraction process, the total mass creation (or loss) for the mixture should vanish. This enables us to write the following relation:

$$\sum_{\alpha} \rho_r^{\alpha} \Gamma^{\alpha} = \rho_r^p \Gamma^p + \rho_r^m \Gamma^m = 0. \tag{4.30}$$

Assuming that the real densities of actin are the same in its monomer and polymer form ($\rho_r^m = \rho_r^p$), the mass equation for the mixture finally becomes:

$$\nabla \cdot \mathbf{J}^f + \nabla \cdot \mathbf{J}^m + \nabla \cdot \mathbf{v} = 0. \tag{4.31}$$

4.4.3 Mass transport through the cytoskeleton

Mass transport within the cytoplasm is an important player in both the passive mechanical response of cells and the dynamics of cell contraction. For instance, mechanical testing procedures, such as micropipette aspiration, clearly exhibit a time-dependency that is usually attributed to a combination of the intrinsic visco-elasticity of the cytoskeleton and the flow driven deformation of the cytoplasm. In terms of cell morphology, it is likely that cytosol flow governs the number and size of cell protrusions. Indeed, Weiss [172], in his analysis on the shape of mesemchymal cells, explained the development of cell extensions (or filopodia) in terms of competitive mechanisms based on the amount of cytosol each protrusion could intake. Complex interactions may exist between the transport and fluid and that of dissolved species, which may result in a quite complex problem. However, it is important to make a few simplifying assumptions for the sake of clarity. The present analysis

is then based on the following points. First, assuming that the concentration of G-actin in the cytosol is small, it is reasonable to say that actin monomers transport does not affect the interstitial flow of cytosol. In other words, cytosol flow can be expressed only in terms of a differential of pressure though Darcy's law as follows:

$$\mathbf{J}^f = -\frac{\mathbf{K}}{\mu} \cdot \nabla p \tag{4.32}$$

where $\mathbf{K}$ is the permeability tensor that depends on the porosity and anisotropy of the cytoskeleton and μ is the dynamic viscosity of the cytosol. Further assuming that the anisotropy of SF does not affect the permeability (this assumption can be relaxed in a future study), an isotropic permeability κ is considered such that $\mathbf{K} = \kappa\mathbf{I}$, where $\mathbf{I}$ is the identity tensor. In addition, the transport of G-actin monomers is assumed to arise from two mechanisms: (a) convection with the cytosol and (b) diffusion through the cytosol with a diffusion coefficient D. One can therefore write:

$$\mathbf{J}^m = -\frac{\phi^m}{\phi^f}\frac{\kappa}{\mu}\nabla p - \phi^f D \nabla\left(\frac{\phi^m}{\phi^f}\right). \tag{4.33}$$

This above relationship implicitly assumes that there are no interactions between G-actin monomers and the cytoskeleton, an assumption that is reasonable with the small relative size of G-actin monomers compared to cytoskeleton mesh-size. Equation (4.33) shows that the diffusion constant D has a role in controlling the rate of cell contractility by providing more or less resistance to the flux of monomers towards the site of SF polymerization.

4.4.4 Mass exchange and SF formation

Actin polymerization and SF formation are anisotropic processes that strongly depend on the level of contractile stress in existing SF. The rate of SF polymerization Γ_θ is therefore derived based on the following assumptions: (a) the chemical reaction between G-actin and F-actin is described by a first-order kinetic equation and (b) *the rate of SF formation is affected by the magnitude of contractile stress T_θ^p in direction θ.* The latter statement is

the main assumption of this chapter and will be shown to be responsible for the mechano-sensitivity of cell contraction. The rate equation describing the chemical equilibrium of SF is then written in terms of rates of formation k^f and dissociation k^d of F-actin as:

$$\Gamma_\theta^p = \frac{M^a}{\rho^a}\left(k^f c^m - k^d c_\theta^p\right) \quad \text{where} \quad k^f = k^f\left(T_\theta^p\right) \tag{4.34}$$

where M^a and ρ^a are the molar mass and real density of actin, assumed to be the same in its polymer (p) and monomer (m) configuration. Furthermore, the concentrations c_θ^p and c^m are related to the respective volume fractions of SF and G-actin monomers by:

$$c_\theta^p = \frac{\rho^a}{M^a}\phi_\theta^p \qquad \text{and} \qquad c^m = \frac{\rho^a}{M^a}\frac{\phi^m}{\phi^f + \phi^m} \approx \frac{\rho^a}{M^a}\frac{\phi^m}{\phi^f}. \tag{4.35}$$

Note that the concentration of F-actin is taken as the number of moles per unit volume of mixture while the concentration of G-actin is the number of moles of G-actin per unit volume of cytosol-G actin mixture. To characterize the rise in SF polymerization with contractile stress T_θ^p, we introduce a linear approximation of the function $k^f\left(T_\theta^p\right)$ appearing in (4.34) as:

$$k^f\left(T_\theta^p\right) = k_0^f + k_1^f T_\theta^p \tag{4.36}$$

where the constant k_0^f denotes the rate of F-actin formation in absence of contractile stress and $k_1^f > 0$ measures the increase in polymerization rate with contraction T_θ^p. Combining the definition of the SF production tensor (4.22) with equations (4.34) and (4.36), and using (4.35), it is possible to derive the following expression for $\mathbf{\Gamma}^p$:

$$\mathbf{\Gamma}^p = \langle\langle \Gamma_\theta^p \rangle\rangle = \left(\frac{1}{2}k_0^f \mathbf{I} - k_1^f \mathbf{T}^p\right)\frac{\phi^m}{\phi^f} - k_0^d \mathbf{\Phi}^p \tag{4.37}$$

where the contractile stress $\mathbf{T}^p$ from SF is defined as the directional average of the contractions stress T_θ^p from individual SF as:

$$\mathbf{T}^p = \langle\langle T_\theta^p \rangle\rangle. \tag{4.38}$$

Equation (4.37) is a critical component of the proposed model as it describes the evolution of SF concentration and distribution in the cell in terms of the level of contractile stress.

Indeed, combining (4.37) and (4.27), the following evolution equation is obtained for $\mathbf{\Phi}^p$

$$\frac{D\mathbf{\Phi}^p}{Dt} = \underbrace{\left(\frac{1}{2}k_0^f\mathbf{I} + k_1^f\mathbf{T}^p\right)\frac{\phi^m}{\phi^f}}_{force\ dependent\ formation} - \underbrace{k_0^d\mathbf{\Phi}^p}_{dissociation} - \underbrace{\mathbf{\Phi}^p\nabla\cdot\mathbf{v}}_{volume\ change} . \tag{4.39}$$

This expression clearly shows that SF formation in various directions depends on the availability of actin monomers (through ϕ^m), the concentration of existing SF (through $\mathbf{\Phi}^p$) and the level of contractile force (through $\mathbf{T}^p$). Finally, the last terms in (4.39) characterizes the change in fiber concentration with volumetric deformation of the cell (through the term $\nabla\cdot\mathbf{v}$).

4.5 Force generation and mechanical equilibrium

The generation of active forces by SF plays a significant role in the process of mechanosensing and cell deformation. Indeed, mechanical force and resulting deformation play two major roles in cell contraction. First, as seen in (4.39), mechanical stress induces SF formation, which directly affects the magnitude of contraction. Second, because SF possess a sarcomeric structure similar to that found in myofibrils of muscle cells, contractile forces are very likely to be highly dependent on the strain-rate and current length of SF, as predicted by cross-bridge dynamics models [22]. To incorporate these mechanisms into the proposed model, this section concentrates on key mechanical aspects of the problem by (a) writing the force equilibrium between the four constituents present in the cell and (b) introducing constitutive relations for SF contraction and cytoskeleton deformation.

4.5.1 Mechanical equilibrium of the cell

Let us first consider the mechanical equilibrium of the cell by writing the balance of momentum associated with each constituent. Introducing $\mathbf{T}^\alpha$ as the partial Cauchy stress associated with constituent α, the momentum balance for each constituent can be written [29] :

$$\rho^\alpha\frac{D^\alpha\mathbf{v}^\alpha}{Dt} = \nabla\cdot\mathbf{T}^\alpha + \rho^\alpha\mathbf{b} + \mathbf{f}^\alpha \tag{4.40}$$

where $\mathbf{b}$ is the external force per unit mass of constituent α and $\mathbf{f}^\alpha$ represents forces (per unit volume) acting on constituent α due to its interactions with other constituents. Assuming that at the mixture level, the net force resulting from interactions between constituent must vanish, the following equality must hold:

$$\sum_{\alpha=1}^{4} \mathbf{f}^\alpha = \mathbf{0}. \tag{4.41}$$

Furthermore, due to the slow time scales associated with cell motion, inertial forces on each constituent may be neglected; this implies that the left hand term in (4.40) can be neglected. The equilibrium of the mutiphasic mixture can then be obtained by adding the contributions (4.40) from each constituent; this yields the following form:

$$\nabla \cdot \mathbf{T} + \rho \mathbf{b} = 0 \tag{4.42}$$

where the total Cauchy stress $\mathbf{T}$ contains a contribution from each constituent (Fig. 4.4):

$$\mathbf{T} = \sum_{\alpha=1}^{4} \mathbf{T}^\alpha = \mathbf{T}^s + \mathbf{T}^f + \mathbf{T}^m + \mathbf{T}^p. \tag{4.43}$$

Here, $\mathbf{T}^s$ may be interpreted as the passive stress arising from cyoskeleton deformation, $\mathbf{T}^p$ is the contractile stress exerted by SF and $\mathbf{T}^f$ results from the pressurization of the cytosol such that

$$\mathbf{T}^f = -\phi^f p \mathbf{I} \tag{4.44}$$

where p is the cytosol pressure. In this study, the partial pressure $\mathbf{T}^m$ due to the presence of G-actin monomers is neglected because of the low concentration of G-actin monomomers in the cytosol. It is also important to mention that since each constituent verifies the balance of angular momentum, partial stresses $\mathbf{T}^\alpha$ (and therefore $\mathbf{T}$) are symmetric tensors.

4.5.2 Active contraction of SF

Let us discuss the contractile stress $\mathbf{T}^p$ originating from the tension developed in SF through acto-myosin interactions. Noting that there are strong similarities between the sarcomeric

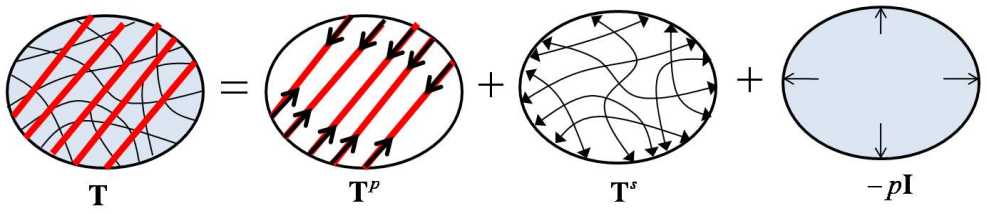

Figure 4.4: Decomposition of the Cauchy stress.

structure of SF and that of myofibriles (in myocytes), one may borrow the extensive body of knowledge on the mechanics of cross-bridge models describing acto-myosing contraction in muscle cells. Considering a one-dimensional SF undergoing contraction, the developed force T is known to be dependent of two quantities: the change of fiber length (the relationship is known as the length-tension relationship [22]) and the rate of change of fiber length (known as the velocity-tension relation [81]). In this work, we introduce a model describing the uniaxial contractile stress T^p in fibers in terms of their normal strain ϵ (measuring the change in fiber length) and strain-rate $\dot{\epsilon}$ (measuring the rate of fiber shortening during contraction). In general, the tension T^p can be written in the form:

$$\frac{T^p}{\bar{T}} = T^\star\left(\epsilon, \dot{\epsilon}\right) \tag{4.45}$$

where $\bar{T}$ is the isometric contraction associated with a single SF in its original length ($\epsilon = 0$) and a vanishing strain rate ($\dot{\epsilon} = 0$). In other words, the function $T^\star$ verifies the equality $T^\star\left(0, 0\right) = 1$. The derivation of function $T^\star$ is now presented based on conventional knowledge of sarcomere contraction.

Length-tension relation. The length-tension relation describes a drop in active acto-myosin contraction T as the length of sarcomere deviates from its original value. Consistent with prediction from the sliding filament theory, sarcomeres exert the highest contractile stress T when $\epsilon = 0$ (or $\ell = \ell_0$) and this force decreases in a nonlinear fashion as the strain deviates from 0, either in a positive or negative manner.

Remark: Note that because SF form at different times, they are usually characterized by

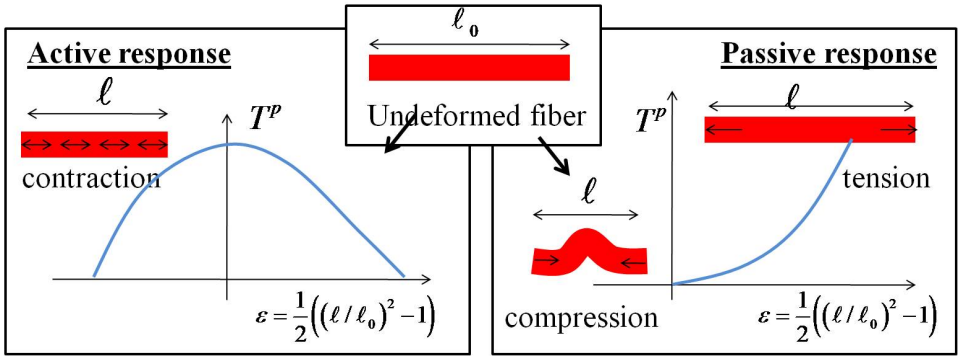

Figure 4.5: *Active and passive response of a SF . The uniaxial contractile stress is T^p and the normal strain ϵ is a function of the ratio of the final fiber length ℓ and initial fiber length ℓ_0.*

different natural configurations (or stress-free state) [109]. Since the change of length of a single SF is measured with respect to its natural configuration, the tension $T^\star$ cannot generally be measured in terms of ϵ. In the present approach, it is assumed that SF formation occurs in a way such that their natural configuration is the same at that of the cytoskeleton and thus the strain ϵ is a good measure of change in length. While this assumption has been applied as a mean to simplify the proposed model, it can be relaxed in future studies by computing the stress from new SF in terms of a time integral as suggested by Humphrey and Rajagopal in [86]

Furthermore, when stretched, SF develop a passive stress that acts in a similar way cables resist tension. However, because resistance in compression is negligible as fibers become slack, the passive behavior of SF is described as follows: (a) for negative strains, passive stress is zero and (b) for tensile strain, SF exhibit a strain hardening response. The active and passive response of SF is summarized in Fig. 4.5. Considering the case of isometric tension ($\dot{\epsilon} = 0$), the change of tensile stress in a SF is written:

$$T^\star(\epsilon, 0) = f(\epsilon) \quad \text{where} \quad f(\epsilon) = \begin{cases} e^{-\left(\frac{\epsilon}{\epsilon_0}\right)^2} & \text{if} \quad \epsilon < 0 \\ e^{-\left(\frac{\epsilon}{\epsilon_0}\right)^2} + \left(\frac{\epsilon}{\epsilon_1}\right)^2 & \text{if} \quad \epsilon \geq 0 \end{cases} \tag{4.46}$$

where the constant ϵ_0 describes how quickly contraction decreases as strain deviates from

zero and ϵ_1 characterizes the passive strain hardening of SF. Note that the above function is such that $f(0) = 1$, in order to satisfy the fact that $T^\star(0,0) = 1$. Fig. 4.6a shows the relationship between $T^\star$ and scaled strain ϵ/ϵ_0 considered in the proposed model (in the case of isometric tension).

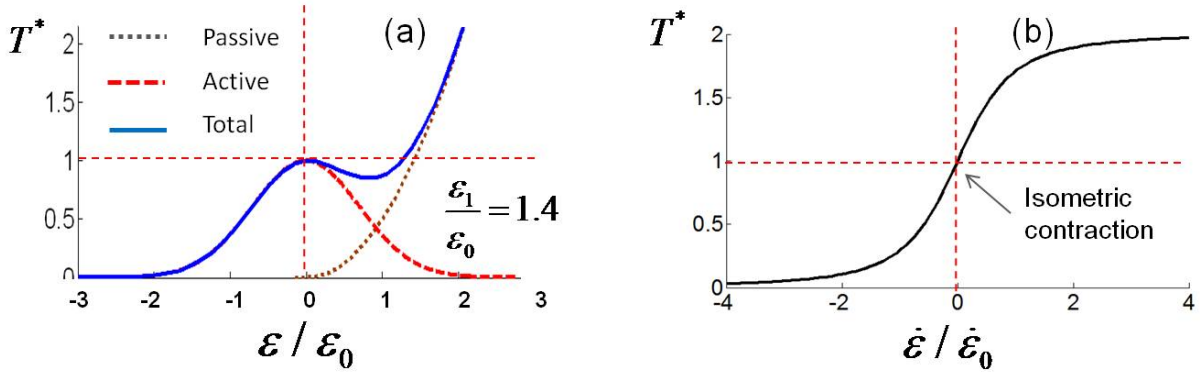

Figure 4.6: *(a) Strain-tension relationship $f(\epsilon)$ and (b) strain-rate tension relationship $g(\dot{\epsilon})$ are used in the study to capture the length and velocity-tension relation, respectively, observed in muscle cells.*

Velocity-tension relation. The rate at which a fiber shortens is also known to affect the magnitude of the contractile force. Typically, contraction declines in a hyperbolic fashion as the rate of shortening increases ($\dot{\epsilon} < 0$) and ultimately vanishes for very high rates of shortening [81]. However, as a sarcomere lengthens ($\dot{\epsilon} > 0$), it is found that contraction increases and reaches a value well above the isometric tension for high values of positive strain rate. To characterize this behavior, we introduce a function g that describes the change in contraction T with strain rate in the particular case of a vanishing strain ϵ (i.e., the fiber length is the initial length ℓ_0)

$$T^\star(0,\dot{\epsilon}) = g(\dot{\epsilon}) = 1 + \frac{\dot{\epsilon}/\dot{\epsilon}_0}{\sqrt{(\dot{\epsilon}/\dot{\epsilon}_0)^2 + 1}}. \tag{4.47}$$

As seen in Fig. 4.6b, function g is antisymmetric and verifies the following criteria: (a) $g \to 0$ as $\epsilon \to -\infty$, (b) $g \to 2$ as $\epsilon \to +\infty$ and (c) $g(0) = 1$. In other words, the maximum contractile stress that can be developed by the fiber is twice the isometric tension

$\bar{T}$. Literature on muscle mechanics [22] has shown that in reality, the force-velocity curve is not exactly antisymmetric but this aspect does not affect the main concepts presented in this chapter.

Uni-directional model of fiber contraction. While the above models are proposed at constant strain rate or constant strain, respectively, in general, fiber contraction is affected by both fiber strain and its rate simultaneously. Assuming that the effects of strain and strain rate on fiber tension are completely independent, it is possible to derive a general model that defines $T^\star$ as the product of functions f and g defined in (4.46) and (4.47). This yields:

$$T^\star(\epsilon,\dot{\epsilon}) = f(\epsilon)g(\dot{\epsilon}) = \begin{cases} \left(1+\frac{\dot{\epsilon}/\dot{\epsilon}_0}{\sqrt{(\dot{\epsilon}/\dot{\epsilon}_0)^2+1}}\right) e^{-\left(\frac{\epsilon}{\epsilon_0}\right)^2} & \text{if} \quad \epsilon < 0 \\ \left(1+\frac{\dot{\epsilon}/\dot{\epsilon}_0}{\sqrt{(\dot{\epsilon}/\dot{\epsilon}_0)^2+1}}\right)\left(e^{-\left(\frac{\epsilon}{\epsilon_0}\right)^2}+\left(\frac{\epsilon}{\epsilon_1}\right)^2\right) & \text{if} \quad \epsilon \geq 0 \end{cases}. \tag{4.48}$$

We give a three-dimensional representation of contraction in terms of ϵ and $\dot{\epsilon}$ in Fig. 4.7.

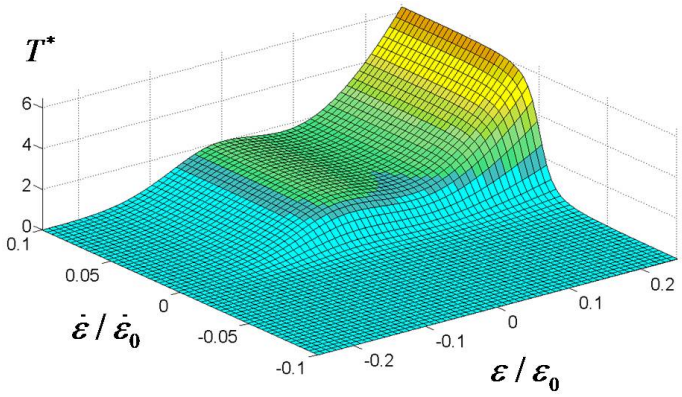

Figure 4.7: Three-dimensional representation of the cell contraction $T^\star$ as a function of SF strain ϵ/ϵ_0 and strain rate $\dot{\epsilon}/\dot{\epsilon}_0$.

Contraction of the SF network. The above model is able to characterizes the contraction of a single SF but does not describe the contraction of an anisotropic network. This issue can be addressed by relating the contraction of a single SF to the contractile stress tensor $\mathbf{T}^p$, as follows. First, we write that the uniaxial contractile stress T^p_θ in a specific direction

θ in terms of the volume fraction of SF and the stress $T = \bar{T}T^{\star}$ in each individual fiber as:

$$T_{\theta}^{p} = \phi_{\theta}\bar{T}T^{\star}. \tag{4.49}$$

Second, the stress tensor $\mathbf{T}^{p}$ is derived from the averaging equation defined in (4.38): $\mathbf{T}^{p} = \langle\langle T_{\theta}^{p}\rangle\rangle$. Referring to the definition of the averaging operation (4.12), the stress $\mathbf{T}^{p}$ can then be found in terms of the Green-Lagrange strain tensor $\mathbf{E}$ and its material time derivative $\dot{\mathbf{E}}$ by computing the integral:

$$\begin{aligned} \mathbf{T}^{p}\left(\mathbf{E},\dot{\mathbf{E}}\right) &= \frac{\bar{T}}{\pi}\int_{-\pi/2}^{\pi/2}\phi_{\theta}^{p}\,T^{\star}\left(\epsilon_{\theta},\dot{\epsilon}_{\theta}\right)\mathbf{M}_{\theta}\,d\theta \\ \text{where} \qquad & \epsilon_{\theta} = \mathbf{E}:\mathbf{M}_{\theta} \;\text{ and }\; \dot{\epsilon}_{\theta} = \dot{\mathbf{E}}:\mathbf{M}_{\theta}. \end{aligned} \tag{4.50}$$

Here, we used the fact that the tensile strain (and its rate) in a certain direction can be found through a double tensor contraction " : " with the matrix $\mathbf{M}_{\theta}$. The above integral can be determined computationally using the Von-Mises distribution and the state of strain and strain rate at a material point. Relation (4.50) therefore clearly establishes a link between contractile stress, fiber distribution and the underlying molecular mechanisms of the cross-bridge dynamics.

4.5.3 Cytoskeleton elasticity

According to the velocity-tension relation, it is clear that contractility is promoted by a scenario in which the rate of SF shortening is limited. There are two elements that contribute to the resistance of contractile deformation: the passive cytoskeleton and the underlying substrate (through cell-matrix attachments provided by focal adhesions). The passive cytoskeleton consists of a filamentous network that can resist actin contraction through the mechanical balance between compressive elements (microtubules), tensile elements (actin and intermediate filaments) and cytosol pressure. These contributions should be accounted for in the description of the cytoskeleton stress $\mathbf{T}^{s}$ through the constitutive relation. According to the effective stress principle [29], this stress is decomposed into pressure and an

effective stress $\mathbf{T}_e^s$ carried by the dry cytoskeleton as follows:

$$\mathbf{T}^s = -\phi^s p\mathbf{I} + \mathbf{T}_e^s\left(\mathbf{E}\right). \tag{4.51}$$

Assuming an isotropic passive cytoskeleton, the effective stress can be related to deformation $\mathbf{E}$ through an isotropic, linear elastic relation. More complex behavior of the cytoskeleton (including its known nonlinear visco-elastic response) may be added to the present model in future studies. Concentrating on a simple hypo-elastic constitutive behavior, an objective rate of the effective stress $\mathbf{T}_e^{\sigma J}$ is written

$$\mathbf{T}_e^{\sigma J} = \mathbf{C}^{^{\sigma J}} : \mathbf{D} \tag{4.52}$$

where the rate of deformation is given by $\mathbf{D} = \mathbf{F}^{-T} \cdot \dot{\mathbf{E}} \cdot \mathbf{F}^{-1}$, $\mathbf{F}$ is the deformation gradient and a superposed dot refers to the material time derivative with respect to cytoskeleton motion. For isotropic flimentous network, the fourth-order elastic matrix $\mathbf{C}^{\sigma J}$ is written in terms of the Lame constants λ and μ as:

$$C_{ijkl}^{\sigma J} = 2\left(\mu - \lambda\ lnJ\right)\delta_{ik}\delta_{jl} + \lambda\ \delta_{ij}\delta_{kl}. \tag{4.53}$$

where δ is the Kronecker delta. The above matrix can be rewritten in terms of the Young's modulus $E = \mu(3\lambda + 2\mu)/(\lambda + \mu)$ that can generally be measured from mechanical testing of cell deformation. It is also important to mention that while the material response of the cytoskeleton is based on linear assumptions, the relation between force and displacement is nonlinear due to geometrical effects associated with finite deformation.

4.6 Model prediction

In this section, we propose to use the multi-physics model to investigate the behavior of cells and their interaction with an external mechanical environment (or support). We are particularly interested in understanding how cell contraction and force generation is affected by the stiffness of the support as predicted by experiments. For this, we consider

two situations: (a) the case of homogeneous contraction of a square cell and (b) the case of a square cell supported by elastic springs at its four corners.

4.6.1 Non-dimensionalization and solution strategy

Before assessing the physical behavior of the system, we recognize that the above model possesses a certain number of parameters, whose respective role in the cell's behavior may be challenging to assess. To simplify the approach, one can scale these parameters with respect to characteristic time, dimension and force that are inherent to cellular systems. Let $t_0 = 1/\dot{\epsilon}_0$, ℓ_0 and $T_0 = \bar{T}$ be the scales of time, length and force, respectively. The non-dimensional variables (denoted with the superscript "$\star$") are then defined as:

$$t^\star = \frac{t}{t_0} = \dot{\epsilon}_0 t \qquad \mathbf{x}^\star = \frac{\mathbf{x}}{\ell_0} \qquad \mathbf{T}^{\alpha\star} = \frac{\mathbf{T}^\alpha}{T_0} = \frac{\mathbf{T}^\alpha}{\bar{T}} \tag{4.54}$$

$$\mathbf{v}^\star = \frac{\mathbf{v}}{\dot{\epsilon}_0 \ell_0} \qquad \dot{\mathbf{E}}^\star = \frac{\dot{\mathbf{E}}}{\dot{\epsilon}_0} \qquad p^\star = \frac{p}{\bar{T}} \qquad \mathbf{J}^{\alpha\star} = \frac{\mathbf{J}^\alpha}{\dot{\epsilon}_0 \ell_0}. \tag{4.55}$$

In addition, the non-dimensional material parameters (diffusion coefficient, permeability, cytosol viscosity, stiffness and rate constants) are given by:

$$D^\star = \frac{D}{\dot{\epsilon}_0 \ell_0^2} \qquad \kappa^\star = \frac{\kappa}{\ell_0^2} \qquad \mu^\star = \frac{\dot{\epsilon}_0}{\bar{T}}\mu \qquad \mathbf{C}^\star = \frac{\mathbf{C}}{\bar{T}} \tag{4.56}$$

$$k^{d\star} = \frac{k^d}{\dot{\epsilon}_0} \qquad k_0^{f\star} = \frac{k_0^f}{\dot{\epsilon}_0} \qquad k_1^{d\star} = \frac{\bar{T}}{\dot{\epsilon}_0} k_1^d. \tag{4.57}$$

The physical state of a material point in the cell is determined by the four following fields: the non-dimensional velocity $\mathbf{v}^\star$, cytosol pressure $p^\star$, fraction of G-actin monomers $\phi^{m\star}$ and SF structure tensor $\mathbf{\Phi}^{p\star}$. These fields are solutions of the system of coupled non-dimensional partial differential equations derived in this chapter that consists of (a) momentum balance

(4.40), (b) mixture mass balance (4.31), (c) cytosol mass balance (4.25) and (d) mass balance of SF (4.27) as follows:

$$\nabla^\star \cdot (\mathbf{T}^{s\star} + \mathbf{T}^{p\star} - p^\star \mathbf{I}) = \mathbf{0} \quad (4.58)$$

$$\frac{D\phi^{f\star}}{Dt^\star} - \frac{\kappa^\star}{\mu^\star}\nabla^{\star 2} p^\star + \phi^{f\star}\nabla^\star \cdot \mathbf{v}^\star = 0 \quad (4.59)$$

$$-\frac{\kappa^\star}{\mu^\star}\left[(1+c^m)\nabla^{\star 2} p^\star + \nabla^\star c^m \cdot \nabla^\star p^\star\right] - D^\star \nabla^\star \cdot \left(\phi^{f\star}\nabla c^m\right) + \nabla^\star \cdot \mathbf{v}^\star = 0 \quad (4.60)$$

$$\frac{D\mathbf{\Phi}^{p\star}}{Dt^\star} - \left(\frac{1}{2}k_0^{f\star}\mathbf{I} + k_1^{f\star}\mathbf{T}^{p\star}\right)\frac{\phi^m}{\phi^f} + \left(k_0^{d\star} + \nabla^\star \cdot \mathbf{v}^\star\right)\mathbf{\Phi}^{p\star} = \mathbf{0} \quad (4.61)$$

where the constitutive relation for cytosol and monomer transport were used and $\phi^m = \frac{M^a}{\rho^a}\phi^f c^m$. Boundary conditions must be applied in order to describe the applied traction $\mathbf{t}^e$ on the cell boundary (written in terms of the total stress $\mathbf{T}$) and ensure that there is no flux of cytosol and actin monomers across the cell membrane Γ:

$$\mathbf{T}\cdot\mathbf{n} = \mathbf{t}^e, \qquad \mathbf{J}^f \cdot \mathbf{n} = 0, \qquad \mathbf{J}^m \cdot \mathbf{n} = 0 \quad (4.62)$$

where $\mathbf{n}$ denotes the outward unit vector to Γ. These equations can be solved using a nonlinear implicit finite element formulation, the details of which will be introduced in a companion chapter [54]. Finally, simulation results shown in the next section were obtained using the parameters shown in Table 4.1. Regarding model constants, the isometric contractile force and cross-sectional area of SF are estimated to be around $600pN$ [156] and $0.03\mu m^2$ [175, 94], respectively. The isometric stress($\bar{T}$) can therefore be calculated to be on the order $20000Pa$ (which is the value chosen in our simulations).

4.6.2 Homogeneous cell contraction

In vivo, most contractile cells adopt a polarized elongated morphology, characterized with strongly oriented SF (aligned along the principal direction of the cell) that drive the direction of contraction. The first example concentrates on such an elongated cell that deforms uniaxially and homogeneously in a constrained environment for which the details

Definition	Symbol	Value	unit	Reference
Cytosol volume fraction	ϕ^c	70	%	[2]
Cytoskeleton volume fraction	ϕ^s	25	%	n/a
F+G actin volume fraction	$\phi^m + \phi^p$	5	%	n/a
Rate of SF formation	k_0^f	0.0001	sec^{-1}	[130]
Mechano-sensitive rate of SF formation	k_1^f	0.05	sec^{-1}	[130]
Rate of SF dissociation	k_0^d	0.1	sec^{-1}	[130]
Cytoskeleton permeability	κ/μ	$1 \cdot 10^{-15}$	$m^4/N \cdot sec$	[69]
G-actin diffusion constant	D	$1 \cdot 10^{-5}$	m^2/sec	[130]
Young's modulus	E	70	Pa	[37]
Poisson's ratio	ν	0.3		[37]
fiber maximum tensile stress	$\bar{T}$	20000	Pa	[175, 94, 156]
model constant	$\dot{\varepsilon}_0$	0.01	sec^{-1}	[37]
model constant	ε	0.1		[22]
F/G molar mass ratio	M^p/M^m	100		n/a
F/G true density ratio	ρ_R^p/ρ_R^m	1		n/a

Table 4.1: Parameters used in the simulations.

of the geometry and constraints are shown in Fig. 4.8. In this problem, cell-substrate adhesion are modeled as rigid connections between the cell and a set of linear elastic springs that characterize the stiffness of the underlying substrate. Because of its one-dimensional feature, this problem is used as a benchmark to assess how the proposed formulation captures cell contraction and quantify the influence of various model parameters.

The first analysis aims at evaluating the effect of the stiffness of the cell support (represented by the nondimensional parameter $K^\star = K/\left(\bar{T}\ell_0\right)$) on cell contraction. Fig. 4.9 shows the time evolution of cell deformation, contractile stress and fiber anisotropy for various values of $K^\star$ ranging from 0 to very large values. Generally, these results show that from its original state (no contraction and no SF), a cell tends to develop a SF network and generate increasing contractile force in time, until it reaches a steady state. Furthermore, one can see that there is a clear relationship between cell contractility (represented by stress component T_{11}^p), SF anisotropy ($\mathbf{\Phi}_{11}^p$) and substrate stiffness $K^\star$. For large spring stiffness, the cell can only undergo very small strains (and strain rates), which results in a quasi-constant

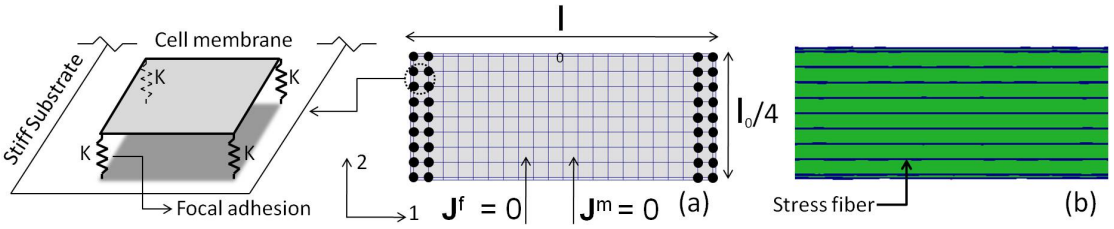

Figure 4.8: *(a) The geometry of the cell and boundary conditions. The cell of length* $\ell_0 = 40\mu m$ *is free to contract in the vertical direction but is constrained in the horizontal direction by linear springs of stiffness* K*. b) Generated SF at steady state.*

SF contraction as described by the length-tension and velocity-tension relationships. This large contraction, in turn, triggers the formation of additional fibers that contribute to a rise in contraction. Steady state is finally reached when the majority of G-actin monomers are consumed by the G-actin/SF reaction. On the contrary, a soft mechanical environment ($K^\star \to 0$) results in large contractile strains and a decrease in both fiber formation and contractile stress. Moreover, the distribution of SF (represented by $\mathbf{\Phi}^p_{11}$) varies from a totally isotropic network ($\mathbf{\Phi}^p_{11}/\phi^p = 0.5$) to an extremely horizontally oriented network ($\mathbf{\Phi}^p_{11}/\phi^p \to 1$) as spring stiffness increases. This clearly shows how SF align in the directions of maximum stiffness.

The next analysis concentrates on assessing the role of mechano-sensitivity of SF formation (represented by the rate constant k_1^f introduced in (4.36)) on cell contractility for a constant spring stiffness $K^\star = 0.01$. Since increasing k_1^f promotes SF formation in direction of maximum contraction, it is associated with a rise in fiber formation, contractile stress and deformation along the horizontal direction. We also note that when $k_1^{f\star}$ vanishes, SF formation is insensitive to contraction, which results in a totally isotropic fiber distribution ($\mathbf{\Phi}^p_{11}/\phi^p = 0.5$) and a very low contraction (which arise from the rate of fiber formation k_0^f). This clearly shows that k_1^f is a critical parameter in capturing the mechano-sensitivity of cell contraction.

To better understand the main trends exhibited by the model, the last analysis focuses on

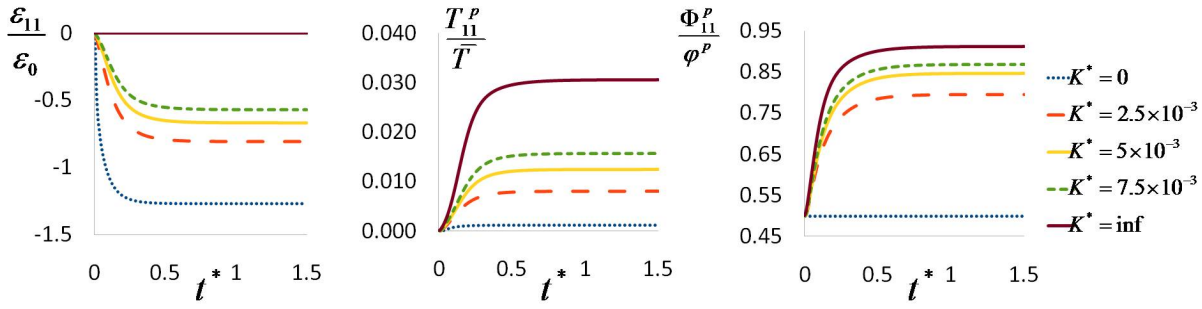

Figure 4.9: *Time evolution of cell deformation, contractile stress and SF anisotropy for different values of support stiffness $K^\star$.*

assessing the steady-state value of strain, contractile stress and fiber distribution variation with spring stiffness and rate constant $k_1^{f\star}$. The results displayed in Fig. 4.11 can be summarized as follows:

- Cell contraction increases with substrate stiffness in a nonlinear fashion until it reaches a maximum value. This value is determined by the initial quantity of actin monomers that can polymerize into SF.
- The intensity of cell contraction and deformation is determined by the mechano-dependent rate of fiber formation $k_1^{f\star}$ and the isometric stress $\bar{T}$ in each SF.
- SF distribution becomes increasingly anisotropic with a rise in spring stiffness and mechano-dependent rate of fiber formation $k_1^{f\star}$. This is explained by the fact that new fibers are formed in the directions of maximum contractile stress, which in turn increases the contraction in this particular direction. This feed-back mechanism is key to understand cell contraction.

4.6.3 Contraction of a square cell attached at its corners

The next example concerns the contraction of a square fibroblast that is constrained at its corners by elastic supports (Fig. 4.12) characterized by a non-dimensional stiffness

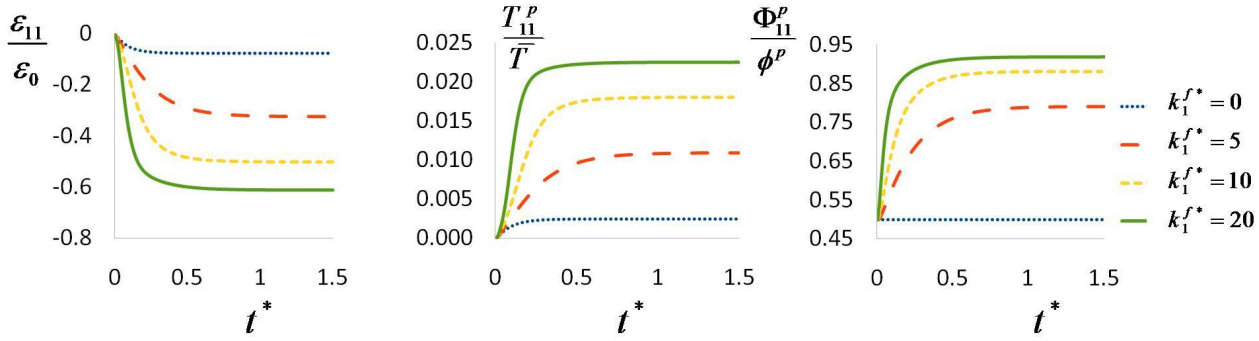

Figure 4.10: *Time evolution of cell deformation, contractile stress and SF anisotropy for different values of mechano-sensitivity coefficient* k_1^f.

$K^\star = K/\left(\bar{T}\ell_0\right)$. This situation has been previously studied both experimentally by Tan and coworkers [150] as well as Bischofs et al. [16] and theoretically by Deshpande et. al. [37, 38]. This example is particularly interesting since it involves heterogeneous cell deformation and the development of a spatially varying SF network. Further, due to the simple geometry and experimental reproducibility, this problem can be used as a benchmark to assess model prediction in terms of contraction, SF distribution and characteristic time-scales. The solution is obtained using a mixed-finite element procedure [1] for which nine node elements are used to describe solid velocity fields while four nodes are used to represent pressure and actin monomer concentration. Large deformations are handled with an updated Lagrangian formulation, that consists of updating the reference configuration of the cell at each time step, therefore facilitating the treatment of the mapping between different material configurations [8]. Finally, time integration is performed with an implicit Backward Euler integration scheme, coupled with a Newton procedure to obtain a solution at each time step. The presented results are obtained after discretizing the cell domain into nine-node elements as shown in Fig. 4.12. Element size was chosen to give satisfactory convergence while minimizing the computational cost. More details on this procedure are given in a companion paper [54].

Starting from out-of-equilibrium initial conditions ($\phi^p = 0$ at $t = 0$), the solution shows that

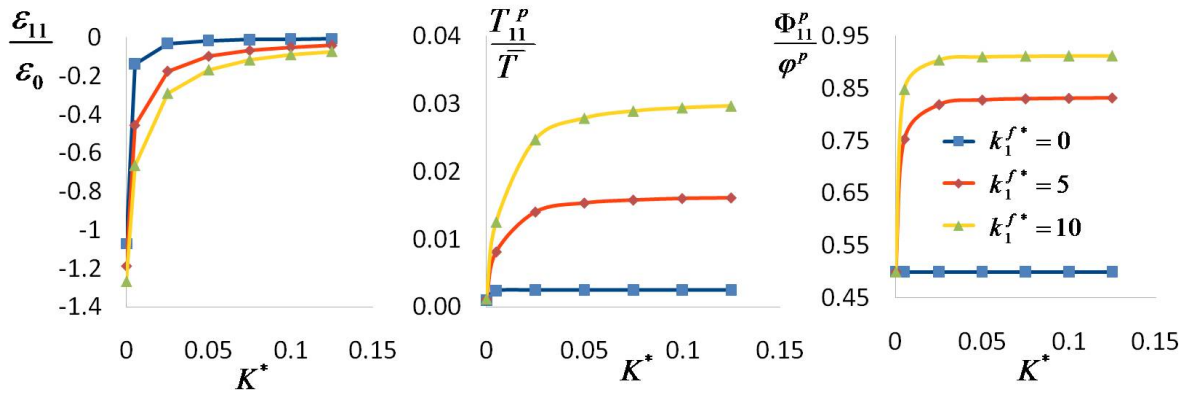

Figure 4.11: *Effect of support stiffness on steady state cell deformation, contractile stress and SF anisotropy for different values of mechano-sensitivity coefficient* $k_1^{f\star}$.

cell contraction originally occurs at fast rates that tends to decay in time in order to reach a steady-state solution for which contraction is maximum. This choice initial condition (out-of equilibrium) is critical to observe cell contraction as it triggered the original SF formation, responsible for the beginning of the positive feedback loop described above. Indeed, no contraction is observed if the initial conditions satisfy both mechanical and chemical equilibrium. However, real cells are known to constantly be out-of-equilibrium, and a change in chemical equilibrium may be enough to start the positive feedback loop observed in the model. Our results suggests that support stiffness has a significant effect on SF formation and distribution. To illustrate this, Fig. 4.12 shows the steady-state cell deformation and the associated SF network for three characteristic support stiffness: $K^\star = 5 \cdot 10^{-6}$, $K^\star = 5 \cdot 10^{-4}$, and $K^\star = 0.15$. These results indicate that as $K^\star$ increases, the following observations can be made:

- SF concentration increases and their orientation is more and more pronounced along directions of maximum stiffness. Indeed, as substrate stiffness increases, boundary conditions on the cell range from an isotonic situation (the cell can deform under the load) to an isometric situation (the cell deformation is prescribed by its support). The velocity-tension relation indicates that the isometric situation results in the

development of strong contractile stresses, which then promote the polymerization of SF (through the mechano-sensitive rate of formation). On the contrary, isotonic situation (especially at small stiffness) decreases contraction and consequently, SF formation.

- Cell morphology tends to become more "stellate" with increasing membrane curvature between attachments. In this context, we note that experimental observation of cell morphology exhibits a uniform curvature [16], a feature that is not predicted by the results shown in Fig. 4.12. This discrepancy can be attributed to the fact that surface elasticity of the cortical membrane has been neglected in the present model. However, we show in another study [166] that including the effects of membrane elasticity result in uniform surface strains and curvature, consistent with experimental observations.

- Contractile forces applied to the external supports rise in a nonlinear fashion (Fig. 4.13) until they reach a maximum value (that can be shown to be determined by the initial amount of G-actin in the cell and the dissociation rate constant k_d). This result may be compared with experimental observations by Ghibaudo et al. [62] of the dependency of cell contractility on support stiffness using micro-patterned substrates (micro-pillars). While quantitative comparison cannot be established here due to differences in cell size and morphology, the results show that the model captures both the order of magnitude of contractile forces as well as the trends in substrate stiffness-cell contraction relationships.

An important consequence of the observed behavior is that the mechanical work performed by the cell is optimized for a specific range of substrate stiffness. To illustrate this, we computed the average work W done by the cell as:

$$W = 4F\delta \tag{4.63}$$

where F and δ are the average force and displacement of focal adhesion, respectively. The number 4 arises due to the fact that the square cell has four focal adhesions. Numerically computing W in terms of spring stiffness clearly shows that an optimum stiffness for our system is located around $1nN/\mu m \leq K \leq 10nN/\mu m$ as show in Fig. 4.14, a results that qualitatively correlates well with experimental studies on cardiac cell contractions [51]. This behavior may be explained by the fact that at low substrate stiffness, very little force is generated by cells ($F \approx 0$) and thus no work is performed while at high stiffness, cell cannot generate substrate deformation ($\delta = 0$) which also implies a vanishing work. The intermediate substrate stiffness which optimizes both force and displacement is most of the time preferable for certain cell phenotypes. Understanding such processes is critical for the design optimized artificial gels for tissue engineering [51].

4.6.4 Effect of cell morphology on cell SF structure

Recent experiments on contractile cells (such as cardiomyocyte) have shown that a strong correlation exists between cell shape and structure [18, 117], indicating that cell function, and in particular contractility, is strongly affected by geometrical factors. This section consists of assessing the prediction of the proposed model in that respect. For this, as a mean of comparison with experimental tests [18, 117, 61, 19], we consider three different cells (Fig. 4.15) each characterized by their own morphology (square, rectangular and triangular shapes) and focal adhesions distribution. In particular, we assume here that a cell adheres to a rigid substrate at specific locations (cell corners), which results in constraining the motion of material points on adhesion islands, represented by black dots in Fig. 4.15a. Initial and boundary conditions are similar to those applied in the previous example.

As depicted in Figs. 4.15 the proposed model is able to capture the general SF organization observed in experiments for various cell morphology ([18, 117, 61, 19]). Both Figures 4.15b and 4.15c show that SF are mostly generated in directions that are restricted in terms of

elongation, i.e. lines between the adhesion islands. As discussed in the previous section, this is explained by the fact that the rate of cytoskeleton's contraction along these directions is very small (close to zero) and thus promotes contractility and SF generation. Overall, these results indicate that interactions between SF formation and mechanics, as described by the proposed model, are sufficient to accurately reproduce key features of cell organization and force generation observed in experiments.

4.7 Concluding remarks

To summarize, this chapter presents a mixture framework that aims at describing the processes by which contractile cells are able to sense their mechanical environment (through stiffness) and react by adjusting the amount of contractile force they generate. By describing the cell's body as a mixture of four critical contractile elements, the proposed model is able to accurately capture the interplay between both mechanical and chemical mechanisms taking place in cells. The key features of the approach are:

- SF contraction is described by the velocity-tension and length-tension relationships arising from cross-bridge dynamics
- SF formation arises from mass exchange with dispersed globular actin monomers and is assumed to depend on the tension in existing SF. This aspect is the main assumption of the model regarding the mechano-sensitivity of contraction. Cytosol and globular actin transport is described by conventional diffusion-convection type laws
- Cell contraction is described in terms of both passive elasticity of the cytoskeleton and active contractile stress from a statistical distribution of SF.

The model exhibits a positive feedback mechanism resulting between mechanical-chemical interplay between constituents. Contractile stress (that depends on strain-rate

through the tension velocity relationship) promotes SF formation and SF formation results in increasing contraction. This loop eventually ends when the stock of available globular actin for SF formation is depleted. The solution to the model shows that this chemo-mechanical cross-talk could be responsible for the sensitivity of cell contraction on substrate stiffness. In other words, the proposed model may be used as a first step to characterize the interactions between a contractile cell and its environment, which is an important feature of the processes of tissue remodeling, would healing and morphogenesis. In addition, the present study has shown how multiscale principles [164](homogenization) and multiphasic mixture concepts can be extended to investigate the active behavior of cells. This approach is very promising as various physical processes including chemistry, mechanics and transport and their interactions can be described in a consistent framework that satisfy basic conservation principles (balance of mass, momentum and energy).

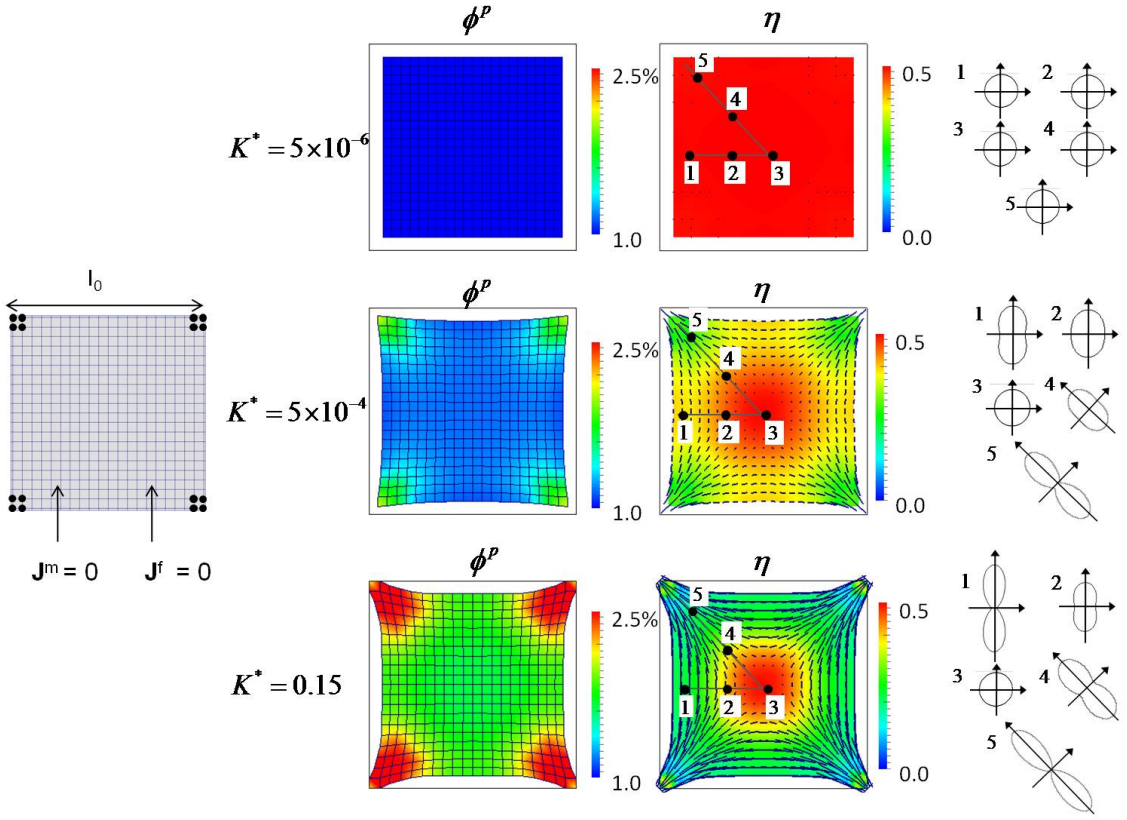

Figure 4.12: *SF volume fraction ϕ^p and distribution at steady-state for three values of support stiffness (ranging from very low to very high). The principal direction of SF are indicated by lines and the parameter η refers to the degree of anisotropy ($\eta = 0.5$ for an isotropic network and $\eta = 0$ for an unidirectional fiber direction). The polar fiber distribution ($\phi^p_\theta(\theta)$) is also shown for 5 characteristic points in the cell.*

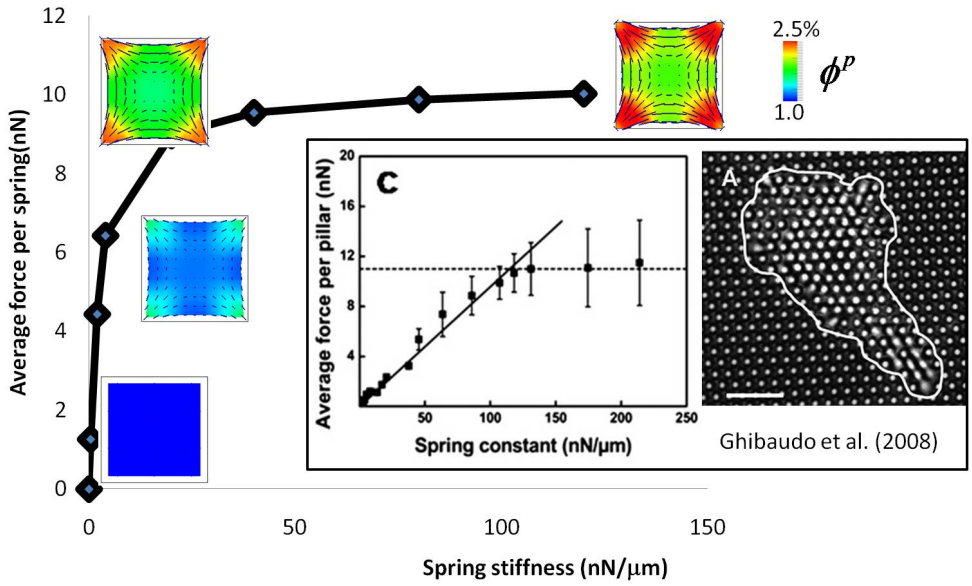

Figure 4.13: *Steady-state contractile force F at focal adhesions as a function of support stiffness $K^\star$ as predicted with the proposed model. The steady-state morphology and corresponding SF distribution are are shown for characteristic values of $K^\star$. For comparison, experimental results from Ghibaudo et al. [62] on the variation contractile forces in terms of pillar stiffness (spring constant) are also reported.*

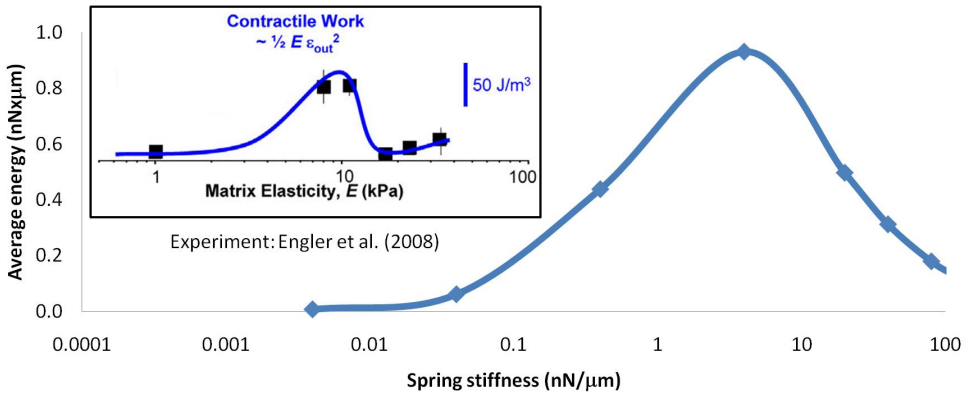

Figure 4.14: *Mechanical work of the cell in terms of substrate stiffness : Qualitative comparison of model prediction and experiments on cardiomyocytes [51]*

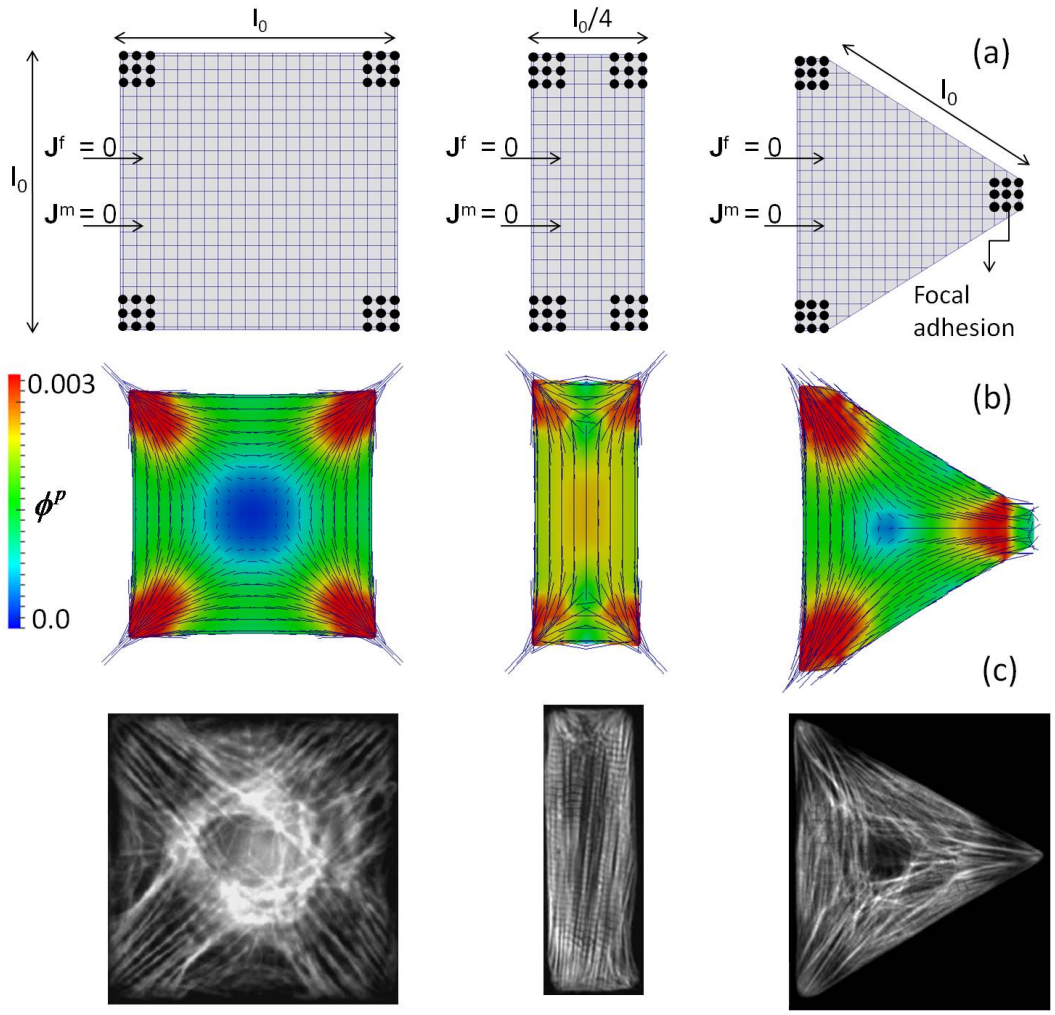

Figure 4.15: *Effect of cell morphology on SF distribution. (a) Definition of focal adhesion complexes, boundary conditions and finite-element discretization ($\ell_0 = 40\mu m$). (b) Computed SF orientation and density for three different shapes and (c) comparison with experimental observations of fibril distribution in cardiomyocytes by Parker and co-workers [18, 117, 61, 19]*

Chapter 5

An XFEM-based numerical strategy to model mechanical interactions between biological cells and a deformable substrate

5.1 Abstract

Contractile cells are known to constantly probe and respond to their mechanical environment through mechano-sensing. While the very mechanisms responsible for this behavior are still obscure, it is now clear that cells make full use of cross-talks between mechanics, chemistry and transport in order to organize their structure and generate forces. To investigate these processes, it is important to derive mathematical and numerical models that can accurately capture the interactions between cells and an underlying deformable substrate. The present chapter therefore introduces a computational framework, based on the extended finite element (XFEM) and the level-set method to model the evolution of two-dimensional (plane-stress) cells lying on an elastic substrate whose properties can be varied. Cells are modeled with a continuum mixture approach previously developed by the authors to describe key phenomena of cell-sensing, such as stress-fiber formation, mechano-sensitive contraction and molecular transport while cell-substrate adhesion is formulated with a linear elastic cohesive model. From a numerical view-point, cell and substrate are discretized on a single, regular finite element mesh, while the potentially complex cell geometry is defined in terms of a level-set function that is independent of discretization. Field discontinuities across the cell membrane are then naturally enforced using enriched shape functions traditionally used in the XFEM formulation. The resulting method provides a flexible platform that can

handle complex cell geometries, avoid expensive meshing techniques, and can potentially be extended to study cell growth and migration on an elastic substrate. In addition, the XFEM formalism facilitates the consideration of the cell's cortical elasticity, a feature that is known to be important during cell deformation. The proposed method is illustrated with a few biologically relevant examples of cell-substrate interactions. Generally, the method is able to capture some key phenomena observed in biological systems and displays numerical versatility and accuracy at a moderate computational cost.

5.2 Introduction

Tissue structure and dynamics are the result of intense mechanical cross-talks between contractile cells and their surrounding matrix but the underlying mechanisms of such interactions are not understood yet. This has hindered critical research advances to translate tissue engineering to a wide varieties of tissues, in which tissue development depends on mechanical forces, extra-cellular matrix (ECM) properties and initial specimen geometry [4]. Number of studies [55, 148, 114] have shown that the contractility of cells was responsible for the large deformations observed in artificial tissues soon after cell encapsulation. It was further found that these deformations were associated with significant changes in cells morphology and ECM structure and were strongly dependent on the mechanical environment of the tissue (such as tissue stiffness, stress and deformation). This behavior is readily observed during the alignment of cells and collagen fibers in directions of maximum tensile stresses [170, 65, 26] and maximum effective stiffness. A key to understand these phenomena resides in our ability to characterize how cells interact with their environment, and especially how they are able to sense their mechanical surrounding and react by producing contractile forces. Recent advances in cell mechanics, combined with latest developments in computational mechanics may provide critical tools to study cell-matrix interactions. The objective of this chapter is therefore to propose a numerical approach that can naturally describe how cells of arbitrary morphologies can sense the mechanical properties of their environment, and respond to it

applying mechanical forces.

Mechanical models of cells can generally be split in two categories: formulations based on prestress fibrous network [107, 14] and those based on continuum mechanics [110, 166]. Due to their flexibility, continuum models are thus far been successful at capturing the chemo-mechanical interactions responsible for the mechano-sensitivity of cells ([37, 39]). For instance, mixture models have proved very efficient at accurately characterizing certain key mechanisms of cell behavior, including transport, chemical reaction and mass exchange [165]. In addition, the role of the cortical membrane surrounding the cell, known to be a critical player in cell deformation, has been the object of several modeling investigations. Models based on fibrous network mechanics have been the first to provide compelling arguments onto the role of membrane stiffness on cell curvature [14]. However, more recently, we have shown that continuum models can naturally incorporate the effect of cortex stiffness with a surface elasticity formulation based on the extended-finite element method [163]. The issue of modeling mechanical interactions between cells and a substrate have mostly been achieved by via cohesive laws in finite element models. ([103, 125, 178, 176]).While successful at capturing interesting behaviors such as debonding, this strategy generally suffers from the fact that cell and substrate are defined on two distinct domains that typically exhibit complex geometries and possibly evolve in time. In many cases, such methods consequently leads to potential meshing issues and require a very fine discretization to reach accurate results.

To fill the gap, the present chapter introduces a continuum formulation, combined with a numerical approach based on the Extended Finite Element (XFEM) and the levelset methods to study the mechanical cross-talks between contractile cells (fibroblasts) and a two-dimensional deformable substrate. The mechano-chemistry of cell contraction is described in terms of a constrained mixture formulation that was recently developed by the authors [165] to capture the phenomena of mechano-sensitive stress-fiber (SF) formation (and dissociation) and contraction. In short, the model is based on the description of the contractile apparatus

of cell in terms of two solid constituents: the cytoskeleton and a population of contractile stress fibers as well as two fluid constituents: the cytosol and soluble contractile units (that can polymerize into stress fibers). The interactions between a cell and its substrate are possible through localized adhesive regions, known as the focal adhesion. From a numerical view-point, the complicated problem of the interactions between two domains (cell and substrate) of different geometry and constitution is greatly simplified by using the advantages of XFEM [43, 105, 9]. Without loss of generality, considering cell and substrate as by two-dimensional domains satisfying plane-stress conditions, we introduce a single finite element mesh for both domains. Cell geometry is then defined in terms of an analytical levelset function defining the contour of cell boundary independently of discretization. Degrees of freedom pertaining to cell are then only associated with nodes belonging to the interior of the domain defined by the levelset, while discontinuities across the cell boundary are naturally represented by enriching finite element shape function with discontinuous functions following the standard XFEM equations. The key advantages of this contribution are then as follows:

- Complex cell geometries may naturally be handled independently of finite-element discretization.
- Because cell and substrate domains are discretized with the same mesh, the numerical treatment of cell-substrate cohesion is accurate and simple.
- The XFEM enrichment functions enable the incorporation of the stiffness of the cortical membrane surrounding the cell; this feature is known to be critical to realistically capture cell morphology.
- The formulation is flexible and has the potential to be extended for describing cell spreading and migration using level-set evolution equations.

The organization of the chapter is as follows. In the next section, we give a summary of the constrained mixture model to characterize cell contraction; we particularly concen-

trate on providing the main equations (conservation of mass and momentum) as well as a set of biologically relevant assumptions to build realistic constitutive relations. In section 3, the problem of the interaction between a cell and a deformable substrate is investigated. Governing equations are derived both in their strong and weak form; which enable a smooth transition to the finite-element formulation presented in section 4. Section 4 then discusses the XFEM-levelset approach to obtain a solution of the cell-substrate interactions, leading to the final form of implicit, time-dependent finite-element equations. The method is then illustrated in section 5 by presenting several experimentally motivated example of cell-substrate interactions with comparison to observations. The chapter finishes with a brief summary and concluding remarks.

5.3 A constrained mixture model of contractile cells

5.3.1 Continuum description of cell's structure

The mechano-sensing capability of cell is closely related to their contractile abilities. The latter has mainly been explained in terms of the formation of a well differentiated network of stress fibers (SFs), that are capable of generating forces through acto-myosin interactions [28, 35, 165]. The main processes behind cell contraction can generally be decomposed as follows: first, the assembly of SF from dissolved contractile units and second, the contractile capacity of SFs. On the one hand, SF assembly and dissociation are known to be very sensitive to mechanical stimuli; mechanical force stabilize existing SFs and promote the assembly of new ones [35]. On the other hand, the contractile capacity of SFs is regulated by cross-bridge dynamics, that is known to be very sensitive to strain and strain rate. The evolution of SF therefore depends on the ability of cells to sense and transmit mechanical force from the substrate through so-called focal adhesion complexes (Fig. 5.6)[168]. These complexes provide a physical attachment between SFs and substrate anchoring molecules (ligands) through cross-membrane proteins (integrins) and may be thought of as cohesion

islands of finite size between cell and substrate [108, 24]. At last, the internal structure of fibroblasts possesses sub-membraneous mechanical reinforcement, known as the cortex, that is found in the form of a thin layer of actin fibers oriented in parallel with the membrane [97, 90, 157, 14]. This component is known to have a significant effect on the cell's morphology and deformation by providing a non-negligible tangential stiffness to the cell membrane [163].

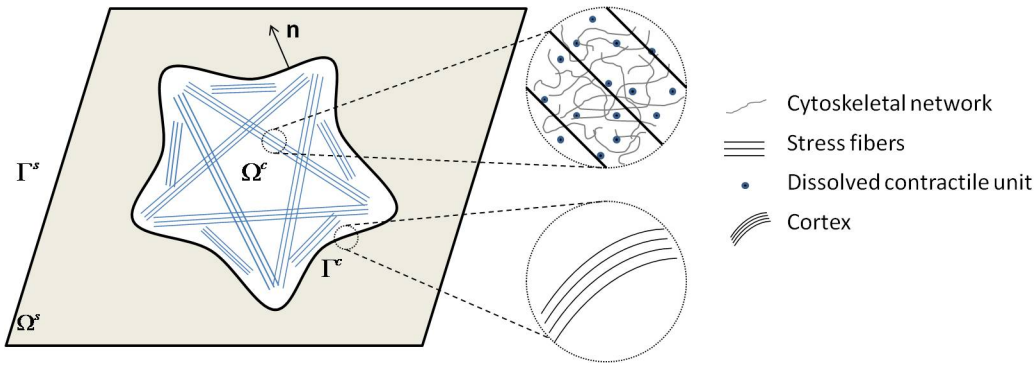

Figure 5.1: A typical cell on a substrate: the definition of domains and boundaries, and cell's main constituents.

From a modeling perspective, cell and substrate can be defined by two physical domains Ω^c and Ω^s in their current configuration, whose boundaries are denoted by Γ^c and Γ^s, respectively (Fig. 5.1). While the substrate is modeled as a purely elastic medium, a contractile cells is viewed as a constrained mixture made of four constituents [165] (Fig. 5.1): two solid constituents: a passive cytoskeleton (mostly made of microtubules and intermediate filaments) and a highly anisotropic SF network, and two fluid components: the cytosol and a population of dissolved contractile units. Measuring material motion with respect to the passive cytoskeleton, for which a point in the original configuration is denoted by $\mathbf{X}$, a description of the mixture at any time t can be given in terms of respective volume fraction ϕ^α of the diverse constituent α at material point $\mathbf{X}$ such that:

$$\sum_{\alpha=1}^{4} \phi^\alpha(\mathbf{X}, t) = 1 \tag{5.1}$$

where $\alpha = s, f, m, p$ for passive cytoskeleton, cytosol, dissolved contractile units and SFs, respectively. When plated on elastic substrates, fibroblasts usually evolve quickly in a configuration in which their thickness is significantly smaller than other dimensions, which motivates our study within the context of two-dimensional plane-stress assumptions. This generally simplifies the analysis as SF directions only occupy the two-dimensional space and can be described in terms of one orientation angle. At any point within the cell, the SF network may then be defined in terms of the so-called structure tensor $\mathbf{\Phi}^p$ given by [165]:

$$\mathbf{\Phi}^p(\mathbf{X}, t) = \phi^p \left[\eta \mathbf{I} + (1 - 2\eta)\, \mathbf{M}_{\theta_0}\right], \qquad \mathbf{M}_{\theta_0} = \begin{bmatrix} cos^2\theta_0 & cos\theta_0 sin\theta_0 \\ cos\theta_0 sin\theta_0 & sin^2\theta_0 \end{bmatrix}, \tag{5.2}$$

providing a description of the anisotropic network in terms of its volume fraction ϕ^p, degree of anisotropy η, and principal orientation θ_0.

5.3.2 Balance of mass and SF evolution

Let us first describe the mass balance of each constituent in a cell during the process of contraction. Using the material time derivative (following the solid constituent), the general form of mass balance equation for constituent α can be written as [165]:

$$\frac{D\phi^f}{Dt} + \phi^f \nabla \cdot \mathbf{v} + \nabla \cdot \mathbf{J}^f = 0 \tag{5.3}$$

$$\frac{D\phi^m}{Dt} + \phi^m \nabla \cdot \mathbf{v} + \nabla \cdot \mathbf{J}^m = \Pi^m \tag{5.4}$$

where the solid velocity $\mathbf{v}$, the relative cytosol flux $\mathbf{J}^f$ and the flux $\mathbf{J}^m$ of unassembled contractile units (measured with respect to solid motion) are defined as:

$$\mathbf{v} = \frac{\partial \mathbf{x}(\mathbf{X}, t)}{\partial t}, \qquad \mathbf{J}^f = \phi^f \left(\mathbf{v}^f - \mathbf{v}\right) \quad \text{and} \quad \mathbf{J}^m = \phi^m \left(\mathbf{v}^m - \mathbf{v}\right) \tag{5.5}$$

The term Γ^m describes the rate of consumption (or production) of unassembled contractile units during their assembly into SFs. The mass and orientation of SFs therefore increases (or decreases) during time due to this chemical reaction. To describe this process, one may

investigate the balance of mass of SFs in specific directions. We showed in [165] that this translate into a tensorial equation of the form:

$$\frac{D\mathbf{\Phi}^p}{Dt} + \mathbf{\Phi}^p \nabla \cdot \mathbf{v} = \mathbf{\Pi}^p \tag{5.6}$$

where $\mathbf{\Pi}^p$ is a second order tensor that represents the directional rate of SF polymerization (or degradation). Importantly, it is assumed that once created, SF become part of the solid cytoskeleton and thus follows the same motion as the passive cytoskeleton. In other words, the velocity $\mathbf{v}^p$ of the SF network is equal to the velocity $\mathbf{v}$ defined in (5.5). Finally, it is critical to specify that no mass can be created or consumed at the level of the entire mixture. This means that the change in mass of unassembled contractile units must be equal to the opposite of the change of mass of SFs at any location and time. This condition is written:

$$trace\,(\mathbf{\Pi}^p) + \Pi^m = 0 \tag{5.7}$$

5.3.3 Balance of momentum

Let us now turn to the governing equation describing the equilibrium of forces within a cell (Fig. 5.2). For this, it is of interest to define the mixture Cauchy stress tensor $\mathbf{T}$

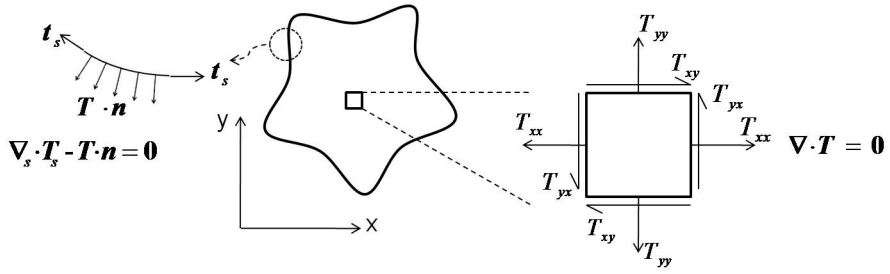

Figure 5.2: Equilibrium of forces in the body and boundary of a cell.

representing the infinitesimal force per unit current area. Using the effective stress principle, the mixture stress may be decomposed into contribution from each constituent as follows:

$$\mathbf{T} = \mathbf{T}^c + \mathbf{T}^p - p\mathbf{I} \tag{5.8}$$

where $\mathbf{T}^c$ is the partial stress in the passive cytoskeleton, $\mathbf{T}^p$ is the stress that originates from the presence of SFs and p is the fluid pressure. Note that the contribution from the pressure of dissolved contractile proteins has been neglected due to its relatively low volume fraction. Considering the balance of momentum for the mixture, the following form can be derived:

$$\nabla \cdot \mathbf{T} + \mathbf{b} = \mathbf{0} \quad \text{in} \quad \Omega^c \tag{5.9}$$

representing the balance of force within the cell domain. Note that dynamical effects (through the inertial term) were neglected due to the slow processes into consideration. Finally, we note that invoking the balance of angular momentum, it can be shown that stresses $\mathbf{T}^c$, $\mathbf{T}^p$ and $\mathbf{T}$ are represented symmetric tensors. Let us now investigate the effect of the cortical membrane stiffness on the equilibrium of force within the cell. Considering a small cortical thickness relative to the cell size, it is possible to represent force in the cortex in terms of a surface stress $\mathbf{T}_\sigma$ that has unit of a force per unit length. As discussed in [163] and [14], one can show that the equilibrium between bulk stress $\mathbf{T}$ and membrane tensile stress $\mathbf{T}_\sigma$ is given by

$$\nabla_\sigma \cdot \mathbf{T}_\sigma - \mathbf{T} \cdot \mathbf{n} \;=\; 0 \quad \text{on} \quad \Gamma^c \tag{5.10}$$

where $\nabla_\sigma \cdot \mathbf{T}_\sigma$ denotes the surface divergence of the cortical stress and $\mathbf{n}$ is the outward normal vector to the cell's boundary Γ^c. A strong analogy may be drown between the above equation and the Young-Laplace equation describing the effect of surface tension on the pressure in a fluid bubble. An increase in surface stress $\mathbf{T}_\sigma$ as well as membrane curvature (captured in the surface divergence operator) results in an increasing bulk stress in a direction normal to the membrane.

5.3.4 Fluid flux and cytoskeleton elasticity

Let us now discuss the constitutive relations describing cytosol and unassembled contractile units transport within the cell, as well as the passive elasticity of the passive cy-

toskeleton and its surrounding cortical membrane. The constitutive relation defining SF formation and contraction is left for the next section. The motion of the fluid phase are determined based on the two following assumptions. First, it is assumed that dissolved proteins are highly diluted and do not affect the motion of the cytosol. This means that one can describe cytosol motion uniquely in terms of the pressure gradient through Darcy's law as:

$$\mathbf{J}^f = -\frac{\kappa}{\mu}\nabla p. \tag{5.11}$$

Here κ denotes the isotropic permeability of the cytoskeleton and μ is the viscosity of the cytosol. Note that due to the appearance of SF, the permeability may become anisotropic in time. This effect is not accounted in the present study. In addition, we assume that the motion of dissolved proteins is driven by two forces: (a) the drag force of the cytosol and (b) the diffusive forces through the cytosol. One can therefore show that the flux $\mathbf{J}^m$ of proteins contains a convection and diffusion term as follows:

$$\mathbf{J}^m = -\frac{\phi^m}{\phi^f}\frac{\kappa}{\mu}\nabla p - \phi^f D\ \nabla\left(\frac{\phi^m}{\phi^f}\right) \tag{5.12}$$

where D is the diffusion coefficient of dissolved proteins in the cytosol.

To characterize the elasticity of the passive cytoskeleton, a hypo-elastic constitutive relation was adopted. Introducing the rate of deformation $\mathbf{D}(\mathbf{X}, t)$ of the solid constituent (Fig. 5.3), an objective rate of Cauchy stress can be determined as:

$$\mathbf{T}^{\nabla J} = \mathbf{C}^{\nabla J} : \mathbf{D} \quad \text{where} \quad \mathbf{D} = \frac{1}{2}\left(\frac{\partial \mathbf{v}}{\partial \mathbf{x}} + \frac{\partial \mathbf{v}}{\partial \mathbf{x}}^T\right) \tag{5.13}$$

Assuming isotropic elasticity, the stiffness matrix $\mathbf{C}^{\nabla J}$ was expressed in terms of Lame constants λ and μ such that its components are given by $C^{\nabla J}_{ijkl} = 2\mu\delta_{ik}\delta_{jl} + \lambda\delta_{ij}\delta_{kl}$. While the nonlinear material behavior of the passive cytoskeleton is not considered in the present formulation, nonlinear effects arising from finite deformation and rotation are still accounted for through the objective Jaumann rate of the Cauchy stress defined by:

$$\mathbf{T}^{\nabla J} = \frac{D\mathbf{T}}{Dt} - \mathbf{W}\cdot\mathbf{T} - \mathbf{T}\cdot\mathbf{W}^T \tag{5.14}$$

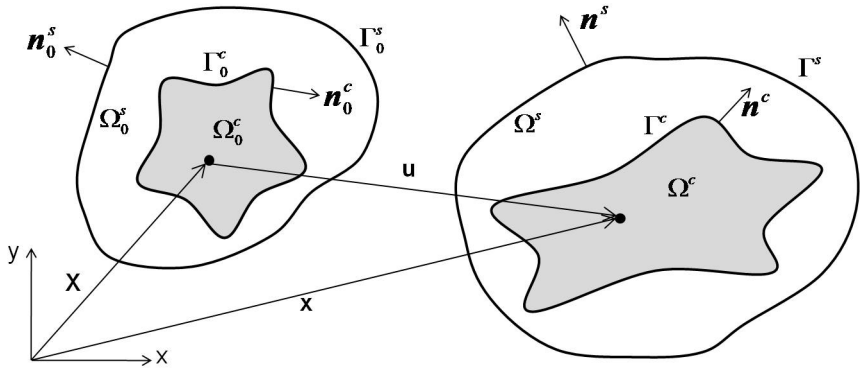

Figure 5.3: Initial and current configurations of cell and substrate domains.

where $\mathbf{W}$ denotes the spin tensor. For consistency, a similar hypo-elastic relation is also adopted to describe the effect of the cortical membrane. Thus, the Jaumann rate of the stress tensor $\mathbf{T}_\sigma$ is written in terms of the tangential velocity gradient on the cell boundary Γ^c as:

$$\mathbf{T}_\sigma^{\sigma J} = \mathbf{C}_\sigma : \mathbf{D}_\sigma \quad \text{where} \quad \mathbf{D}_\sigma = \mathbf{P} \cdot \mathbf{D} \cdot \mathbf{P} \tag{5.15}$$

Here the tangential projection operator is given by $\mathbf{P} = \mathbf{I} - \mathbf{n} \otimes \mathbf{n}$. Note that for two-dimensional plane stress problems, the cortical membrane is represented by a line whose axial stiffness is given in terms of a single parameter E_σ. In this context, the components of the fourth order cortical elasticity tensor $\mathbf{C}_\sigma$ is simply given by:

$$C_{\sigma,ijkl} = E_\sigma \delta_{ik} \delta_{jl} \tag{5.16}$$

5.3.5 Mechano-sensitive SF formation and contraction

We now concentrate on the constitutive relation describing the active behavior of contractile cells, comprised of two distinct mechanisms: SF formation (or dissociation) and SF contraction. As mentioned previously, these processes are highly mechano-sensitive and the model should reflect such observations. Our formulation therefore builds upon the two following ideas (Fig. 5.4):

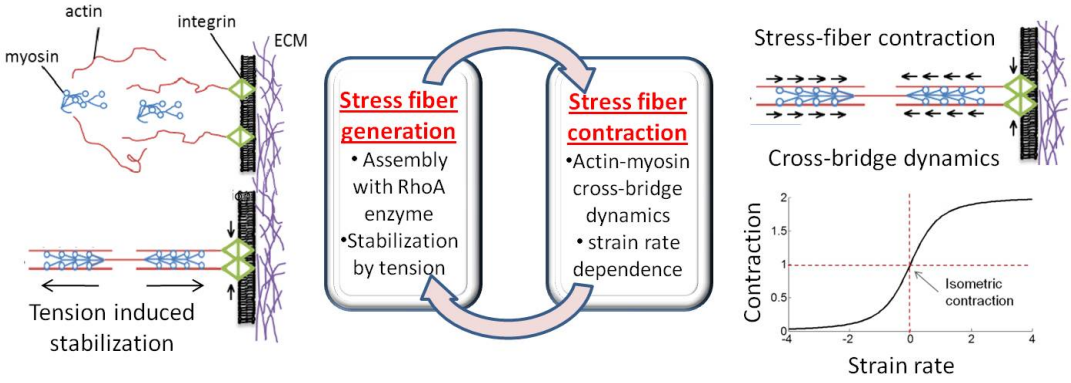

Figure 5.4: Feedback mechanism between SF formation and contraction

- SF formation in a specific direction is promoted by the existence of a contractile stress in that particular direction. This assumptions is supported by a variety of experimental observations such as [35, 94, 140, 28, 119, 14, 57]. To capture this feature, we write the rate of SF formation $\mathbf{\Pi}^p$ in term of a first order kinetic equation whose rate of formation is stress dependent:

$$\mathbf{\Pi}^p = \underbrace{\left(\frac{1}{2}k_0^f\mathbf{I} + k_1^f\mathbf{T}^p\right)\frac{\phi^m}{\phi^f}}_{\text{contraction dependent formation}} - \underbrace{k_0^d\mathbf{\Phi}^p}_{\text{Dissociation}} \tag{5.17}$$

  Here k_0^f and k_0^d are the tension independent rate of formation and dissociation while k_1^f characterize the sensitivity of formation to the level of contraction, represented by the tensor $\mathbf{T}^p$. Note that the above equation is tensorial and is therefore capable of capturing direction dependent SF formation and dissociation.

- SF contraction is dependent on the unidirectional strain and strain rate of SFs. This behavior is a well known consequence of cross-bridge dynamics between thin and thick filaments at the molecular scale [22, 81]. In short, the model predicts a drop in contraction when the rate of shortening is negative and an increase in contraction with SF lengthening (Fig 5.4); this behavior is known as the tension-velocity relationship ([81]) and is represented by the normalized function g of strain

rate $\dot{\epsilon}$ as follows (Fig. 5.5):

$$g(\dot{\varepsilon}) = 1 + \frac{\dot{\varepsilon}/\dot{\varepsilon}_0}{\sqrt{\left(\dot{\varepsilon}/\dot{\varepsilon}_0\right)^2 + 1}} \tag{5.18}$$

In addition, the contraction magnitude is known to be optimal when SF are in their original (strain free) configuration. However, as they shorten or lengthen, their contractile capacity decreases to eventually vanish. This behavior, known as the length-tension relationship ([22]), is captured with by introducing the following function of uniaxial strain ϵ (Fig. 5.5):

$$f\left(\varepsilon\right) = exp\left(-\frac{\varepsilon}{\varepsilon_0}\right)^2 + H(\epsilon)\left(\frac{\varepsilon}{\varepsilon_1}\right)^2 \tag{5.19}$$

where H is the Heaviside function that is such that $H = 0$ when $\epsilon < 0$ and $H = 1$ when $\epsilon \geq 0$. In the above equation, the first term captures the length-tension relation while the second term describes the nonlinear, strain hardening passive elastic response of SF when stretched. This term is important in capturing the increase in cell stiffness as more SF are assembled. The stress tensor arising from SF may then be determined by taking a directional average of their contribution in each direction. Assuming that the normalized uniaxial stress in a specific direction is given by the product of function g and f, weighted by their volume fraction ϕ^p, the stress $\mathbf{T}^p$ is defined by:

$$\mathbf{T}^p = \frac{\bar{T}}{\pi}\int_{-\pi/2}^{\pi/2} \phi^p(\theta) f\left(\varepsilon\right)\ g\left(\dot{\varepsilon}\right) \begin{bmatrix} cos^2\theta & cos\theta sin\theta \\ cos\theta sin\theta & sin^2\theta \end{bmatrix} d\theta \tag{5.20}$$

where ε is related to the Green- Lagrange strain tensor $\mathbf{E}$ by $\varepsilon = E_{11}cos^2(\theta) + E_{22}sin^2(\theta) + 2E_{12}sin(\theta)cos(\theta)$ and the quantity $\bar{T}$ denotes the typical magnitude of SF isometric contraction in fibroblasts. Note that the value of ϕ^p for different directions is determined from the knowledge of the structure's tensor $\mathbf{\Phi}^p$ as described in Appendix A.

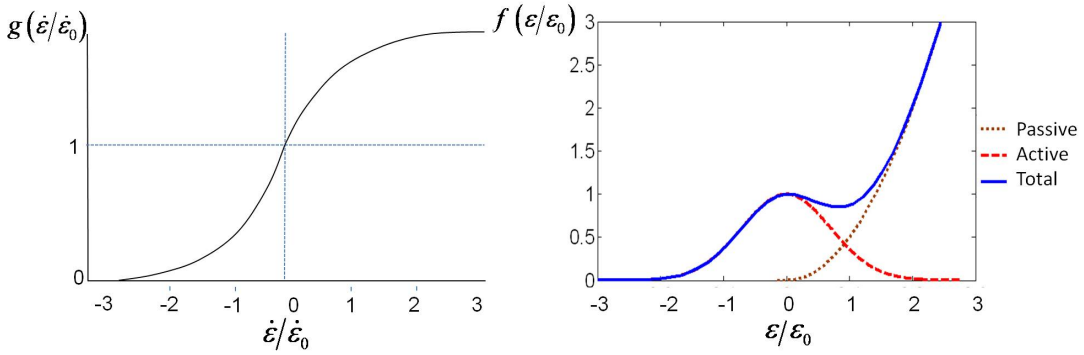

Figure 5.5: Tension of a single stress fiber as a function of strain and rate of strain.

A particularity of the above model of cell contraction is that it generates a positive feed-back mechanism between fiber contraction and formation in direction in which fiber shortening is mostly resisted. For instance, when cells adhere to a stiff substrate, their contraction only generates little deformation, which according to the tension-velocity curve, enables SF to keep a level of isometric contraction. The presence of such a contraction consequently promotes more SF formation in this particular direction as described by the mechano-sensitive formation model of (5.17). Inversly, a cell adhering to a soft substrate generates a significant amount of negative strains as a result of contraction. This results in switching the strain rate to the left on the tension-velocity curve of Fig. 5.5, and thus decreasing the magnitude of SF contraction. Ultimately, this is translated into a drop in the rate of fiber formation and a loss of SF density.

5.4 Governing equations for the cell-substrate interaction problem

We now turn to the formulation of the interactions between cells and their mechanical environment. We particularly concentrate on the problem of cells lying on a two-dimensional elastic substrate, a situation that often arises both in-vivo and in experiments.

5.4.1 Substrate elasticity

The mechanical behavior of the substrate is known to be an important factor driving cell morphology, contraction and structure [90, 179, 50, 42, 168]. While this behavior can be extremely complex, involving nonlinear elasticity, viscous effects and inelasticity, the present work concentrates on the case of a simple linear isotropic elastic material with varying stiffness. Describing substrate deformation in terms of a displacement field $\mathbf{u}^s$, one can introduce a rate of deformation and an objective rate for the substrate Cauchy stress $\mathbf{T}^s$ in a similar form as that shown in (5.13). In other words, substrate elasticity is described in terms of two paramters (λ^s, μ^s), or equivalently by the set (E^s, ν^s) denoting the Young's modulus and Poisson's ratio. It is finally straightforward to show that substrate equilibrium is written in terms of the divergence of the Cauchy stress as:

$$\nabla \cdot \mathbf{T}^s + \mathbf{b}^s = \mathbf{0} \tag{5.21}$$

where $\mathbf{b}^s$ represents the body force vector in the substrate. In the following analysis, we assume that the substrate consists of a very thin layer that can be modeled in plane-stress conditions. While this situation may not acurately represent actual experimental conditions, the assumption is not expected to affect the main trends exhibited by cell in terms of different substrate elasticity.

5.4.2 Adhesion complexes

Cell-substrate adhesion is provided by the attachment between trans-membrane molecules (known as integrins) and molecular complex (the ligands) laying on the surface of the substrate (Fig. 5.6). Integrins easily diffuse through the cell membrane [36] in order to attach to free ligands on the substrate. It is thus realistic to assume that the magnitude of the adhesive force $\mathbf{t}_a$ per unit area is directly related to the density η_l of ligands on the substrate by:

$$\mathbf{t}_a = \eta_l \mathbf{f}_a \tag{5.22}$$

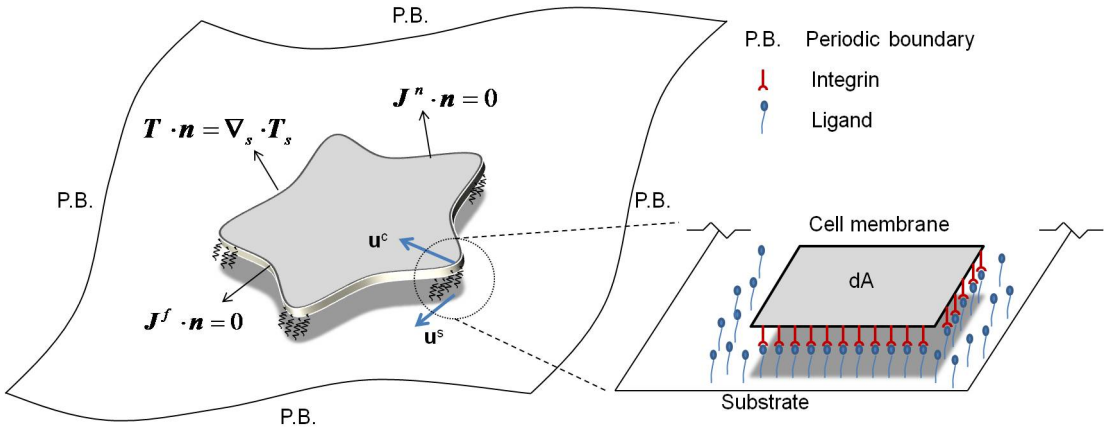

Figure 5.6: The general details of adhesion complexes between cell and substrate combined of integrins and ligands; together with the boundary conditions applied to cell and substrate.

where η_l denotes the number of ligands per unit substrate area and $\mathbf{f}_a$ is the force in a single ligand-integrin complex. Further assuming that the mechanical behavior of ligand-integrin complex is represented by a linear force-separation relation with stiffness K_{li}, the continuum traction force (per unit area) is given by:

$$\mathbf{t}_a = K_a\left(\mathbf{u}^c - \mathbf{u}^s\right) \qquad \text{where} \qquad K_a = \eta_l K_{li} \tag{5.23}$$

where the term $\mathbf{u}^c - \mathbf{u}^s$ represents the separation between cell membrane and substrate surface. The above equation clearly states the stiffness of the adhesion stiffness increases linearly with ligand density. It also shows that if no ligand are present $\eta_l = 0$, no cell-substrate adhesion is possible ($\mathbf{t}_a = 0$).

5.4.3 Summary of the governing equations under plane stress conditions: Strong form

Considering that the cell and substrate lie in the x-y plane of the (x,y,z)-coordinate system, plane stress conditions imply that stress components associated with the z-direction vanish. In addition, adhesion forces $\mathbf{t}_a$ acting on the bottom cell surface and the top substrate surface are represented by vectors in the x-y plane and are equivalent to "body forces" acting

in cell and substrate with equal magnitude but opposite directions. In other words, the body forces $\mathbf{b}$ and $\mathbf{b}^s$ appearing in (5.9) and (5.21) are replaced by adhesive forces such that the mechanical equilibrium for cell and substrate is written:

$$\nabla \cdot \mathbf{T}^s + \mathbf{t}_a = 0 \quad \text{in} \quad \Omega^s \qquad\qquad \mathbf{u}^s = \mathbf{u}^* \quad \text{on} \quad \Gamma^s \tag{5.24}$$

$$\nabla \cdot \mathbf{T} - \mathbf{t}_a = 0 \quad \text{in} \quad \Omega^c \qquad\qquad \mathbf{T} \cdot \mathbf{n} = \nabla_\sigma \cdot \mathbf{T}_\sigma \quad \text{on} \quad \Gamma^c \tag{5.25}$$

Note that the elastic constitutive relations are affected by the plane-stress conditions. For clarity, a detailed description of these equations is left in Appendix B. In addition, one can show that mass conservation equation ((5.3),(5.4)) in the cell domain Ω^c under plane stress conditions take the following form:

$$\alpha \, \nabla \cdot \mathbf{v} + \beta \, \dot{p} + \nabla \cdot \mathbf{J}^f + \nabla \cdot \mathbf{J}^m = 0 \quad \text{in } \Omega^c \qquad\qquad \mathbf{J}^m \cdot \mathbf{n} = 0 \ \text{ on } \ \Gamma^c \tag{5.26}$$

$$\frac{D\phi^f}{Dt} + \alpha\phi^f \, \nabla \cdot \mathbf{v} + \beta\phi^f \dot{p} + \nabla \cdot \mathbf{J}^f = 0 \quad \text{in } \Omega^c \qquad\qquad \mathbf{J}^f \cdot \mathbf{n} = 0 \ \text{ on } \ \Gamma^c \tag{5.27}$$

where coefficients α and β depend on Poisson's ratio ν and Young's modulus E of the cell's cytoskeleton as follows (Appendix B):

$$\alpha = \frac{1-2\nu}{1-\nu} \quad \text{and} \quad \beta = \frac{(1+\nu)(1-2\nu)}{E(1-\nu)}$$

Similarly, the SF evolution equation (5.6) becomes:

$$\frac{D\mathbf{\Phi}^p}{Dt} + \mathbf{\Phi}^p \, \alpha \, \nabla \cdot \mathbf{v} + \mathbf{\Phi}^p \, \beta \, \dot{p} = \mathbf{\Pi}^p \quad \text{in} \quad \Omega^c \tag{5.28}$$

In the end, the five equations (5.24), (5.25), (5.26), (5.27) and (5.28) subjected to the given boundary conditions can be solved to determine five unknowns that consist of (a) the displacement field $\mathbf{u}^s(\mathbf{X}, t)$ in the substrate domain Ω^s, (b) the displacement field $\mathbf{u}(\mathbf{X}, t)$ in the cell domain Ω^c, (c) the cytosol volume fraction $\phi^f(\mathbf{X}, t)$ in Ω^c, (d) the monomer volume fraction $\phi^m(\mathbf{X}, t)$ in Ω^c and finally (e) the structure tensor $\mathbf{\Phi}^p(\mathbf{X}, t)$ describing the SF distribution in Ω^c.

5.4.4 Summary of the governing equations: Weak form

The above coupled differential equations constitute a highly non-linear system whose solution lays in the three-dimensional space (x, y, t). A numerical strategy, based on the finite element method is therefore necessary to obtain a solution in the most general case. Such a formulation require that governing equations are rewritten in an integral form (or weak form) as described in this section. For this, we introduce arbitrary admissible weighting functions denoted by scalars functions θ and λ, vector functions $\boldsymbol{\omega}$ and $\boldsymbol{\omega}^s$, and a second order tensor function $\boldsymbol{\Lambda}$. Multiplying each governing equation (5.24), (5.25), (5.26), (5.27) and (5.28) with a corresponding weight function and integrating over their associated domain, we obtain five scalar equations as follows:

$$\int_{\Omega^s} \boldsymbol{\omega}^s \cdot (\nabla \cdot \mathbf{T}^s + \mathbf{t}_a) \; d\Omega^s = 0 \tag{5.29}$$

$$\int_{\Omega^c} \boldsymbol{\omega} \cdot [\nabla \cdot (\mathbf{T}^c + \mathbf{T}^p - p\mathbf{I}) - \mathbf{t}_a] \; d\Omega^c = 0 \tag{5.30}$$

$$\int_{\Omega^c} \theta \left[\; \alpha \; \nabla \cdot \mathbf{v} + \; \beta \; \dot{p} + \nabla \cdot \mathbf{J}^f + \nabla \cdot \mathbf{J}^m \right] \; d\Omega^c = 0 \tag{5.31}$$

$$\int_{\Omega^c} \lambda \left[\frac{D\phi^f}{Dt} + \phi^f \; \alpha \; \nabla \cdot \mathbf{v} + \phi^f \; \beta \; \dot{p} + \nabla \cdot \mathbf{J}^f \right] \; d\Omega^c = 0 \tag{5.32}$$

$$\int_{\Omega^c} \boldsymbol{\Lambda} : \left[\frac{D\boldsymbol{\Phi}^p}{Dt} + \boldsymbol{\Phi}^p \; \alpha \; \nabla \cdot \mathbf{v} + \boldsymbol{\Phi}^p \; \beta \; \dot{p} - \boldsymbol{\Pi}^p \right] \; d\Omega^c = 0 \tag{5.33}$$

Integrating by part and applying the divergence theorem, the weak form may be rewritten in the more convenient form:

$$\int_{\Omega^s} \nabla\boldsymbol{\omega}^s : \mathbf{T}^s \; d\Omega^s - \int_{\Omega^c} \boldsymbol{\omega}^s \cdot \mathbf{t}_a \; d\Omega^c = 0 \tag{5.34}$$

$$\int_{\Omega^c} \nabla\boldsymbol{\omega} : (\mathbf{T}^c + \mathbf{T}^p - p\mathbf{I}) \; d\Omega^c + \int_{\Omega^c} \boldsymbol{\omega} \cdot \mathbf{t}_a \; d\Omega^c + \int_{\Gamma^c} (\mathbf{P} \cdot \nabla\boldsymbol{\omega} \cdot \mathbf{P}) : \mathbf{T}_\sigma \; d\Gamma^c = 0 \tag{5.35}$$

$$\int_{\Omega^c} \theta \; (\; \alpha \; \nabla \cdot \mathbf{v} + \; \beta \; \dot{p}) \; d\Omega^c + \int_{\Omega^c} \nabla\theta \cdot \frac{\kappa}{\mu} \nabla p \; d\Omega^c +$$

$$\int_{\Omega^c} \nabla\theta \cdot \left(\frac{\phi^m}{\phi^f} \frac{\kappa}{\mu} \nabla p + D \; \nabla\phi^m - \frac{\phi^m}{\phi^f} D \; \nabla\phi^f \right) \; d\Omega^c = 0 \tag{5.36}$$

$$\int_{\Omega^c} \lambda \dot{\phi}^f \; d\Omega^c + \int_{\Omega^c} \lambda \phi^f \; (\; \alpha \; \nabla \cdot \mathbf{v} + \; \beta \; \dot{p}) \; d\Omega^c + \int_{\Omega^c} \nabla\lambda \cdot \frac{\kappa}{\mu} \nabla p \; d\Omega^c = 0 \tag{5.37}$$

$$\int_{\Omega^c} \boldsymbol{\Lambda} : \dot{\boldsymbol{\Phi}}^p \; d\Omega^c + \int_{\Omega^c} \boldsymbol{\Lambda} : \boldsymbol{\Phi}^p \, (\; \alpha \; \nabla \cdot \mathbf{v} + \; \beta \; \dot{p}) \; d\Omega^c -$$

$$\int_{\Omega^c} \boldsymbol{\Lambda} : \left[\frac{M^p}{M^m} \left(\frac{1}{2} k_0^f \mathbf{I} + k_1^f \mathbf{T}^p \right) \frac{\phi^m}{\phi^f} - k_0^d \boldsymbol{\Phi}^p \right] \; d\Omega^c = 0 \tag{5.38}$$

The above system of equation is then linearized in order to obtain a numerical solution using the modified Newton-Raphson iterative method. In a nutshell, a function f is linearized about its current value according to $f = \tilde{f} + \delta f$ where $\tilde{f}$ is the value of f obtained in last increment, and δf defines the partial change in f during the current time increment. The solution may then be obtained with an incremental methods whose details are given in Appendix C.

5.5 Levelset- XFEM formulation

5.5.1 Numerical strategy for cell-substrate interactions

From a numerical viewpoint, the cell-substrate interaction under plane stress assumptions involves two superposed domains Ω^s and Ω^c, of arbitrary shapes, on which different, but interacting fields must be computed (Fig. 5.1). To solve such a problem, two strategies may be adopted. The first would consist in introducing different discretizations for each domain, on which solutions would be computed separately but can interact through a numerical treatment of the interactions at cell-substrate adhesions. This option is limited by

the following drawbacks:

(1) Because different meshes are used for each domain, the integration of cell-substrate cohesive forces is evaluated differently on each domain. This may lead to numerical issues regarding convergence and accuracy.

(2) The integration of cell surface tension cannot be naturally accounted for.

(3) While not considered in this particular work, problems on cellular mechanics typically involve cell growth and spreading. In this context, a discretization that follows cell shape implies that cell growth is associated with remeshing techniques, known to be computationally intensive and gruesome.

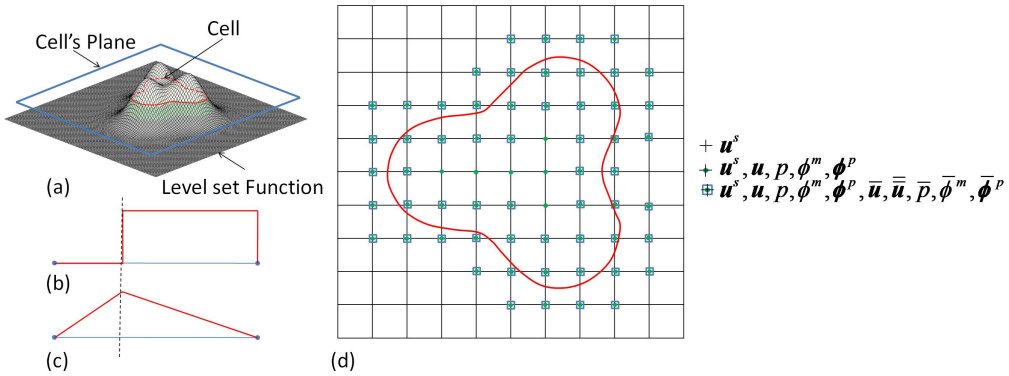

Figure 5.7: (a) Example of levelset function used to describe cell geometry, (b) Heavy side and (c) Ridge functions used to enrich the finite element interpolation. (d) Degrees of freedom associated with nodes in and outside of the cell. The enriched nodes are shown with blue squares.

For this reason, this chapter introduces a different formulation that only requires a single discretization, used for both cell and substrate. In this approach, while the substrate domain Ω^s is entirely contained in the computational domain, the cell domain Ω^c is defined in terms of a level-set function that defines the arbitrary contour of the cell. Referring to Fig. 5.7a, the levelset function $\phi(\mathbf{X})$ is a function of space (in the undeformed configuration)

that is represented by a two-dimensional surface in a three-dimensional space. The two-dimensional morphology of the cell is then defined as the intersection of this surface with the x-y plane of the cell (Fig. 5.7a). The function ϕ is chosen such that its sign is opposite in two sides of the cell boundary, which enables a clear definition concerning the location of material point P located at $\mathbf{X}$ with respect to the cell domain:

$$\text{if } \phi(\mathbf{X}) > 0, \quad P \in \Omega^c \tag{5.39}$$

$$\text{if } \phi(\mathbf{X}) = 0, \quad P \in \Gamma^c \tag{5.40}$$

$$\text{if } \phi(\mathbf{X}) < 0, \quad P \notin \Omega^c \tag{5.41}$$

In addition, the levelset function enables the definition of the unit vector $\mathbf{n}_0$ that is normal to the cell boundary Γ^c in its original configuration:

$$\mathbf{n}_0(\mathbf{X}) = \frac{\nabla_{\mathbf{X}}\phi(\mathbf{X})}{||\nabla_{\mathbf{X}}\phi(\mathbf{X})||} \tag{5.42}$$

where $\nabla_{\mathbf{X}}$ denotes the gradient with respect to the initial coordinate $\mathbf{X}$ and $||\cdot||$ denotes the L_2 norm. This strategy enables us to define arbitrary cell morphologies, independently from finite-element discretization. Furthermore, node located outside of the cell domain are only associated with substrate displacement $\mathbf{u}^s$ while nodes that are located in Ω^c are associated with degrees of freedom related to both substrate ($\mathbf{u}^s$) and cell ($\mathbf{u}$, p, ϕ^m, $\mathbf{\Phi}^p$). As discussed in the next section, this approach, when combined with the extended finite element method, has various advantages:

(1) Since the same numerical domain is used for both cell and substrate, there are no issues related to interaction terms (through cohesive forces) between the two domains.

(2) The integration of cell surface tension will naturally accounted for as demonstrated in [54, 166].

(3) The problem of cell growth and spreading can naturally be incorporated in the formulation by using level-set evolution equations [93, 136, 146, 147].

5.5.2 Multifield Extended Finite-Element formulation

The main issue with the aforementioned method is that continuum fields associated with the cell domain are typically discontinuous across the cell boundary Γ^c. For instance, a continuum field $\mathbf{f}$ associated with the cell domain (that can be $\mathbf{u}$, p, ϕ^m or $\mathbf{\Phi}^p$) is typically non-zero in Ω^c but vanishes outside Ω^c, therefore creating a jump in $\mathbf{f}$ across Γ^c. This generally pauses a problem with the standard finite-element method as shape functions are continuous within an element and yet, Γ^c exists within element domains (Fig. 5.7d). To circumvent this obstacle, the proposed approach uses the XFEM methodology [43, 79] for its strength in describing various types of discontinuities within element domains [105, 9, 7, 181, 54]. In this context (Fig. 5.7d), the elements cut by the levelset, and their nodes, are considered as enriched elements/nodes. To introduce discontinuities in a continuum field $\mathbf{f}$ (denoted as strong discontinuity) and its gradient (denoted as weak discontinuity) across the cell boundary, fictitious degrees of freedom $\bar{\mathbf{f}}$ and $\bar{\bar{\mathbf{f}}}$ are added to the enriched nodes such that a numerical approximation $\tilde{\mathbf{f}}$ of the function $\mathbf{f}$ can be introduced using conventional finite element shape functions as follows:

$$\tilde{\mathbf{f}}(\mathbf{x}) = \sum_{I=1}^{n} \mathbf{N}_I(\mathbf{x})\mathbf{f}_I + \sum_{J=1}^{m} \mathbf{N}_J(\mathbf{x})(H(\mathbf{x}) - H(\mathbf{x}_J))\bar{\mathbf{f}}_J + \sum_{J=1}^{m} \mathbf{N}_J(\mathbf{x})\left(\chi(\mathbf{x}) - \chi(\mathbf{x}_J)\right)\bar{\bar{\mathbf{f}}}_J \quad (5.43)$$

where $\mathbf{N}_I(\mathbf{x})$ are shape functions associated with node I. The matrix $\mathbf{N}_I$ has the form:

$$\mathbf{N}_I(\mathbf{x}) = \begin{bmatrix} N_I(\mathbf{x}) & 0 \\ 0 & N_I(\mathbf{x}) \end{bmatrix} \quad (5.44)$$

In (5.43), $\mathbf{N}_J(\mathbf{x})$ are ordinary shape functions of the enriched nodes, i.e. the nodes of the elements cut by levelset function while n and m give the total number of nodes and the number of enriched nodes per element, respectively. In addition, the Heaviside and ridge functions, denoted as $H(\mathbf{x})$ and $\chi(\mathbf{x})$ take the form:

$$H(\mathbf{X}) = \begin{cases} 1 & \phi(\mathbf{X}) > 0 \\ 0 & \phi(\mathbf{X}) < 0 \end{cases} \quad \text{and} \quad \chi(\mathbf{X}) = |\phi(\mathbf{X})| \quad (5.45)$$

The function $H(\mathbf{x})$ is used to introduce a jump in the fields $\dot{\mathbf{u}}^c, \dot{p}, \dot{\phi}^m$ and $\dot{\mathbf{\Phi}}^p$ across the cell's membrane, whereas the ridge function is used to define discontinuities in their spatial derivative [105, 106]. A one-dimensional representation of the Heaviside and ridge function is provided in Fig. 5.7b and 5.7c

5.5.3 Discretization and time integration

The linearized finite element equation is obtained by substituting the XFEM approximation (5.43) corresponding to each continuum field $\mathbf{u}^s, \mathbf{u}, p, \phi^m$, and $\mathbf{\Phi}^p$ into the linearized weak form equations (5.34-5.38). Note that the enrichement functions are only used for elements that are cut by the cell's interface Γ^c. In these elements, while all fields are enriched with a strong discontinuity, only the cell's displacement field $\mathbf{u}$ is enriched with the Ridge function (weak discontinuity). Indeed, the weakly discontinuous displacement field is only important to capture the jump in strain between the cell and its surrounding due to surface tension [163]. Furthermore, a mixed-element formulation is adopted, based on quadratic bilinear, four point, Lagrange interpolation functions to approximate cytosol pressure p, G-actin monomer volume fraction ϕ^m, F-actin SF volume fraction $\mathbf{\Phi}^p$ and nine point, Lagrange interpolation functions to approximate the displacement field $\mathbf{u}$. The nodal values of the continuum fields in element e are then given by a vector $\mathbf{U}^e$ as follows:

$$\mathbf{U}_I^e = \begin{bmatrix} \mathbf{u}_I^{s,e} & \mathbf{u}_I^e & \mathbf{p}_I^e & \boldsymbol{\phi}_I^{m,e} & \mathbf{\Phi}_I^{p,e} \end{bmatrix}^T \tag{5.46}$$

where I denotes the nodes number in the local element numbering scheme. In other words, $I = 1, ..., 4$ for four-node elements and $I = 1, ..., 9$ for nine-node elements. Finite element approximation in an element is then expressed in terms of these nodal values by (5.43). After substitution of the above approximation into the weak form equations, integration is performed numerically by using a nine-point quadrature rule for conventional elements while considering the following treatment for enriched elements. Since enriched element are cut into two domains by interface Γ^c a number of sub-triangles can be constructed on each

side of the interface. Element integration is thus decomposed into integration on each of these sub-triangles by using a thirteen points gauss rule for maximum accuracy. In addition, numerical integration along the cell's surface Γ^c is done using a one-dimensional three points Gauss rule. For more details of using sub-triangles and integration on surface, the reader is referred to [44, 54]. After a long but straightforward calculations for which the details are given in Appendix D, we find that final XFEM equation takes the following form:

$$\mathbf{C} \cdot \dot{\mathbf{U}} + \mathbf{K} \cdot \delta\mathbf{U} + \mathbf{F} = \mathbf{0} \tag{5.47}$$

where $\mathbf{U}$ denote the global displacement vector. Indeed, the global force vector, as well as the tangent and damping matrices, are assembled from their element counterparts as:

$$\mathbf{F} = \mathscr{A}_{e=1}^{nel}\mathbf{F}^e \qquad \mathbf{K} = \mathscr{A}_{e=1}^{nel}\mathbf{K}^e \quad \text{and} \quad \mathbf{C} = \mathscr{A}_{e=1}^{nel}\mathbf{C}^e. \tag{5.48}$$

Here, $\mathscr{A}$, e and nel denote the assembly operation, element number, and the number of elements; while the element force vector, damping and stiffness matrices are given by:

$$\mathbf{F} = \begin{bmatrix} \mathbf{F}^{u^s} \\ \mathbf{F}^u \\ \mathbf{F}^f \\ \mathbf{F}^m \\ \mathbf{F}^p \end{bmatrix} ; \mathbf{C} = \begin{bmatrix} 0 & 0 & 0 & 0 & 0 \\ 0 & \mathbf{C}^{uu} & 0 & 0 & 0 \\ 0 & \mathbf{C}^{fu} & \mathbf{C}^{ff} & 0 & 0 \\ 0 & \mathbf{C}^{mu} & \mathbf{C}^{mf} & \mathbf{C}^{mm} & \mathbf{C}^{mp} \\ 0 & \mathbf{C}^{pu} & \mathbf{C}^{pf} & 0 & \mathbf{C}^{pp} \end{bmatrix} ; \mathbf{K} = \begin{bmatrix} \mathbf{K}^{ss} & \mathbf{K}^{su} & 0 & 0 & 0 \\ \mathbf{K}^{us} & \mathbf{K}^{uu} & \mathbf{K}^{uf} & 0 & \mathbf{K}^{up} \\ 0 & \mathbf{K}^{fu} & \mathbf{K}^{ff} & \mathbf{K}^{fm} & \mathbf{K}^{fp} \\ 0 & 0 & \mathbf{K}^{mf} & 0 & 0 \\ 0 & \mathbf{K}^{pu} & \mathbf{K}^{pf} & \mathbf{K}^{pm} & \mathbf{K}^{pp} \end{bmatrix} \tag{5.49}$$

A precise form of the components appearing in above equations are given in Appendix E. Equation (5.47) is solved using a nonlinear, updated Lagrangian formulation [10] following the algorithm presented in Fig 5.8. Furthermore, time integration is performed using a backwards Euler integration scheme that approximates a field at a given time step based on the approximate derivative at the next time step. This is written as follows:

$$\delta\mathbf{U} = \delta\dot{\mathbf{U}} \cdot \Delta t \tag{5.50}$$

where Δt denote the time increment. Due to the inherent nonlinearity of the contraction problem, the solution for $\dot{\mathbf{U}}(t+\Delta t)$ is solved for iteratively at time increment $t+\Delta t$. The value $\dot{\mathbf{U}}^i(t+\Delta t)$ at the i^{th} iteration is calculated by:

$$\dot{\mathbf{U}}^i(t+\Delta t) = \dot{\mathbf{U}}^{i-1}(t+\Delta t) + \delta\dot{\mathbf{U}}^i \tag{5.51}$$

substituting equations (5.50) and (5.51) into equation (5.47), the iterative rate vector $\delta\dot{\mathbf{U}}^i$ is computed as:

$$\left(\mathbf{C}^{i-1}_{t+\Delta t} + \Delta t.\mathbf{K}^{i-1}_{t+\Delta t}\right).\delta\dot{\mathbf{U}}^i = -\left(\mathbf{F}^{i-1}_{t+\Delta t} + \mathbf{C}^{i-1}_{t+\Delta t}\cdot\dot{\mathbf{U}}^{i-1}_{t+\Delta t}\right) \equiv \mathbf{H}^{i-1}_{t+\Delta t} \tag{5.52}$$

where the notation $\mathbf{H}$ is used for residual vector. Iterations are then repeated until the norm of the partial rate vector $|\delta\mathbf{U}^i| < tol$ where tol is a small tolerance.

- Define the total time t_{tot} and the time step Δt.
- Initialize the unknowns
- Start time steps (t)
  - Start nonlinear iterative loop (i)
    - Start loop on gauss points for each element (e)
      - Update gauss point values such as stress and strain
      - Calculate $\mathbf{K}^{i-1,e}_{t+\Delta t}$, $\mathbf{C}^{i-1,e}_{t+\Delta t}$, *and* $\mathbf{F}^{i-1,e}_{t+\Delta t}$ for each element
    - End gauss point and element loop
    - Assembly of $\mathbf{K}^{i-1,e}_{t+\Delta t}$, $\mathbf{C}^{i-1,e}_{t+\Delta t}$, *and* $\mathbf{F}^{i-1,e}_{t+\Delta t}$
    - Apply boundary conditions
    - Solve for $\delta\dot{\mathbf{U}}$: $\left(\mathbf{C}^{i-1}_{t+\Delta t} + \Delta t.\mathbf{K}^{i-1}_{t+\Delta t}\right).\delta\dot{\mathbf{U}}^i = -\left(\mathbf{F}^{i-1}_{t+\Delta t} + \mathbf{C}^{i-1}_{t+\Delta t}\cdot\dot{\mathbf{U}}^{i-1}_{t+\Delta t}\right)$
    - Update the unknowns: $\dot{\mathbf{U}}^i_{t+\Delta t} = \dot{\mathbf{U}}^{i-1}_{t+\Delta t} + \delta\dot{\mathbf{U}}^i$ and $\mathbf{U}^i_{t+\Delta t} = \mathbf{U}^i_t + \Delta t\cdot\dot{\mathbf{U}}^i_{t+\Delta t}$
  - End nonlinear iterative loop if norm$\left(\delta\dot{\mathbf{U}}^i\right) <$ tol
  - Update nodal coordinates of mesh
  - Update the cell's surface shape
- End time steps

Figure 5.8: The nonlinear updated Lagrangian algorithm used to solve Eq. (5.52).

5.6 Numerical investigation of cell contraction on elastic substrates

The proposed numerical approach is now assessed in several ways. First, we consider the case of an originally square-shaped cell, attached to its underlying substrate through

focal adhesion at its corners. The numerical behavior of the system, as well as convergence studies are presented. We then build upon this analysis to investigate the contractile behavior and structural evolution of cells sitting on substrate with varying elasticity and compare our predictions to experimental observations. Furthermore, taking advantage of the levelset formulation, we investigate the effect of cell morphology on its structural organization as well as on the deformation of the substrate. Finally, we assess the role of the cortical membrane stiffness on SF formation and substrate stresses. The presented simulations are obtained by using a set of physiologically relevant parameters that are characteristic of fibroblasts (Table 5.1).

Definition	Symbol	Value	unit	Reference
Cytosol volume fraction	ϕ^c	70	%	[2]
Cytoskeleton volume fraction	ϕ^s	25	%	n/a
F+G actin volume fraction	$\phi^m + \phi^p$	5	%	n/a
Rate of SF formation	k_0^f	0.0001	sec^{-1}	[130]
Mechano-sensitive rate of SF formation	k_1^f	0.05	sec^{-1}	[130]
Rate of SF dissociation	k_0^d	0.1	sec^{-1}	[130]
Cytoskeleton permeability	κ/μ	$1 \cdot 10^{-15}$	$m^4/N \cdot sec$	[69]
G-actin diffusion constant	D	$1 \cdot 10^{-5}$	m^2/sec	[130]
Young's modulus	E	70	Pa	[37]
Poisson's ratio	ν	0.3		[37]
Fiber maximum tensile stress	$\bar{T}$	20000	Pa	[175, 94, 156]
Reference strain rate (Eq. (5.18))	$\dot{\varepsilon}_0$	0.01	sec^{-1}	[37]
Reference active strain (Eq. (5.19))	ε_0	0.1		[22]
Reference passive strain (Eq. (5.19))	ε_1	0.15		[22]
F/G molar mass ratio	M^p/M^m	100		n/a
F/G true density ratio	ρ_R^p/ρ_R^m	1		n/a
Integrin density	η_l	1000	m^{-2}	n/a
Single adhesion complex stiffness	K_{li}	10^7	N/m	n/a

Table 5.1: Parameters used in the simulations.

5.6.1 Convergence analysis

In this section, we propose to assess the convergence of the solution method by considering the particular problem of the evolution of a square cell interacting with an elastic substrate through adhesion regions located near its four corners (Fig. 5.11a). For all analyses, the Young's modulus of the substrate is chosen to be $E^s = 100\ Pa$ and initial conditions are such that no SFs are present in the cell at time $t = 0$ (i.e., actin is present in its monomer form only). Convergence is then evaluated at steady state (when both chemical and mechanical equilibrium are reached) with respect to mesh size and Newton iteration number at fixed time steps.

Convergence with respect to mesh size is first evaluated by studying the change in the magnitude of a relevant global quantity G with increasing element number. Here, we choose G as the average SF volume fraction at steady state:

$$G = \frac{1}{A_0^c} \int_{\Omega^c} trace(\mathbf{\Phi}^p \left(\mathbf{X}, t^f\right)) \, d\Omega^c, \tag{5.53}$$

where A_0^c and t^f are initial cell's area and the time at which the system has reached its steady state solution, respectively. Furthermore, we introduce G_k as the value of G numerically obtained $k \times k$ square finite elements. As expected, the quantity G_k converges to a fixed point $G = 0.415\%$ as k increases (Fig. 5.9). The rate of convergence can be assessed by considering the formula:

$$|G_k - G| \leq Ck^{-q} \tag{5.54}$$

where C is chosen a constant value, and q is a positive integer that gives the rate of convergence with respect to spatial discretization. Fig. 5.9b shows that for any element number, the numerical error $E = |G_k - G|$ remains below the curve represented by Ck^{-q} with $q = 2$ (quadratic convergence). In view of this result, the simulations presented in the remainder of the chapter are based on a mesh of 20×20 elements (in the cell domain); this choice gave us an optimal combination of accuracy and numerical efficiency. We also investigated the

convergence of the presented numerical scheme in term of iteration number by plotting the norm of the residual vector $\mathbf{H}^i$ (defined in Eq. (5.52)) in terms of the iteration number i for fixed term increment. As depicted in Fig. 5.10, we observed a linear convergence rate, i.e. the rate of convergence $\mu = 0.615 < 1$ is obtained using equation

$$\lim_{i\to\infty} \frac{|\mathbf{H}^i|}{|\mathbf{H}^{i-1}|^q} = \mu \tag{5.55}$$

for $q = 1$ (linear convergence) [132].

5.6.2 Effect of cell morphology on SF development

As noted above, one main advantage of using the XFEM- levelset method relies in that cell geometry can be defined independently from discretization. In this example, we take advantage of this capability to investigate the SF evolution in four cells, characterized by different geometries (square, rectangle, triangle, and diamond) and substrate adhesion (Fig. 5.11a-d) on an elastic substrate whose elastic modulus is $100Pa$. While initial conditions are similar as in the previous section, we applied periodic boundary conditions on the substrate domain in order to simulate an infinitely large domain with a periodic cell's structure. Figs. 5.11(e-h) show the first stress invariant in the substrates due to cell contraction at steady state. These results clearly show that compressive state of stress beneath the cell and the tensile stress between cells (neighboring cells are represented by periodic boundary conditions). The importance of this formulation is clear as it is able to represent the interactions between cells of arbitrary shapes (information that can be obtained from imaging) and elastic substrates. Furthermore, SF distribution at steady state was obtained for each cell morphology (Fig. 5.11l-n) and compared with experimental observations for similar conditions (Fig. 5.11i-k) ([18, 117, 61, 19]). Here, our result show that SF are preferably generated in directions of maximum apparent stiffness, corresponding to lines connecting adhesion islands. This can be explained as follows. In directions of maximum stiffness, the

constraints on tensile deformation result in a decreased strain rate, which, according to the Hill model, results in optimal contraction (Fig. 5.5). Since SF formation increases with contraction (Eq. (5.17)), this explains the high density of SFs along direction of high apparent stiffness. This type of simulations is critical to interpret a variety of experimental procedures that can measure mechanical forces and deformation with arrays of micropillars or elastic gels in which fluorescent beads are embedded [51, 94, 145].

5.6.3 Effect of substrate's stiffness on cell contraction and deformation

Experimental studies have shown that cell contractility and SF structure are strongly influenced by the stiffness of the underlying matrix. Here, we propose to assess how the proposed model captures these effects and compare model predictions with experimental studies of fibroblasts contracting on micro-pillars. For this we consider the square cell shown in Fig. 5.11a adhering to a substrate of varying stiffness through focal adhesions located at its corners. Similarly to previous examples, initial conditions are such that no SFs are present at $t = 0$ and the substrate is subjected to periodic boundary conditions. To assess the magnitude of cell contraction, we computed the normalized average tensile force in focal adhesions $F/(\bar{T}\ d^2)$ when the steady state was reached (Here d is the typical dimension of the cell). This quantity was computed for values of normalized substrate's stiffness E^s/E^c ranging from 0 to 300 which led to the nonlinear contraction-stiffness relationship depicted in Fig. 5.12. The result of Fig. 5.12 can generally be explained by the fact that increasing substrate stiffness tends to decrease the strain rates undergone by SF and thus increase contraction (according to Hill's model). This increased contraction subsequently promotes more SF formation, which leads to a rise in SF density and contractility. The time evolution of contraction is also shown in the box of Fig. 5.12 in terms of the normalized time $t^\star = t\dot{\varepsilon}_0$ for the case $E^s = 1000\ Pa$. A relevant question in biology is to understand how the mechanical work performed by cells is affected by the stiffness of the substrate they lie on. Here, we assess the average mechanical work of a cell as $W = Fd$ where F is the average force it

applies to its focal adhesion and d is the resulting average displacement. Fig. 5.13 shows the changes of work W as the relative substrate's stiffness varies from 0 to 1000. The figure clearly displays that no work is done for small and large values of substrate stiffness; indeed small stiffness results in no contraction (Fig. 5.12) while large stiffness precludes substrate deformation. A consequence is that there exists an optimal substrate stiffness for which the work done by cells is maximum (with our parameters, this optimum occurs in the range of $10E_c < E_s < 50E_c$), a phenomenon that has been observed experimentally for cardiomyocytes by Engler et al. [51]. This result therefore illustrate why such simulation can be essential for the choice of artificial gels with optimal mechanical properties in the context of tissue engineering.

5.6.4 Effect of cortical stiffness on cell contractility

In the last example, we propose to investigate the influence of cortical stiffness on the evolution of SF and cell contractility [14, 163]. We concentrated on the particular case of a square cell lying on substrate whose stiffness is $E_s = 1000E_c$. The geometry and numerical discretization for this problem are displayed in the previous example. The normalized cortex stiffness $K_s/(\bar{T}d)$ is then varied from 0 to 1000 and the steady-state SF distribution is evaluated for various cases.

As discussed in [14] and [163], the existence of a stiff cortical layer around a cell tends to homogenize membrane curvature.This effect is nicely captured by the graph of Fig. 5.14 that shows the decreasing average cortex curvature ($\kappa \cdot d$) with increasing cortical stiffness. The effect of cortical stiffness on SF generation was also significant. Indeed, Fig. 5.14 shows that SF tend to increasingly align in parallel with the cortex as cortical stiffness increases. The reason is clear: increasing cortical stiffness results in rising stiffness in directions that are tangential to the cell membrane. As the model predicts SF formation in directions of maximum stiffness, more SF are generated near and in parallel to the membrane. These results have been confirmed by previous study ([15]) showing that the existence of a

constrained boundary leads to generation of SF along the boundary.

5.7 Summary and Concluding remarks

In summary, this chapter presented a numerical approach to study the behavior of contractile cells and their interactions with a two-dimensional elastic substrate. The continuum model of cell contraction is based on a constrained mixture formulation [165] that describes the contractile apparatus of cells in terms of four major constituents, namely cytoskeleton, cytosol, G-actin monomers and F-actin (or SF) polymers. This framework enables us to characterize important processes of cell contraction such as SF formation (mass exchange between actin monomers and SF), actin diffusion and convection as well as the evolution of a anisotropic contractile network in time. Biologically, the model rests on two key assumptions: (a) SF contraction increases with decreasing strain rate (Hill's model) and (b) SF formation is promoted by contraction. The interactions of cells with their underlying substrate were then considered through focal adhesions, modeled here by an elastic cohesive law between the two continua.

The main contribution of this work was the introduction of an XFEM/level set method to accurately and efficiently model the interactions between cells of arbitrary shapes and an underlying deformable substrate. The key feature of the proposed method are as follows:

- Despite being represented by two distinct domains, cell and substrate are discretized by a single, regular finite-element mesh. The (possibly complex) cell geometry is then defined in terms of an analytical function (the level-set function) that is independent of discretization. This feature has the merit of greatly simplifying the numerical issues associated with meshing complex geometries and handling interactions between bodies discretized by distinct meshes.

- The stiffness of the thin cortical layer surrounding cells can naturally be accounted for by incorporating surface elasticity on the cell boundary. This feature is possible

by enriching the XFEM shape functions with weak discontinuity functions, that enable a jump in stress across the cell membrane.

- Since cell geometry is independent of discretization, the method can be extended to describe cell growth, migration and spreading without resorting to remeshing techniques, known to be computationally expensive. Instead, more efficient techniques involving level-set evolution equations can be invoked. This will be the object of future studies.

The performance of the method was then assessed by considering biologically relevant problems of cell-substrate interactions. Generally, our results showed that the proposed numerical method, together with the constrained mixture formulation, led to realistic behaviors that correlated very well with experimental observations. The coupling of XFEM and the levelset method therefore provides a promising route to study a variety of biological problems involving cell-substrate interactions, such as morphogenesis, tissue engineering, cell spreading and migration as well as wound contraction.

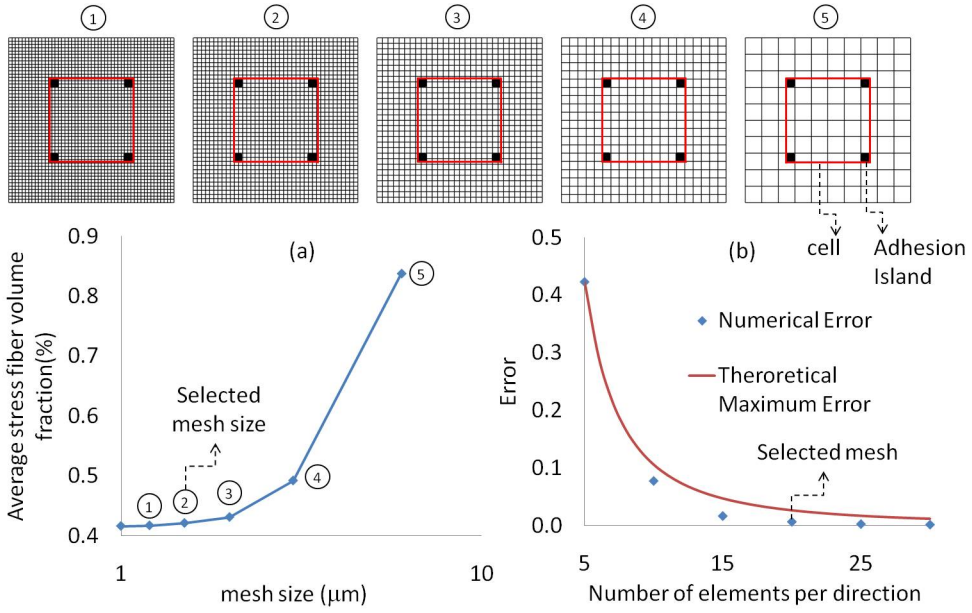

Figure 5.9: a) Discretization convergence of the numerical solution to estimate average SF volume fraction in cell by changing mesh size. b) Proof of quadratic convergence of the discretization according to Eq. 5.54.

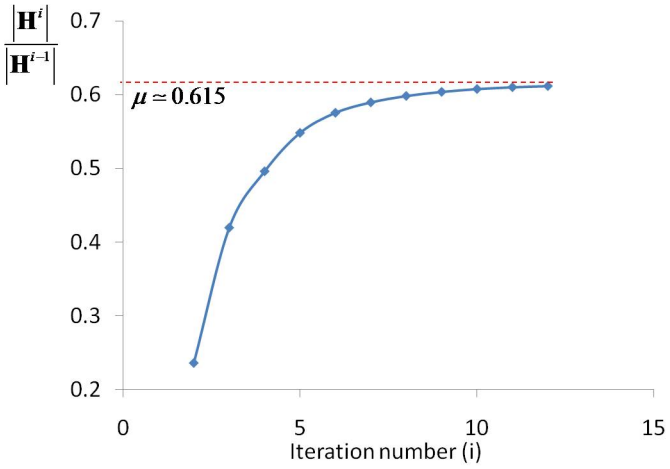

Figure 5.10: Linear convergence of the nonlinear solution method

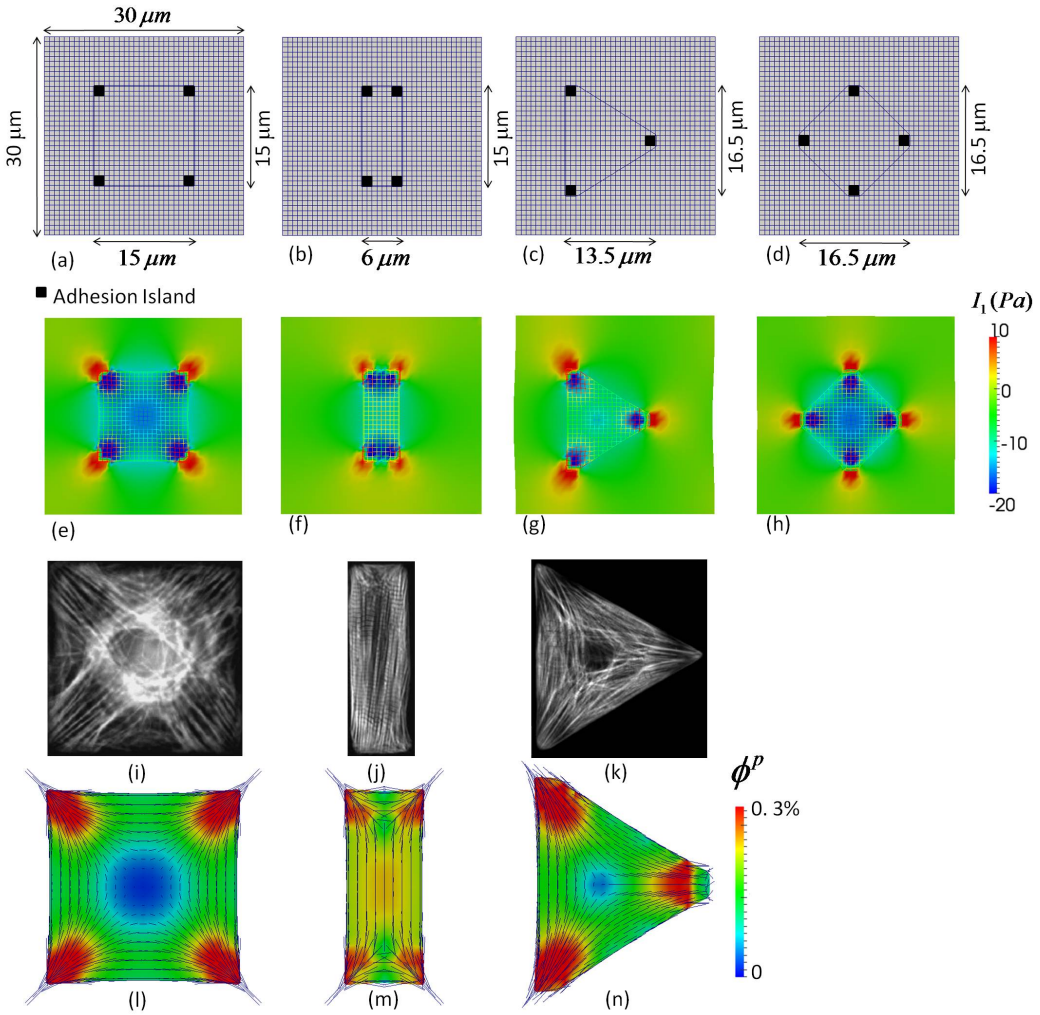

Figure 5.11: a-d) Initial configurations of cells with different shapes on substrate. The dimensions of the adhesion island are $1.5\mu m \times 1.5\mu m$ for all cases. e-h) Deformed configuration of the cells together with the first invariant of the stress in the substrate. i-k) Experimental results of SF formation in myocites ([18, 117, 61, 19]). l-n) Deformed configuration cells with different shapes together with their stress fiber orientation in steady state to be compared with the experiments depicted in parts i-k.

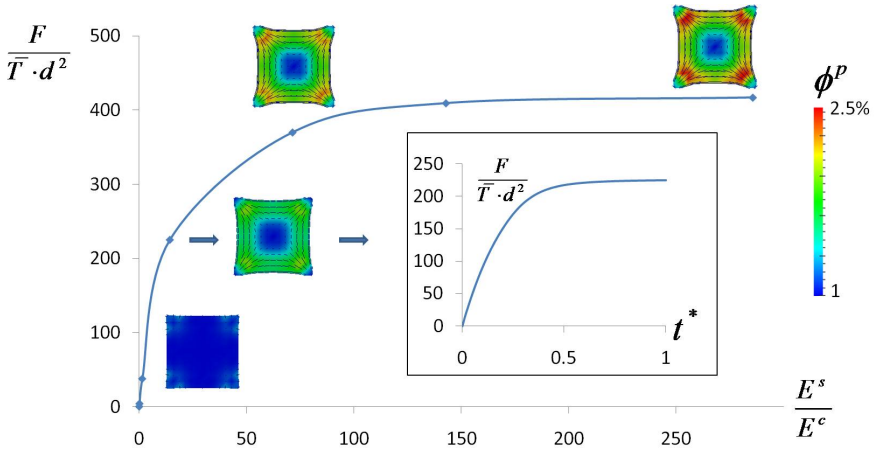

Figure 5.12: Changes of the normalized force applied to the substrate by the cell in an adhesion island as a function of normalized substrate's stiffness and normalized time, together with the volume fraction and orientation of SFs generated in the cell.

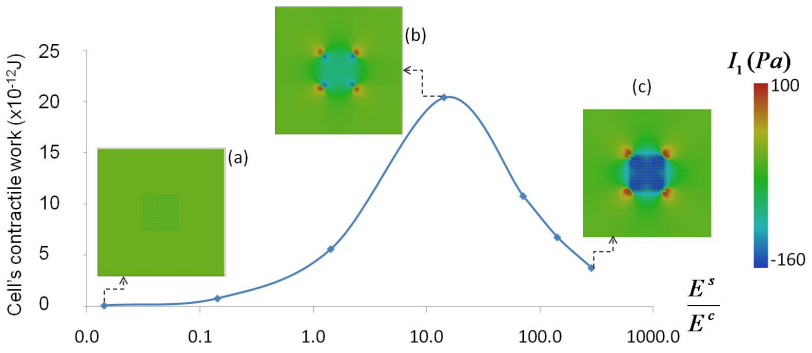

Figure 5.13: The changes of the work done by focal adhesion force on the cell with substrate's stiffness; and the substrate's first invariant of stress tensor I_1 for different substrates young's modulus: a) $E^s = 1\ Pa$, b) $E^s = 1000\ Pa$, c) $E^s = 20000\ Pa$.

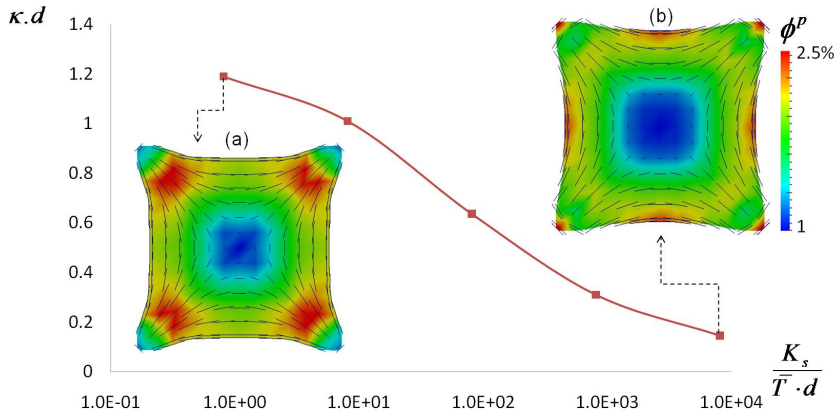

Figure 5.14: The effect of cortex stiffness on its curvature and SFs formation. a) $E_\sigma = 0$, b)$E_\sigma = 100N/m$.

Chapter 6

A mathematical model to characterize the chemical mechanical interactions in cells and their effect on spreading and contraction

6.1 Abstract

Recent research have shown that cell spreading is highly dependent on the contractile behavior of the cell and mechanical properties of the environment it is located in. The dynamics of such process is critical for the development of tissue engineering strategy but is also a key player in wound contraction, tissue maintenance and angiogenesis. To better understand the underlying physics of such phenomena, this presentation describes a mathematical formulation of cell spreading and contraction that couples the processes of stress fiber formation, protrusion growth through actin polymerization at the cell edge and dynamics of cross-membrane protein (integrins) enabling cell-substrate attachment. The model is based on mixture model which accurately capture the interactions and mass exchange between three constituents, namely, the cell's cytoskeleton, actin monomers and stress fibers. On the one hand, monomers are allowed to polymerize into stress fiber to generate contraction while on the other hand, they may polymerize into an actin meshwork at the cell's boundary to push the membrane forward. In addition, a mechano-sensitive model of the diffusion and attachment integrins to the substrate permit to quantify the physics of the above processes in terms of substrate mechanical properties. A numerical solution of this moving boundary problem is then derived using the extended finite element method, combined with a levelset formulation. Consistent with experimental observations, our model is able to capture

the dependency of cell spreading area and contraction on substrate stiffness and the cell's mechanical environment.

6.2 Introduction

The contractile behavior of cell and cell spreading depend highly on the chemo-mechanical properties of cell constituents [55, 148, 114], focal adhesion complexes [96, 36], and substrate they adhere to [180, 121, 65, 26]. Different range of substrate stiffness or ligand (adhesion proteins on substrate surface) concentration leads to different stress fiber concentration/orientation in cell [170], as well as different cell area after spreading [129, 138]. The better understanding of the process during which cell spreading and contraction happens helps us to find out more details about what happens in natural phenomena such as wound contraction, tissue maintenance and angiogenesis [4, 15, 133].

During spreading, cell extends a branched network of actin filaments on the border of cell called lamellipodia [30, 64, 115, 124]. Lamellipodia is typically 0.5 μm thick and 1-10 μm long from front to back [30]. Lamellipodia protrusion depends on actin polymerization that depends on signals received according to the cell's environment mechanical properties [31, 126]. The polymerization of actin fibers leads to the generation of physical force beneath the plasma membrane that pushes it forward [32, 40, 115, 124]. Also, some research show that in spreading/migrating cells, there are periodic contractions of lamellipodia that depend on cell's environment properties. The period of contraction depends on F-actin movement along lamellipodia. They proved that cofilin decreases the period and shortens lamellipodia width [63]. In contrast with the pushing force, the resistance of membrane as an elastic material, and the instantly backward movement of the generated fiber network (called retrograde flow), prevents cell spreading [159, 167, 177]. Retrograde flow may be the result of contractile force that comes from myosin motors [137, 89]. At the end of spreading, cell optimizes its surface by enhancing the adhesion to the substrate on the edges of the cell, and by the contraction of polymerized stress fibers in the body of the cell.

Focal adhesions provide a mechanical attachment between cell membrane and substrate (or extracellular matrix). These adhesion complexes are multi protein links generated as the result of mechanosensing (feeling substrate mechanical properties by cell and responding to them [15]). The cell part of focal adhesions (Fig. 6.2) includes on-membrane proteins called integrins, and a submembrane plaque consists of a lot of proteins such as talin, α-actinin, filamin, FA kinase, vinculin, paxillin, and tensin [36]. Some of these proteins provide the mechanical requirements for the adhesion beneath the membrane, while some others receive or send signals to form or dissociate the adhesion [36]. It has been observed in previous research that the formation of FAs is a function of the traction generated in the cell-substrate contact area, such that, the traction increases the concentration of adhesion complexes [151, 123, 11, 182, 112, 111]. Also, it has been proved that the mentioned traction changes by the shape of cell and the cytoskeleton's structure [116, 20, 23]. On the substrate side of focal adhesions, the mechanical properties of substrate and the density of ligands are important factors determining the formation of FAs and their concentration [138, 99]. Previous observations proved that greater substrate stiffness and higher ligand concentration on its surface lead to increase in formation of FAs [129, 138].

As we discussed above, both cell growth and focal adhesion formation depend strongly on contractile behavior of the cell, thus stress fibers play the most important role in contractile behavior of the cell [55, 148, 114]. These fibers are the result of grouping filament bundles that are generated by G-actin monomer polymerization. Under specific situations, stress fibers may depolymerize to convert back to G-actin monomers [165]. Polymerization and depolymerization of G-actins and stress fibers, as well as stress fiber orientation, depend on the mechanical properties of the environment they are located in [180, 121, 65, 26]. For example, more stress fibers are formed on stiff substrates because of the higher force generated in focal adhesion complexes in this case. They also orient parallel to free boundaries and perpendicular to constraint boundaries of cell or substrate (if the cell is close enough to substrate boundary) [55, 148].

There are some mechanical models for cell contraction/spreading in two forms of fibrous network models [107, 14] and continuum models [110, 166]. Fibrous network models were the first models that studied the effect of cortical membrane tension on cell deformation [14]. On the other hand, continuum models seem much better because of their flexibility in considering the role of chemo-mechanical reactions in the process of cell contraction [37, 39]. Some of the continuum models are based on mixture theory to take into account the interactions between several cell constituents such as G-actin and stress fibers mass exchange, and G-actin flux in the cell [165]. Furthermore, because of the importance of focal adhesions in the process of cell contraction and spreading, a lot of research has been done on defining and modeling cohesive laws between cell and substrate surfaces in finite element frameworks [103, 125, 178, 176]. These models are not able to consider chemo-mechanical interactions happen on cell membrane and substrate surface to generate adhesion complexes. To fill this gap, the authors of reference [36] presented a mechanism based on integrins chemo-mechanical free energy equilibrium on cell membrane to describe what happens during integrin-ligand complex formation. But their research does not consider the vital effect of pushing and resisting forces during cell spreading as well as the effects of considering cell as a mixture. Furthermore, some models were presented to describe the rate of cell or fillopodia growth based on the fact that polymerization of new actin filaments beneath the membrane is the fundamental phenomenon leads to cell/fillopodia spreading [122, 93]. In another recent approach, the authors of reference [83] integrated in their model the kinematics of fish epidermal keratocyte growth and kinetics of the proteins that play important role in extension/detachment steps of cell crawling/spreading. But membrane forces and chemo-mechanical interactions on cell membrane between integrins cannot be captured in this model.

To fill the gaps mentioned above, in this chapter we present a single mathematical model for cell contraction and growth based on chemical and mechanical interactions in cell such that it accounts for the effect of all following phenomena:

(1) A mixture model for cell contractile behavior is developed based on the mass exchange and chemo-mechanical reactions between main constituents as well as G-actin and cytosol flux in the cell. For this purpose, the equilibrium state corresponding to free energy of G-actin and stress fiber controls polymerization and depolymerization of fibers in according to [56]. In addition, a similar strategy is followed to consider mass exchange between G-actin and cytoskeleton as a fibrous network.

(2) Instead of modeling focal adhesions by elastic springs in predefined areas, our model includes integrins in cell membrane and ligands on substrate to capture focal adhesions (integrin-ligand complexes) formation during the process discussed above [96].

(3) A growth model is presented to investigate the rate of cell spreading at the growing border of cell as well as cell area at steady state. In the proposed model, cell grows on its boundary by formation of new cytoskeleton based on the important criteria mentioned in literature such as G-actin and cytoskeleton volume fraction at the cell's boundary, cell membrane forces, cell contractile behavior, substrate properties, and focal adhesion formation.

(4) The existing numerical approaches (such as [103, 125, 178, 176]) use two different mesh for cell and substrate, and connect them by contact meshes that are needed to be very fine to provide enough accuracy in addition to all numerical issues accompanied with interactions between two different domains. Thus, we introduce a numerical approach based on extended finite element (XFEM) and levelset method [43, 105, 9], to provide the following features:

- The same mesh is used for cell and substrate to avoid the difficulties of dealing with two different mesh interaction.
- Cell border is defined as the intersection of a 2D curve, called levelset function,

and cell 1D domain (Fig. 6.4a), as a result, we do not have to change the mesh during cell evolution to define cell's border.

- Cell surface tension is naturally taken into account using XFEM/levelset features [163].

The outlook of the proposed work is as follows: first we present the mathematical details for our model of contractile behavior of the cell, cell spreading, and integrin-ligand focal adhesion formation on an elastic substrate in plane stress axisymmetric condition. This section ends with a summary of force, mass, and chemo-mechanical equations corresponding to cell-substrate interactions via focal adhesion during cell contraction and spreading. Then, a numerical method based on XFEM/levelset is introduced to solve the governed nonlinear equations during time. This section is followed by several numerical simulations to verify the agreement of the proposed framework with experiments done previously by other researchers. Finally the chapter finishes by presenting a summary of results and concluding remarks.

6.3 Mathematical model of cell contraction/growth

Contractile behavior of cell together with focal adhesion formation play important role in cell spreading . Although a lot of materials and factors affect cell contraction and spreading, in this chapter we simplify the cell by limiting its constituents to only important ones, while trying to mimic contraction and spreading of cell on elastic substrate. In the proposed framework, both cell and substrate behavior is approached under plane stress and axisymmetric conditions (for simplicity, while it does not affect the results). In this approach, as explained in details in [165, 53], the constituents of cell's body include: cytoskeleton (the major solid phase formed of a randomly oriented fibrous network), cytosol (fluid phase), stress fibers (contractile constituents), and G-actin monomers (monomers of stress fibers and cytoskeleton that exchange mass with them under specific circumstances) (Fig. 6.1). Stress fibers are the result of grouping filaments which are the result of G-actin polymerization

in locations and directions of cell body with constraints against displacement [165]. Stress fibers are part of cell's body solid phase and can not move relatively to cytoskeleton. On the other hand, G-actin monomers can flux with/through the fluid phase, cytosol.

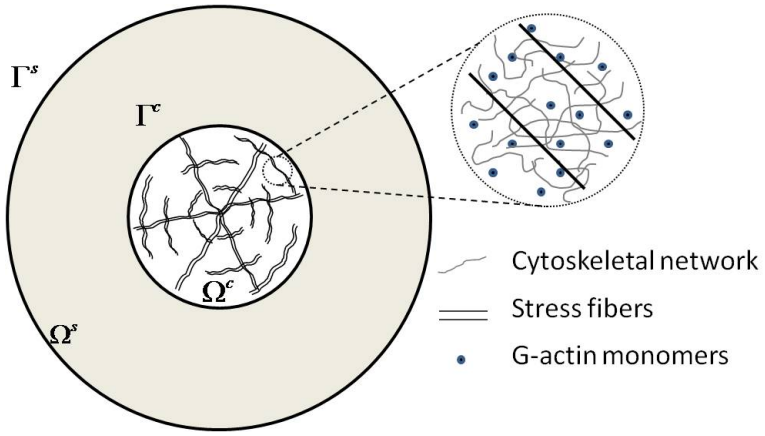

Figure 6.1: General configuration of an axisymmetric cell located on an elastic substrate, and cell's main constituents

Furthermore, all cell's body constituents are confined with cell membrane that plays two important roles in our model. First, because of its surface tension and elasticity, cell membrane resists cell growth [122]. On the other hand, it contains important proteins (known as integrins) in its cytoplasm playing basic role in focal adhesion complex formation [96]. Integrins are found in two active (or straight, or high affinity) and inactive (or bent, or low affinity) states as depicted in Fig. 6.2. While these two kinds of integrins can convert to each other as the result of a chemical reaction, only high affinity integrins are able to bound some proteins on substrate, called ligands, to form focal adhesion [96, 36]. As explained in details in the following, there is close dependency between contractile behavior of cell and formation of high-affinity integrins and focal adhesions. high-affinity integrins are attached to cytoskeleton, and thus, cannot migrate in membrane. But low-affinity integrins are free and migrate through the membrane cytoplasm fluid [36].

In the following parts of this section, the mathematical equations associated with momentum balance of cell mixture and substrate, mass balance of constituents, and equilibrium

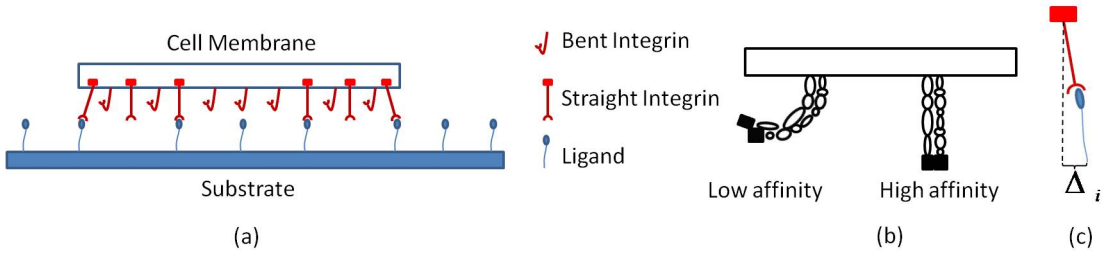

Figure 6.2: Integrin-ligand complexes: a) Ligands, low affinity integrins, and bound/unbound high-affinity integrins, b) Integrin states, c) relative displacement between two sides of integrin-ligand complex.

between the mass exchanging constituents are governed to finally, using the obtained equations, we can calculate the unknowns of our problem that are continuum fields substrate radial displacement u^s, cytoskeleton radial displacement u^c, cytosol pure pressure p (associated with its volume fraction ϕ^f), cytoskeleton volume fraction ϕ^c, G-actin monomer volume fraction ϕ^m, radial stress fiber volume fraction ϕ_r^{SF}, circumferential stress fiber volume fraction ϕ_θ^{SF}, low-affinity integrin concentration (number per unit membrane area) c^L and high-affinity integrin concentration (number per unit membrane area) c^H. It is assumed that the cell is saturated by its constituents such that $\phi^c + \phi^f + \phi^m + \phi_r^{SF} + \phi_\theta^{SF} = 1$. In the proposed formulation, there are some changes/modifications compared to our previous contractile model [165, 53]:

- Mass exchange is considered between cytoskeleton and G-actin monomer in addition to stress fibers and G-actin monomer.
- The rate of polymerization/depolymerization of G-actin monomers, stress fibers, and cytoskeleton is very fast in comparison with other time dependent procedures in the cell such as G-actin migration. Consequently, instead of polymerization/depolimerization rate equation, the balance of free energy of constituents at equilibrium is governed.
- In spite of previous work, focal adhesions are not considered as predefined areas of springs, instead, formation of integrin-ligand adhesion complexes is proposed.

6.3.1 Mass balance

As mentioned above, solid phases of cell body can exchange mass with G-actin monomers. In addition G-actin monomers and low-affinity integrins are able to migrate in cytosol and membrane fluid, respectively. High-affinity integrins can also exchange mass with low-affinity integrins. During contraction, total mass of cell body and membrane constituents, including cytoskeleton c, cytosol f, G-actin monomer m, radial stress fiber r, circumferential stress fiber θ, low-affinity integrin L, and high-affinity integrin H, is conserved.

Cell body (G-actin monomers, stress fibers, and cytoskeleton)- Using material time derivative of mass for each constituent($\frac{Dm}{Dt}$, time derivative of mass following the solid phase), the general form of mass balance equation in the body of cell is written as bellow for constituent α [165]:

$$\frac{D\rho^{\alpha}}{Dt} + \nabla \cdot (\rho^{\alpha} v^{\alpha}) = \rho^{\alpha} \Pi^{\alpha} \qquad in\ \Omega^{c} \qquad \alpha = c, SF, m, f \tag{6.1}$$

where ρ^{α}, v^{α}, and $\rho^{\alpha}\Pi^{\alpha}$ denote mass per total volume, velocity, and rate of mass formation per total volume for each constituent α, respectively. Indeed, the operator "$\nabla\cdot$" is used to show the divergence field. The above equation is written in terms of volume fraction ϕ^{α} of constituent α by using equation $\rho^{\alpha} = \phi^{\alpha}\rho_{r}^{\alpha}$ where ρ_{r}^{α} is true density of constituent α that has a constant value due to incompressibility assumption for all constituents. The final equation takes the form:

$$\frac{D\phi^{\alpha}}{Dt} + \nabla \cdot (\phi^{\alpha} v^{\alpha}) = \frac{\rho^{\alpha}\Pi^{\alpha}}{\rho_{r}^{\alpha}} \qquad in\ \Omega^{c} \qquad \alpha = c, SF, m, f \tag{6.2}$$

In the latter equation, whenever $\alpha = SF$, total stress fiber volume fraction ϕ^{SF} is the summation of radial and circumferential stress fiber volume fractions ([165]) such that: $\phi^{SF} = \phi_{r}^{SF} + \phi_{\theta}^{SF}$. Assuming that stress fibers move with cytoskeleton, and only cytosol and G-actin

monomer can migrate through the cell body, Eq. (6.2) splits to two different forms such that:

$$\frac{D\phi^{\alpha}}{Dt} + \phi^{\alpha}\nabla \cdot v^{c} + \nabla \cdot J^{\alpha} = \frac{\rho^{\alpha}\Pi^{\alpha}}{\rho_{r}^{\alpha}} \qquad in\ \Omega^{c} \qquad \alpha = m, f \tag{6.3}$$

$$\frac{D\phi^{\alpha}}{Dt} + \phi^{\alpha}\nabla \cdot v^{c} = \frac{\rho^{\alpha}\Pi^{\alpha}}{\rho_{r}^{\alpha}} \qquad in\ \Omega^{c} \qquad \alpha = c, SF \tag{6.4}$$

where $J^{\alpha} = \phi^{\alpha}(v^{\alpha} - v^{c})$ denote the flux of constituent $\alpha = m, f$.

No total mass is lost or generated during contraction, thus $\sum \rho^{\alpha}\Pi^{\alpha} = 0$. Then assuming $\rho_{r}^{c} = \rho_{r}^{SF} = \rho_{r}^{m}$, and $\phi^{c} + \phi^{SF} + \phi^{m} + \phi^{f} = 1$, cytosol and mixture mass balance (the summation of all constituents mass balance equations) are respectively written for plane stress and axisymmetry (there is no displacement or change in any field along θ direction) situation as:

$$\dot{\phi}^{f} + \alpha\phi^{f}\left(\frac{\partial v^{c}}{\partial r} + \frac{v^{c}}{r}\right) + \beta\phi^{f}\dot{p} + \left(\frac{\partial J^{f}}{\partial r} + \frac{J^{f}}{r}\right) = 0 \tag{6.5}$$

$$\alpha\left(\frac{\partial v^{c}}{\partial r} + \frac{v^{c}}{r}\right) + \beta\dot{p} + \left(\frac{\partial J^{f}}{\partial r} + \frac{J^{f}}{r}\right) + \left(\frac{\partial J^{m}}{\partial r} + \frac{J^{m}}{r}\right) = 0 \tag{6.6}$$

in above equation, the coefficients α and β are functions of ν^{c} and E^{c}, cytoskeleton's Poisson's ratio and Young's modulus, respectively, due to the effect of plane stress condition for cell that means $T_{zz} = p$ where T and zz denote cytoskeleton Cauchy stress and normal direction to cell's surface, respectively. For more details reader is referred to [53]. α and β take the form:

$$\alpha = \frac{1 - 2\nu^{c}}{1 - \nu^{c}}, \qquad \beta = \frac{(1 + \nu^{c})(1 - 2\nu^{c})}{E^{c}(1 - \nu^{c})} \tag{6.7}$$

In addition, in Eqs. (6.5) and (6.6), $\dot{\phi}^{f}$ shows material time derivative of cytosol volume fraction, and using the assumption of the cell's body is saturated by the mentioned constituents is written as:

$$\dot{\phi}^{f} = -\frac{1}{1 + \phi_{f}^{m}}\left(\phi^{f}\dot{\phi}_{f}^{m} + \dot{\phi}^{c} + \dot{\phi}^{p}\right) \tag{6.8}$$

where $\phi_{f}^{m} = \phi^{m}/\phi^{f}$. Also J^{f} and J^{m} denote cytosol and G-actin monomer flux, respectively, such that [165]:

$$J^{f} = -\frac{\kappa}{\mu}\nabla p, \qquad J^{m} = -\phi_{f}^{m}\frac{\kappa}{\mu}\nabla p - \phi^{f} D\ \nabla\phi_{f}^{m} \tag{6.9}$$

where κ, μ, and D denote solid phase permeability, cytosol viscosity, and G-actin diffusion constant in cytosol, respectively.

Cell membrane (integrins)- Similarly to Eqs. (6.3) and (6.4), for low-affinity and high-affinity integrins on cell membrane we can write the mass balance equations as:

$$\frac{Dc^L}{Dt} + c^L \nabla \cdot v^c + \nabla \cdot J^L = c^L \Pi^L \qquad on\ \Omega^c \tag{6.10}$$

$$\frac{Dc^H}{Dt} + c^H \nabla \cdot v^c = c^H \Pi^H \qquad on\ \Omega^c \tag{6.11}$$

where c^L and c^H denote low affinity and high affinity integrin concentration (number per membrane unit area), respectively. Also, $c^L\Pi^L$ and $c^H\Pi^H$ show the rate of low-affinity and high-affinity integrins formation per unit membrane area, respectively. Thus, because no integrin is added or lost during contraction of the cell to the total number of integrins, we can write $c^L\Pi^L + c^H\Pi^H = 0$. As a result, for the mixture of low-affinity and High-affinity integrins, mass balance equation takes the form:

$$\frac{D\left(c^L + c^H\right)}{Dt} + \left(c^L + c^H\right)\left(\frac{\partial v^c}{\partial r} + \frac{v^c}{r}\right) + \left(\frac{\partial J^L}{\partial r} + \frac{J^L}{r}\right) = 0 \qquad on\ \Omega^c \tag{6.12}$$

In above equation, it is assumed that high-affinity integrin is attached to the solid phase, and thus, cannot migrate in membrane cytoplasm fluid [36], but low-affinity integrins can migrate in membrane cytoplasm fluid such that their flux J^L is computed by [96]:

$$J^L = -m\nabla c^L \tag{6.13}$$

where m denote low-affinity integrin mobility coefficient.

6.3.2 Momentum balance of mixture

Cell/Substrate momentum balance equations: In this section we present equations regarding balance of forces in a cell and substrate. For this purpose, the components of mixture Cauchy stress $\mathbf{T}$ is used such that T_r and T_θ denote radial and circumferential components, respectively. As a reminder, Cauchy stress denote infinitesimal force per

unit current area of mixture. Mixture Cauchy stress components are written in terms of their constituents such that for both radial and circumferential components one can write $T = T^c + T^{SF} - p$ where p represents fluid pressure and T^c and T^{SF} denote the part of mixture stress that come from cytoskeleton passive behavior and stress fiber passive and active response, respectively. Then the balance of momentum for mixture under axisymmetric conditions leads to the equation:

$$\frac{\partial T_r}{\partial r} + \frac{1}{r}(T_r - T_\theta) + b_r = 0 \quad in\ \Omega^c \tag{6.14}$$

$$\tag{6.15}$$

where b_r represents radial body force of cell given by:

$$b_r = -\frac{t^i}{h} \tag{6.16}$$

In above equation, h denote the cell height and t^i is the traction force applied to cell surface coming from integrin-ligand adhesion complexes.

To consider the effect of surface tension and membrane elasticity on cell deformation, we follow the surface theory presented in [71] and used in [163, 165, 54, 53]. According to the mentioned references, the traction on cell surface is computed as a function of strain dependent and constant surface tensions ($\mathbf{T}^\sigma$ and $\mathbf{T}_0^\sigma$, respectively) which have the unit of force per unit length (or energy per unit surface area) by:

$$\mathbf{T} \cdot \mathbf{n} = \nabla_\sigma \cdot (\mathbf{T}^\sigma + \mathbf{T}_0^\sigma) \quad on\ \Gamma^c \tag{6.17}$$

where $\mathbf{n}$ and ∇_σ denote out-normal unit vector for cell's surface and surface divergence, respectively. It can easily be shown that for axisymmetric situation, Eq. (6.17) takes the form:

$$T_r = -\frac{1}{a}\left(T^\sigma + T_0^\sigma\right) \quad on\ \Gamma^c \tag{6.18}$$

where a is current cell radius.

The balance of momentum equation for substrate Cauchy stress T^s takes the same form as mentioned for cell's mixture such that:

$$\frac{\partial T_r^s}{\partial r} + \frac{1}{r^s}(T_r^s - T_\theta^s) - b_r = 0 \quad in\ \Omega^s \tag{6.19}$$

$$\tag{6.20}$$

Cell/Substrate body constitutive equations: To complete the momentum balance equations, constitutive relations between different components of Cauchy stress (cytoskeleton, stress fiber, and substrate) and strain are needed. As mentioned previously, both cell and substrate are considered in plane stress axisymmetric condition for simplicity, although this assumption does not affect the results. Plane stress condition means that for both cell and substrate total Cauchy stress is zero along the direction perpendicular to cell/substrate plane. For the substrate it easily means $T_{zz}^s = 0$, while for the cell because of its being made of solid-fluid mixture, the plane stress condition leads to $T_{zz}^c - p = 0$, where T^c and p denote cytoskeleton passive Cauchy stress and cytosol pressure, respectively. Finally, as it is proved in details in [53], and by assuming linear elastic behavior for both cell and substrate because of their small deformations (about one percent), the following constitutive equations are obtained for cell and substrate:

$$T_r^c = \frac{E^c}{1-\nu^{c2}}\left(\varepsilon_r^c + \nu^c \varepsilon_\theta^c\right) + \frac{\nu^c}{1-\nu^c}p, \quad T_r^s = \frac{E^s}{1-\nu^{s2}}\left(\varepsilon_r^s + \nu^s \varepsilon_\theta^s\right) \tag{6.21}$$

$$T_\theta^c = \frac{E}{1-\nu^{c2}}\left(\nu^c \varepsilon_r^c + \varepsilon_\theta^c\right) + \frac{\nu^c}{1-\nu^c}p, \quad T_\theta^s = \frac{E}{1-\nu^{s2}}\left(\nu^s \varepsilon_r^s + \varepsilon_\theta^s\right) \tag{6.22}$$

where E and ν are Young's modulus and Poisson's ratio, and the superscripts c and s denote cytoskeleton and substrate, respectively. Also, in Eqs. (6.21) and (6.22), the small deformation radial and circumferential strains, ε_r and ε_θ, respectively, are given for both cell's solid phase and substrate by following equations under axisymmetric conditions as a function of their radial displacement u:

$$\varepsilon_r = \frac{\partial u}{\partial r}, \qquad \varepsilon_\theta = \frac{u}{r} \tag{6.23}$$

Stress fiber constitutive equation: Let us now talk about the part of Cauchy stress in cell that comes from stress fibers. As discussed in details in [165], stress fiber stress comes from its two different responses to its environment: passive and active. The passive response is similar to any elastic material, and depends on stress fiber material properties and its strain. While stress fiber active response is the result of its inherent contractile behavior generated by acto-myosin motors [165]. In this chapter, we use the new modified definitions for stress fiber contractile stress presented in [56] such that for any direction, including r and θ, total stress fiber contractile stress T^{SF} takes the form:

$$T^{SF} = \phi^{SF} \left(E_1 \varepsilon + T^* \right) \tag{6.24}$$

where E_1 and T^* denote stress fiber Young's modulus and inherent contractile stress of one stress fiber, respectively. In Eq. (6.24), the first term proposes passive response of stress fibers, while the second term denote their active response.

Integrin-ligand adhesion constitutive equation: The traction on cell and substrate surface t^i, generated by integrin-ligand adhesion complexes, depends on the complex stiffness λ_s (with unit of force per length) and relative cell-substrate deformation $\Delta_i = u^c - u^s$ (Fig. 6.2b). In this view, the focal adhesion traction is computed such as a stretched spring such that:

$$t^i = c^{BH} \lambda_s (u^c - u^s) \tag{6.25}$$

where c^{BH} denote integrin-ligand complex (or bound high-affinity integrin) concentration with the unit of number per unit surface area. The concentration of focal adhesion complexes and their relation with ligand and high-affinity integrins is discussed in details in next section.

Cell membrane constitutive equation: Because of its thin thickness in comparison with the other cell and substrate dimensions, cell membrane is assumed to act such cable that surrounds the cell in its border Γ^c (Fig. 6.1). Cell membrane is the only part in our

model that undergoes large deformation during cell spreading. Cell's area may end with an area even more than three times the initial area [129, 138]. This change in area is the result of growth (mass is generated during growth) not deformation, while membrane does not grow in the proposed framework, but stretches during cell growth. Consequently, instead of infinitesimal strain ε, Green strain E^σ is used for cell membrane such that [10]:

$$E^\sigma = \frac{1}{2}\left(\frac{l^2}{l_0^2} - 1\right) = \frac{1}{2}\left(\frac{a^{c2}}{a_0^{c2}} - 1\right) \tag{6.26}$$

where l and a^c denote current membrane length and cell radius, respectively; while the values with subscript 0 represent initial values at $time = 0$. Then the constitutive relation between membrane axial Green strain and its axial second Piola-Kirchhoff stress S^σ is given by [10]:

$$S^\sigma = k^\sigma E^\sigma \tag{6.27}$$

where k^σ denotes membrane axial stiffness (force per unit length). Membrane stiffness is obtained as the result of the derivative of its strain energy ψ with respect to its Green strain E^σ such that [10]:

$$k^\sigma = \frac{\partial \psi}{\partial E^\sigma} \tag{6.28}$$

Then, membrane Cauchy stress T^σ of membrane is computed by [10]:

$$T^\sigma = S^\sigma F \tag{6.29}$$

where $F = \partial a / \partial a_0$ denote deformation gradient of cell membrane.

6.3.3 Free energy and equilibrium state of constituents

6.3.3.1 Free energy

Integrins: The adhesion proteins on cell membrane, called integrins, are found in two conditions (Fig 6.2b): bent and straight (or low affinity integrins and high affinity integrins, respectively). Low affinity integrins do not have the ability to make adhesion complex. These

integrins can migrate on the cell membrane toward the area with more traction forces on the cell surface. On the other side, high affinity integrins are activated integrins able to make a bond with ligands on the substrate surface to generate an focal adhesion. These integrins are mostly attached to cytoskeleton, and can not migrate on the cell membrane.

To find the chemical potential of low affinity integrins, it is assumed that they make a dilute solution in the membrane fluid. As a result, their free energy (μ^L) is given as a function of low affinity number per unit area (c^L) by [36]:

$$\mu^L = \mu_0^L + k_B T \; ln\left(\frac{c^L}{c_0^I}\right) \tag{6.30}$$

where μ_0^L and c_0^I are low-affinity integrin's free energy and concentration in standard condition, respectively. The free energy of unbound high-affinity integrins rises from their chemical potential such that:

$$\mu^{UH} = \mu_0^H + k_B T \; ln\left(\frac{c^H}{c_0^I}\right) \tag{6.31}$$

where μ^{UH}, μ_0^H and C^{UH} are current and standard unbound high-affinity integrins free energy and unbound high-affinity integrin concentration (number per unit area), respectively. For bound integrins, their free energy includes mechanical energy of integrin-ligand complex in addition to their chemical potential. In this case the free energy of bound high-affinity integrins is written as [36]:

$$\mu^{BH} = \mu_0^H + k_B T \; ln\left(\frac{c^H}{c_0^I}\right) + \phi(\Delta_i) - F_i\Delta_i \tag{6.32}$$

where μ^{BH} and c^{BH} are current bound high-affinity integrins free energy and bound high-affinity integrin (or integrin-ligand) concentration, respectively. The last two terms in equation (6.32) come from the stretching of the integrin-ligand bonds as a function of the bond's stretching $\Delta_i = u^c - u^s$ where u^c and u^s are cell-side and substrate-side displacement of the adhesion complex, respectively. $\phi(\Delta_i)$ denote the stretch energy stored in integrin-ligand complex, while $F_i = \frac{\partial \phi}{\partial \Delta_i}$ is work conjugate force. In the case of a continuum model of

integrins and ligands, the stretch energy is given by:

$$\phi(\Delta_i) = \frac{1}{2}\lambda_s \Delta_i^2 \tag{6.33}$$

Defining N^{UH} and N^{BH} as unbound and bound high-affinity integrin numbers, the total number of high-affinity integrins N^H is given by $N^H = N^{UH} + N^{BH}$. As a result total high-affinity integrin free energy is computed as $N^H\mu^H = N^{UH}\mu^{UH} + N^{BH}\mu^{BH}$, or $\mu^H = \phi^{UH}\mu^{UH} + \phi^{BH}\mu^{BH}$ where ϕ^{UH} and ϕ^{BH} denote unbound and bound integrin percents, respectively, such that $\phi^H = \phi^{UH} + \phi^{BH}$. Following [96] ligand-integrin complex concentration (or bound high-affinity integrin concentration c^{BH}) at equilibrium is computed by:

$$c^{BH} = \frac{c^{lg}}{1 + c^{lg}} c^H \tag{6.34}$$

where c^{lg} denotes ligand concentration. Consequently, using Eqs (6.31) and (6.32), the free energy of high-affinity integrins is written as:

$$\mu^H = \mu_0 + k_B T \; ln\left(\frac{c^H}{c_0^I}\right) + \frac{c^{lg}}{1 + c^{lg}} \left[\phi(\Delta_i) - F_i\Delta_i\right] \tag{6.35}$$

where

$$\mu_0 = \mu_0^H + k_B T \left[\frac{c^{lg}}{1 + c^{lg}} ln(c^{lg}) - ln(1 + c^{lg})\right] \tag{6.36}$$

Because of their straight shape, high affinity integrins are less stable than low infinity integrins before being bond to ligands. It means that $\mu_0^H > \mu_0^L$. As a result, if the high-affinity integrins are not bound to the integrins, they tend to convert to bent condition to reach more stable condition. But when high-affinity integrins are attached to ligands, the stretch of the integrin-ligand bond decreases the free energy μ^{BH} to stabilize the adhesion. When equilibrium is reached, the free energy of low and high affinity integrins are equal ($\mu^H = \mu^L$). This equilibrium is reached very fast compared to the other time dependent phenomena in the cell such as G-actin monomers or low-affinity integrin migration.

G-actin-monomers: The potential of actin monomers μ^m at absolute temperature T is given by only their chemical potential defined as a function of their volume fraction ϕ_f^m

by [56]:

$$\mu^m = \mu_0^m + k_B T ln\left(\phi_f^m\right) \tag{6.37}$$

where μ_0^m and k_B denote actin monomer chemical potential at $\phi_f^m = 1$ and $Boltzman$ constant, respectively.

Stress Fibers: On the other hand, chemo-mechanical potential of stress fibers μ^{SF} at temperature T comes from both chemical and mechanical potential stored in stress fibers such that for any direction one can write [152, 56]:

$$\mu^{SF} = \mu_0^{SF} + k_B T \left(ln\left(\phi^{SF}\right) + a_\mu \left(\frac{\phi^{SF}}{\phi^{SF*}}\right)^{5/4} \right) + E^{SF} \tag{6.38}$$

Also, the cytoskeleton overlap volume fraction ϕ^{c*} corresponds to the state in which cytoskeleton chains are congested in mixture.

where μ_0^{SF}, a_μ and E^{SF} denote stress fiber chemical potential at $\phi^{SF} = 1$, a constant independent of the number of monomers in a chain of cytoskeleton as a polymer, and the mechanical potential energy of a single stress fiber, respectively. Also, stress fiber overlap volume fraction ϕ^{SF*} corresponds to the state in which cytoskeleton chains are congested in mixture. The potential E^{SF} is given by:

$$E^{SF} = \frac{1}{2} E_1 \varepsilon^2 - T^* \varepsilon \tag{6.39}$$

where E_1, ε, and T^* denote stress fiber's Young's modulus, stress fiber's axial strain, and inherent tension of a single stress fiber, respectively. The first term in Eq. (6.39) gives the elastic energy stored in a stress fiber, while the second term introduces the relaxation in a stress fiber due to its inherent contraction. Eq. (6.39) explains the formation or dissociation of stress fiber as a function of its mechanical properties and also its strain (which is the same as cytoskeleton's strain in the direction of stress fiber). We conclude from Eq. (6.39) that if $\varepsilon < 0$, E^{SF} is positive which leads to increase in stress fiber chemo-mechanical potential. This causes the stress fiber to be unstable and depolymerize to actin monomer. On the other hand, in the case of $\varepsilon > 0$, E^{SF} is negative that leads to formation of stress fibers due to

their low potential level and high stability. This happens up to the critical positive strain $\varepsilon_{cr} = \frac{2T^*}{E_1}$ where stress fiber cannot resist the tension, and so, depolymerizes.

Cytoskeleton: Cytoskeleton-cytosol mixture is considered as a semidilute solution [152]. In according to *blob model* ([152]), chemical potential of cytoskeleton μ^c is approximated by the following equation valid from dilute to semidilute solutions:

$$\mu^c = \mu_0^c + k_B T \left(ln\left(\phi^c\right) + a_\mu \left(\frac{\phi^c}{\phi^{c*}} \right)^{5/4} \right) \tag{6.40}$$

where μ_0^c and a_μ denote stress fiber chemical potential at reference state $\phi^c = 1$ and a constant independent of the number of monomers in a chain of cytoskeleton as a polymer. Also, the cytoskeleton overlap volume fraction ϕ^{c*} corresponds to the state in which cytoskeleton chains are congested in mixture.

The free energy of cytoskeleton in the growing boundary of the cell is a little different from cell's body due to the process of cell growth, in which actin monomers try to overcome resisting forces and polymerize to form new network of fibers. The resisting forces come from two sources. First, local bending of membrane (f^l), generated as the result of new actin monomer inserting between membrane and existing fiber (Fig. 6.3b); and second, global membrane resistance (f^g) due to its resistance against being stretched as an elastic material. In contrast to the resisting forces, the pulling force coming from focal adhesion complexes at the cell's boundary helps the process of cell growth in the way explained in the following. As a result, despite the cell's body, the free energy of cytoskeleton in the growing boundary of cell is not only included of its chemical potential, but also of the mechanical energy of the mentioned forces. Fig. 6.3 shows that one cycle of actin monomer polymerization includes two steps. During the first step, shown in Fig. 6.3b, membrane is deformed locally such that a new actin monomer can be inserted between the tip of existing filament and membrane. In this step, there are some forces that resist polymerization. One of these forces comes from the bending resistance of the membrane (f^l). As depicted in Fig. 6.3b, to insert a monomer to the end of a filament, the membrane needs to be bent such that

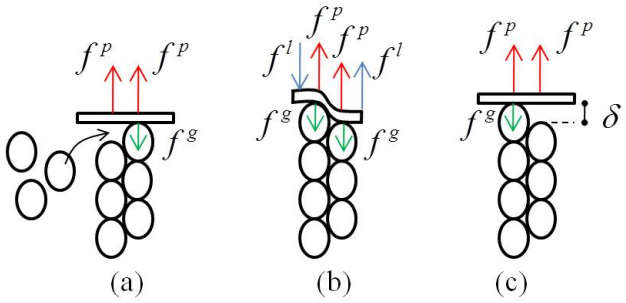

Figure 6.3: A cycle of actin polymerization beneath the cell membrane: a) G-actin monomers try to insert between the existing filament and cell membrane, b) Cell membrane is bent such that one monomer is bound at the end of the existing filament, and c) Cell membrane returns to its unbent configuration.

an additional space of δ (half monomer size) is provided for the monomer to be inserted. Consequently, the corresponding work is $f^l \cdot \delta$. The other resistance against actin insertion comes from global membrane resistance (f^g) due to its stretching. Since this force is applied to the contact point of filament and membrane, the work needed to overcome the mentioned resistance is calculated by $f^g \cdot \delta$. On the other hand, there is a pulling force coming from contractile behavior of stress fibers in the body of cell that helps monomer insertion. As Fig. 6.3b shows, this force helps providing enough space for insertion of a new monomer. As a result, it helps the polymerization process by decreasing the system energy by $f^p \cdot \delta$. As a summary, in the step of membrane local deformation in order to insert a new actin monomer between filament and membrane, the change in cytoskeleton-membrane energy is given by:

$$\Delta\mu_I^c = f^l \cdot \delta + f^g \cdot \delta - f^p \cdot \delta \tag{6.41}$$

To have complete a cycle of actin monomer polymerization, as depicted in Fig. 6.3c, membrane should return to its unbent configuration. In this step the elastic energy stored in membrane during first step as the result of its bending ($f^l \cdot \delta$), is released. Also, the pulling force f^p helps the mentioned process; as a result the needed energy for detaching is computed as $-f^p \cdot \delta$. Consequently, the total change in system energy during the second

step is given by:

$$\Delta\mu^c_{II} = -f^l \cdot \delta - f^p \cdot \delta \tag{6.42}$$

Combining equations (6.41) and (6.42), the total change in cytoskeleton free energy to complete a cycle of one actin monomer polymerization takes the form:

$$\Delta\mu^c_{tot} = f^g \cdot \delta - 2f^p \cdot \delta \tag{6.43}$$

Finally, total free energy of cytoskeleton on the growing boundary of the cell is computed by adding the mechanical energy of Eq. (6.43) to the chemical potential of cytoskeleton presented before such that:

$$\mu^c = \mu^c_0 + k_B T \left(ln\left(\phi^c\right) + a_\mu \left(\frac{\phi^c}{\phi^{c*}} \right)^{5/4} \right) + f^g \cdot \delta - 2f^p \cdot \delta \tag{6.44}$$

6.3.3.2 Equilibrium state

Three kind of mass exchange happens in a cell as the result of chemical reactions (polymerization). The first kind of mass exchange happens on the cell's membrane between low affinity and high affinity integrins. Also, another kind of mass exchanges is the result of polymerization of actin monomers that results in formation of stress fibers that are the result of binding filament bundles. The reverse reaction (depolymerization of stress fibers) leads to generation of actin monomers. In a similar approach as actin monomer and stress fiber chemo-mechanical equilibrium, the chemo-mechanical equilibrium should be satisfied between actin monomers and cytoskeleton because actin monomers are able to polymerize to form cytoskeletal network, while on the other hand, cytoskeleton may depolymerize to actin monomers.

It is assumed that all reactions (except actin monomer polymerization on the growing surface of cell) are very fast compared to the other time consuming phenomena in the cell such as actin monomer, L-integrin, and cytosol flux. As a result, only the equilibrium of their chemo-mechanical potential is considered to be satisfied at each time at each point of the cell's body/surface.

As a summary, at equilibrium state, the free energy of cell's constituents must satisfy the following equations:

$$\text{High-affinity and low affinity integrins:} \qquad \mu^H = \mu^L \tag{6.45}$$

$$\text{Stress fibers and G-actin monomers:} \qquad \mu^{SF} = \mu^m \tag{6.46}$$

$$\text{Cytoskeleton and G-actin monomers:} \qquad \mu^c = \mu^m \tag{6.47}$$

On the cell's growing boundary, the value of cytoskeleton and actin monomer free energy provides information about growth to be favorable or unfavorable. if $\mu^c < \mu^m$, it means that polymerization decreases the energy level of the system and it is favorable and continues. In contrast, if $\mu^c > \mu^m$ means polymerization is not favorable. Also, in the case of $\mu^c = \mu^m$, the total monomer and filament concentration will not change during time and system is in equilibrium. in this case, using equation (6.44), $\phi^m_{f,cr}$, the minimum actin monomer concentration needed for polymerization, can be computed as:

$$\phi^m_{f,cr} = \phi^c \; exp\left(-\frac{-\Delta\mu_0 - f^g \cdot \delta + 2f^p \cdot \delta}{k_B T} + a_\mu \left(\frac{\phi^c}{\phi^{c*}}\right)^{5/4}\right) \tag{6.48}$$

where $\Delta\mu_0 = \mu^c_0 - \mu^m_0$. Equation (6.48) shows that the actin monomer concentration needed for polymerization increases exponentially by global membrane resistance force , f^g, while it decreases exponentially by the pulling force f^p.

6.3.4 The rate of growth

As mentioned briefly, the rate of mass exchange between actin monomers and stress fibers or cytoskeleton in the body of cell, and also mass exchange between low affinity and high affinity integrins on the cell membrane are very fast in comparison with other time dependent procedures in cell which are actin monomer, cytosol, and low affinity integrin flux. Consequently, the mentioned rates are neglected in this chapter. In contrast, since membrane resists polymerization of cytoskeleton in the growing surface of the cell, the rate of polymerization in this part is not negligible. On the other hand, this rate gives information about the velocity of growth of cell that is interested and important in studying cell spreading.

The rate of polymerization, k, depends highly on the activating energy, needed to start polymerization [93]. This activation energy E_r depends on the factors resist or help polymerization during the first step (Fig. 6.3a,b). The resisting forces include global membrane force and local membrane force needed for its local bending. On the other hand, the pulling force f^p and actin monomer concentration help polymerization. Thus, the total activating energy is given by:

$$E_r = f^l \cdot \delta + f^g \cdot \delta - f^p \cdot \delta + \Delta\mu_0 + k_B T \left(ln\left(\phi^c\right) + a_\mu \left(\frac{\phi^c}{\phi^{c*}}\right)^{5/4} \right) - k_B T ln(\phi_f^m) \quad (6.49)$$

Following [93] and according to the *Arrhenius* law, the rate of polymerization (monomer per time) is computed by:

$$k = k_0 exp\left(-\frac{E_r}{k_B T}\right) \quad (6.50)$$

Since at each polymerization cycle, filament size is increases by δ (Fig. 6.3), the rate of filament (or cell) growth (length per time) is computed as:

$$V = k_0 \cdot \delta exp\left(-\frac{E_r}{k_B T}\right) \quad (6.51)$$

By substituting the activating energy E_r from Eq. (6.49) into above equation, the following equation is derived for the rate of cell growth:

$$V = k \cdot \delta \cdot exp\left(-\frac{f^l \cdot \delta + f^g \cdot \delta - f^p \cdot \delta}{k_B T}\right) \quad (6.52)$$

where $k = k_0 \frac{\phi_f^m}{\phi^c} \cdot exp\left(-\frac{\Delta\mu_0}{k_B T} - a_\mu \left(\frac{\phi^c}{\phi^{c*}}\right)^{5/4}\right)$. Eq. (6.52) shows that the membrane resisting forces f^l and f^g decrease the rate of cell's growth; while the pulling force f^p increases polymerization and growth rate. It also proves that the more concentration of actin monomer leads to more growth while by decreasing monomer concentration, the cell's growth slows down. It also should be kept in mind that polymerization continues as long as monomer concentration is greater than its critical value $\phi_{f,cr}^m$ (Eq.(6.48)).

Furthermore, by neglecting the effect of pulling force and local membrane resistance, f^p and f^l, respectively, one can derive the following equation from Eq. (6.52):

$$V = k \cdot \delta \cdot exp\left(-\frac{f^g \cdot \delta}{k_B T}\right) \quad (6.53)$$

The above equation is in complete agreement with what derived for cell growth by using the concept of Brownian-Ratchet in [122].

As a summary of this section, the summary of equations corresponding to substrate momentum balance, cell momentum balance, cytosol mass balance, cell mixture mass balance, integrins mass balance, and also the free energy equilibrium state between cytoskeleton and G-actin, radial stress fiber and G-actin, circumferential stress fiber and G-actin, and integrins are shown respectively as follows:

$$\frac{\partial T_r^s}{\partial r} + \frac{1}{r}(T_r^s - T_\theta^s) + t^i = 0 \tag{6.54}$$

$$\frac{\partial T_r^c}{\partial r} + \frac{1}{r}(T_r^c - T_\theta) + \frac{\partial T_r^{SF}}{\partial r} + \frac{1}{r}(T_r^{SF} - T_\theta^{SF}) - \frac{\partial p}{\partial r} - t^i = 0 \tag{6.55}$$

$$\dot{\phi}^f + \alpha\phi^f\left(\frac{\partial v^c}{\partial r} + \frac{v^c}{r}\right) + \beta\phi^f\dot{p} + \left(\frac{\partial J^f}{\partial r} + \frac{J^f}{r}\right) = 0 \tag{6.56}$$

$$\alpha\left(\frac{\partial v^c}{\partial r} + \frac{v^c}{r}\right) + \beta\dot{p} + \left(\frac{\partial J^f}{\partial r} + \frac{J^f}{r}\right) + \left(\frac{\partial J^m}{\partial r} + \frac{J^m}{r}\right) = 0 \tag{6.57}$$

$$\frac{D\left(c^L + c^H\right)}{Dt} + \left(c^L + c^H\right)\left(\frac{\partial v^c}{\partial r} + \frac{v^c}{r}\right) + \left(\frac{\partial J^L}{\partial r} + \frac{J^L}{r}\right) = 0 \tag{6.58}$$

$$\mu^c - \mu^m = 0 \tag{6.59}$$

$$\mu_r^{SF} - \mu^m = 0 \tag{6.60}$$

$$\mu_\theta^{SF} - \mu^m = 0 \tag{6.61}$$

$$\mu^H - \mu^L = 0 \tag{6.62}$$

6.4 Numerical solution of governed equations

6.4.1 Numerical strategy for cell contraction/spreading on substrate

The set of equations governed in previous section needs a numerical method to solve for unknown fields. As shown in Fig. 6.1, the axisymmetric plane stress domain under study includes two separate domains: cell Ω^c and substrate Ω^s. If these domains are approached by two different mesh frames, we will face to the following difficulties:

- Due to cell spreading, at each time step the mesh should be updated for both cell

and substrate.

- The adhesion between cell and substrate via adhesion complexes asks for interaction between two separate domains with its specific difficulties.
- The surface tension on cell's membrane cannot be naturally considered.
- Although not considered in this chapter, in a 2D or 3D case, the random shape of cell, especially during evolution, asks for different meshes for each case/time step.

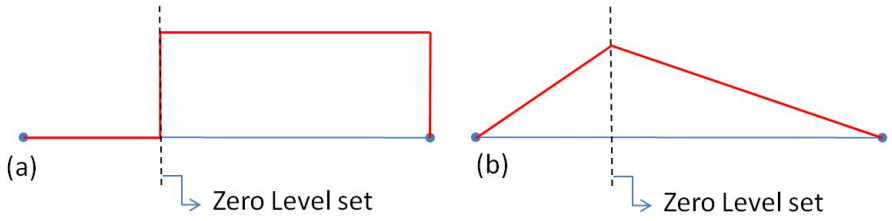

Figure 6.4: (a) Levelset function, enriched element and enriched nodes, (b) Heavy side and (c) Ridge functions used to enrich the finite element interpolation.

For these reasons, in this chapter, we introduce a numerical approach which needs only one mesh frame for both domains. The mesh frame covers the whole substrate while the cell domain Ω^c is defined by a function $\phi(r)$, called levelset function (Fig. 6.4a), where r is radial distance of a point from center of cell. For our problem, levelset is a 2D curve/line such that the border of the cell is defined as the intersection of this line with axis r (cell's level, Fig. 6.4a). The function $\phi(r)$ is defined such that it has different sign in two sides of cell's boundary. As a result it is very easy to determine if a material point P located at r is inside, outside, or on the boundary of the cell such that:

$$\text{if } \phi(r) > 0, \quad P \in \Omega^c \tag{6.63}$$

$$\text{if } \phi(r) = 0, \quad P \in \Gamma^c \tag{6.64}$$

$$\text{if } \phi(r) < 0, \quad P \notin \Omega^c \tag{6.65}$$

This method enables us to define cell's domain with different sizes during evolution independently from finite element mesh. In addition, nodes located outside the cell have only substrate displacement degree of freedom u^s, while nodes located outside the cell associate with substrate displacement u^s and cell degrees of freedom $u^c, p, \phi^c, \phi^m, \phi_r^{SF}, \phi_\theta^{SF}, c^L$, and c^H.

The main difficulty of the problem under study when approached by ordinary finite element method is that the continuum domain of cell is associated with discontinuities on its boundary. For example, a typical cell continuum field f has a value inside the cell, while it vanishes outside the cell boundary Γ^c. The reason is that the shape functions used in ordinary finite element method are continuous, and the boundary Γ^c is located inside an element. To overcome the mentioned difficulties, in this chapter we use extended finite element [43, 79] that is very efficient in describing different types of discontinuity in a continuum field within an element [105, 9, 7, 181, 54]. In this context (Fig. 6.4a), the elements cut by the levelset, and their nodes, are considered as enriched elements/nodes. To introduce discontinuities in a continuum field f (denoted as strong discontinuity) and its gradient (denoted as weak discontinuity) across the cell boundary, fictitious degrees of freedom $\bar{f}$ and $\bar{\bar{f}}$ are added to the enriched nodes such that a numerical approximation $\tilde{f}$ of the function f can be introduced using conventional finite element shape functions as follows:

$$\tilde{f}(r) = \sum_{I=1}^{n} N_I(r) f_I + \sum_{J=1}^{m} N_J(r)(H(r) - H(r_J))\bar{f}_J + \sum_{J=1}^{m} N_J(r)\left(\chi(r) - \chi(r_J)\right)\bar{\bar{f}}_J \qquad (6.66)$$

where N_I and N_J are ordinary shape functions of ordinary and enriched nodes, respectively. As depicted in Fig. 6.4a, the element cut by levelset function is enriched element, and its nodes are considered as enriched nodes. Also in Eq. (6.66), n and m denote the total number of nodes and number of enriched nodes of an element, respectively. In addition, the Heaviside and ridge functions, denoted as $H(r)$ and $\chi(r)$ take the form:

$$H(r) = \begin{cases} 1 & \phi(r) > 0 \\ 0 & \phi(r) < 0 \end{cases} \quad \text{and} \quad \chi(r) = |\phi(r)| \qquad (6.67)$$

The function $H(r)$ is used to introduce a jump in the fields $\dot{u}^c, \dot{p}, \dot{\phi}^c, \dot{\phi}^m, \dot{\phi}_r^{SF}, \dot{\phi}_\theta^{SF}, \dot{c}^L$ and $\dot{c}^H$ across the cell's membrane, whereas the ridge function is used to define discontinuities in the spatial derivatives of $\dot{u}^s$ and $\dot{u}^c$ ([105, 106]) due to the adhesion complex traction force on substrate and the effect of cell membrane surface tension on cell, respectively. A one-dimensional representation of the Heaviside and ridge function is provided in Fig. 6.4b and 6.4c.

As a summary, the proposed framework has the following advantages compared with ordinary finite element method:

(1) Because of using the same mesh for cell and substrate, the difficulties of interaction between two separate domains is avoided.

(2) The effect of cell membrane surface tension on cell deformation is naturally considered as described in [54, 166].

(3) The problem of cell spreading is naturally incorporated by using the advantage of levelset evolution [93, 136]. As a result, remeshing is not needed at each time step during evolution.

6.4.2 Discretization and time integration

The proposed XFEM approximation Eq. (6.66) is substituted for continuum fields $\dot{u}^s$, $\dot{u}^c$, $\dot{p}$, $\dot{\phi}^c$, $\dot{\phi}^m$, $\dot{\phi}_r^{SF}$, $\dot{\phi}_\theta^{SF}$, $\dot{c}^L$ and $\dot{c}^H$ in the set of equations (6.54)-(6.62). It should be noted that just the nodes corresponding to elements cut by zero levelset function are enriched. Also, all fields except substrate displacement u^s are considered to have strong discontinuity across cell border Γ^c, while only u^s and u^c have weak discontinuity across Γ^c. The jump in gradient field of u^s happens because of vanishing the traction force of focal adhesions outside the cell area. In addition, the weak discontinuity for the gradient field of u^c is considered due to the effect of cell membrane surface tension that leads to jump in strain and stress fields of cell's body [163].

Furthermore, the domain is discretized to *nel* 3-node elements, and corresponding Lagrangian shape functions N_I are used to interpolate the continuum fields between element nodes. The nodal degrees of freedom $\mathbf{U}_I^e$ for any element e are then defined by the following vector:

$$\mathbf{U}_I^e = \begin{bmatrix} \mathbf{u}_I^e & \bar{\mathbf{u}}_I^e & \bar{\bar{\mathbf{u}}}_I^e \end{bmatrix}^T \tag{6.68}$$

where

$$\mathbf{u}_I^e = \begin{bmatrix} u_I^{s,e} & u_I^{c,e} & p_I^e & \phi_I^{m,e} & \phi_I^{c,e} & \phi_{r,I}^{SF,e} & \phi_{\theta,I}^{SF,e} & c_I^{L,e} & c_I^{H,e} \end{bmatrix}^T \tag{6.69}$$

$$\bar{\mathbf{u}}_I^e = \begin{bmatrix} \bar{u}_I^{c,e} & \bar{p}_I^e & \bar{\phi}_I^{m,e} & \bar{\phi}_I^{c,e} & \bar{\phi}_{r,I}^{SF,e} & \bar{\phi}_{\theta,I}^{FS,e} & \bar{c}_I^{L,e} & \bar{c}_I^{H,e} \end{bmatrix}^T \tag{6.70}$$

$$\bar{\bar{\mathbf{u}}}_I^e = \begin{bmatrix} \bar{\bar{u}}_I^{s,e} & \bar{\bar{u}}_I^{c,e} \end{bmatrix}^T \tag{6.71}$$

where $I = 1, 2, 3$ denotes the local node number for each element. It should be noted that the terms $\bar{\mathbf{u}}_I^e$ and $\bar{\bar{\mathbf{u}}}_I^e$ correspond to strong and weak degrees of freedom and are vanished for non-enriched (normal) elements. Then, using above nodal values in approximation (6.66), and substituting it in set of governed equations (6.54)-(6.62), integration over each element domain is performed numerically using 3-node Gaussian quadrature rule for normal elements with no enriched node, and 5-node Gaussian quadrature rule for normal elements neighboring the enriched element (with one enriched node). The latter is called partially enriched element. To integrate over the enriched element, the element is split to two sub-elements in two sides of cell's border Γ^c. Then 8-node Gaussian quadrature rule is used, for maximum accuracy, to integrate over each sub-element following partition of unity for the whole element. It should be noted that these sub-elements are used for only integration purposes and do not increase elements or degrees of freedoms. Furthermore, on cell surface, there is only one point due to axisymmetry, thus no numerical integration is needed on cell surface.

After long but straightforward calculations, the following final matrix form XFEM equation is governed:

$$\mathbf{C} \cdot \dot{\mathbf{U}} + \mathbf{K} \cdot \delta\mathbf{U} + \mathbf{F} = \mathbf{0} \tag{6.72}$$

where $\mathbf{U}$ denote global degrees of freedom vector. In addition, all components of Eq. (6.72), are resulted from assembly of elemental values as following:

$$\mathbf{F} = \mathscr{A}_{e=1}^{nel}\mathbf{F}^e \qquad \mathbf{K} = \mathscr{A}_{e=1}^{nel}\mathbf{K}^e \quad \text{and} \quad \mathbf{C} = \mathscr{A}_{e=1}^{nel}\mathbf{C}^e. \tag{6.73}$$

where $\mathscr{A}$ denote assembly operator. As a result, the final force vector, damping matrix, and stiffness matrix take the forms:

$$\mathbf{F} = \left[\mathbf{F}^{u^s},\ \mathbf{F}^{u^c},\ \mathbf{F}^{f},\ \mathbf{F}^{m},\ \mathbf{F}^{c},\ \mathbf{F}^{SF,r},\ \mathbf{F}^{SF,\theta},\ \mathbf{F}^{L},\ \mathbf{F}^{H}\right]^T \tag{6.74}$$

$$\mathbf{C} = \begin{bmatrix} 0 & 0 & 0 & 0 & 0 & 0 & 0 & 0 & 0 \\ 0 & 0 & 0 & 0 & 0 & 0 & 0 & 0 & 0 \\ 0 & \mathbf{C}^{fu} & \mathbf{C}^{ff} & \mathbf{C}^{fm} & \mathbf{C}^{fc} & \mathbf{C}^{fr} & \mathbf{C}^{f\theta} & 0 & 0 \\ 0 & \mathbf{C}^{mu} & \mathbf{C}^{mf} & 0 & 0 & 0 & 0 & 0 & 0 \\ 0 & 0 & 0 & 0 & 0 & 0 & 0 & 0 & 0 \\ 0 & 0 & 0 & 0 & 0 & 0 & 0 & 0 & 0 \\ 0 & 0 & 0 & 0 & 0 & 0 & 0 & 0 & 0 \\ 0 & \mathbf{C}^{Lu} & 0 & 0 & 0 & 0 & 0 & \mathbf{C}^{LL} & \mathbf{C}^{LH} \\ 0 & 0 & 0 & 0 & 0 & 0 & 0 & 0 & 0 \end{bmatrix} \tag{6.75}$$

$$\mathbf{K} = \begin{bmatrix} \mathbf{K}^{ss} & \mathbf{K}^{su} & 0 & 0 & 0 & 0 & 0 & 0 & \mathbf{K}^{sH} \\ \mathbf{K}^{us} & \mathbf{K}^{uu} & \mathbf{K}^{uf} & 0 & 0 & \mathbf{K}^{ur} & \mathbf{K}^{u\theta} & 0 & \mathbf{K}^{uH} \\ 0 & 0 & \mathbf{K}^{ff} & 0 & 0 & 0 & 0 & 0 & 0 \\ 0 & 0 & \mathbf{K}^{mf} & \mathbf{K}^{mm} & \mathbf{K}^{mc} & \mathbf{K}^{mr} & \mathbf{K}^{m\theta} & 0 & 0 \\ 0 & 0 & 0 & \mathbf{K}^{cm} & \mathbf{K}^{cc} & 0 & 0 & 0 & 0 \\ 0 & \mathbf{K}^{ru} & 0 & \mathbf{K}^{rm} & 0 & \mathbf{K}^{rr} & 0 & 0 & 0 \\ 0 & \mathbf{K}^{\theta u} & 0 & \mathbf{K}^{\theta m} & 0 & 0 & \mathbf{K}^{\theta\theta} & 0 & 0 \\ 0 & 0 & 0 & 0 & 0 & 0 & 0 & \mathbf{K}^{LL} & 0 \\ \mathbf{K}^{Hs} & \mathbf{K}^{Hu} & 0 & 0 & 0 & 0 & 0 & \mathbf{K}^{HL} & \mathbf{K}^{HH} \end{bmatrix} \tag{6.76}$$

The detailed format of the components of above equations is brought in Appendix F. The final nonlinear matrix form equation (6.72) is solved at each time step using Newton-Raphson nonlinear iterations. Indeed, a backward Euler integration method is used to compute the unknown fields at each time step based on its time derivative at the next time step such that:

$$\delta \mathbf{U} = \delta \dot{\mathbf{U}} \cdot \Delta t \tag{6.77}$$

where Δt denote the time increment. As mentioned above, the contraction/growth problem is inherently nonlinear; thus, we solve iteratively for $\dot{\mathbf{U}}(t + \Delta t)$ at time step $t + \Delta t$. Then, the value $\dot{\mathbf{U}}^i(t + \Delta t)$ at iteration i^{th} is computed by:

$$\dot{\mathbf{U}}^i(t + \Delta t) = \dot{\mathbf{U}}^{i-1}(t + \Delta t) + \delta \dot{\mathbf{U}}^i \tag{6.78}$$

Finally, the value $\delta \dot{\mathbf{U}}^i$ is computed for each iteration by substituting equations (6.77) and (6.78) into equation (6.72) that leads to the following equation:

$$\left(\mathbf{C}^{i-1}_{t+\Delta t} + \Delta t.\mathbf{K}^{i-1}_{t+\Delta t}\right).\delta \dot{\mathbf{U}}^i = -\left(\mathbf{F}^{i-1}_{t+\Delta t} + \mathbf{C}^{i-1}_{t+\Delta t} \cdot \dot{\mathbf{U}}^{i-1}_{t+\Delta t}\right) \tag{6.79}$$

Iterations are then repeated until the norm of the vector $|\delta \mathbf{U}^i|$ is smaller than a small tolerance tol.

6.4.3 Cell growth and levelset evolution

As mentioned previously, the zero level of a levelset function defines the border of the cell Γ^c (6.4a) in its undeformed configuration. One great advantage of the proposed XFEM framework is that the cell growth is approached by evolving the levelset function during time with no need to change the mesh. On the other words, the velocity of levelset function is the same as growth rate in undeformed configuration of the cell.

As described before, if $\phi(r)$ defines the levelset value at material point P located at coordinate r, to evolve ϕ during time the following levelset evolution equation is used [45]:

$$\frac{D\phi}{Dt} = \frac{\partial \phi}{\partial t} + V||\frac{\partial \phi}{\partial r}|| = 0 \tag{6.80}$$

where V denote cell surface velocity (defined in Eq. (6.52)). In the case of using signed distance as levelset function, because of its good reported stability ([45]), the term $||\frac{\partial \phi}{\partial r}|| = 1$. Consequently, the levelset value of material point P at time $t + \Delta t$ is computed by:

$$\phi^{t+\Delta t} = \phi^t + V \cdot \Delta t \tag{6.81}$$

Because new material is added to the grown boundary of the cell, assumptions are needed for their unknown fields u^c, p, ϕ^c, ϕ^m, ϕ_r^{SF}, ϕ_θ^{SF}, c^L and c^H as initial condition at the beginning of next time step. In this chapter it is assumed that all the mentioned fields follow the same behavior of old surface such that for any field f of new material point P located at r:

$$f(r) = f^{\Gamma^{old}} + \nabla f^{\Gamma^{old}} \cdot (r - a^{old}) \tag{6.82}$$

where $f^{\Gamma^{old}}$ and a^{old} denote the value of f at old surface material point and old cell radius, respectively, both in undeformed configuration. The above assumption is made base on the continuous and smooth changes of cell's fields with no jump in the field or its gradient inside the cell.

6.5 Simulations to verify the mathematical model

In this section some simulations are presented to verify the validity of the proposed work using previous studies and experiments. In all examples, an axisymmetric circular cell with radius a_0^c is located on a similar substrate with radius a_0^s, and several features of the proposed work, related to contractile behavior of the cell and cell spreading, are investigated. First, the effect of substrate stiffness is studied on rate of cell growth and its steady state area. In this case, it is assumed that there are enough ligands on substrate surface to have all high-affinity integrins attached to substrate. Then, we investigate the force induced to substrate from cell via adhesion complexes for different substrate stiffnesses. This force is the result of contractile behavior of the cell. Finally, we show how ligand concentration affects the mentioned force and steady state area of the cell, studied in previous examples. We also

show the distribution of high affinity integrins and stress fibers (radial and circumferential) in cell for different substrate stiffness and at several steps during cell growth. The physical parameters used in following simulations for cell and substrate characteristics are listed in Table 6.1.

Definition	**Symbol**	**Value**	**unit**	**Ref.**
Cytosol volume fraction	ϕ^f	70	%	[2]
Cytoskeleton volume fraction	ϕ^c	25	%	n/a
SF+G-actin volume fraction	$\phi^m + \phi^{SF}$	5	%	n/a
Straight+bent integrin concentration	$c^H + c^L$	5e15	$\#/m^2$	[36]
Cytoskeleton permeability	κ/μ	$1e{-}15$	$m^4/N \cdot sec$	[69]
G-actin diffusion constant	D	$5e{-}12$	m^2/sec	[113]
L-integrin mobility coefficient	m	$10e{-}12$	m^2/sec	[96]
Cytoskeleton Young's modulus	E^c	1	kPa	[138]
Cytoskeleton Poisson's ratio	ν^c	0.3		[37]
Substrate Young's modulus	E^s	$1 - 10000$	kPa	[138]
Substrate Poisson's ratio	ν^s	0.3		[37]
Stress fiber maximum tensile stress	T^*	10	kPa	[175]
Stress fiber Young's modulus	E_1	100	kPa	[91]
Integrin-ligand complex stiffness	λ_s	0.15	$nN/\mu m$	[36]
membrane stiffness	k^σ	0.01	N/m	[82]
Absolute temperature	T	310	K	[36]
Membrane surface tension	T_0^σ	$1e{-}2$	N/m	n/a
Filament - G-actin standard potential	$\Delta\mu_0^p$	$1k_BT$	J	[56]
Straight - bent integrin standard potential	$\Delta\mu_0^I$	$5k_BT$	J	[36]
Cell initial radius	a_0^c	14	μm	[138]
Substrate initial radius	a_0^s	30	μm	n/a
Rate of actin polymerization	k_0	280	sec^{-1}	[122]
Cell and substrate thichness	h	1	μm	[36]

Table 6.1: Parameters used in the simulations.

6.5.1 Effect of substrate stiffness on cell contractile and spreading behavior

In this set of simulations, a circular cell is considered to be located on a circular substrate, both under plane stress and axisymmetric conditions. We want to see what changes happen to cell spreading and contractile behavior as the result of change in substrate

stiffness. We expect to observe higher rate of growth, as well as larger steady state area, for the cells located on stiffer substrate [138]. In this example, we provide enough ligands on substrate ($c^{lg} \to \infty$) to make sure that all high-affinity integrins are making adhesion complexes. We also assume that the new material needed for cell body during growth are provided by external sources.

Fig. 6.5, depicts the changes of cell area with time for different substrate stiffness (substrate Young's modulus E^s varies between 1.0 and 1e4 kPa). As expected, we observe that the cells located on stiffer substrates grow faster than the cells located on soft substrates that is in good agreement with experiments done by other researches [138]. The difference between our results and presented experimental results is in quantities. The observed difference is accepted becuause the values (both cell area and time) are of the same order in both figures. Also, because of many other factors affecting cell spreading (not considered in this chapter) we cannot expect our model to give exactly the same values as experimental results.

The rate of cell growth is the same value we presented in Eq. (6.52). In this equation, the pulling force f^p plays the most important role in cell growth rate at the beginning of spreading (because at this step all other parameters including resisting membrane forces f^l and f^g are the same for soft and stiff substrates). As discussed previously, the pulling force f^p is the force applied to cell membrane from adhesion complexes on cell border Γ^c, facilitates cell growth process, and is the result of cell contraction. The stiffness of substrate leads to more relative displacement between cell and substrate that stabilizes high-affinity integrins in the vicinity of cell border Γ^c according to Eq. (6.35). As a result, the traction force of adhesion complexes applied to cell surface increases regarding Eq. (6.25). The increase in focal adhesion force means applying more restriction to cell contraction that leads to generation of more stress fibers, and thus, more contractile force in the body of cell (Eq. (6.24) and [165, 53]). This increased force should be transfered to cell's support (substrate) via adhesion complexes. Consequently, the pulling force f^p increases. The cycle of cell

contraction, increasing relative cell-substrate displacement, high-affinity integrins formation, and adhesion complex force increasing repeats until steady state were the resisting membrane forces f^g and f^l overcome the pulling force f^p and cell stops spreading.

Fig. 6.5 also gives some good information about stress fiber distribution in cell. First, following the process discussed above, more stress fibers are generated in the cell's body in the case of being located on stiffer substrate. But the other fact explored from Fig. 6.5, is that the concentration of both radial and circumferential stress fibers increases by approaching the cell's center. The reason is the contractile force that accumulatively increases toward the center for radial stress fibers, and more circumferential resistance to contraction in the vicinity of center due to the circular configuration of the cell. The other result we can get from Fig. 6.5 is that the reduction of circumferential stress fibers by approaching cell border is less than radial stress fibers reduction that represent almost no radial stress fiber in the vicinity of cell membrane. The reason for this fact is as follows. As we approach the cell border, by decreasing the remaining cell's area with focal adhesion tractions, the contractile force that leads to generation of radial fibers decreases. But in the circumferential direction, even in the cell border, because of circumferential resistance of the circular cell against contraction, there is still a significant amount of stress fibers in the mentioned direction.

Fig. 6.6 depicts the result of what we discussed above about the pulling force f^p that facilitates the cell growth, and the resisting forces f^g and f^l that resist it. While the pulling force increases by substrate stiffness increasing, the global membrane resisting force f^g increases by membrane stretching Eq. (6.29). As a result, the pulling force that is initially much larger than the resisting forces is gradually overcome by membrane being stretched such that the growth stops. It is obvious that the greater the pulling force is, the more deformation is needed for the membrane to overcome the pulling force. On the other hand, for the cells located on very soft substrate, the constant resisting terms, such as f^l that is the result of local deformation of the membrane, are great enough to stop cell spreading. The results depicted in Fig. 6.6, are in very good qualitative and even quantitative agreement

with the experimental results such as what presented in [138].

Furthermore, colored plotted field in Fig. 6.6, represent bound high-affinity integrin concentration (number per unit membrane area)in cell for different substrate stiffneses. It is observed that while the bound high-affinity concentration increases very fast by approaching cell's border, its maximum value at the cell border increases by increase in substrate stiffness. Both these phenomena can be explained by the mechanical term of free energy of bound high-affinity integrins (Eq. (6.35)) that stabilizes them. The absolute value of the mentioned mechanical energy increases by increase in relative cell-substrate displacement $\Delta_i = u^c - u^s$. Δ_i increases by approaching cell's border because of cell's displacement being accumulatively increased. Also, as the substrate stiffness increases, following what we discussed above, integrin-ligand force increases, due to formation of more stress fibers, that leads to increasing the absolute value of the mechanical term of free energy of bound high-affinity integrins, and then more stabilization in high-affinity integrins happens, and thus more high-affinity integrins are generated.

6.5.2 Effect of ligand concentration on cell contractile and spreading behavior

In previous simulations, we assumed infinity number of ligands available on substrates surface such that all high-affinity integrins were attached to substrate. Let us now study the effect of ligand concentration, ranging from 1e-3 to 1e3, on different phenomena discussed above such as cell area in steady state and focal adhesion force.

Fig. 6.7 depicts the changes of cell grown area as a function of ligand concentration for different substrate stiffness. It is obvious in the figure that by increasing ligand concentration, the final cell area increases. The reason is explained by what we presented in Eq. (6.34) as bound high-affinity definition. The number of bound high-affinity integrins increase by increasing ligand concentration. As a result, more pulling force (integrin-ligand force) is produced that leads to larger grown area for the cell according to what we explained in the previous examples. The lower limit of the curves shown in Fig. 6.7 converges to the value

presented in previous set of simulations for very soft substrate. The reason is that in the case of cell being located on very soft substrate, as discussed previously, substrate resistance to cell contraction is very small, as a result even if there are a lot of ligands available, the contractile force and stabilizing term of high-affinity integrins free energy is not large enough to make integrin-ligand complexes that is vital for cell spreading. On the other hand, the upper limit of the curves converges to the maximum values shown in the previous example for different substrate stiffnesses because we assumed in previous simulations that ligand concentration was infinity. between these two limits, there is an almost linear transition region that fits experimental results done in reference [129] (Fig. 6.7).

Finally, Fig. 6.8 depicts what we explained about the cell contractile force (or integrin-ligand complex force) as a function of substrate stiffness and ligand concentration. The figure shows that the mentioned force increases by increasing ligand concentration or substrate stiffness, such that it finally converges to a value related to the cell located on a very stiff substrate with infinite number of ligands on it. Both substrate stiffness and ligand concentration provide more constraint against cell contraction that leads to generation of more stress fibers, and thus, contractile force.

6.6 Summary and concluding remarks

As a summary, in this chapter we presented a mathematical model to study cell contraction and spreading as the result of mechanical and chemical interacting with the elastic substrate it is located on. Our model has the following benefits:

- We introduced a stress plane axisymmetric mixture model for cell contractile behavior including its main constituents, namely cytoskeleton, stress fibers, G-actin monomers, and cytosol. This model is able to capture the main factors affecting its contraction such as G-actin flux and formation of stress fibers as the result of chemo-mechanical equilibrium state between G-actin monomer and stress fiber. Generally

stress fibers are generated in the areas (along the directions) that are more restricted to deformation.

- Focal adhesions (integrin-ligand complexes) are modeled in this chapter based on a chemo-mechanical reactions between high-affinity and low-affinity integrins on cell membrane and ligands on substrate. In the proposed model integrin-ligand complexes are formed mostly in areas with more traction force on cell/substrate surface. There is an interaction mechanism between the traction force and contraction force in the cell body such that each of them increases the other until steady state is reached.

- Another feature of the proposed framework is the model we introduced for cell growth. We presented a Ratchet in which cytoskeletal filaments are formed by G-actin polymerization beneath the cell membrane. In this model the difference between G-actin monomer and filament chemical potentials, and membrane resistance, due to its local deformation and global stretching, resist the cell growth. On the other hand, the traction force on cell membrane increases the rate of growth. Growth (cell spreading) continues until global membrane resistance overcomes the pulling force.

- We presented a numerical approach based on extended finite element and levelset such that we are able to discretize both cell and substrate using only one mesh for both of them. This feature helps to avoid the difficulties of dealing with the interactions between two different domains. Also, as the cell border is defined by levelset function (not by mesh), we do not change the mesh at each time step during cell growth. Indeed, we are able to consider the effect of cell membrane surface tension on its deformation naturally by using XFEM/levelset features.

At the end, we verified our model by presenting some simulations and comparing them with experimental results done by other researchers. In all simulations we showed that our model is able to predict cells contractile/spreading behavior, such as traction forces on the cell due to focal adhesion formation, grown area and its rate of growth as a function of substrate stiffness and ligand concentration on substrate. In all cases, our model results are in good quantitative and qualitative agreement with experiments.

We are developing our model to 2D case to be able to estimate what is happening during some biological problems related to cell- substrate interactions and cell spreading such as cell migration, morphogenesis, tissue engineering, and wound contraction.

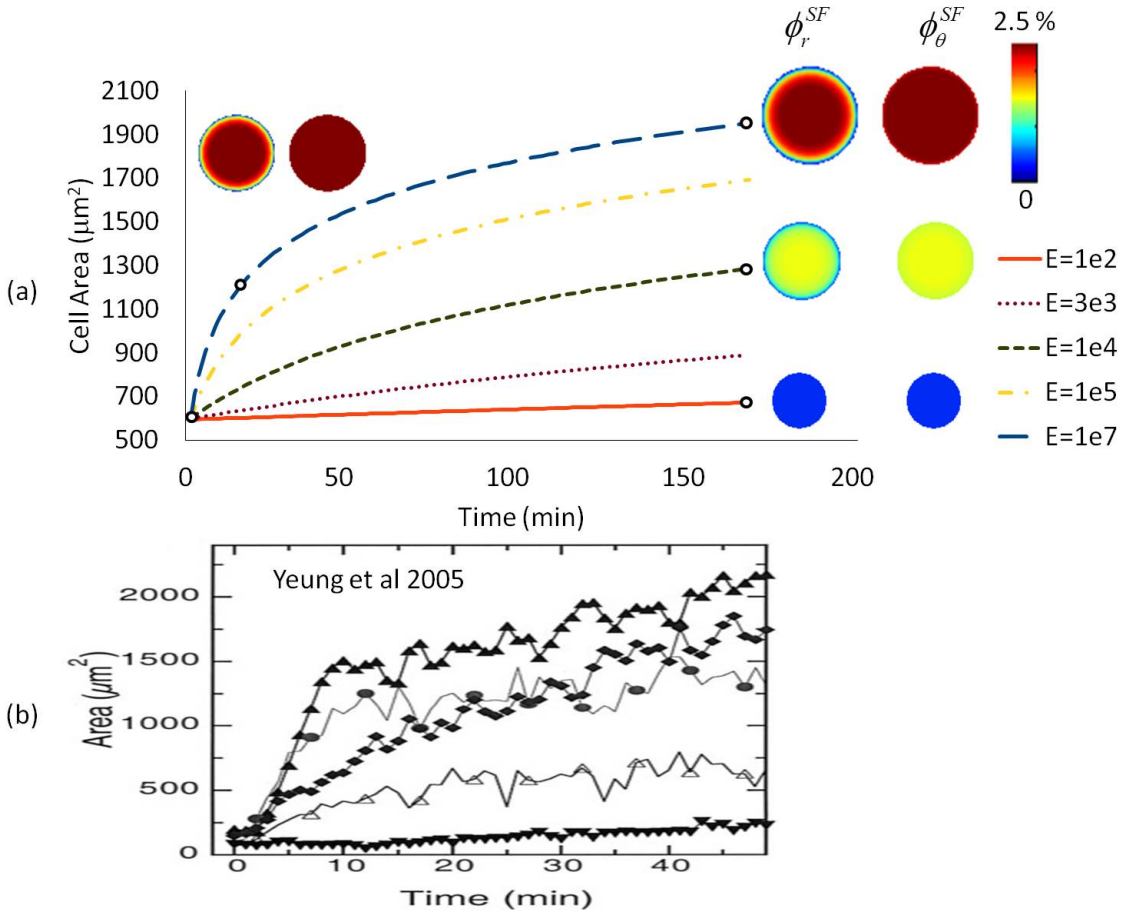

Figure 6.5: a) Changes of cell area and stress fiber volume fraction during growth for different substrate stiffness, and b) a) Experimental results of reference [180].

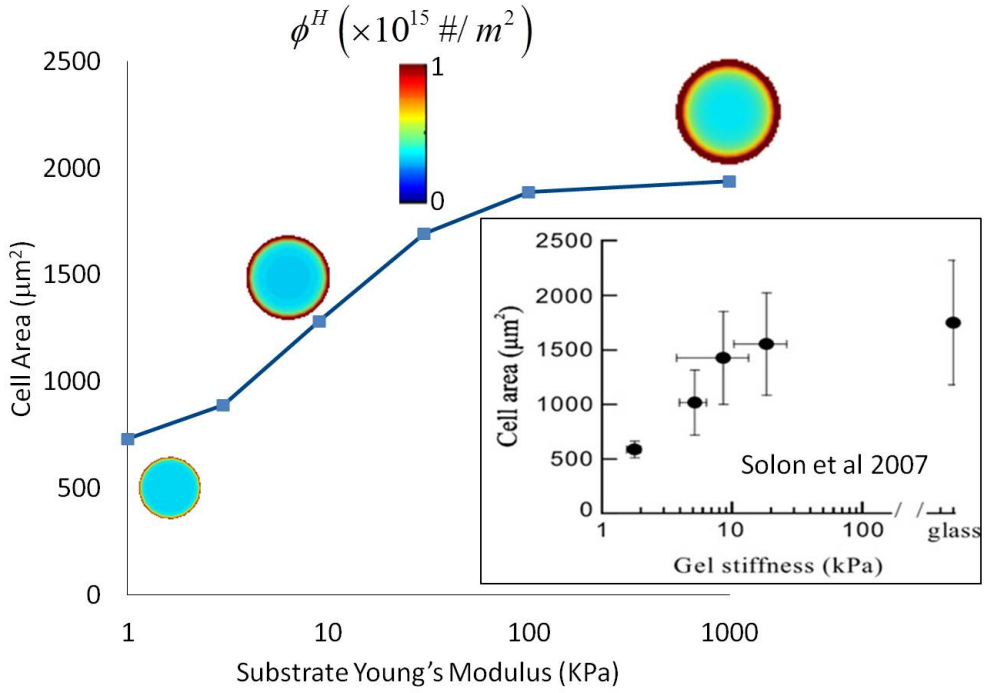

Figure 6.6: Changes of cell area and high-affinity integrin concentration at steady state for different substrate stiffness, and comparison with experimental results of [138]

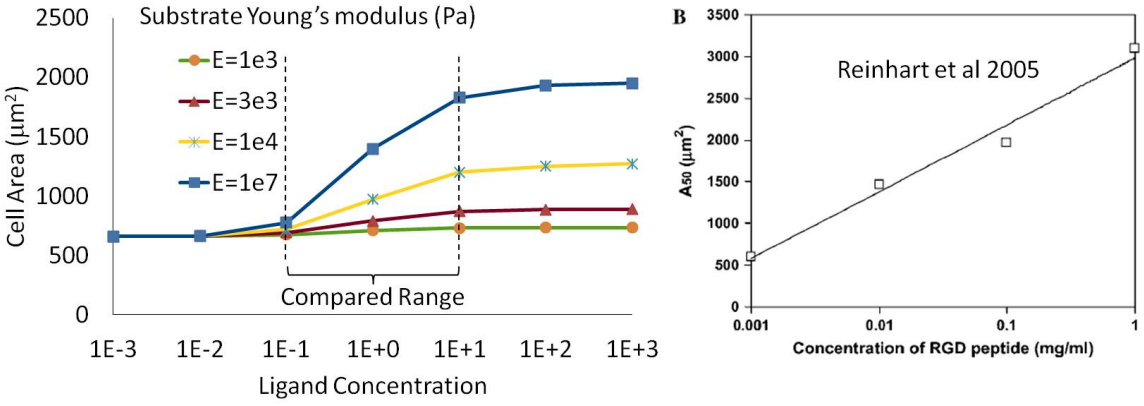

Figure 6.7: Changes of cell area at steady state for different ligand concentration, and comparison with experimental results of [129]

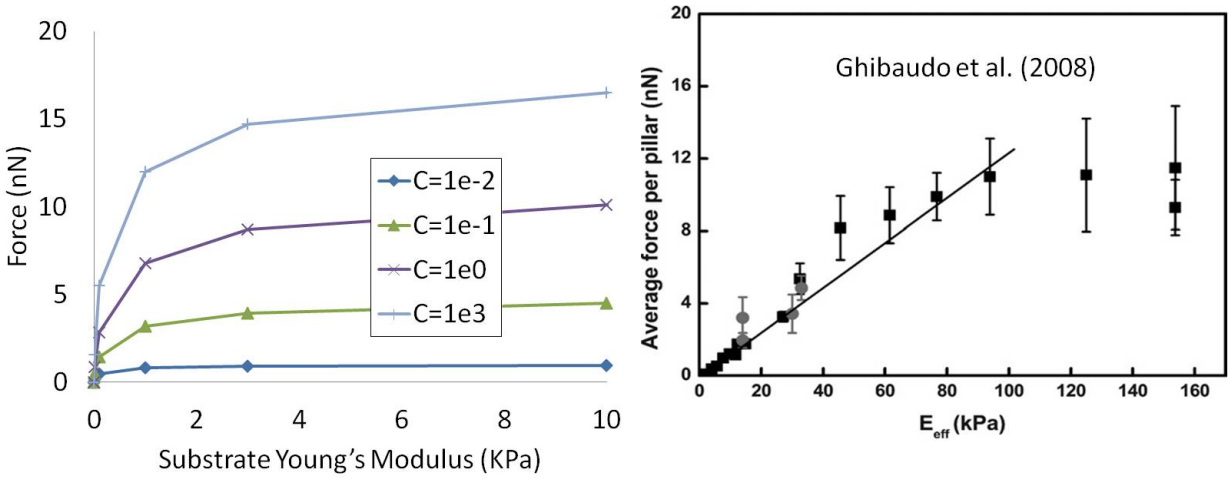

Figure 6.8: Changes of integrin-ligand complex force at steady state for different substrate stiffness and ligand concentration, and comparison with experimental results of [62]

Chapter 7

Summary, Concluding Remarks, and Suggestions for Future Work

In summary, this thesis presented a new theoretical/computational framework to model the large deformation of cells, accounting for the effect of a stiff surrounding cortical membrane. Under the assumption of a very small cortical thickness, the equations of surface elasticity, originally developed for free surface stresses in solids, were developed in the case of large deformations following the Eulerian description. A numerical formulation, based on the XFEM/level-set method was then introduced and utilized to study the effect of cortical elasticity on the deformation of a contractile cell. The contributions and advantages of the proposed method can be summarized as follows:

- The geometry of the cell is entirely represented by level-set functions that are defined independently from the finite element mesh. Simple, regular FEM meshes may thus be used regardless of the geometric complexity of the cell.

- Discontinuities in velocities and deformations resulting from the governing equations are naturally taken into account within the XFEM methodology.

- The model provides an efficient and flexible way to incorporate the contribution of cortical membrane in cell mechanics. In particular, it can easily be extended to incorporate more sophisticated descriptions of the cell's cytoskeleton and its cortical membrane.

Our analysis on the effects of the cortical membrane on cell deformation generally showed that by adding stiffness to the cell's surface, the presence of the cortex induced homogeneous membrane strains and curvature. While this aspect had been shown with a simple analysis considering a cable deforming under the action of an external perpendicular force, the model neglected the effects of cytoskeletal elasticity on surface deformation. Because it is able to incorporate the effect of both cytoskeleton and cortical membrane deformation, the proposed framework could overcome these limitations and accurately capture the distinct role of surface and bulk elasticity in cell deformation. Results showed that while the analytical solution provides a good approximation of membrane curvature when the cytoskeleton is much softer than the cortical membrane, it greatly overestimated its value for low values of cortical stiffness. The numerical method was then used to investigate the variation of cell deformation for various cytoskeleton elastic parameters as well as cortical tension and elasticity. This technique may therefore prove very useful in the determination of cell properties through the analysis of its shape.

Furthermore, this thesis presents a mixture framework that aims at describing the processes by which contractile cells are able to sense their mechanical environment (through stiffness) and react by adjusting the amount of contractile force they generate. By describing the cell's body as a mixture of four critical contractile elements, the proposed model is able to accurately capture the interplay between both mechanical and chemical mechanisms taking place in cells. The key features of the approach are:

- SF contraction is described by the velocity-tension and length-tension relationships arising from cross-bridge dynamics

- SF formation arises from mass exchange with dispersed globular actin monomers and is assumed to depend on the tension in existing SF. This aspect is the main assumption of the model regarding the mechano-sensitivity of contraction. Cytosol and globular actin transport is described by conventional diffusion-convection type

laws

- Cell contraction is described in terms of both passive elasticity of the cytoskeleton and active contractile stress from a statistical distribution of SF.

The model exhibits a positive feedback mechanism resulting between mechanical-chemical interplay between constituents. Contractile stress (that depends on strain-rate through the tension velocity relationship) promotes SF formation and SF formation results in increasing contraction. This loop eventually ends when the stock of available globular actin for SF formation is depleted. The solution to the model shows that this chemo-mechanical cross-talk could be responsible for the sensitivity of cell contraction on substrate stiffness. In other words, the proposed model may be used as a first step to characterize the interactions between a contractile cell and its environment, which is an important feature of the processes of tissue remodeling, would healing and morphogenesis. In addition, the present study has shown how multiscale principles [164](homogenization) and multiphasic mixture concepts can be extended to investigate the active behavior of cells. This approach is very promising as various physical processes including chemistry, mechanics and transport and their interactions can be described in a consistent framework that satisfy basic conservation principles (balance of mass, momentum and energy).

In addition, this we presented a numerical approach to study the behavior of contractile cells and their interactions with a two-dimensional elastic substrate. The continuum model of cell contraction is based on a constrained mixture formulation [165] that describes the contractile apparatus of cells in terms of four major constituents, namely cytoskeleton, cytosol, G-actin monomers and F-actin (or SF) polymers. This framework enables us to characterize important processes of cell contraction such as SF formation (mass exchange between actin monomers and SF), actin diffusion and convection as well as the evolution of a anisotropic contractile network in time. Biologically, the model rests on two key assumptions: (a) SF contraction increases with decreasing strain rate (Hill's model) and (b)

SF formation is promoted by contraction. The interactions of cells with their underlying substrate were then considered through focal adhesions, modeled here by an elastic cohesive law between the two continua.

The main contribution of this work was the introduction of an XFEM/level set method to accurately and efficiently model the interactions between cells of arbitrary shapes and an underlying deformable substrate. The key feature of the proposed method are as follows:

- Despite being represented by two distinct domains, cell and substrate are discretized by a single, regular finite-element mesh. The (possibly complex) cell geometry is then defined in terms of an analytical function (the level-set function) that is independent of discretization. This feature has the merit of greatly simplifying the numerical issues associated with meshing complex geometries and handling interactions between bodies discretized by distinct meshes.

- The stiffness of the thin cortical layer surrounding cells can naturally be accounted for by incorporating surface elasticity on the cell boundary. This feature is possible by enriching the XFEM shape functions with weak discontinuity functions, that enable a jump in stress across the cell membrane.

- Since cell geometry is independent of discretization, the method can be extended to describe cell growth, migration and spreading without resorting to remeshing techniques, known to be computationally expensive. Instead, more efficient techniques involving level-set evolution equations can be invoked. This will be the object of future studies.

The performance of the method was then assessed by considering biologically relevant problems of cell-substrate interactions. Generally, our results showed that the proposed numerical method, together with the constrained mixture formulation, led to realistic behaviors that correlated very well with experimental observations. The coupling of XFEM

and the levelset method therefore provides a promising route to study a variety of biological problems involving cell-substrate interactions, such as morphogenesis, tissue engineering, cell spreading and migration as well as wound contraction.

Finally, in this thesis we presented a mathematical model to study cell contraction and spreading as the result of mechanical and chemical interacting with the elastic substrate it is located on. Our model has the following benefits:

- We introduced a stress plane axisymmetric mixture model for cell contractile behavior including its main constituents, namely cytoskeleton, stress fibers, G-actin monomers, and cytosol. This model is able to capture the main factors affecting its contraction such as G-actin flux and formation of stress fibers as the result of chemo-mechanical equilibrium state between G-actin monomer and stress fiber. Generally stress fibers are generated in the areas (along the directions) that are more restricted to deformation.

- Focal adhesions (integrin-ligand complexes) are modeled in this thesis based on a chemo-mechanical reactions between high-affinity and low-affinity integrins on cell membrane and ligands on substrate. In the proposed model integrin-ligand complexes are formed mostly in areas with more traction force on cell/substrate surface. There is an interaction mechanism between the traction force and contraction force in the cell body such that each of them increases the other until steady state is reached.

- Another feature of the proposed framework is the model we introduced for cell growth. We presented a Ratchet in which cytoskeletal filaments are formed by G-actin polymerization beneath the cell membrane. In this model the difference between G-actin monomer and filament chemical potentials, and membrane resistance, due to its local deformation and global stretching, resist the cell growth. On the other hand, the traction force on cell membrane increases the rate of growth.

Growth (cell spreading) continues until global membrane resistance overcomes the pulling force.

- We presented a numerical approach based on extended finite element and levelset such that we are able to discretize both cell and substrate using only one mesh for both of them. This feature helps to avoid the difficulties of dealing with the interactions between two different domains. Also, as the cell border is defined by levelset function (not by mesh), we do not change the mesh at each time step during cell growth. Indeed, we are able to consider the effect of cell membrane surface tension on its deformation naturally by using XFEM/levelset features.

At the end, we verified our model by presenting some simulations and comparing them with experimental results done by other researchers. In all simulations we showed that our model is able to predict cells contractile/spreading behavior, such as traction forces on the cell due to focal adhesion formation, grown area and its rate of growth as a function of substrate stiffness and ligand concentration on substrate. In all cases, our model results are in good quantitative and qualitative agreement with experiments.

Bibliography

[1] E.S. Almeida and R.L. Spilker. Mixed and penalty finite element models for the nonlinear behavior of biphasic soft tissues in finite deformationl part 1- alternate formulations. Computer Methods and Biomechanics and Biomedical Engineering, 1:25–46, 1997.

[2] G.A. Ateshian, M. Likhitpanichkul, and C.T. Hung. A mixture theory analysis for passive transport in osmotic loading of cells. Journal of Biomechanics, 39:464–475, 2006.

[3] R. Bar-Ziv, T. Tlusty, E. Moses, S. A. Safran, and A. Bershadsky. Pearling in cells: A clue to understanding cell shape. Proc. Natl. Acad. Sci., 96:10140–10145, 1999.

[4] S. C. Baxter, M. O. Morales, and E. C. Goldsmith. Adaptive changes in cardiac fibroblast morphology and collagen organization as a result of mechanical environment. Cell Biochem Biophys, 51:33–44, 2008.

[5] E. Bell, B. Invarsson, and C. Merrill. Production of a tissue-like structure by contraction of collagen lattices by human fibroblasts of different proliferative potential in vitro. PNAS, 76:1274–1278, 1979.

[6] E. Bell, B. Ivarsson, and C. Merrill. Production of a tissue-like structure by contraction of collagen lattices by human fibroblasts of different proliferative potential in vitro. Proc. Natl. Acad. Sci. USA, 76:1274–1278, 1979.

[7] T. Belytschko and R. Gracie. On xfem applications to dislocatios and interfaces. International Journal of Plasticity, 23(10-11):1721–1738, 2007.

[8] T. Belytschko, W.K. Liu, and B. Moran. Nonlinear finite elements for continua and structures. Wiley and Sons, 2000.

[9] T. Belytschko, Ch. Parimi, N. Moes, N. Sukumar, and Sh. Usui. Structured extended finite element methods for solids defined by implicit surfaces. International Journal for Numerical Methods in Engineering, 56(4):609–635, 2003.

[10] Ted Belytschko, Wing Kam Liu, and Brian Moran. Nonlinear Finite Elements for Continua and Structures. John Wiley & Sons LTD, 2006.

[11] A D Bershadsky, N Q Balaban, and B Geiger. Adhesion dependent cell mechanosensitivity. Annu. Rev. Cell Dev. Biol, 19:677–695, 2003.

[12] M.A. Biot. General theory of three-dimensional consolidation. Journal of Applied Physics, 12:155–164, 1941.

[13] M.A. Biot. The elastic coefficients of the theory of consolidation. Journal of Astrophysics and Astronomy, 24:594–601, 1957.

[14] I. B. Bischofs, F. Klein, D. Lehnert, M. Bastmeyer, and U. S. Schwuartz. Filamentous network mechanics and active contractility determine cell and tissue shape. Biophysics Journal, 95:3488–3496, 2008.

[15] I. B. Bischofs and U. S. Schwarz. Cell organization in soft media due to active mechanosensing. Proceedings of the National Academy of Science, 100(16):9274–9279, 2003.

[16] I.B. Bischofs, F. Klein, D. Lehnert, M. Bastmeyer, and U.S. Schwarz. Filamentous network mechanics and active contractility determine cell and tissue shape. Biophysical Journal, 95:3488–3496, 2008.

[17] R.M. Bowen. Incompressible porous media models by the use of the theory of mixtures. International Journal of Engineering Science, 18:1129–1148, 1980.

[18] M. Bray, S. P. Sheehy, and K. K. Parker. Sarcomere alignment is regulated by myocyte shape. Cell Motility and the Cytoskeleton, 65:641–651, 2008.

[19] M. P. Bray, W. J. Adams, N. A. Geisse, A. W. Feinberg, S. P. Sheehy, and K. K. Parker. Nuclear morphology and deformation in engineered cardiac myocytes and tissues. Biomaterials, 31:5143–5150, 2010.

[20] A Brock, E Chang, C Ho, P Leduc, X Jiang, G M Whitesides, and D E Ingber. Geometric determinants of directional cell motility revealed using microcontact printing. Langmuir, 19:1611–1617, 2003.

[21] D.T. Butcher, T. Alliston, and V.M. Weaver. A tense situation: forcing tumour progression. Nat. Rev. Cancer, 9:108–122, 2009.

[22] F.D. Carlson and D.R. Wilkie. Muscle Physiology. Prentice Hall, 1974.

[23] C S Chen, J L Alonso, E Ostuni, G M Whitesides, and D E Ingber. Cell shape provides global control of focal adhesion assembly. Biochem. Biophys. Res. Commun., 307:355–361, 2003.

[24] D. Choquet, D. F. Felsenfeld, and M. P. Sheetz. Extracellular matrix rigidity causes strengthening of integrin-cytoskeletal linkages. Cell, 88:39–48, 1997.

[25] M. Chrzanowska-Wodnicka and K. Burridge. Rho-stimulated contractility drives the formation of stress fibers and focal adhesions. The Rockefeller University Press, 133(6):1403–1415, 1996.

[26] K.D. Costa, E.J. Lee, and J.W. Holmes. Creating alignement and anisotropy and engineering heart tissue: role of boundary conditions in a model three-dimensional culture system. Tissue Engineering, 9(4):567–577, 2003.

[27] K.D. Costa, E.J. Lee, and J.W. Holmes. Creating alignment and anisotropy in engineered heart tissue: Role of boundary conditions in model three-dimensional culture system. Tissue Engineering, 9:567–577, 2003.

[28] Mark F. Coughlin and Dimitrije Stamenovic. A prestressed cable network model of the adherent cell cytoskeleton. Biophysics Journal, 84:1328–1336, 2003.

[29] O. Coussy. Poromechanics. Jon Wiley and Sons, Ltd, Third Edition, 2004.

[30] Louise P. Cramer. Molecular mechanism of actin-dependent retrograde flow in lamellipodia of motile cells. Frontiers in Bioscience, 2:d26–270, 1997.

[31] Louise P Cramer, Timothy J Mitchison, and Julie A Theriot. Actin-dependent motile forces and cell motility. Current Opinion in Cell Biology, 6:82–86, 1994.

[32] Damien Cuvelier, Manuel Thery, Yeh-Shiu Chu, Sylvie Dufour, Jean-Paul Thiery, Michel Bornens, Pierre Nassoy, and L. Mahadevan. The universal dynamics of cell spreading. Current Biology, 17:694–699, 2007.

[33] J. Dai and M.P. Sheetz. Membrane tether formation from blebbing cells. Biophysical Journal, 77:3363–3370, 1999.

[34] J.C. Dallon and H.P. Ehrlich. A review of fibroblast-populated collagen lattices. Wound repair and Regeneration, 16:472–479, 2008.

[35] Vikram S. Deshpande, Robert M. McMeeking, and Anthony G. Evans. A bio-chemo-mechanical model for cell contractility. Proceedings of the National Academy of Science, 103(38):14015–14020, 2006.

[36] Vikram S. Deshpande, Milan Mrksichb, Robert M. McMeekingc, and Anthony G. Evans. A bio-mechanical model for coupling cell contractility with focal adhesion formation. Journal of the Mechanics and Physics of Solids, 56:1484–1510, 2008.

[37] V.S. Deshpande, R.M. McMeeking, and A.G. Evans. A bio-chemo-mechanical model for cell contractibility. PNAS, 103(38):14015–14020, 2006.

[38] V.S. Deshpande, R.M. McMeeking, and A.G. Evans. A model for the contractility of the cytoskeleton including the effects of stress-fibre formation and dissociation. Proc. R. Soc. A, 463:787–815, 2007.

[39] V.S. Deshpande, M. Mrksich, R.M. McMeeking, and A.G. Evans. A bio-mechanical model for coupling cell contractility with focal adhesion formation. Journal of the Mechanics and Physics of Solids, 56:1484–1510, 2008.

[40] P.A. DiMilla, K. Barbee, and D.A. Lauffenburger. Mathematical model for the effects of adhesion and mechanics on cell migration speed. biophysical Journal, 60:15–37, 1991.

[41] D. E. Discher, P. Janmey, and Y. Wang. Tissue cells feel and respond to the stiffness of their substrate. Science., 310(5751):1139–1143, 2005.

[42] Dennis E. Discher, Paul Janmey, and Yu li Wang. Tissue cells feel and respond to the stiffness of their substrate. Science, 310:1139–1143, 2005.

[43] J. Dolbow, N. Moes, and T. Belytschko. An extended finite element method for modeling crack growth with frictional contact. Computer Methods in Applied Mechanics and Engineering, 190(51-52):6825–6846, 2001.

[44] John Dolbow and Belytschko. Finite element method for crack growth without remeshing. International Journal for Numerical Methods in Engineering, 46(1):131–150, 1999.

[45] Ravindra Duddu, Stephane Bordas, David Chop, and Brian Moran. A combined extended finite element and level set method for biofilm growth. ijnme, 74:848–870, 2008.

[46] G.A. Dunn and T. Ebendal. Contact guidance on oriented collagen gels. Exp Cell Res, 111(2):475–479, 1978.

[47] M. Eastwood, V. C. Mudera, D. A. McGrouther, and R. A. Brown. Effect of precise mechanical loading on fibroblast populated collagen lattices: Morphological changes. Cell, 40:13–21, 1998.

[48] H.P. Ehrlich, G. Gabbiani, and P. Meda. Cell coupling modulates the contraction of fibroblast-populated collagen lattices. Journal of Cellular Physiology, 184:86–92, 2000.

[49] R. Engelke, Heinrich. D., and J. Radler. Probing gfp-actin diffusion in living cells using fluorescence correlation spectroscopy. Phys. Biol., 7:1–9, 2010.

[50] A. J. Engler, S. Sen, H. L. Sweeney, and D. E. Discher. Matrix elasticity directs stem cell lineage specification. Cell, 26:687–689, 2006.

[51] Adam J. Engler, Christine Carag-Krieger, Colin P. Johnson, Matthew Raab, Hsin-Yao Tang, David W. Speicher, Joseph W. Sanger, Jean M. Sanger, and Dennis E. Discher. Embryonic cardiomyocytes beat best on a matrix with heart-like elasticity: scar-like rigidity inhibits beating. Journal of Cell Science, 121:3794–3802, 2008.

[52] O Fackler and R Grosse. Cell motility through plasma membrane blebbing. The Journal of Cell Biology, 181:879–884, 2008.

[53] Mehdi Farsad and Franck Vernerey. A multiphysics computational strategy for the modelling of cell-substrate interactions. International Journal for Numerical Methods in Engineering, page under review, 2011.

[54] Mehdi Farsad, Franck J. Vernerey, and Harold S. Park. An extended finite element/level set method to study surface effects on the mechanical behavior and properties of nanomaterials. International Journal for Numerical Methods in Engineering, 84(12):1466–1489, 2010.

[55] P. Fernandez and A.R. Bausch. The compaction of gels by cells: a case of collective mechanical activity. Integrative biology, 1:252–259, 2009.

[56] Louis Focard and Franck J. Vernerey. A thermodynamical model for stress-fiber organization in contractile cells. Applied Physics Letters, page under review, 2011.

[57] M. L. Gardel, J. H. Shin, F. C. MacKintosh, L. Mahadevan, P. Matsudaira, and D. A. Weitz. Elastic behavior of cross-linked and bundled actin networks. Science, 304:1301–1305, 2004.

[58] K. Garikipati, E.M. Arruda, K. Grosh, H. Narayanan, and S. Calve. A continuum treatment of growth in biological tissue: the coupling of mass transport and mechanics. Journal of the Mechanics and Physics of Solids, 52:1595–1625, 2004.

[59] T.C. Gasser, R.W. Ogden, and G.A Holzapfel. Hyperleastic modelling of arterial layers with distributed collagen fibre orientations. Journal of the Royal Society Interface, 3:15–35, 2006.

[60] B. Geiger and A. Bershadsky. Exploring the neighborhood: adhesion-coupled cell mechanosensors. Cell, 110:139–142, 2002.

[61] N. A. Geisse, S. P. Sheehy, and K. K. Parker. Control of myocyte remodeling in vitro with engineered substrates. In Vitro Cell.Dev.Biol.-Animal, 45:343–350, 2009.

[62] Marion Ghibaudo, Alexandre Saez, , Le Trichet, Alain Xayaphoummine, Julien Browaeys, Pascal Silberzan, Axel Buguinb, and Benot Ladoux. Traction forces and rigidity sensing regulate cell functions. Soft Material, 4:1836–1843, 2008.

[63] Gregory Giannone, Benjamin J. Dubin-Thaler, Hans-Gunther Dobereiner, Nelly Kieffer, Anne R. Bresnick, and Michael P. Sheetz. Periodic lamellipodial contractions correlate with rearward actin waves. Cell, 116:431–443, 2004.

[64] Nir S. Gov and Ajay Gopinathan. Dynamics of membranes driven by actin polymerization. Biophysical Journal, 90:454–469, 2006.

[65] F. Grinnel and C.R. Lamke. Reorganization of hydrated collagen lattices by human skin fibroblasts. Journal of Cell Science, 66:51–63, 1984.

[66] W.Y. Gu, W.M. Lai, and V.C. Mow. Transport of multi-electrolytes in charged hydrated biological soft tissues. Transport in Porous Media, 34:143–157, 1999.

[67] F. Guilak, G.R. Erickson, and H. Ping Ting-Beall. The effects of osmotic stress on the viscoelastic and physical properties of articular chondrocytes. Biophysical Journal, 82:720–727, 2002.

[68] F. Guilak, M.A. Haider, L.A. Setton, T.A. Laursen, and F.P.T Baaijens. Multiphasic models of cell mechanics. Cytoskeletal Mechanics: models and measurements, Cambridge University Press, pages 84–102, 2006.

[69] F. Guilak and V.C. Mow. The mechanical environment of the chondrocyte: a biphasic finite element model of cell-matrix interactions in articular cartilage. Journal of Biomechanics, 33:1663–1673, 2000.

[70] W.H. Guo, M.T. Frey, N.A. Burnham, and Y.L. Wang. Substrate rigidity regulates the formation and maintenance of tissues. Biophysical Journal, 90:2213–2220, 2006.

[71] M. E. Gurtin. A general theory of curved deformable interfaces in solids at equilibrium. Philosophical Magazine A, 78(5):1093–1109, 1998.

[72] J. C. Hansen, R. Skalak, S. Chien, and A. Hoger. An elastic network model based on the structure of the red blood cell membrane skeleton. Biophysics Journal, 70:146–166, 1996.

[73] J. C. Hansen, R. Skalak, S. Chien, and A. Hoger. Influence of network topology on the elasticity of the red blood cell membrane skeleton. Biophysics Journal, 72:2369–2381, 1997.

[74] A. K. Harris, D. Stopak, and P. Warner. Generation of spatially periodic patterns by a mechanical instability: A mechanical alternative to the turing model. Journal of Embryology and Experimental Morphology, 80:1–20, 1984.

[75] A. K. Harris, P. Wild, and D. Stopak. Silicone rubber substrata: a new wrinkle in the study of cell locomotion. Science, 208:177–179, 1980.

[76] A.K. Harris, D. Stopak, and P. Wild. Fibroblast traction as a mechanism for collagen morphogenesis. Nature, 290:249–251, 1980.

[77] John H. Hartwig and Patty Shevlin. The architecture of actin filaments and the ultrastructural location of actin-binding protein in the periphery of lung macrophages. The Journal of Cell Biology, 103:1007–1020, 1986.

[78] W. S. Haston, J. M. Shields, and P. C. Wilkinson. The orientation of fibroblasts and neutrophils on elastic substrata. Exp. Cell Res, 146:117–126, 1983.

[79] T. Hettich, A. Hund, and E. Ramm. Modeling of failure in composites by x-fem and level sets within a multiscale framework. Computer Methods in Applied Mechanics and Engineering, 197:414–424, 2008.

[80] A.V Hill. The heat of shortening and the dynamic constant of muscles. The Rockefeller University Press, 126:136–195, 1938.

[81] A.V. Hill. The heat of shortening and the dynamic constant of muscles. Proc. R. Soc. B, 126:136–195, 1938.

[82] R. M. HOCHMUTH, N. MOHANDAS, and P. L. BLACKSHEAR. Measurement of the elastic modulus for red cell membrane using a fluid mechanical technique. Biophysics Journal, 13:747–762, 1973.

[83] Neil Hodge and Panayiotis Papadopoulos. Continuum modeling and numerical simulation of cell motility. Journal of Mathematical Biology, 2011.

[84] Michael J. Hogan and Lynette Feeney. The ultrastructure of the retinal vessels: Iii. vascular-glial relationships. Journal of Ultra Research, 9:47–64, 1963.

[85] S. Huang and D.E. Ingber. The structural and mechanical complexity of cell-growth control. Nature Cell Biology, 1:E131–E138, 1999.

[86] J.D. Humphrey and K.R. Rajagopal. A constrained mixture model for growth and remodeling of soft tissues. Mathematical Models and Methods in Applied Sciences, 12:407–430, 2002.

[87] D.E. Ingber. Tensegrity i. cell structure and hierarchical systems biology. Journal of Cell Science, 116:1157–1173, 2003.

[88] D.E. Ingber. Tensegrity ii. how structural networks influence cellular information processing networks. Journal of Cell Science, 116:1397–1408, 2003.

[89] Daniel G. Jay. The clutch hypothesis revisited: Ascribing the roles of actin-associated proteins in filopodial protrusion in the nerve growth cone. Journal of Neurobiology, 44:114–125, 2000.

[90] H. Karcher, J. Lammerding, H. Huang, R. T. Lee, R. D. Kamm, and M. R. Kaazempur-Mofrad. A three-dimensional viscoelastic model for cell deformation with experimental verification. Biophysics Journal, 85:3336–3349, 2003.

[91] K. Kawabata, Y. Sado, M. Nagayama, T. Nitta, K. Nemoto, Y. Koyama, and H. Haga. Visualization of dynamic organization of cytoskeleton gels in living cells by hybrid-spm. Chinese Journal of Polymer Science, 2:169–174, 2003.

[92] Hansuli Keller and Peter Eggli. Actin accumulation in pseudopods or in the tail of polarized walker carcinosarcoma cells quantitatively correlates with local folding of the cell surface membrane. Cell Motility and the Cytoskeleton, 40:342–353, 1998.

[93] Michael M. Kozlov and Alexander D. Bershadsky. Processive capping by formin suggests a forcedriven mechanism of actin polymerization. The Journal of Cell Biology, 167:1011–1017, 2004.

[94] S. Kumar, I. Z. Maxwell, A. Heisterkamp, T. R. Polte, T. P. Lele, M. Salanga, E. Mazur, and D. E. Ingber. Viscoelastic retraction of single living stress fibers and its impact on cell shape, cytoskeletal organization, and extracellular matrix mechanics. Biophysics Journal, 85:3762–3773, 2006.

[95] A. Lambert, B.V. Nusgens, and M. Lapiere. Mechano-sensing and mechano-reaction of soft connective tissue cells. Adv. Space Res, 21(8/9):1081–1091, 1998.

[96] Douglas A Lauffenburger and Jennifer J Linderman. Receptors models for binding, trafficking, and signaling. Oxford University Press, New York, 1993.

[97] Thomas Lecuit and Pierre-Franois Lenne. Cell surface mechanics and the control of cell shape, tissue patterns and morphogenesis. Nature Reviews Molecular Cell Biology, 8:633–644, 2007.

[98] I. Levental, P.C. Georges, and P.A. Janmey. Soft biological materials and their impact on cell function. Soft Matter, 2:1–9, 2006.

[99] C.M. Lo, H.B. Wang, M. Dembo, and Y.L. Wang. Cell movement is guided by the rigidity of the substrate. Biophysical Journal, 79:144–152, 2000.

[100] F.C. MacKintosh, J. Kas, and P.A. Janmey. Elasticity of semi flexible biopolymer networks. Physical Review Letters, 75:4425, 1995.

[101] M. Makale. Cellular mechanobiology and cancer metastasis. Birth Defects Research (Part C), 81:329–343, 2007.

[102] P. Martin. Wound healing: Aiming for perfect skin regeneration. Science, 276:75–81, 1997.

[103] J P McGarry, B P Murphy, and P E McHugh. Computational mechanics modelling of cellsubstrate contact during cyclic substrate deformation. Journal of the Mechanics and Physics of Solids, 53:2597–2637, 2005.

[104] A. Menzel, M. Harrysson, and M. Ristinmaa. Towards an orientation-distribution-based multi-scale approach for remodelling biological tissues. Computer Methods in Biomechanics and Biomedical Engineering, 11(5), 2008.

[105] N. Moes, M. Cloirec, P. Cartraud, and J.-F. Remacle. A computational approach to handle complex microstructure geometries. Computer Methods in Applied Mechanics and Engineering, 192:3163–3177, 2003.

[106] S. Mohammadi. Extended Finite Element Method. Blackwell, 2008.

[107] C. Mohrdieck, A. Wanner, R. Wouter, A. Roth, E. Sackmann, J. Spatz, and E. Arzt. A theoretical description of elastic pillar substrates in biophysical experiments. ChemPhysChem, 6:1492–1498, 2005.

[108] n. Wang, J. P. Butler, and D. E. Ingber. Mechanotransduction across the cell surface and through the cytoskeleton. Science, 260:1124–1127, 1993.

[109] S. Na, G.A. Meininger, and J.D. Humphrey. A theoretical model for f-actin remodeling in vascular smooth muscle cells subjected to cyclic stretch. Journal of Theoretical Biology, 246:87–99, 2007.

[110] C. M. Nelson, R.P. Jean, J.L. Tan, W.F. Liu, N.J. Snladeckl, A.A. Spector, and C. S. Chen. Emergent patterns of growth controlled by multicellular form and mechanics. PNAS, 102(33):11594–11599, 2005.

[111] A Nicolas and S A Safran. Limitation of cell adhesion by the elasticity of the extracellular matrix. Biophysical Journal, 91:61–73, 2006.

[112] I L Novak, B M Sllepchenko, A Mogilner, and L M Loew. Cooperativity between cell contractility and adhesion. Physical Review Letters, 93:268109:1–4, 2004.

[113] Igor L Novak, Boris M Slepchenko, and Alex Mogilner. Quantitative analysis of g-actin transport in motile cells. Biophysics Journal, 95:1627–1638, 2008.

[114] T. K. Ohsumi, J. E. Flaherty, M.C. Evans, and V.H Barocas. Three-dimensional simulation of anisotropic cell-driven collagen gel compaction. Biomechan Model Mechanobiol, 7:53–62, 2008.

[115] George F. Oster and Alan S. Perelson. Cell spreading and motility: A model lamellipod. Journal of Mathematical Biology, 21:383–388, 1985.

[116] K K Parker, A L Brock, C Brangwynne, R J Mannix, N Wang, E Ostuni N A Geisse, J C Adams, G M Whitesides, and D E Ingber. Directional control of lamellipodia extension by constraining cell shape and orienting cell tractional forces. FASEB J, 16:1195–1204, 2002.

[117] K. K. Parker, J. T., Christopher S. C., and L. Tung. Myofibrillar architecture in engineered cardiac myocytes. Journall of the American Heart Association, DOI: 10.1161/CIRCRESAHA.108.182469:1–12, 2008.

[118] M. Paszek, N. Zahir, K Johnson, J. Lakins, G. Rozenberg, A Gefen, C.A. Reinhart-King, S. Margulies, M. Dembo, D. Boettiger, D.A. Hammer, and V.M. Weaver. Tensional homeostasis and the malignant phenotype. Cancer Cell, 8:241–254, 2005.

[119] Raja Paul, Patrick Heil, Joachim P. Spatz, and Ulrich S. Schwarz. Propagation of mechanical stress through the actin cytoskeleton toward focal adhesions: Model and experiment. Biophysics Journal, 94:1470–1482, 2008.

[120] R. J. Pelham and Y. L. Wang. Cell locomotion and focal adhesions are regulated by substrate flexibility. Proc. Natl. Acad. Sci. USA, 94:13661–13665, 1997.

[121] R.J. Pelham and Y.L. Wang. Cell locomotion and focal adhesions are regulated by substrate flexibility. Cell Biology, 94:13661–13665, 1997.

[122] Charles S. Peskin, Garrett M. Odell, and George F. Oster. Cellular motions and thermal fluctuations: The brownian ratchet. Biophysical Journal, 65:316–324, 1993.

[123] W M Petrol, L Ma, and J V Jester and. Direct correlation of collagen matrix deformation with focal adhesion dynamics in living corneal fibroblasts. Journal of Cell Science, 56:1484–1510, 2003.

[124] Thomas D. Pollard and Gary G. Borisy. Cellular motility driven by assembly and disassembly of actin filaments. Cell, 112:453–465, 2003.

[125] Jun Qiua, Tao Tanga, Meng Zhanga, and Zhuo Zhuang. 2-d finite element simulation of cell-substrate debonding during cyclic stretch. Tsinghua Science and Technology, 14(2):27–31, 2009.

[126] Susanne M. Rafelski and Julie A. Theriot. Crawling toward a unified model of cell motility: Spatial and temporal regulation of actin dynamics. Annual Review of Biochemistry, 73:209–239, 2004.

[127] K.R. Rajagopal and L. Tao. Mechanics of mixture. Series on Advances in Mathematics for Applied Science, 35, 1995.

[128] K.R. Rajagopal and A.S. Wineman. Developement in the mechanics of interactions between a fluid and a highly elastic solid. Recent Developement in Structured Continua. Vol. II, Longman Scientific and Technical, New York, pages 249–292, 1990.

[129] Cynthia A. Reinhart-King, Micah Dembo, and Daniel A. Hammer. The dynamics and mechanics of endothelial cell spreading. Biophysics Journal, 89:676–689, 2005.

[130] B. Rubinstein, K. Jacobson, and A. Mogilner. Multiscale two-dimensional modeling of a motile simple-shaped cell. Multiscale Model. Simul., 3(2):413–439, 2005.

[131] R.K. Sawhney and J. Howard. Slow local movements of collagen fibers by fibroblasts drive the rapid global self organization of collagen gels. The Journal of Cell Biology, 157(6):1083–1091, 2002.

[132] Michelle Schatzman. Numerical analysis: a mathematical introduction. Clarendon Press, Oxford, UK, 2002.

[133] U. S. Schwarz and I. B. Bischofs. Physical determinants of cell organization in soft media. Medical Engineering and Physics, 27:763–772, 2005.

[134] U.S. Schwarz and I.B. Bischofs. Physical determinants of cell organization in soft media. Medical Engineering and Physics, 27:763–772, 2005.

[135] T. Semesh, B. Geiger, A.D. Bershadsky, and M. Kozlov. Focal adhesions as mechanosensors: a physical mechanism. PNAS, 102(35):12383–12388, 2005.

[136] J A Sethian. Levelset methods and fast marching methods: evolving interfaces in computational geometry, fluid mechanics, computer vision, and material science. Cambridge University Press, Cambridge, UK, 1999.

[137] Lubomir B. Smilenov, Alexei Mikhailov, Robert J. Pelham Jr., Eugene E. Marcantonio, and Gregg G. Gundersen. Focal adhesion motility revealed in stationary fibroblasts. Science, 286(5442):1172–1174, 1999.

[138] J. Solon, I. Levental, K. Sengupta and. P. C. Georges, and P. A. Janmey. Fibroblast adaptation and stiffness matching to soft elastic substrates. Biophys J., pages 4453–4461, 2007.

[139] J. Solon, I. Levental, K. Sengupta, P.C. Georges, and P.A. Janmey. Fibroblast adaptation and stiffness matching to soft elastic substrates. Biophysical Journal, 93:4453–4461, 2007.

[140] Matthew R Stachowiak and Ben OShaughnessy. Kinetics of stress fibers. 10:1–26, 2008.

[141] D. Stamenovic, J. Fredberg, N. Wang, D.T. Butcher, and D.E. ingber. A microstructural approach to cytoskeletal mechanics based on tensegrity. J. theor. Biol, 181:125–136, 1996.

[142] W. E. Stehbens. The basal attachment of endothelial cells. Journal of Ultra Research, 15:389–399, 1966.

[143] D. N. Sun, W. Y. Gu, X. E. Guo, W. M. Lai, , and V. C. Mow. A mixed finite element formulation of triphasic mechano-electrochemical theory for charged, hydrated biological soft tissues. International Journal for Numerical Methods in Engineering, 45:1375–1402, 2008.

[144] D.N. Sun, W.Y. Gu, X.E. Guo, W.M. Lai, and V.C. Mow. A mixed finite element formulation of triphasic mechano-electromechanical theory for charged, hydrated biological soft tissues. International Journal for Numerical Methods in Engineering, 45:1375–1402, 1999.

[145] R Sunyer, X Trepat, J J Fredberg, R Farre, , and D Navajas. The temperature dependence of cell mechanics measured by atomic force microscopy. Physical Biologyl, 6:025009: 10pp, 2009.

[146] M Sussman, A Almgren, J B Bell, P Colella, LL H Howell, and M L Welcome. An adaptive level set approach for incompressible two-phase flows. Journal of Computational Physics, 148(1):81–124, 1999.

[147] M Sussman and E Fatemi. An efficient interface preserving level set redistancing algorithm and its application to interfacial incompressible fluid flow. Journal of Scientific Computing, 20(4):1165–1191, 1999.

[148] Freyman. T., I. Yannas, R. Yokoo, and L.J. Gibson. Fibroblast contraction of a collagen-gag matrix. Biomaterials, 22:2883–2891, 2001.

[149] E. Tamariz and F. Grinnell. Modulation of fibroblast morphology and adhesion during collagen matrix remodeling. Molecular Biology of the Cell, 13:3915–3929, 2002.

[150] J.L. Tan, J. Tien, D.M. Pirone, D.S. Gray, K. Bhadriraju, and C.S. Chen. Cells lying on a bed of microneedles: an approach to isolate mechanical force. Pro Natl Acad Sci USA, 100:1484–1489, 2003.

[151] John L. Tan, Joe Tien, Dana M. Pirone, Darren S. Gray, Kiran Bhadriraju, and Christopher S. Chen. Cells lying on a bed of microneedles: an approach to isolate mechanical force. pnas, 100(4):1484–1489, 2003.

[152] Iwao Teraoka. Polymers solutions an introduction to physical properties. Wiley-interscience, New York, 2002.

[153] K. Terzaghi. Theoretical soil mechanics. Wiley, New York; Chapman and Hall, London, 1943.

[154] J-Y Tinevez, U Schulze, G. Salbreux, J. Roensch, J.F. Joanny, and Paluch E. Role of cortical tension in bleb growth. PNAS, 106:18581–18586, 2009.

[155] C. Truesdell and W Noll. Non-linear field theories of mechanics. Handbuch des Physik, Springer, Berlin, pages 537–541, 1965.

[156] Y. Tsuda, H. Yasutake, A. Ishijima, and T. Yanagida. Torsional rigidity of single actin filaments and actinactin bond breaking force under torsion measured directly by in vitro micromanipulation. pnas, 93:12937–12942, 1996.

[157] G. U. Unnikrishnan and V. U. Unnikrishnan. Constitutive material modeling of cell: A micromechanics approach. 129:315–323, 2007.

[158] G. U. Unnikrishnan, V. U. Unnikrishnan, and J.N. Reddy. Constitutive material modeling of cell: A micromechanics approach. Journal of Biomechanical Engineering, 129:315–323, 2007.

[159] Pascal Vallotton, Gaudenz Danuser, Sophie Bohnet, Jean-Jacques Meister, and Alexander B. Verkhovsky. Tracking retrograde flow in keratocytes: News from the front. Molecular Biology of the Cell, 16:1223–1231, 2005.

[160] F. J. Vernerey. On the application of multiphasic theories to the problem of cell-substrate mechanical interactions. Advances in Cell Mechanics, 2010.

[161] F. J. Vernerey. Advances in Cell Mechanics, On the application of multiphasic theories to the problem of cell-substrate mechanical interactions. Springer, 2011.

[162] F. J. Vernerey and et al. A micromorphic model for the multiple scale failure of heterogeneous materials. Journal of the Mechanics and Physics of Solids, 56(4):1320–1347, 2008.

[163] F. J. Vernerey and M. Farsad. An eulerian/xfem formulation for the large deformation of cortical cell membrane. Computer Methods in Biomechanics and Biomedical Engineering, 14(5):433–445, 2011.

[164] F.J. Vernerey, W.K Liu, and B. Moran. Multi-scale micromorphic theory for hierarchical materials. Journal of the Mechanics and Physics of Solids, 55:2603–2651, 2007.

[165] Franck J. Vernerey and Mehdi Farsad. A constrained mixture approach to mechanosensing and force generation in contractile cells. Journal of the Mechanical Behavior of Biomedical Materials, 2011.

[166] Franck J Vernerey, Eric Greenwald, and S. Bryant. Triphasic mixture model of cell-mediated enzymatic degradation of hydrogels. Computer Methods in Biomechanics and Biomedical Engineering, accepted, 2011.

[167] Tetsuro Wakatsuki, Robert B. Wysolmerski, and Elliot L. Elson. Mechanics of cell spreading: role of myosin ii. Journal of Cell Science, 116:1617–1625, 2003.

[168] Sam Walcott and Sean X. Sun. A mechanical model of actin stress fiber formation and substrate elasticity sensing in adherent cells. Proceedings of the National Academy of Science, 107(17):7757–7762, 2010.

[169] H.B. Wang, M. Dembo, and Y.L. Wang. Substrate flexibility regulates growth and apoptosis of normal but not transformed cells. Am J Physiol Cell Physiol, 279:C1345–C1350, 2000.

[170] J.H. Wang, F. Jia, T.W. Gilbert, and S.L. Woo. Cell orientation determines teh alignment of cell-produced collagenous matrix. Journal of Biomechanics, 36(1):97–102, 2003.

[171] N. Wang, K. Naruse, D. Stamenovic, J. Fredberg, S. Mijallovich, I. Tolic-Nørrelykke, T. Polte, R. Mannix, and D.E. Ingber. Mechanical behavior in living cells consistent with the tensegrity model. PNAS, 98(14):7765–7770, 2001.

[172] P. Weiss and B. Garber. Shape and movement of mesenchyme cells as functions of the physical structure of the medium. contribution to a quantitative morphology. Zoology, 38:264–280, 1952.

[173] P. Weiss and B. Garber. Shape and movement of mesenchyme cells as functions of the physical structure of the mediumcontributions to a quantitative morphology. Proc Natl Acad Sci USA, 38(3):264–280, 1952.

[174] P. Weiss and B. Garber. Shape and movement of mesenchyme cells as functions of the physical struture of the medium contributions to a quantitative morphology. PNAS, 38:264–280, 1952.

[175] Glenn E White and Keigi Fujiwara. Expression and intracellular distribution of stress fibers in aortic endothelium. The Journal of Cell Biology, 103:63–70, 1986.

[176] Henry C. Wong and William C. Tang. Finite element analysis of the effects of focal adhesion mechanical properties and substrate stiffness on cell migration. Journal of Biomechanics, 44(6):1046–1050, 2011.

[177] Yuguang Xiong, Padmini Rangamani, Marc-Antoine Fardin, Azi Lipshtat, Benjamin Dubin-Thaler, Olivier Rossier, Michael P. Sheetz, , and Ravi Iyengar. Mechanisms controlling cell size and shape during isotropic cell spreading. Biophysical Journal, 98:2136–2146, 2010.

[178] Hiroshi Yamada, Norihide Mouri, and Shinji Nobuhara. Three-dimensionalmorphometry of single endothelial cells with substrate stretching and image-based finite elementmodeling. EURASIP Journal on Advances in Signal Processing, 2010:Article ID 616091, 10 pages, 2010.

[179] Tony Yeung, Penellope C. George, Lisa A. Flanagan, Beatrice Marge, Miguellina Ortiz, Makoto Funaki, Nastaran Zahir, Wenyu Ming, Valerie Weaver, and Paul A. Janmey. Effects of substrate stiffness on cell morphology, cytoskeletal structure, and adhesion. Cell Motility and the Cytoskeleton, 60:24–34, 2005.

[180] Tony Yeung, Penelope C. Georges, Lisa A. Flanagan, Beatrice Marg, Miguelina Ortiz, Makoto Funaki, Nastaran Zahir, Wenyu Ming, Valerie Weaver, , and Paul A. Janmey. Effects of substrate stiffness on cell morphology, cytoskeletal structure, and adhesion. Cell Motility and the Cytoskeleton, 60:24–34, 2005.

[181] J Yvonnet, H Le Quang, and Q-C He. An XFEM/level set approach to modelling surface/interface effects and to computing the size-dependent effective properties of nanocomposites. Computational Mechanics, 42:119–131, 2008.

[182] C Zhu, G Bao, and N Wang. Cell mechanics: mechanical response, cell adhesion, and molecular deformation. Ann. Rev. Cell and Dev. Biol., 02:189–226, 2000.

Appendix A

Computing angular SF distribution using structure matrix

The angular distribution of SFs, ϕ_θ^p, is defined as the volume occupied by of the SFs oriented along the direction that makes angle θ from horizontal axis per total volume. The distribution function ϕ_θ^p (Fig. A.1) is assumed to follow π-periodic Von-Mises distribution function defined as [59]:

$$\phi_\theta^p(\theta) = \phi^p \left(\frac{exp\left[b\ cos\left(2\theta - 2\theta_0\right)\right]}{I_0(b)} \right) \tag{A.1}$$

where $I_0(b)$ is the Bessel's function of the first kind of order zero given by:

$$I_0(b) = \frac{1}{\pi} \int_0^\pi exp\left(b\ cos\theta\right) d\theta. \tag{A.2}$$

The Von-Mises distribution is represented in Fig. A.1b when the largest fiber density is along the θ_0-direction. On the figure, it can clearly be seen that the parameter b in (A.1) captures the degree of anisotropy. In particular, when increasing b from 0 to ∞, the SFs orientation varies from a totally isotropic distribution to a strongly oriented distribution in the direction $\theta = \theta_0$.

Following [165], the structure matrix $\mathbf{\Phi}^p$ can be represented in terms of three independent variables $\{\phi^p, \eta, \theta_0\}$, where η refers to the degree of anisotropy and θ_0 shows the principal direction of SFs. In this context, the structure tensor may be constructed in the form:

$$\mathbf{\Phi}^p = \phi^p \left[\eta \mathbf{I} + (1 - 2\eta) \begin{bmatrix} cos^2\theta & cos\theta sin\theta \\ cos\theta sin\theta & sin^2\theta \end{bmatrix} \right]. \tag{A.3}$$

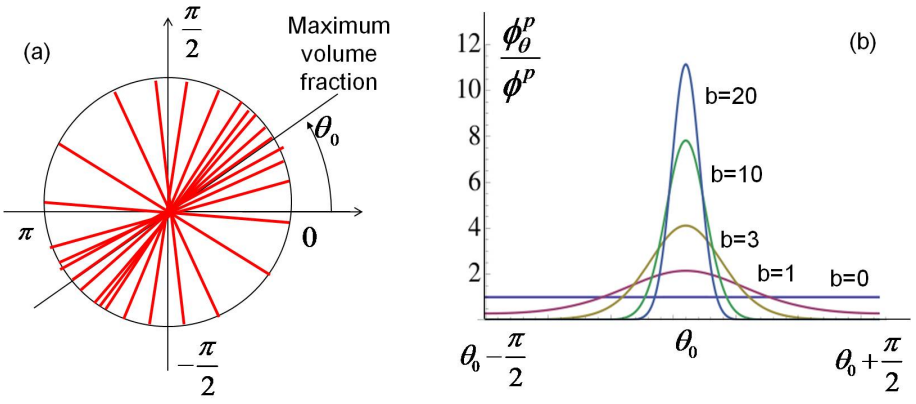

Figure A.1: Illustration of SF volume fraction at a continuum point and its representation with a Von-Mises distribution function.

where $\mathbf{I}$ is the identity tensor. It can be seen that if $\eta = 0$, all fibers are aligned in the same direction (defined by angle θ_0), whereas as $\eta \to 1/2$, the distribution becomes isotropic. Knowing structure matrix $\mathbf{\Phi}^p$, one can compute the independent variables $\{\phi^p, \eta, \theta_0\}$ as the trace of $\mathbf{\Phi}^p$, the smaller eigenvalue and the direction corresponding the greater eigenvalue of matrix $\mathbf{\Phi}^p/\phi^p$, respectively.

Because of their similar physical interpretation, it is possible to find a relationship between parameters b (appearing in the Von-Mises distribution) and η by substituting (A.1) into (A.3). One can show that:

$$\eta = \frac{1}{\pi} \int_{-\pi/2}^{\pi/2} \frac{exp\left[b\ cos\left(2\theta\right)\right] sin^2\theta}{I_0\left(b\right)} d\theta. \tag{A.4}$$

This integral may be computed numerically to determine the $b - \eta$ curve as shown in Fig. A.2. This ensures that there is a one-to-one mapping between the structure tensor shown in (A.3) and the Von-Mises distribution (A.1).

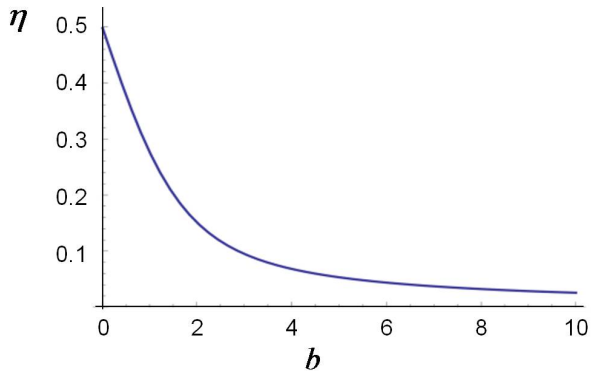

Figure A.2: Relationship between parameters b and η.

Appendix B

Governing equations for plane stress assumptions

As mentioned previously, both cell and substrate are considered in 2D x-y plane stress because of small thickness for the cell and simplicity for the substrate. For substrate as a homogeneous material it is assumed that $T^s_{zz} = T^s_{xz} = T^s_{yz} = 0$ where T^s is substrate's Cauchy stress. The details of 2D plane-stress condition for a solid can be found in any mechanic of materials book. But the condition of plane-stress for cell as a mixture is different because of the existence of the fluid phase, and is written as $T_{xz} = T_{yz} = 0$, $T_{zz} - p = 0$ or $T^{\sigma J}_{xz} = T^{\sigma J}_{yz} = 0$, $T^{\sigma J}_{zz} - \dot{p} = 0$. To find stress-strain relationship for this situation, one can start from the general material rate form of stress-strain relationship written in voigt notation as [10]:

$$\begin{bmatrix} T^{\sigma J}_{xx} \\ T^{\sigma J}_{yy} \\ T^{\sigma J}_{zz} \\ T^{\sigma J}_{yz} \\ T^{\sigma J}_{xz} \\ T^{\sigma J}_{xy} \end{bmatrix} = \begin{bmatrix} 2\mu' + \lambda & \lambda & \lambda & 0 & 0 & 0 \\ \lambda & 2\mu' + \lambda & \lambda & 0 & 0 & 0 \\ \lambda & \lambda & 2\mu' + \lambda & 0 & 0 & 0 \\ 0 & 0 & 0 & \mu' & 0 & 0 \\ 0 & 0 & 0 & 0 & \mu' & 0 \\ 0 & 0 & 0 & 0 & 0 & \mu' \end{bmatrix} \begin{bmatrix} D_{xx} \\ D_{yy} \\ D_{zz} \\ 2D_{yz} \\ 2D_{xz} \\ 2D_{xy} \end{bmatrix} \tag{B.1}$$

where $\mu' = \mu - \lambda\, lnJ$. Then, by applying the plane-stress conditions to above equation, the following equation can easily be derived:

$$D_{zz} = \frac{1}{1-\nu}\left[\frac{p}{E}(1+\nu)(1-2\nu) - \nu(D_{xx} + D_{yy})\right] \tag{B.2}$$

where E and ν are cytoskeleton's Young's modulus and Poisson's ratio, respectively, and are given by:

$$E = \frac{\mu'(3\lambda + 2\mu')}{\lambda + \mu'} \quad ; \text{and} \quad \nu = \frac{\lambda}{2(\lambda + \mu')} \tag{B.3}$$

Consequentely the Jaumann rate of cytoskeleton Cauchy stress is written as:

$$\begin{bmatrix} T_{xx}^{\sigma J} \\ T_{yy}^{\sigma J} \\ T_{xy}^{\sigma J} \end{bmatrix} = \frac{E}{(1-\nu^2)} \begin{bmatrix} 1 & \nu & 0 \\ \nu & 1 & 0 \\ 0 & 0 & \frac{1-\nu}{2} \end{bmatrix} \begin{bmatrix} D_{xx} \\ D_{yy} \\ 2D_{xy} \end{bmatrix} + \frac{\nu}{1-\nu} p \begin{bmatrix} 1 \\ 1 \\ 0 \end{bmatrix} \tag{B.4}$$

Eq. (B.4) is written in matrix notation in x-y plane as $\mathbf{T}^{\sigma J} = \mathbf{C}^c : \mathbf{D} + \frac{\nu}{1-\nu} p\mathbf{I}$. Furthermore, using eq. (B.2), and 3D divergence of cytoskeleton velocity $\nabla^{(3)} \cdot \mathbf{v} = D_{xx} + D_{yy} + D_{zz}$, it is concluded that $\nabla^{(3)} \cdot \mathbf{v} = \alpha \ \nabla \cdot \mathbf{v} + \beta \ \dot{p}$ where $\nabla \cdot \mathbf{v} = D_{xx} + D_{yy}$ introduces 2D divergence of velocity, and the constants α and β are given as a function of cytoskeleton's material properties (Young's modolus and Poisson's ratio) given by:

$$\alpha = \frac{1-2\nu}{1-\nu} \quad ; \text{and} \quad \beta = \frac{(1+\nu)(1-2\nu)}{E(1-\nu)} \tag{B.5}$$

Appendix C

Incremental weak form of the governed equations

Before writing the incremental form of the set of derived equations, it is needed to find equations for $\delta\phi^f$ and $\dot{\phi}^f = \frac{D\phi^f}{Dt}$ as a function of cell's variables. As mentioned before, cell's body is assumed to be satuarated by four constituents: cytoskeletal network, cytosol, SF polymers and G-actin monomers; consequently, one can write $\phi^f + \phi^c + \phi^p + \phi^m = 1$. After deriving the material time derivative of the latter equation, the following formula is obtained: $\dot{\phi}^f = \dot{\phi}^c - \dot{\phi}^p - \dot{\phi}^m$, where ϕ denotes the volume fraction of each cell's component, and the superscripts $f,\ c,\ p$ and m stand for cytosol, cytoskeleton, polymers and monomers, respectively. Furthermore, following [165] and considering plane-stress condition for the cell, the balance of mass equation for cytoskeleton takes the form: $\frac{D\phi^c}{Dt} = \dot{\phi}^c = -\phi^c\ \alpha\ \nabla\cdot\dot{\mathbf{u}} - \phi^c\ \beta\ \dot{p}$.

As a result:

$$\begin{cases} \dot{\phi}^f = \phi^c\ \alpha\ \nabla\cdot\dot{\mathbf{u}} + \phi^c\ \beta\ \dot{p} - tr\left(\dot{\mathbf{\Phi}}^p\right) - \dot{\phi}^m \\ \delta\phi^f = \phi^c\ \alpha\ \nabla\cdot\delta\mathbf{u} + \phi^c\ \beta\ \delta p - tr\left(\delta\mathbf{\Phi}^p\right) - \delta\phi^m \end{cases} \tag{C.1}$$

To write the non-linear form, Jaumann rate is used for Cauchy stress values because of large

deformations of cell and substrate [10]. As a result, the nonlinear equations take the form:

$$\int_{\Omega^s} \nabla\boldsymbol{\omega}^s : \left[\tilde{\mathbf{T}}^s + \left(\mathbf{C}^s : \mathbf{D}^s + \mathbf{W}^s \cdot \tilde{\mathbf{T}}^s + \tilde{\mathbf{T}}^s \cdot \mathbf{W}^{sT}\right) \cdot \delta t\right] \, d\Omega^s -$$
$$\int_{\Omega^c} \boldsymbol{\omega}^s \cdot \left[\tilde{\mathbf{t}}_a + \mathbf{K}_a \left(\mathbf{v}^c - \mathbf{v}^s\right) \cdot \delta t\right] \, d\Omega^c = 0 \tag{C.2}$$
$$\int_{\Omega^c} \nabla\boldsymbol{\omega} : \left[\left(\tilde{\mathbf{T}}^c + \tilde{\mathbf{T}}^p - \tilde{p}\ \mathbf{I}\right) + \left(\mathbf{C}^c : \mathbf{D} + \left(\frac{\nu}{1-\nu}\right) \dot{p}\mathbf{I} + \mathbf{W} \cdot \tilde{\mathbf{T}}^c + \tilde{\mathbf{T}}^c \cdot \mathbf{W}^T\right) \cdot \delta t + \right.$$
$$\left. \frac{\partial \mathbf{T}^p}{\partial \boldsymbol{\Phi}^p} : \delta\boldsymbol{\Phi}^p + \frac{\partial \mathbf{T}^p}{\partial \mathbf{E}} : \delta\mathbf{E} + \frac{\partial \mathbf{T}^p}{\partial \dot{\mathbf{E}}} : \delta\dot{\mathbf{E}} + \left(\mathbf{W} \cdot \tilde{\mathbf{T}}^p + \tilde{\mathbf{T}}^p \cdot \mathbf{W}^T\right) \cdot \delta t - \delta p\ \mathbf{I}\right] \, d\Omega^c +$$
$$\int_{\Omega^d} \boldsymbol{\omega} \cdot \left[\tilde{\mathbf{t}}_a + \mathbf{K}_a \left(\mathbf{v}^c - \mathbf{v}^s\right) \cdot \delta t\right] \, d\Omega^d +$$
$$\int_{\Gamma^c} \left(\mathbf{P} \cdot \nabla\boldsymbol{\omega} \cdot \mathbf{P}\right) : \left[\tilde{\mathbf{T}}_\sigma + \left(\mathbf{S}_\sigma : \mathbf{D}_\sigma + \mathbf{W}_\sigma \cdot \tilde{\mathbf{T}}_\sigma + \tilde{\mathbf{T}}_\sigma \cdot \mathbf{W}_\sigma^T\right) \cdot \delta t\right] \, d\Gamma^c = 0 \tag{C.3}$$

$$\int_{\Omega^c} \theta \ \left[\ \alpha\ \nabla \cdot \mathbf{v} + \ \beta\ \dot{p}\right] \, d\Omega^c +$$
$$\int_{\Omega^c} \nabla\theta \cdot \left[\frac{\kappa}{\mu}\nabla\tilde{p} + \left(\frac{\tilde{\phi}^m}{\tilde{\phi}^f}\frac{\kappa}{\mu}\nabla\tilde{p} + D\ \nabla\tilde{\phi}^m - \frac{\tilde{\phi}^m}{\tilde{\phi}^f} D\ \nabla\tilde{\phi}^f\right) + \right.$$
$$\frac{\kappa}{\mu}\nabla\delta p + \left(\frac{\delta\phi^m}{\tilde{\phi}^f}\frac{\kappa}{\mu}\nabla\tilde{p} + \frac{\tilde{\phi}^m}{\tilde{\phi}^f}\frac{\kappa}{\mu}\nabla\delta p + D\ \nabla\delta\phi^m - \frac{\delta\phi^m}{\tilde{\phi}^f} D\ \nabla\tilde{\phi}^f\right) +$$
$$\frac{\tilde{\phi}^m}{\tilde{\phi}^f}\left(-\frac{1}{\tilde{\phi}^f}\frac{\kappa}{\mu}\nabla\tilde{p} + \frac{1}{\tilde{\phi}^f} D\ \nabla\tilde{\phi}^f\right) \cdot \left(\tilde{\phi}^c\ \alpha\ \nabla \cdot \delta\mathbf{u} + \tilde{\phi}^c\ \beta\ \delta p - tr\left(\delta\boldsymbol{\Phi}^p\right) - \delta\phi^m\right) -$$
$$\left. \frac{\tilde{\phi}^m}{\tilde{\phi}^f} D\ \nabla\left(\tilde{\phi}^c\ \alpha\ \nabla \cdot \delta\mathbf{u} + \tilde{\phi}^c\ \beta\ \delta p - tr\left(\delta\boldsymbol{\Phi}^p\right) - \delta\phi^m\right)\right] \, d\Omega^c = 0 \tag{C.4}$$

$$\int_{\Omega^c} \lambda \left[\left(\tilde{\phi}^c\ \alpha\ \nabla \cdot \dot{\mathbf{u}} + \tilde{\phi}^c\ \beta\ \dot{p} - tr\left(\dot{\boldsymbol{\Phi}}^p\right) - \dot{\phi}^m\right) + \right.$$
$$\left. \tilde{\phi}^f\ \left(\ \alpha\ \nabla \cdot \dot{\mathbf{u}} + \ \beta\ \dot{p}\right)\right] \, d\Omega^c + \int_{\Omega^c} \nabla\lambda \cdot \left(\frac{\kappa}{\mu}\nabla\tilde{p} + \frac{\kappa}{\mu}\nabla\delta p\right) \, d\Omega^c = 0 \tag{C.5}$$

$$\int_{\Omega^c} \mathbf{\Lambda} : \Bigg[\dot{\mathbf{\Phi}}^p + \tilde{\mathbf{\Phi}}^p \left(\alpha \ \nabla \cdot \mathbf{v} + \ \beta \ \dot{p} \right) - \left(\frac{M^p}{M^m} \left(\frac{1}{2} k_0^f \mathbf{I} + k_1^f \tilde{\mathbf{T}}^p \right) \frac{\tilde{\phi}^m}{\tilde{\phi}^f} - k_0^d \tilde{\mathbf{\Phi}}^p \right) -$$

$$\left(\frac{M^p}{M^m} k_1^f \left(\frac{\partial \mathbf{T}^p}{\partial \mathbf{\Phi}^p} : \delta \mathbf{\Phi}^p + \frac{\partial \mathbf{T}^p}{\partial \mathbf{E}} : \delta \mathbf{E} + \frac{\partial \mathbf{T}^p}{\partial \dot{\mathbf{E}}} : \delta \dot{\mathbf{E}} \right) \frac{\tilde{\phi}^m}{\tilde{\phi}^f} + \right.$$

$$\left. \frac{M^p}{M^m} k_1^f \left(\mathbf{W} \cdot \tilde{\mathbf{T}}^p + \tilde{\mathbf{T}}^p \cdot \mathbf{W}^T \right) \frac{\tilde{\phi}^m}{\tilde{\phi}^f} \right) -$$

$$\left(\frac{M^p}{M^m} \left(\frac{1}{2} k_0^f \mathbf{I} + k_1^f \tilde{\mathbf{T}}^p \right) \frac{\delta \phi^m}{\tilde{\phi}^f} - k_0^d \ \delta \mathbf{\Phi}^p \right) - \frac{M^p}{M^m} \left(\frac{1}{2} k_0^f \mathbf{I} + k_1^f \tilde{\mathbf{T}}^p \right) \frac{-\tilde{\phi}^m}{{\tilde{\phi}^f}^2} \cdot$$

$$\left(\tilde{\phi}^c \ \alpha \ \nabla \cdot \delta \mathbf{u} + \tilde{\phi}^c \ \beta \ \delta p - tr \left(\delta \mathbf{\Phi}^p \right) - \delta \phi^m \right) \Bigg] \ d\Omega^c = 0 \tag{C.6}$$

Appendix D

Discretized form of the governed equations

To discretize the equations derived formerly, voigt notation is used for all symmetric tensors. In voigt notation, all stress and strain tensors are written as:

$$\{\mathbf{T}\} = \begin{bmatrix} T_{11} \\ T_{22} \\ T_{12} \end{bmatrix}; \quad \{\mathbf{E}\} = \begin{bmatrix} E_{11} \\ E_{22} \\ 2\ E_{12} \end{bmatrix}; \quad \{\mathbf{D}\} = \begin{bmatrix} D_{11} \\ D_{22} \\ 2\ D_{12} \end{bmatrix}; \quad \{\mathbf{W}\} = \begin{bmatrix} W_{11} \\ W_{22} \\ 2\ W_{12} \end{bmatrix} \tag{D.1}$$

For structural matrix we use:

$$\{\mathbf{\Phi}^p\} = \begin{bmatrix} \phi^p_{11} \\ \phi^p_{22} \\ \phi^p_{12} \end{bmatrix} \tag{D.2}$$

Also, we make the following definitions:

$$\mathbf{W}\cdot\mathbf{T} + \mathbf{T}\cdot\mathbf{W}^T \equiv \{\{\mathbf{T}\}\}\cdot\mathbf{G}\cdot\dot{\mathbf{u}}^e \tag{D.3}$$

$$\delta\mathbf{W}\cdot\mathbf{T} + \mathbf{T}\cdot\delta\mathbf{W}^T \equiv \{\{\mathbf{T}\}\}\cdot\mathbf{G}\cdot\delta\mathbf{u}^e \tag{D.4}$$

where;

$$\{\{\mathbf{T}\}\} = \begin{bmatrix} 2\ T_{12} \\ -2\ T_{12} \\ T_{22} - T_{11} \end{bmatrix} \tag{D.5}$$

$$\mathbf{G} = \begin{bmatrix} \mathbf{G}_1 & \mathbf{G}_2 & ... & \mathbf{G}_{9+m} \end{bmatrix} \quad \text{and} \quad \mathbf{G}_I = 0.5 \begin{bmatrix} \frac{\partial N_I(\mathbf{x})}{\partial x_2} & & -\frac{\partial N_I(\mathbf{x})}{\partial x_1} \end{bmatrix} \tag{D.6}$$

for substrate:

$$\mathbf{G}^s = \begin{bmatrix} \mathbf{G}_1 & \mathbf{G}_2 & ... & \mathbf{G}_9 \end{bmatrix} \tag{D.7}$$

In this paper, quadratic 9-node (commonly called Q9) elements are used for displacement fields $\mathbf{u}^s$ and $\mathbf{u}$; while, for the other three fields (p, ϕ^m and $\mathbf{\Phi}^p$), quadratic 4-node (commonly called Q4) elements are used. As a result, the parameter n in Eq. (6.66) is 9 for displacement fields, and 4 for the other fields.

Furthermore, the following definitions will be used for descretization:

$$\boldsymbol{\omega}^s = \mathbf{N}^s \cdot \boldsymbol{\omega}^{s,e}; \quad \boldsymbol{\omega} = \mathbf{N} \cdot \boldsymbol{\omega}^e; \quad \theta = \mathbf{N}_f \cdot \boldsymbol{\theta}^e; \quad \lambda = \mathbf{N}_f \cdot \boldsymbol{\lambda}^e; \quad \mathbf{\Lambda} = \mathbf{N}_p \cdot \mathbf{\Lambda}^e \tag{D.8}$$

$$\mathbf{u}^s = \mathbf{N}^s \cdot \mathbf{u}^{s,e}; \quad \mathbf{u} = \mathbf{N} \cdot \mathbf{u}^e; \quad p = \mathbf{N}_f \cdot \mathbf{p}^e; \quad \phi^m = \mathbf{N}_f \cdot \mathbf{\Phi}^{m,e}; \quad \mathbf{\Phi}^p = \mathbf{N}_p \mathbf{\Phi}^{p,e} \tag{D.9}$$

$$\nabla\boldsymbol{\omega}^s = \mathbf{B}^s \cdot \boldsymbol{\omega}^{s,e}; \quad \nabla\boldsymbol{\omega} = \mathbf{B} \cdot \boldsymbol{\omega}^e; \quad \nabla\theta = \mathbf{B}_f \cdot \boldsymbol{\theta}^e; \quad \nabla\lambda = \mathbf{B}_f \cdot \boldsymbol{\lambda}^e \tag{D.10}$$

$$\nabla\mathbf{u}^s = \mathbf{B}^s \cdot \mathbf{u}^{s,e}; \quad \nabla\mathbf{u} = \mathbf{B} \cdot \mathbf{u}^e; \quad \nabla p = \mathbf{B}_f \cdot \mathbf{p}^e; \quad \nabla\phi^m = \mathbf{B}_f \cdot \mathbf{\Phi}^{m,e} \tag{D.11}$$

$$\nabla \cdot \mathbf{u} = \tilde{\mathbf{B}} \cdot \mathbf{u}^e; \quad \{\mathbf{D}\} = \mathbf{B} \cdot \dot{\mathbf{u}}^e; \quad \{\mathbf{D}^s\} = \mathbf{B}^s \cdot \dot{\mathbf{u}}^{s,e} \tag{D.12}$$

The same definitions are used for rates. In above equations, if it is assumed that m and m' are the number of enriched nodes in Q9 and Q4 elements, respectively, the following definitions are given:

$$\mathbf{N}^s = \begin{bmatrix} \mathbf{N}^1 & \mathbf{N}^2 & \cdots & \mathbf{N}^9 \end{bmatrix}; \quad \mathbf{N} = \begin{bmatrix} \mathbf{N}^1 & \mathbf{N}^2 & \cdots & \mathbf{N}^{9+m} \end{bmatrix}; \quad \mathbf{N}^I = \begin{bmatrix} N^I & 0 \\ 0 & N^I \end{bmatrix} \tag{D.13}$$

$$\mathbf{N}_f = \begin{bmatrix} M^1 & M^2 & \cdots & M^{4+m'} \end{bmatrix} \tag{D.14}$$

$$\mathbf{N}_p = \begin{bmatrix} \mathbf{N}^1 & \mathbf{N}^2 & \cdots & \mathbf{N}^{4+m'} \end{bmatrix}; \quad \mathbf{N}^I = \begin{bmatrix} M^I & 0 & 0 \\ 0 & M^I & 0 \\ 0 & 0 & M^I \end{bmatrix} \tag{D.15}$$

where N^I and M^I are qudrature 9-node and 4-node shape functions, respectively. Also:

$$\mathbf{B}^s = \begin{bmatrix} \mathbf{B}^1 & \mathbf{B}^2 & \cdots & \mathbf{B}^9 \end{bmatrix}; \quad \mathbf{B} = \begin{bmatrix} \mathbf{B}^1 & \mathbf{B}^2 & \cdots & \mathbf{B}^{9+m} \end{bmatrix}; \quad \mathbf{B}^I = \begin{bmatrix} \frac{\partial N^I}{\partial x_1} & 0 \\ 0 & \frac{\partial N^I}{\partial x_2} \\ \frac{\partial N^I}{\partial x_2} & \frac{\partial N^I}{\partial x_1} \end{bmatrix} \tag{D.16}$$

$$\tilde{\mathbf{B}} = \left[\tilde{\mathbf{B}}^1 \quad \tilde{\mathbf{B}}^2 \quad \cdots \quad \tilde{\mathbf{B}}^{9+m}\right]; \quad \tilde{\mathbf{B}}^I = \left[\frac{\partial N^I}{\partial x_1} \quad \frac{\partial N^I}{\partial x_2}\right] \tag{D.17}$$

$$\mathbf{B}_f = \left[\mathbf{B}_f^1 \quad \mathbf{B}_f^2 \quad \cdots \quad \mathbf{B}_f^{4+m'}\right]; \quad \mathbf{B}_f^I = \left[\frac{\partial M^I}{\partial x_1} \quad \frac{\partial M^I}{\partial x_2}\right]^T \tag{D.18}$$

Furthermore, knowing that, in matrix notation, $\dot{\mathbf{E}} = \mathbf{F}^T \cdot \mathbf{D} \cdot \mathbf{F}$, $\mathbf{F}^m$ is chosen such that in voigt notation one can write $\{\dot{\mathbf{E}}\} = \mathbf{F}^m \cdot \{\mathbf{D}\}$; where,

$$\mathbf{F}^m = \begin{bmatrix} F_{11}^2 & F_{21}^2 & F_{11}\ F_{21} \\ F_{12}^2 & F_{22}^2 & F_{12}\ F_{22} \\ 2\ F_{11}\ F_{12} & 2\ F_{21}\ F_{22} & F_{11}\ F_{22} + F_{12}\ F_{21} \end{bmatrix} \tag{D.19}$$

As a result, the descretized nonlinear weak form of Eqs. (C.2)-(C.6) takes the form:

$$\begin{aligned}
&\boldsymbol{\omega}^{s,eT} \int_{\Omega^{s,e}} \mathbf{B}^{sT} \cdot \left(\{\tilde{\mathbf{T}}^s\} + \{\mathbf{C}^s\} \cdot \mathbf{B}^s \cdot \delta\mathbf{u}^{s,e} + \{\{\mathbf{T}^s\}\} \cdot \mathbf{G}^s \cdot \delta\mathbf{u}^{s,e} \right) d\Omega^{s,e} - \\
&\boldsymbol{\omega}^{s,eT} \int_{\Omega^{c,e}} \mathbf{N}^{sT} \cdot \left[\tilde{\mathbf{t}}_a + \mathbf{K}_a \cdot (\mathbf{N} \cdot \delta\mathbf{u}^e - \mathbf{N}^s \cdot \delta\mathbf{u}^{s,e}) \right] d\Omega^{c,e} = 0 \qquad \text{(D.20)} \\
&\boldsymbol{\omega}^{eT} \int_{\Omega^{c,e}} \Big[\mathbf{B}^T \cdot \Big(\{\tilde{\mathbf{T}}^c\} + \{\tilde{\mathbf{T}}^p\} + \{\mathbf{C}^c\} \cdot \mathbf{B} \cdot \delta\mathbf{u}^e + \{\{\mathbf{T}^c\}\} \cdot \mathbf{G} \cdot \delta\mathbf{u}^e + \\
&\frac{\{\partial \mathbf{T}^p\}}{\{\partial \mathbf{\Phi}^p\}} \cdot \mathbf{N}^p \cdot \delta\mathbf{\Phi}^{p,e} + \frac{\partial \{\mathbf{T}^p\}}{\partial \{\mathbf{E}\}} \cdot \mathbf{F}^m \cdot \mathbf{B} \cdot \delta\mathbf{u}^e + \frac{\partial \{\mathbf{T}^p\}}{\partial \{\dot{\mathbf{E}}\}} \cdot \mathbf{F}^m \cdot \mathbf{B} \cdot \dot{\mathbf{u}}^e + \{\{\mathbf{T}^p\}\} \cdot \mathbf{G} \cdot \delta\mathbf{u} \Big) - \\
&\tilde{\mathbf{B}}^T \cdot \left(\tilde{p} + \frac{1-2\nu}{1-\nu} \mathbf{N}_f \cdot \delta\mathbf{p}^e \right) \Big] \ d\Omega^{c,e} + \\
&\boldsymbol{\omega}^{eT} \int_{\Omega^{c,e}} \mathbf{N}^T \cdot \left[\tilde{\mathbf{t}}_a + \mathbf{K}_a \cdot (\mathbf{N} \cdot \delta\mathbf{u}^e - \mathbf{N}^s \cdot \delta\mathbf{u}^{s,e}) \right] d\Omega^a - \\
&\boldsymbol{\omega}^{eT} \int_{\sigma} \mathbf{B}^T \cdot \mathbf{M}_p^T \cdot \left(\{\tilde{\mathbf{T}}_\sigma\} + \{\mathbf{S}^s\} \cdot \mathbf{M}_p \cdot \mathbf{B} \cdot \delta\mathbf{u}^e + \{\{\mathbf{T}_\sigma\}\} \cdot \mathbf{M}_p \cdot \mathbf{G} \cdot \delta\mathbf{u}^e \right) d\Gamma^{c,e} = 0 \qquad \text{(D.21)}
\end{aligned}$$

$$\begin{aligned}
&\boldsymbol{\theta}^{eT} \int_{\Omega^{c,e}} {\mathbf{N}_f}^T \left[\ \alpha\ \tilde{\mathbf{B}} \cdot \dot{\mathbf{u}}^e + \ \beta\ \mathbf{N}_f \cdot \dot{\mathbf{p}}^e \right] \ d\Omega^{c,e} + \\
&\boldsymbol{\theta}^{eT} \int_{\Omega^{c,e}} {\mathbf{B}_f}^T \cdot \left[\frac{\kappa}{\mu} \mathbf{B}_f \cdot \mathbf{p}^e + \left(\frac{\tilde{\phi}^m}{\tilde{\phi}^f} \frac{\kappa}{\mu} \mathbf{B}_f \cdot \mathbf{p}^e + D\ \mathbf{B}_f \cdot \boldsymbol{\phi}^{m,e} - \frac{\tilde{\phi}^m}{\tilde{\phi}^f} D\ \nabla\tilde{\phi}^f \right) + \right. \\
&\frac{\kappa}{\mu} \mathbf{B}_f \cdot \delta\mathbf{p}^e + \left(\frac{\mathbf{N}_f \cdot \delta\boldsymbol{\phi}^{m,e}}{\tilde{\phi}^f} \frac{\kappa}{\mu} \mathbf{B}_f \cdot \mathbf{p}^e + \frac{\tilde{\phi}^m}{\tilde{\phi}^f} \frac{\kappa}{\mu} \mathbf{B}_f \cdot \delta\mathbf{p}^e + D\ \mathbf{B}_f \cdot \delta\boldsymbol{\phi}^{m,e} - \right. \\
&\left. \frac{\mathbf{N}_f \cdot \delta\boldsymbol{\phi}^{m,e}}{\tilde{\phi}^f} D\ \nabla\tilde{\phi}^f \right) + \frac{\tilde{\phi}^m}{\tilde{\phi}^f} \left(-\frac{1}{\tilde{\phi}^f} \frac{\kappa}{\mu} \mathbf{B}_f \cdot \mathbf{p}^e + \frac{1}{\tilde{\phi}^f} D\ \nabla\tilde{\phi}^f \right) \cdot \\
&\left(\tilde{\phi}^c\ \alpha\ \tilde{\mathbf{B}} \cdot \delta\mathbf{u}^e + \tilde{\phi}^c\ \beta\ \mathbf{N}_f \cdot \delta\mathbf{p}^e - \mathbf{m}^T \cdot \mathbf{N}_p \cdot \delta\mathbf{\Phi}^{p,e} - \mathbf{N}_f \cdot \delta\boldsymbol{\phi}^{m,e} \right) - \\
&\left. \frac{\tilde{\phi}^m}{\tilde{\phi}^f} D\ \mathbf{B} \left(\tilde{\phi}^c \alpha \tilde{\mathbf{B}} \cdot \delta\mathbf{u}^e + \tilde{\phi}^c \beta \mathbf{N}_f \cdot \delta\mathbf{p}^e - \mathbf{m}^T \cdot \mathbf{N}_p \cdot \delta\mathbf{\Phi}^{p,e} - \mathbf{N}_f \cdot \delta\boldsymbol{\phi}^{m,e} \right) \right] d\Omega^{c,e} = \qquad \text{(D.22)}
\end{aligned}$$

$$\boldsymbol{\lambda}^{eT}\int_{\Omega^{c,e}}\mathbf{N}_f^T\Big[\Big(\tilde{\phi}^c\ \alpha\ \tilde{\mathbf{B}}\cdot\dot{\mathbf{u}}^e+\tilde{\phi}^c\ \beta\ \mathbf{N}_f\cdot\dot{\mathbf{p}}^e-\mathbf{m}^T\cdot\mathbf{N}_p\cdot\dot{\mathbf{\Phi}}^{p,e}-\mathbf{N}_f\cdot\dot{\boldsymbol{\phi}}^{m,e}\Big)+$$
$$\tilde{\phi}^f\left(\alpha\tilde{\mathbf{B}}\cdot\dot{\mathbf{u}}^e+\beta\mathbf{N}_f\cdot\dot{\mathbf{p}}^e\right)\Big]\,d\Omega^{c,e}+\boldsymbol{\lambda}^{eT}\int_{\Omega^{c,e}}\mathbf{B}_f^T\left(\frac{\kappa}{\mu}\mathbf{B}_f\cdot\tilde{p}+\frac{\kappa}{\mu}\mathbf{B}_f\cdot\delta\mathbf{p}^e\right)d\Omega^{c,e}=0 \quad \text{(D.23)}$$

$$\mathbf{\Lambda}^{eT}\int_{\Omega^{c,e}}\mathbf{N}_p^T\Big[\mathbf{N}_p\cdot\dot{\mathbf{\Phi}}^{p,e}+\{\mathbf{\Phi}^p\}\Big(\ \alpha\ \tilde{\mathbf{B}}\cdot\dot{\mathbf{u}}^e+\ \beta\ \mathbf{N}_f\cdot\dot{\mathbf{p}}^e\Big)-$$
$$\left(\frac{M^p}{M^m}\left(\frac{1}{2}k_0^f\mathbf{m}+k_1^f\{\tilde{\mathbf{T}}^p\}\right)\frac{\tilde{\phi}^m}{\tilde{\phi}^f}-k_0^d\mathbf{N}_p\cdot\mathbf{\Phi}^{p,e}\right)-$$
$$\left(\frac{M^p}{M^m}k_1^f\left(\frac{\{\partial\mathbf{T}^p\}}{\{\partial\mathbf{\Phi}^p\}}\cdot\mathbf{N}^p\cdot\delta\mathbf{\Phi}^{p,e}+\frac{\partial\{\mathbf{T}^p\}}{\partial\{\mathbf{E}\}}\cdot\mathbf{F}^m\cdot\mathbf{B}\cdot\delta\mathbf{u}^e+\right.\right.$$
$$\left.\left.\frac{\partial\{\mathbf{T}^p\}}{\partial\{\dot{\mathbf{E}}\}}\cdot\mathbf{F}^m\cdot\mathbf{B}\cdot\dot{\mathbf{u}}^e+\{\{\mathbf{T}^p\}\}\cdot\mathbf{G}\cdot\delta\mathbf{u}\right)\frac{\tilde{\phi}^m}{\tilde{\phi}^f}\right)-$$
$$\left(\frac{M^p}{M^m}\left(\frac{1}{2}k_0^f\mathbf{m}+k_1^f\{\tilde{\mathbf{T}}^p\}\right)\frac{\mathbf{N}_p\cdot\delta\boldsymbol{\phi}^{m,e}}{\tilde{\phi}^f}-k_0^d\ \mathbf{N}_p\cdot\delta\mathbf{\Phi}^{p,e}\right)-$$
$$\frac{M^p}{M^m}\left(\frac{1}{2}k_0^f\mathbf{m}+k_1^f\{\tilde{\mathbf{T}}^p\}\right)\frac{-\tilde{\phi}^m}{{\tilde{\phi}^f}^2}\cdot$$
$$\Big(\tilde{\phi}^c\ \alpha\ \tilde{\mathbf{B}}\cdot\delta\mathbf{u}^e+\tilde{\phi}^c\ \beta\ \mathbf{N}_f\cdot\delta\mathbf{p}^e-\mathbf{m}^T\cdot\mathbf{N}_p\cdot\delta\mathbf{\Phi}^{p,e}-\mathbf{N}_f\cdot\delta\boldsymbol{\phi}^{m,e}\Big)\Big]\ d\Omega^{c,e}=0 \quad \text{(D.24)}$$

In above equations, $\mathbf{m}^T=\{1\ 1\ 0\}$, and the matrix $\mathbf{M}_p$ is defined such that in voigt notation one can write $\{\mathbf{A}_\sigma\}=\mathbf{M}_p\cdot\{\mathbf{A}\}$, where $\{\mathbf{A}_\sigma\}$ and $\{\mathbf{A}\}$ are vector forms of symmetric tensors $\mathbf{A}_\sigma$ and $\mathbf{A}$, respectively. As a result, the matrix $\mathbf{M}_p$ takes the form [181]:

$$\mathbf{M}_p=\begin{bmatrix}P_{11}^2 & P_{12}^2 & P_{11}P_{12}\\ P_{12}^2 & P_{22}^2 & P_{22}P_{12}\\ 2P_{11}P_{12} & 2P_{22}P_{12} & P_{12}^2+P_{11}P_{22}\end{bmatrix} \quad \text{(D.25)}$$

Also, the cortex's stiffness matrix $\{\mathbf{S}_\sigma\}$ can be calculated by using its elastic matrix $\{\mathbf{C}_\sigma\}$ by $\{\mathbf{S}_\sigma\}=\mathbf{M}_p^T\cdot\{\mathbf{C}_\sigma\}\cdot\mathbf{M}_p$. Furthermore, the notations $\{\mathbf{C}\}$ is used to define the forth order constitutive matrix $\mathbf{C}$ as a second order matrix in voigt notation.

Appendix E

Components of final equation (6.72)

The components of Eq. (6.72) are given by:

$$\mathbf{F}^{u^s,e} = \int_{\Omega^s} \mathbf{B}^{sT} \cdot \{\tilde{\mathbf{T}}^s\}\ d\Omega^s - \int_{\Omega^c} \mathbf{N}^{sT} \cdot \tilde{\mathbf{t}}_a\ d\Omega^c \tag{E.1}$$

$$\mathbf{F}^{u,e} = \int_{\Omega^c} \left[\mathbf{B}^T \left(\{\tilde{\mathbf{T}}^c\} + \{\tilde{\mathbf{T}}^p\}\right) - \tilde{\mathbf{B}}^T \cdot p + \mathbf{N}^T \cdot \tilde{\mathbf{t}}_a\right] d\Omega^c + \int_{\Gamma^c} \mathbf{B}^T \mathbf{M}_p^T \cdot \{\tilde{\mathbf{T}}_\sigma\} d\Gamma \tag{E.2}$$

$$\mathbf{F}^{f,e} = \int_{\Omega^c} {\mathbf{B}_f}^T \left[\frac{\kappa}{\mu}\mathbf{B}_f \cdot \mathbf{p}^e + \left(\frac{\tilde{\phi}^m}{\tilde{\phi}^f}\frac{\kappa}{\mu}\mathbf{B}_f \cdot \mathbf{p}^e + D\ \mathbf{B}_f \cdot \boldsymbol{\phi}^{m,e} - \frac{\tilde{\phi}^m}{\tilde{\phi}^f} D\ \nabla\tilde{\phi}^f\right)\right] d\Omega^c \tag{E.3}$$

$$\mathbf{F}^{m,e} = \int_{\Omega^c} \mathbf{B}_f^T \cdot \frac{\kappa}{\mu}\mathbf{B}_f \cdot \mathbf{p}^e\ d\Omega^c \tag{E.4}$$

$$\mathbf{F}^{p,e} = -\int_{\Omega^c} \mathbf{N}_p^T \cdot \left(\frac{M^p}{M^m}\left(\frac{1}{2}k_0^f \mathbf{m} + k_1^f\{\tilde{\mathbf{T}}^p\}\right)\frac{\tilde{\phi}^m}{\tilde{\phi}^f} - k_0^d \mathbf{N}_p \cdot \boldsymbol{\Phi}^{p,e}\right) d\Omega^c \tag{E.5}$$

and

$$\mathbf{K}^{ss,e} = \int_{\Omega^s} \mathbf{B}^{sT} \cdot \{\mathbf{C}^s\} \cdot \mathbf{B}^s\ d\Omega^s + \int_{\Omega^c} \mathbf{N}^{sT} \cdot \mathbf{K}_a \cdot \mathbf{N}^s\ d\Omega^c \tag{E.6}$$

$$\mathbf{K}^{su,e} = -\int_{\Omega^c} \mathbf{N}^{sT} \cdot \mathbf{K}_a \cdot \mathbf{N}\ d\Omega^c \tag{E.7}$$

$$\mathbf{K}^{us,e} = -\int_{\Omega^c} \mathbf{N}^T \cdot \mathbf{K}_a \cdot \mathbf{N}^s \; d\Omega^c \tag{E.8}$$

$$\begin{aligned}\mathbf{K}^{uu,e} &= \int_{\Omega^c} \mathbf{B}^T \cdot \left(\{\mathbf{C}^c\} \cdot \mathbf{B} + \{\{\mathbf{T}^c\}\} \cdot \mathbf{G} + \frac{\partial \{\mathbf{T}^p\}}{\partial \{\mathbf{E}\}} \cdot \mathbf{F}^m \cdot \mathbf{B} + \{\{\mathbf{T}^p\}\} \cdot \mathbf{G} \right) \; d\Omega^c \\ &+ \int_{\Omega^c} \mathbf{N}^T \cdot \mathbf{K}_a \cdot \mathbf{N} \; d\Omega^c \\ &+ \int_{\Gamma^c} \left(\mathbf{B}^T \cdot \mathbf{M}_p^T \cdot \{\mathbf{S}^s\} \cdot \mathbf{M}_p \cdot \mathbf{B} + \mathbf{B}^T \cdot \mathbf{M}_p^T \cdot \{\{\mathbf{T}_\sigma\}\} \cdot \mathbf{M}_p \cdot \mathbf{G} \right) \; d\Gamma^c \end{aligned} \tag{E.9}$$

$$\mathbf{K}^{uf,e} = -\int_{\Omega^c} \tilde{\mathbf{B}}^T \cdot \frac{1-2\nu}{1-\nu} \mathbf{N}_f \; d\Omega^c \tag{E.10}$$

$$\mathbf{K}^{up,e} = \int_{\Omega^c} \mathbf{B}^T \cdot \frac{\{\partial \mathbf{T}^p\}}{\{\partial \mathbf{\Phi}^p\}} \cdot \mathbf{N}_p \; d\Omega^c \tag{E.11}$$

$$\begin{aligned}\mathbf{K}^{fu,e} &= \int_{\Omega^c} \mathbf{B}_f^T \frac{\tilde{\phi}^m}{\tilde{\phi}^f} \left(-\frac{1}{\tilde{\phi}^f} \frac{\kappa}{\mu} \mathbf{B}_f \cdot \mathbf{p}^e + \frac{1}{\tilde{\phi}^f} D \; \nabla \tilde{\phi}^f \right) \cdot \tilde{\phi}^c \; \alpha \; \tilde{\mathbf{B}} \; d\Omega^c \\ &- \int_{\Omega^c} \mathbf{B}_f^T \frac{\tilde{\phi}^m}{\tilde{\phi}^f} D \; \mathbf{B} \left(\tilde{\phi}^c \; \alpha \; \tilde{\mathbf{B}} \right) \; d\Omega^c \end{aligned} \tag{E.12}$$

$$\begin{aligned}\mathbf{K}^{ff,e} &= \int_{\Omega^c} \mathbf{B}_f^T \left(1 + \frac{\tilde{\phi}^m}{\tilde{\phi}^f} \right) \frac{\kappa}{\mu} \mathbf{B}_f \; d\Omega^c \\ &+ \int_{\Omega^c} \mathbf{B}_f^T \frac{\tilde{\phi}^m}{\tilde{\phi}^f} \left(-\frac{1}{\tilde{\phi}^f} \frac{\kappa}{\mu} \mathbf{B}_f \cdot \mathbf{p}^e + \frac{1}{\tilde{\phi}^f} D \; \nabla \tilde{\phi}^f \right) \cdot \tilde{\phi}^c \; \beta \; \mathbf{N}_f \; d\Omega^c \\ &- \int_{\Omega^c} \mathbf{B}_f^T \frac{\tilde{\phi}^m}{\tilde{\phi}^f} D \; \mathbf{B} \left(\tilde{\phi}^c \; \beta \; \mathbf{N}_f \right) \; d\Omega^c \end{aligned} \tag{E.13}$$

$$\begin{aligned}\mathbf{K}^{fm,e} &= \int_{\Omega^c} \mathbf{B}_f^T \left(\frac{1}{\tilde{\phi}^f} \frac{\kappa}{\mu} \mathbf{B}_f \cdot \mathbf{p}^e \cdot \mathbf{N}_f + D \; \mathbf{B}_f - \frac{1}{\tilde{\phi}^f} D \; \nabla \tilde{\phi}^f \cdot \mathbf{N}_f \right) \; d\Omega^c \\ &+ \int_{\Omega^c} \mathbf{B}_f^T \frac{\tilde{\phi}^m}{\tilde{\phi}^f} \left(-\frac{1}{\tilde{\phi}^f} \frac{\kappa}{\mu} \mathbf{B}_f \cdot \mathbf{p}^e + \frac{1}{\tilde{\phi}^f} D \; \nabla \tilde{\phi}^f \right) \cdot (-\mathbf{N}_f) \; d\Omega^c \\ &- \int_{\Omega^c} \mathbf{B}_f^T \frac{\tilde{\phi}^m}{\tilde{\phi}^f} D \; \mathbf{B} \left(-\mathbf{N}_f \right) \; d\Omega^c \end{aligned} \tag{E.14}$$

$$\begin{aligned}\mathbf{K}^{fp,e} &= \int_{\Omega^c} \mathbf{B}_f^T \frac{\tilde{\phi}^m}{\tilde{\phi}^f} \left(-\frac{1}{\tilde{\phi}^f} \frac{\kappa}{\mu} \mathbf{B}_f \cdot \mathbf{p}^e + \frac{1}{\tilde{\phi}^f} D \; \nabla \tilde{\phi}^f \right) \cdot \left(-\mathbf{m}^T \cdot \mathbf{N}_p \right) \; d\Omega^c \\ &- \int_{\Omega^c} \mathbf{B}_f^T \frac{\tilde{\phi}^m}{\tilde{\phi}^f} D \; \mathbf{B} \left(-\mathbf{m}^T \cdot \mathbf{N}_p \right) \; d\Omega^c \end{aligned} \tag{E.15}$$

$$\mathbf{K}^{mf,e} = \int_{\Omega^c} \mathbf{B}_f^T \cdot \left(\frac{\kappa}{\mu} \mathbf{B}_f \right) \; d\Omega^c \tag{E.16}$$

$$\mathbf{K}^{pu,e} = -\int_{\Omega^c} \mathbf{N}_p^T \left(\frac{M^p}{M^m} k_1^f \left(\frac{\partial\{\mathbf{T}^p\}}{\partial\{\mathbf{E}\}} \cdot \mathbf{F}^m \cdot \mathbf{B} + \{\{\mathbf{T}^p\}\} \cdot \mathbf{G} \right) \frac{\tilde{\phi}^m}{\tilde{\phi}^f} \right) \, d\Omega^c$$

$$- \int_{\Omega^c} \mathbf{N}_p^T \frac{M^p}{M^m} \left(\frac{1}{2} k_0^f \mathbf{m} + k_1^f \{\tilde{\mathbf{T}}^p\} \right) \frac{-\tilde{\phi}^m}{\tilde{\phi}^{f^2}} \cdot \left(\tilde{\phi}^c \; \alpha \; \tilde{\mathbf{B}} \right) \, d\Omega^c \tag{E.17}$$

$$\mathbf{K}^{pf,e} = -\int_{\Omega^c} \mathbf{N}_p^T \frac{M^p}{M^m} \left(\frac{1}{2} k_0^f \mathbf{m} + k_1^f \{\tilde{\mathbf{T}}^p\} \right) \frac{-\tilde{\phi}^m}{\tilde{\phi}^{f^2}} \cdot \tilde{\phi}^c \; \beta \; \mathbf{N}_f \, d\Omega^c \tag{E.18}$$

$$\mathbf{K}^{pm,e} = -\int_{\Omega^c} \mathbf{N}_p^T \left(\frac{M^p}{M^m} \left(\frac{1}{2} k_0^f \mathbf{m} + k_1^f \{\tilde{\mathbf{T}}^p\} \right) \frac{1}{\tilde{\phi}^f} \mathbf{N}_p \right) \, d\Omega^c$$

$$- \int_{\Omega^c} \mathbf{N}_p^T \frac{M^p}{M^m} \left(\frac{1}{2} k_0^f \mathbf{m} + k_1^f \{\tilde{\mathbf{T}}^p\} \right) \frac{-\tilde{\phi}^m}{\tilde{\phi}^{f^2}} \cdot (-\mathbf{N}_f) \, d\Omega^c \tag{E.19}$$

$$\mathbf{K}^{pp,e} = -\int_{\Omega^c} \mathbf{N}_p^T \left[\left(\frac{M^p}{M^m} k_1^f \left(\frac{\{\partial \mathbf{T}^p\}}{\{\partial \mathbf{\Phi}^p\}} \cdot \mathbf{N}^p \right) \frac{\tilde{\phi}^m}{\tilde{\phi}^f} \right) - k_0^d \; \mathbf{N}_p \right] \, d\Omega^c$$

$$- \int_{\Omega^c} \mathbf{N}_p^T \frac{M^p}{M^m} \left(\frac{1}{2} k_0^f \mathbf{m} + k_1^f \{\tilde{\mathbf{T}}^p\} \right) \frac{-\tilde{\phi}^m}{\tilde{\phi}^{f^2}} \cdot \left(-\mathbf{m}^T \cdot \mathbf{N}_p \right) \, d\Omega^c \tag{E.20}$$

and

$$\mathbf{C}^{uu,e} = \int_{\Omega^c} \mathbf{B}^T \frac{\partial\{\mathbf{T}^p\}}{\partial\{\dot{\mathbf{E}}\}} \cdot \mathbf{F}^m \cdot \mathbf{B} \, d\Omega^c \tag{E.21}$$

$$\mathbf{C}^{fu,e} = \int_{\Omega^c} {\mathbf{N}_f}^T \left[\; \alpha \; \tilde{\mathbf{B}} \right] \, d\Omega^c \tag{E.22}$$

$$\mathbf{C}^{ff,e} = \int_{\Omega^c} {\mathbf{N}_f}^T \left[\; \beta \; \mathbf{N}_f \right] \, d\Omega^c \tag{E.23}$$

$$\mathbf{C}^{mu,e} = \int_{\Omega^c} \mathbf{N}_f^T \cdot \left(\phi^c + \phi^f \right) \; \alpha \; \tilde{\mathbf{B}} \, d\Omega^c \tag{E.24}$$

$$\mathbf{C}^{mf,e} = \int_{\Omega^c} \mathbf{N}_f^T \left(\phi^c + \phi^f \right) \; \beta \; \mathbf{N}_f \, d\Omega^c \tag{E.25}$$

$$\mathbf{C}^{mm,e} = \int_{\Omega^c} \mathbf{N}_f^T \left(-\mathbf{N}_f \right) \, d\Omega^c \tag{E.26}$$

$$\mathbf{C}^{mp,e} = \int_{\Omega^c} \mathbf{N}_f^T \left(-\mathbf{m}^T \cdot \mathbf{N}_p \right) \, d\Omega^c \tag{E.27}$$

$$\mathbf{C}^{pu,e} = \int_{\Omega^c} \left[\mathbf{N}_p^T \cdot \{\mathbf{\Phi}^p\} \; \alpha \; \tilde{\mathbf{B}} \cdot \dot{\mathbf{u}}^e - \mathbf{N}_p^T \cdot \frac{M^p}{M^m} k_1^f \left(\frac{\partial\{\mathbf{T}^p\}}{\partial\{\dot{\mathbf{E}}\}} \cdot \mathbf{F}^m \cdot \mathbf{B} \right) \frac{\tilde{\phi}^m}{\tilde{\phi}^f} \right] \, d\Omega^c \tag{E.28}$$

$$\mathbf{C}^{pf,e} = \int_{\Omega^c} \mathbf{N}_p^T \cdot \{\mathbf{\Phi}^p\} \; \beta \; \mathbf{N}_f \, d\Omega^c \tag{E.29}$$

$$\mathbf{C}^{pp,e} = \int_{\Omega^c} \mathbf{N}_p^T \cdot \mathbf{N}_p \, d\Omega^c \tag{E.30}$$

Appendix F

Computing the details of equations (6.74)-(6.76)

substrate:

$$\int_{\Omega^s} \omega^s \left(\frac{\partial T_r^s}{\partial r^s} + \frac{T_r^s - T_\theta^s}{r^s} + \frac{1}{h^s} \gamma c^H k^a \left(u^c - u^s \right) \right) r^s dr^s = 0 \tag{F.1}$$

$$\int_{\Omega^s} \left[\frac{\partial}{\partial r^s} \left(\omega^s r^s T_r^s \right) - \frac{\partial}{\partial r^s} \left(\omega^s r^s \right) T_r^s + \omega^s T_r^s - \omega^s T_\theta^s + \omega^s r^s \frac{1}{h^s} \gamma c^H k^a \left(u^c - u^s \right) \right] dr^s = 0 \tag{F.2}$$

$$\int_{\Omega^s} \left[\frac{\partial \omega^s}{\partial r^s} r^s T_r^s + \omega^s T_\theta^s - \omega^s r^s \frac{1}{h^s} \gamma c^H k^a \left(u^c - u^s \right) \right] dr^s = \left[\omega^s r^s T_r^s \right]_{r^s = a^s} = 0 \tag{F.3}$$

$$\begin{aligned} \int_{\Omega^s} \Bigg[& \frac{\partial \omega^s}{\partial r^s} r^s \tilde{T}_r^s + \omega^s \tilde{T}_\theta^s - \omega^s r^s \frac{1}{h^s} \gamma \tilde{c}^H k^a \left(\tilde{u}^c - \tilde{u}^s \right) \\ & + \frac{\partial \omega^s}{\partial r^s} r^s \left(\frac{E^s}{1 - \nu^{s2}} \left(\delta \varepsilon_r^s + \nu^s \delta \varepsilon_\theta^s \right) \right) + \omega^s \left(\frac{E^s}{1 - \nu^{s2}} \left(\nu^s \delta \varepsilon_r^s + \delta \varepsilon_\theta^s \right) \right) \\ & - \omega^s r^s \frac{1}{h^s} \gamma \ \delta c^H k^a \left(\tilde{u}^c - \tilde{u}^s \right) - \omega^s r^s \frac{1}{h^s} \gamma \tilde{c}^H k^a \left(\delta u^c - \delta u^s \right) \Bigg] dr^s = 0 \end{aligned} \tag{F.4}$$

$$\begin{aligned} \boldsymbol{\omega}^{s,eT} \int_{\Omega^s} \Bigg[& \mathbf{B}^T r^s \tilde{T}_r^s + \mathbf{N}^T \tilde{T}_\theta^s - \mathbf{N}^T r^s \frac{1}{h^s} \gamma \tilde{c}^H k^a \left(\tilde{u}^c - \tilde{u}^s \right) \\ & + \mathbf{B}^T r^s \left(\frac{E^s}{1 - \nu^{s2}} \left(\mathbf{B} \cdot \delta \mathbf{u}^{s,e} + \nu^s \frac{1}{r^s} \mathbf{N} \cdot \delta \mathbf{u}^{s,e} \right) \right) + \mathbf{N}^T \left(\frac{E^s}{1 - \nu^{s2}} \left(\nu^s \mathbf{B} \cdot \delta \mathbf{u}^{s,e} + \frac{1}{r^s} \mathbf{N} \cdot \delta \mathbf{u}^{s,e} \right) \right) \\ & - \mathbf{N}^T r^s \frac{1}{h^s} \gamma \ \mathbf{N} \cdot \delta \mathbf{c}^{H,e} k^a \left(\tilde{u}^c - \tilde{u}^s \right) - \mathbf{N}^T r^s \frac{1}{h^s} \gamma \tilde{c}^H k^a \left(\mathbf{N} \cdot \delta \mathbf{u}^{c,e} - \mathbf{N} \cdot \delta \mathbf{u}^{s,e} \right) \Bigg] dr^s = 0 \end{aligned} \tag{F.5}$$

$$\mathbf{F}^{s,e} = \int_{\Omega^s} \left[\mathbf{B}^T r^s \tilde{T}_r^s + \mathbf{N}^T \tilde{T}_\theta^s - \mathbf{N}^T r^s \frac{1}{h^s} \gamma \tilde{c}^H k^a \left(\tilde{u}^c - \tilde{u}^s \right) \right] dr^s \tag{F.6}$$

$$\begin{aligned} \mathbf{K}^{ss,e} &= \int_{\Omega^s} \left[\frac{E^s}{1-\nu^{s2}} \left(\mathbf{B}^T r^s \mathbf{B} + \mathbf{B}^T r^s \nu^s \frac{1}{r^s} \mathbf{N} + \nu^s \mathbf{N}^T \mathbf{B} + \frac{1}{r^s} \mathbf{N}^T \mathbf{N} \right) \right. \\ &+ \left. \mathbf{N}^T r^s \frac{1}{h^s} \gamma \tilde{c}^H k^a \mathbf{N} \right] dr^s \end{aligned} \tag{F.7}$$

$$\mathbf{K}^{su,e} = \int_{\Omega^s} -\mathbf{N}^T r^s \frac{1}{h^s} \gamma \tilde{c}^H k^a \mathbf{N} dr^s \tag{F.8}$$

$$\mathbf{K}^{sH,e} = -\int_{\Omega^s} \mathbf{N}^T r^s \frac{1}{h^s} \gamma \ \mathbf{N} k^a \left(\tilde{u}^c - \tilde{u}^s \right) \tag{F.9}$$

Cell:

$$\int_{\Omega^c} \omega^c \left(\frac{\partial T_r^c}{\partial r^c} + \frac{T_r^c - T_\theta^c}{r^c} + \frac{\partial T_r^{sf}}{\partial r^c} + \frac{T_r^{sf} - T_\theta^{sf}}{r^c} - \frac{\partial p}{\partial r^c} - \frac{1}{h^c} \gamma c^H k^a \left(u^c - u^s \right) \right) r^c dr^c = 0 \tag{F.10}$$

$$\begin{aligned} &\int_{\Omega^c} \left[\frac{\partial}{\partial r^c} \left(\omega^c r^c T_r^c \right) - \frac{\partial}{\partial r^c} \left(\omega^c r^c \right) T_r^c + \omega^c T_r^c - \omega^c T_\theta^c \right. \\ &+ \frac{\partial}{\partial r^c} \left(\omega^c r^c T_r^{sf} \right) - \frac{\partial}{\partial r^c} \left(\omega^c r^c \right) T_r^{sf} + \omega^c T_r^{sf} - \omega^c T_\theta^{sf} \\ &\left. - \omega^c r^c \frac{\partial p}{\partial r^c} - \omega^c r^c \frac{1}{h^c} \gamma c^H k^a \left(u^c - u^s \right) \right] dr^c = 0 \end{aligned} \tag{F.11}$$

$$\begin{aligned} &\int_{\Omega^c} \left[\frac{\partial \omega^c}{\partial r^c} r^c T_r^c + \omega^c T_\theta^c + \frac{\partial \omega^c}{\partial r^c} r^c T_r^{sf} + \omega^c T_\theta^{sf} + \omega^c r^c \frac{\partial p}{\partial r^c} + \omega^c r^c \frac{1}{h^c} \gamma c^H k^a \left(u^c - u^s \right) \right] dr^c \\ &= \left[\omega^c r^c T_r^c + \omega^c r^c T_r^{sf} \right]_{r^c = a^c} = -\omega^c \left(T^\sigma + T_0^\sigma \right) \end{aligned} \tag{F.12}$$

$$\begin{aligned} &\int_{\Omega^c} \left[\frac{\partial \omega^c}{\partial r^c} r^c \tilde{T}_r^c + \omega^c \tilde{T}_\theta^c + \frac{\partial \omega^c}{\partial r^c} r^c \tilde{T}_r^{sf} + \omega^c \tilde{T}_\theta^{sf} + \omega^c r^c \frac{\partial \tilde{p}}{\partial r^c} + \omega^s r^c \frac{1}{h^c} \gamma \tilde{c}^H k^a \left(\tilde{u}^c - \tilde{u}^s \right) \right. \\ &+ \frac{\partial \omega^c}{\partial r^c} r^c \left(\frac{E^c}{1-\nu^{c2}} \left(\delta \varepsilon_r^c + \nu^c \delta \varepsilon_\theta^c \right) + \frac{\nu^c}{1-\nu^c} \delta p \right) + \omega^c \left(\frac{E^c}{1-\nu^{c2}} \left(\nu^c \delta \varepsilon_r^c + \delta \varepsilon_\theta^c \right) + \frac{\nu^c}{1-\nu^c} \delta p \right) \\ &+ \frac{\partial \omega^c}{\partial r^c} r^c \delta \phi_r^{sf} \left(E_1 \tilde{\varepsilon}_r^c + T^* \right) + \frac{\partial \omega^c}{\partial r^c} r^c \tilde{\phi}_r^{sf} E_1 \delta \varepsilon_r^c + \omega^c \delta \phi_\theta^{sf} \left(E_1 \tilde{\varepsilon}_\theta^c + T^* \right) + \omega^c \tilde{\phi}_\theta^{sf} E_1 \delta \varepsilon_\theta^c + \omega^c r^c \frac{\partial \delta p}{\partial r^c} \\ &\left. + \omega^c r^c \frac{1}{h^c} \gamma \ \delta c^H k^a \left(\tilde{u}^c - \tilde{u}^s \right) + \omega^c r^c \frac{1}{h^c} \gamma \tilde{c}^H k^a \left(\delta u^c - \delta u^s \right) \right] dr^c + \omega^c \left(\tilde{T}^\sigma + T_0^\sigma \right) + \omega^c \delta T^\sigma = 0 \end{aligned} \tag{F.13}$$

$$\boldsymbol{\omega}^{c,eT}\int_{\Omega^c}\Bigg[\mathbf{B}^T r^c\tilde{T}_r^c+\mathbf{N}^T\tilde{T}_\theta^c+\mathbf{B}^T r^c\tilde{T}_r^{sf}+\mathbf{N}^T\tilde{T}_\theta^{sf}+\mathbf{N}^T r^c\mathbf{B}\mathbf{p}^e+\mathbf{N}^T r^c\frac{1}{h^c}\gamma\tilde{c}^H k^a\left(\tilde{u}^c-\tilde{u}^s\right)$$
$$+\mathbf{B}^T r^c\left(\frac{E^c}{1-\nu^{c2}}\left(\mathbf{B}\cdot\delta\mathbf{u}^{c,e}+\nu^s\frac{1}{r^c}\mathbf{N}\cdot\delta\mathbf{u}^{c,e}\right)+\frac{\nu^c}{1-\nu^c}\mathbf{N}\delta\mathbf{p}^e\right)$$
$$+\mathbf{N}^T\left(\frac{E^c}{1-\nu^{c2}}\left(\nu^c\mathbf{B}\cdot\delta\mathbf{u}^{c,e}+\frac{1}{r^c}\mathbf{N}\cdot\delta\mathbf{u}^{c,e}\right)+\frac{\nu^c}{1-\nu^c}\mathbf{N}\delta\mathbf{p}^e\right)$$
$$+\mathbf{B}^T r^c\mathbf{N}\delta\boldsymbol{\phi}_r^{sf,e}\left(E_1\tilde{\varepsilon}_r^c+T^*\right)+\mathbf{B}^T r^c\tilde{\phi}_r^{sf}E_1\mathbf{B}\cdot\delta\mathbf{u}^{c,e}$$
$$+\mathbf{N}^T\mathbf{N}\delta\boldsymbol{\phi}_\theta^{sf,e}\left(E_1\tilde{\varepsilon}_\theta^c+T^*\right)+\mathbf{N}^T\tilde{\phi}_\theta^{sf}E_1\frac{1}{r^c}\mathbf{N}\cdot\delta\mathbf{u}^{c,e}+\mathbf{N}^T r^c\mathbf{B}\delta\mathbf{p}^e$$
$$+\mathbf{N}^T r^c\frac{1}{h^c}\gamma\ \mathbf{N}\cdot\delta\mathbf{c}^{H,e}k^a\left(\tilde{u}^c-\tilde{u}^s\right)+\mathbf{N}^T r^c\frac{1}{h^c}\gamma\tilde{c}^H k^a\left(\mathbf{N}\cdot\delta\mathbf{u}^{c,e}-\mathbf{N}\cdot\delta\mathbf{u}^{s,e}\right)\Bigg]\,dr^c$$
$$+\boldsymbol{\omega}^{c,eT}\left(\mathbf{N}^T\left(\tilde{T}^\sigma+T_0^\sigma\right)+\mathbf{N}^T k^\sigma\frac{1}{a_0^c}\mathbf{N}\delta\mathbf{u}^{c,e}\left(\frac{3a^{c2}}{a_0^{c2}}-1\right)\right)=0 \tag{F.14}$$

$$\begin{aligned}
\mathbf{F}^{u,e} &= \int_{\Omega^c}\left[\mathbf{B}^T r^c\tilde{T}_r^c+\mathbf{N}^T\tilde{T}_\theta^{sf}\mathbf{B}^T r^c\tilde{T}_r^{sf}+\mathbf{N}^T\tilde{T}_\theta^c+\mathbf{N}^T r^c\frac{1}{h^c}\gamma\tilde{c}^H k^a\left(\tilde{u}^c-\tilde{u}^s\right)\right]dr^c \\
&+ \mathbf{N}^T\left(\tilde{T}^\sigma+T_0^\sigma\right) \qquad (F.15)\\
\mathbf{K}^{uu,e} &= \int_{\Omega^c}\left[\frac{E^c}{1-\nu^{c2}}\left(\mathbf{B}^T r^c\mathbf{B}+\mathbf{B}^T\nu^c\mathbf{N}+\nu^c\mathbf{N}^T\mathbf{B}+\frac{1}{r^c}\mathbf{N}^T\mathbf{N}\right)\right. \\
&+ \left.\mathbf{B}^T r^c\tilde{\phi}_r^{sf}E_1\mathbf{B}+\mathbf{N}^T\tilde{\phi}_\theta^{sf}E_1\frac{1}{r^c}\mathbf{N}+\mathbf{N}^T r^c\frac{1}{h^c}\gamma\tilde{c}^H k^a\mathbf{N}\right]\ dr^c \\
&+ \mathbf{N}^T k^\sigma\frac{1}{a_0^c}\mathbf{N}\left(\frac{3a^{c2}}{a_0^{c2}}-1\right) \qquad (F.16)\\
\mathbf{K}^{us,e} &= \int_{\Omega^c}-\mathbf{N}^T r^c\frac{1}{h^c}\gamma\tilde{c}^H k^a\mathbf{N}\ dr^c \qquad (F.17)\\
\mathbf{K}^{up,e} &= \int_{\Omega^c}\left[\mathbf{N}^T r^c\mathbf{B}+\mathbf{B}^T r^c\frac{\nu^c}{1-\nu^c}\mathbf{N}+\mathbf{N}^T\frac{\nu^c}{1-\nu^c}\mathbf{N}\right]dr^c \qquad (F.18)\\
\mathbf{K}^{ur,e} &= \int_{\Omega^c}\mathbf{B}^T r^c\mathbf{N}\left(E_1\tilde{\varepsilon}_r^c+T^*\right)\ dr^c \qquad (F.19)\\
\mathbf{K}^{u\theta,e} &= \int_{\Omega^c}\mathbf{N}^T\mathbf{N}\left(E_1\tilde{\varepsilon}_\theta^c+T^*\right)\ dr^c \qquad (F.20)\\
\mathbf{K}^{uH,e} &= \int_{\Omega^c}\mathbf{N}^T r^c\frac{1}{h^c}\gamma\ \mathbf{N}k^a\left(\tilde{u}^c-\tilde{u}^s\right) \qquad (F.21)
\end{aligned}$$

Mixture Mass:

$$\int_{\Omega^c} \omega \left[\alpha \left(\frac{\partial \dot{u}^c}{\partial r^c} + \frac{\dot{u}^c}{r^c} \right) + \beta \dot{p} + \left(\frac{\partial J^f}{\partial r^c} + \frac{J^f}{r^c} \right) + \left(\frac{\partial J^m}{\partial r^c} + \frac{J^m}{r^c} \right) \right] r^c dr^c = 0 \tag{F.22}$$

$$\begin{aligned} \int_{\Omega^c} \Bigg[& \omega r^c \alpha \left(\frac{\partial \dot{u}^c}{\partial r^c} + \frac{\dot{u}^c}{r^c} \right) + \omega r^c \beta \dot{p} \\ & + \left(\frac{\partial}{\partial r^c} \left(\omega r^c J^f \right) - \frac{\partial \omega}{\partial r^c} r^c J^f \right) + \left(\frac{\partial}{\partial r^c} \left(\omega r^c J^m \right) - \frac{\partial \omega}{\partial r^c} r^c J^m \right) \Bigg] dr^c = 0 \end{aligned} \tag{F.23}$$

$$\int_{\Omega^c} \left[\omega r^c \alpha \left(\frac{\partial \dot{u}^c}{\partial r^c} + \frac{\dot{u}^c}{r^c} \right) + \omega r^c \beta \dot{p} - \frac{\partial \omega}{\partial r^c} r^c \left(J^f + J^m \right) \right] dr^c = -\omega a^c \left[J^f + J^m \right]_{r^c = a^c} \tag{F.24}$$

$$\begin{aligned} \int_{\Omega^c} \Bigg[& \omega r^c \alpha \left(\frac{\partial \dot{u}^c}{\partial r^c} + \frac{\dot{u}^c}{r^c} \right) + \omega r^c \beta \dot{p} - \frac{\partial \omega}{\partial r^c} r^c \left(\tilde{J}^f + \tilde{J}^m \right) \\ & + \frac{\partial \omega}{\partial r^c} r^c \frac{\kappa}{\mu} \frac{\partial \delta p}{\partial r^c} + \frac{\partial \omega}{\partial r^c} r^c \left(\frac{\kappa}{\mu} \frac{\partial \tilde{p}}{\partial r^c} \delta \phi_f^m + \tilde{\phi}_f^m \frac{\kappa}{\mu} \frac{\partial \delta p}{\partial r^c} + \tilde{\phi}_f^m D \frac{\partial \delta \phi_f^m}{\partial r^c} \right) \\ & - \frac{\partial \omega}{\partial r^c} r^c \left(D \frac{\partial \tilde{\phi}_f^m}{\partial r^c} \frac{1}{1 + \tilde{\phi}_f^m} \left(\delta \phi^c + \tilde{\phi}^f \delta \phi_f^m + \delta \phi_r^{sf} + \delta \phi_\theta^{sf} \right) \right) \Bigg] dr^c = -\omega a^c \left[J^f + J^m \right]_{r^c = a^c} \end{aligned} \tag{F.25}$$

$$\begin{aligned} \boldsymbol{\omega}^{eT} \int_{\Omega^c} \Bigg[& \mathbf{N}^T r^c \alpha \left(\mathbf{B} \dot{\mathbf{u}}^{c,e} + \frac{1}{r^c} \mathbf{N} \dot{\mathbf{u}}^{c,e} \right) + \mathbf{N}^T r^c \beta \mathbf{N} \dot{\mathbf{p}}^e - \mathbf{B}^T r^c \left(\tilde{J}^f + \tilde{J}^m \right) \\ & + \mathbf{B}^T r^c \frac{\kappa}{\mu} \mathbf{B} \delta \mathbf{p}^e + \mathbf{B}^T r^c \left(\frac{\kappa}{\mu} \frac{\partial \tilde{p}}{\partial r^c} \mathbf{N} \delta \boldsymbol{\phi}_f^{m,e} + \tilde{\phi}_f^m \frac{\kappa}{\mu} \mathbf{B} \delta \mathbf{p}^e + \tilde{\phi}_f^m D \mathbf{B} \delta \boldsymbol{\phi}_f^{m,e} \right) \\ & - \mathbf{B}^T r^c \left(D \frac{\partial \tilde{\phi}_f^m}{\partial r^c} \frac{1}{1 + \tilde{\phi}_f^m} \left(\mathbf{N} \delta \boldsymbol{\phi}^{c,e} + \tilde{\phi}^f \mathbf{N} \delta \boldsymbol{\phi}_f^{m,e} + \mathbf{N} \delta \boldsymbol{\phi}_r^{sf,e} + \mathbf{N} \delta \boldsymbol{\phi}_\theta^{sf,e} \right) \right) \Bigg] dr^c \\ & = -\boldsymbol{\omega}^{eT} \mathbf{N}^T a^c \left[J^f + J^m \right]_{r^c = a^c} \end{aligned} \tag{F.26}$$

$$\mathbf{F}^m = \int_{\Omega^c} -\mathbf{B}^T r^c \left(\tilde{J}^f + \tilde{J}^m\right) dr^c + \mathbf{N}^T a^c \left[J^f + J^m\right]_{r^c=a^c} \tag{F.27}$$

$$\mathbf{C}^{mu} = \int_{\Omega^c} \mathbf{N}^T r^c \alpha \left(\mathbf{B} + \frac{1}{r^c}\mathbf{N}\right) dr^c \tag{F.28}$$

$$\mathbf{C}^{mp} = \int_{\Omega^c} \mathbf{N}^T r^c \beta \mathbf{N} dr^c \tag{F.29}$$

$$\mathbf{K}^{mm} = \int_{\Omega^c} \left[\mathbf{B}^T r^c \left(\frac{\kappa}{\mu}\frac{\partial \tilde{p}}{\partial r^c}\mathbf{N} + \tilde{\phi}_f^m D\mathbf{B}\right) - \mathbf{B}^T r^c \left(D\frac{\partial \tilde{\phi}_f^m}{\partial r^c}\frac{1}{1+\tilde{\phi}_f^m}\tilde{\phi}^f \mathbf{N}\right)\right] dr^c \tag{F.30}$$

$$\mathbf{K}^{mr} = \int_{\Omega^c} -\mathbf{B}^T r^c \left(D\frac{\partial \tilde{\phi}_f^m}{\partial r^c}\frac{1}{1+\tilde{\phi}_f^m}\mathbf{N}\right) dr^c \tag{F.31}$$

$$\mathbf{K}^{m\theta} = \int_{\Omega^c} -\mathbf{B}^T r^c \left(D\frac{\partial \tilde{\phi}_f^m}{\partial r^c}\frac{1}{1+\tilde{\phi}_f^m}\mathbf{N}\right) dr^c \tag{F.32}$$

$$\mathbf{K}^{mp} = \int_{\Omega^c} \mathbf{B}^T r^c \frac{\kappa}{\mu}\mathbf{B}\left(1+\tilde{\phi}_f^m\right) dr^c \tag{F.33}$$

$$\mathbf{K}^{mc} = \int_{\Omega^c} -\mathbf{B}^T r^c \left(D\frac{\partial \tilde{\phi}_f^m}{\partial r^c}\frac{1}{1+\tilde{\phi}_f^m}\mathbf{N}\right) dr^c \tag{F.34}$$

Cytosol Mass:

$$\int_{\Omega^c} \omega \left[\dot{\phi}^f + \alpha\phi^f\left(\frac{\partial \dot{u}^c}{\partial r^c} + \frac{\dot{u}^c}{r^c}\right) + \beta\phi^f\dot{p} + \left(\frac{\partial J^f}{\partial r^c} + \frac{J^f}{r^c}\right)\right] r^c dr^c = 0 \tag{F.35}$$

$$\int_{\Omega^c} \left[\omega r^c\dot{\phi}^f + \omega r^c\alpha\phi^f\left(\frac{\partial \dot{u}^c}{\partial r^c} + \frac{\dot{u}^c}{r^c}\right) + \omega r^c\beta\phi^f\dot{p} + \left(\frac{\partial}{\partial r^c}\left(\omega r^c J^f\right) - \frac{\partial \omega}{\partial r^c}r^c J^f\right)\right] dr^c = 0 \tag{F.36}$$

$$\int_{\Omega^c} \left[\omega r^c\dot{\phi}^f + \omega r^c\alpha\phi^f\left(\frac{\partial \dot{u}^c}{\partial r^c} + \frac{\dot{u}^c}{r^c}\right) + \omega r^c\beta\phi^f\dot{p} - \frac{\partial \omega}{\partial r^c}r^c J^f\right] dr^c = -\omega a^c\left[J^f\right]_{r^c=a^c} \tag{F.37}$$

$$\int_{\Omega^c} \left[-\omega r^c\frac{1}{1+\phi_f^m}\left(\dot{\phi}^c + \tilde{\phi}^f\dot{\phi}_f^m + \dot{\phi}_r^{sf} + \dot{\phi}_\theta^{sf}\right) + \omega r^c\alpha\tilde{\phi}^f\left(\frac{\partial \dot{u}^c}{\partial r^c} + \frac{\dot{u}^c}{r^c}\right) + \omega r^c\beta\tilde{\phi}^f\dot{p} - \frac{\partial \omega}{\partial r^c}r^c\tilde{J}^f + \frac{\partial \omega}{\partial r^c}r^c\frac{\kappa}{\mu}\frac{\partial \delta p}{\partial r^c}\right] dr^c = -\omega a^c\left[J^f\right]_{r^c=a^c} \tag{F.38}$$

$$\boldsymbol{\omega}^{eT}\int_{\Omega^c}\left[-\mathbf{N}^T r^c\frac{1}{1+\phi_f^m}\left(\mathbf{N}\dot{\boldsymbol{\phi}}^c+\tilde{\phi}^f\mathbf{N}\dot{\boldsymbol{\phi}}_f^m+\mathbf{N}\dot{\boldsymbol{\phi}}_r^{sf}+\mathbf{N}\dot{\boldsymbol{\phi}}_\theta^{sf}\right)\right.$$
$$\left.+\mathbf{N}^T r^c\alpha\tilde{\phi}^f\left(\mathbf{B}\dot{\mathbf{u}}^{c,e}+\frac{1}{r^c}\mathbf{N}\dot{\mathbf{u}}^{c,e}\right)+\mathbf{N}^T r^c\beta\tilde{\phi}^f\mathbf{N}\dot{\mathbf{p}}^e-\mathbf{B}^T r^c\tilde{J}^f+\mathbf{B}^T r^c\frac{\kappa}{\mu}\mathbf{B}\delta\mathbf{p}^e\right]dr^c$$
$$=-\boldsymbol{\omega}^{eT}\mathbf{N}^T a^c\left[J^f\right]_{r^c=a^c} \quad \text{(F.39)}$$

$$\mathbf{F}^f = \int_{\Omega^c}-\mathbf{B}^T r^c\tilde{J}^f dr^c+\mathbf{N}^T a^c\left[J^f\right]_{r^c=a^c} \quad \text{(F.40)}$$

$$\mathbf{C}^{fu} = \int_{\Omega^c}\mathbf{N}^T r^c\alpha\tilde{\phi}^f\left(\mathbf{B}+\frac{1}{r^c}\mathbf{N}\right)dr^c \quad \text{(F.41)}$$

$$\mathbf{C}^{fm} = \int_{\Omega^c}-\mathbf{N}^T r^c\frac{1}{1+\tilde{\phi}_f^m}\mathbf{N}dr^c \quad \text{(F.42)}$$

$$\mathbf{C}^{fr} = \int_{\Omega^c}-\mathbf{N}^T r^c\frac{1}{1+\tilde{\phi}_f^m}\mathbf{N}dr^c \quad \text{(F.43)}$$

$$\mathbf{C}^{f\theta} = \int_{\Omega^c}-\mathbf{N}^T r^c\frac{1}{1+\tilde{\phi}_f^m}\mathbf{N}dr^c \quad \text{(F.44)}$$

$$\mathbf{C}^{fc} = \int_{\Omega^c}-\mathbf{N}^T r^c\frac{1}{1+\tilde{\phi}_f^m}\mathbf{N}dr^c \quad \text{(F.45)}$$

$$\mathbf{C}^{ff} = \int_{\Omega^c}\mathbf{N}^T r^c\beta\tilde{\phi}^f\mathbf{N}dr^c \quad \text{(F.46)}$$

$$\mathbf{K}^{mm} = \int_{\Omega^c}\mathbf{B}^T r^c\frac{\kappa}{\mu}\mathbf{B}dr^c \quad \text{(F.47)}$$

Cytoskeleton-monomer chemical potential

$$\int_{\Omega^c}\omega\left[\mu^c-\mu^m\right]r^c dr^c=0 \quad \text{(F.48)}$$

$$\int_{\Omega^c}\omega\left[\Delta\mu_0^p+k_BT\left(ln(\phi^c)-ln(\phi^m)\right)\right]r^c dr^c=0 \quad \text{(F.49)}$$

$$\int_{\Omega^c}\left[\omega r^c\Delta\mu_0^p+\omega r^c k_BT\left(ln(\tilde{\phi}^c)-ln(\tilde{\phi}^m)\right)+\omega r^c k_BT\left(\frac{1}{\tilde{\phi}^c}\delta\phi^c-\frac{1}{\tilde{\phi}^m}\delta\phi^m\right)\right]dr^c=0 \quad \text{(F.50)}$$

$$\boldsymbol{\omega}^{eT}\int_{\Omega^c}\Big[\mathbf{N}^T r^c\Delta\mu_0^p+\mathbf{N}^T r^c k_BT\left(ln(\tilde{\phi}^c)-ln(\tilde{\phi}^m)\right)$$
$$+\mathbf{N}^T r^c k_BT\left(\frac{1}{\tilde{\phi}^c}\mathbf{N}\delta\boldsymbol{\phi}^c-\frac{1}{\tilde{\phi}^m}\mathbf{N}\delta\boldsymbol{\phi}^m\right)\Big]dr^c=0 \tag{F.51}$$

$$\mathbf{F}^c = \int_{\Omega^c}\Big[\mathbf{N}^T r^c\Delta\mu_0^p+\mathbf{N}^T r^c k_BT\left(ln(\tilde{\phi}^c)-ln(\tilde{\phi}^m)\right)\Big]dr^c \tag{F.52}$$

$$\mathbf{K}^{cc} = \int_{\Omega^c}\mathbf{N}^T r^c k_BT\frac{1}{\tilde{\phi}^c}\mathbf{N}dr^c \tag{F.53}$$

$$\mathbf{K}^{cm} = \int_{\Omega^c}-\mathbf{N}^T r^c k_BT\frac{1}{\tilde{\phi}^m}\mathbf{N}dr^c \tag{F.54}$$

radial stress fiber - monomer chemical potential

$$\int_{\Omega^c}\omega\left[\mu_r^{sf}-\mu^m\right]r^c dr^c=0 \tag{F.55}$$

$$\int_{\Omega^c}\omega\left[\Delta\mu_0^p+k_BT\left(ln(\phi_r^{sf})-ln(\phi^m)\right)+E_r^{sf}\right]r^c dr^c=0 \tag{F.56}$$

$$\int_{\Omega^c}\Big[\omega r^c\Delta\mu_0^p+\omega r^c k_BT\left(ln(\tilde{\phi}_r^{sf})-ln(\tilde{\phi}^m)\right)+\omega r^c\tilde{E}_r^{sf}$$
$$+\omega r^c k_BT\left(\frac{1}{\tilde{\phi}_r^{sf}}\delta\phi_r^{sf}-\frac{1}{\tilde{\phi}^m}\delta\phi^m\right)+\omega r^c V^{cu}\left(E_1\tilde{\varepsilon}_r^c-T^*\right)\delta\varepsilon_r^c\Big]dr^c=0 \tag{F.57}$$

$$\boldsymbol{\omega}^{eT}\int_{\Omega^c}\Big[\mathbf{N}^T r^c\Delta\mu_0^p+\mathbf{N}^T r^c k_BT\left(ln(\tilde{\phi}_r^{sf})-ln(\tilde{\phi}^m)\right)+\mathbf{N}^T r^c\tilde{E}_r^{sf}$$
$$+\mathbf{N}^T r^c k_BT\left(\frac{1}{\tilde{\phi}_r^{sf}}\mathbf{N}\delta\boldsymbol{\phi}_r^{sf}-\frac{1}{\tilde{\phi}^m}\mathbf{N}\delta\boldsymbol{\phi}^m\right)+\mathbf{N}^T r^c V^{cu}\left(E_1\tilde{\varepsilon}_r^c-T^*\right)\mathbf{B}\delta\mathbf{u}^{c,e}\Big]dr^c=0 \tag{F.58}$$

$$\mathbf{F}^r = \int_{\Omega^c} \left[\mathbf{N}^T r^c \Delta\mu_0^p + \mathbf{N}^T r^c k_B T \left(ln(\tilde{\phi}_r^{sf}) - ln(\tilde{\phi}^m)\right) + \mathbf{N}^T r^c \tilde{E}_r^{sf}\right] dr^c \quad \text{(F.59)}$$

$$\mathbf{K}^{ru} = \int_{\Omega^c} \mathbf{N}^T r^c V^{cu} \left(E_1 \tilde{\varepsilon}_r^c - T^*\right) \mathbf{B} dr^c \quad \text{(F.60)}$$

$$\mathbf{K}^{rr} = \int_{\Omega^c} \mathbf{N}^T r^c k_B T \frac{1}{\tilde{\phi}_r^{sf}} \mathbf{N} dr^c \quad \text{(F.61)}$$

$$\mathbf{K}^{rm} = \int_{\Omega^c} -\mathbf{N}^T r^c k_B T \frac{1}{\tilde{\phi}^m} \mathbf{N} dr^c \quad \text{(F.62)}$$

Similarly for θ stress fiber - G-actin monomer

$$\mathbf{F}^\theta = \int_{\Omega^c} \left[\mathbf{N}^T r^c \Delta\mu_0^p + \mathbf{N}^T r^c k_B T \left(ln(\tilde{\phi}_\theta^{sf}) - ln(\tilde{\phi}^m)\right) + \mathbf{N}^T r^c \tilde{E}_\theta^{sf}\right] dr^c \quad \text{(F.63)}$$

$$\mathbf{K}^{\theta u} = \int_{\Omega^c} \mathbf{N}^T r^c V^{cu} \left(E_1 \tilde{\varepsilon}_\theta^c - T^*\right) \frac{1}{r^c} \mathbf{N} dr^c \quad \text{(F.64)}$$

$$\mathbf{K}^{\theta\theta} = \int_{\Omega^c} \mathbf{N}^T r^c k_B T \frac{1}{\tilde{\phi}_\theta^{sf}} \mathbf{N} dr^c \quad \text{(F.65)}$$

$$\mathbf{K}^{\theta m} = \int_{\Omega^c} -\mathbf{N}^T r^c k_B T \frac{1}{\tilde{\phi}^m} \mathbf{N} dr^c \quad \text{(F.66)}$$

Integrin Mass:

$$\int_{\Omega^c} \omega \left[\left(\dot{c}^L + \dot{c}^H\right) + \left(c^L + c^H\right) \left(\frac{\partial \dot{u}^c}{\partial r^c} + \frac{\dot{u}^c}{r^c}\right) + \left(\frac{\partial J^L}{\partial r^c} + \frac{J^L}{r^c}\right)\right] r^c dr^c = 0 \quad \text{(F.67)}$$

$$\int_{\Omega^c} \left[\omega r^c \left(\dot{c}^L + \dot{c}^H\right) + \omega r^c \left(c^L + c^H\right) \left(\frac{\partial \dot{u}^c}{\partial r^c} + \frac{\dot{u}^c}{r^c}\right) + \left(\frac{\partial}{\partial r^c}\left(\omega r^c J^L\right) - \frac{\partial \omega}{\partial r^c} r^c J^L\right)\right] dr^c = 0 \quad \text{(F.68)}$$

$$\int_{\Omega^c} \left[\omega r^c \left(\dot{c}^L + \dot{c}^H\right) + \omega r^c \left(c^L + c^H\right) \left(\frac{\partial \dot{u}^c}{\partial r^c} + \frac{\dot{u}^c}{r^c}\right) - \frac{\partial \omega}{\partial r^c} r^c J^L\right] dr^c = -\omega a^c \left[J^L\right]_{r^c = a^c} \quad \text{(F.69)}$$

$$\int_{\Omega^c} \left[\omega r^c \left(\dot{c}^L + \dot{c}^H\right) + \omega r^c \left(c^L + c^H\right) \left(\frac{\partial \dot{u}^c}{\partial r^c} + \frac{\dot{u}^c}{r^c}\right) - \frac{\partial \omega}{\partial r^c} r^c \tilde{J}^L + \frac{\partial \omega}{\partial r^c} r^c m \frac{\partial \delta c^L}{\partial r^c}\right] dr^c = -\omega a^c \left[J^L\right]_{r^c = a^c} \quad \text{(F.70)}$$

$$\boldsymbol{\omega}^{eT}\int_{\Omega^c}\left[\mathbf{N}^T r^c\left(\mathbf{N}\dot{\mathbf{c}}^{L,e}+\mathbf{N}\dot{\mathbf{c}}^{H,e}\right)\right.$$
$$\left.+\mathbf{N}^T r^c\left(\tilde{c}^L+\tilde{c}^H\right)\left(\mathbf{B}\dot{\mathbf{u}}^{c,e}+\frac{1}{r^c}\mathbf{N}\dot{\mathbf{u}}^{c,e}\right)-\mathbf{B}^T r^c\tilde{J}^L+\mathbf{B}^T r^c m\mathbf{B}\delta\mathbf{c}^{L,e}\right]dr^c$$
$$=-\boldsymbol{\omega}^{eT}\mathbf{N}^T a^c\left[J^L\right]_{r^c=a^c} \tag{F.71}$$

$$\mathbf{F}^L = \int_{\Omega^c}-\mathbf{B}^T r^c\tilde{J}^L dr^c+\mathbf{N}^T a^c\left[J^L\right]_{r^c=a^c} \tag{F.72}$$

$$\mathbf{C}^{Lu} = \int_{\Omega^c}\mathbf{N}^T r^c\left(\tilde{c}^L+\tilde{c}^H\right)\left(\mathbf{B}+\frac{1}{r^c}\mathbf{N}\right)dr^c \tag{F.73}$$

$$\mathbf{C}^{LL} = \int_{\Omega^c}-\mathbf{N}^T r^c\mathbf{N}dr^c \tag{F.74}$$

$$\mathbf{C}^{LH} = \int_{\Omega^c}-\mathbf{N}^T r^c\mathbf{N}dr^c \tag{F.75}$$

$$\mathbf{K}^{LL} = \int_{\Omega^c}\mathbf{B}^T r^c m\mathbf{B}dr^c \tag{F.76}$$

H - L chemical potential

$$\int_{\Omega^c}\omega\left[\mu^H-\mu^L\right]r^c dr^c=0 \tag{F.77}$$

$$\int_{\Omega^c}\omega\left[\Delta\mu_0^I+k_BT\left(ln(c^H)-ln(c^L)\right)+E^H\right]r^c dr^c=0 \tag{F.78}$$

$$\int_{\Omega^c}\left[\omega r^c\Delta\mu_0^I+\omega r^c k_BT\left(ln(\tilde{c}^H)-ln(\tilde{c}^L)\right)+\omega r^c\tilde{E}^H\right.$$
$$\left.+\omega r^c k_BT\left(\frac{1}{\tilde{c}^H}\delta c^H-\frac{1}{\tilde{c}^L}\delta c^L\right)-\omega r^c\gamma k^a\left(\tilde{u}^c-\tilde{u}^s\right)\delta u^c+\omega r^c\gamma k^a\left(\tilde{u}^c-\tilde{u}^s\right)\delta u^s\right]dr^c=0 \tag{F.79}$$

$$\boldsymbol{\omega}^{eT}\int_{\Omega^c}\left[\mathbf{N}^T r^c\Delta\mu_0^I+\mathbf{N}^T r^c k_BT\left(ln(\tilde{c}^H)-ln(\tilde{c}^L)\right)+\mathbf{N}^T r^c\tilde{E}^H+\mathbf{N}^T r^c k_BT\left(\frac{1}{\tilde{c}^H}\mathbf{N}\delta\mathbf{c}^H-\frac{1}{\tilde{c}^L}\mathbf{N}\delta\mathbf{c}^L\right)\right.$$
$$\left.-\mathbf{N}^T r^c\gamma k^a\left(\tilde{u}^c-\tilde{u}^s\right)\mathbf{N}\delta\mathbf{u}^{c,e}+\mathbf{N}^T r^c\gamma k^a\left(\tilde{u}^c-\tilde{u}^s\right)\mathbf{N}\delta\mathbf{u}^{s,e}\right]dr^c=0 \tag{F.80}$$

$$\mathbf{F}^H = \int_{\Omega^c} \left[\mathbf{N}^T r^c \Delta\mu_0^I + \mathbf{N}^T r^c k_B T \left(ln(\tilde{c}^H) - ln(\tilde{c}^L) \right) + \mathbf{N}^T r^c \tilde{E}^H \right] dr^c \quad \text{(F.81)}$$

$$\mathbf{K}^{Hs} = \int_{\Omega^c} \mathbf{N}^T r^c \gamma k^a \left(\tilde{u}^c - \tilde{u}^s \right) \mathbf{N} dr^c \quad \text{(F.82)}$$

$$\mathbf{K}^{Hu} = \int_{\Omega^c} -\mathbf{N}^T r^c \gamma k^a \left(\tilde{u}^c - \tilde{u}^s \right) \mathbf{N} dr^c \quad \text{(F.83)}$$

$$\mathbf{K}^{HH} = \int_{\Omega^c} \mathbf{N}^T r^c k_B T \frac{1}{\tilde{c}^H} \mathbf{N} dr^c \quad \text{(F.84)}$$

$$\mathbf{K}^{HL} = \int_{\Omega^c} -\mathbf{N}^T r^c k_B T \frac{1}{\tilde{c}^L} \mathbf{N} dr^c \quad \text{(F.85)}$$